Surface Chemistry Of Lead and Lead Free Metal Halide Nanocrystals

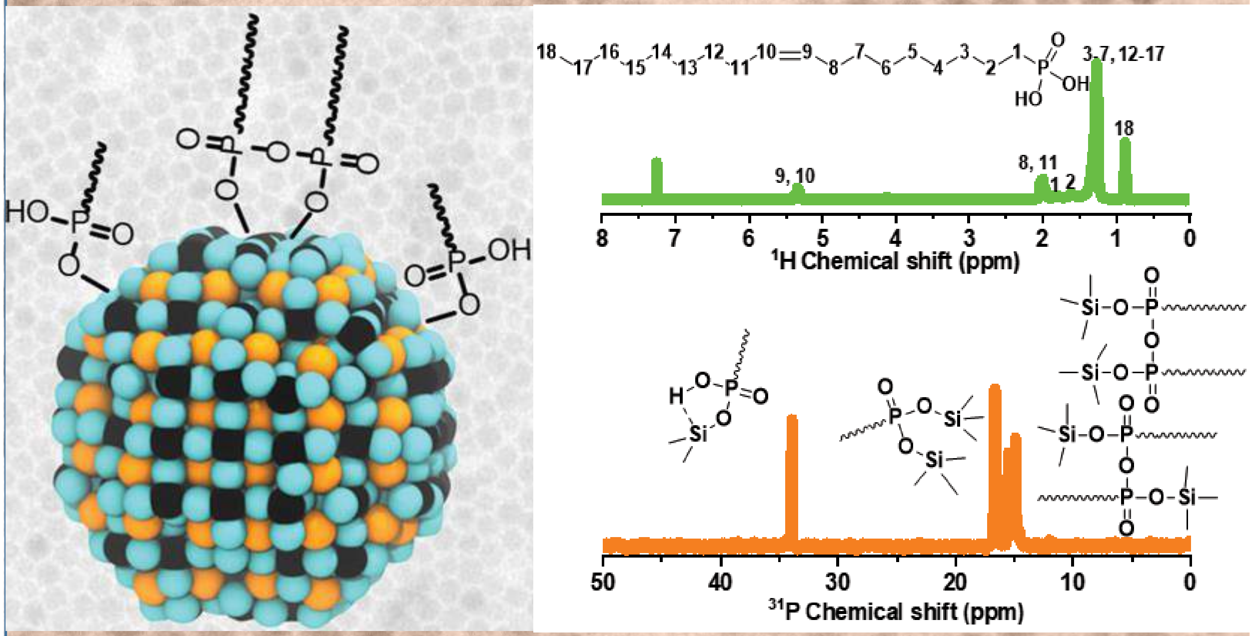

Baowei Zhang

Surface Chemistry of Lead and Lead Free Metal Halides Nanocrystals:

About the cover: **Surface chemistry is the key concept of nano sized materials. The cover figure draw how the phosphonic acid bind with the surface of CsPbBr3 nanocrystals and its influence on morphology.**

PhD Thesis, Università degli Studi di Genova,

All research was conducted at the Istituto Italiano di Tecnologia, Genova.

Tutor: Liberato Manna (IIT)
Co-tutors: Luca De Trizio (IIT) and Ferretti Maurizio (Unige)

Author: Baowei Zhang

8th of October 2021.

Table of Contents

Chapter 1: Surface Chemistry of Colloidal Nanocrystals

Abstract: Surface could be defined as any interface between two phases.[1-5] The concept of surface science was first derived from the heterogeneous catalyst chemistry. In hydrogenation processes, the surface of the metal catalyst was found to be the most reactive point.[6] Nowadays, the surface chemistry is found to play key roles on various scientific fields including heterogeneous catalysis,[7] semiconductor,[8] fuel cells,[4] self-assemble behavior,[3] and adhesives.[2] Along the size reduction of given materials, the surface/volume ratio of the materials would increases, as shown in Figure 1-1. Up to a point, in nano-sized crystals where most of the atoms lie on the surface playing a key role on the nano materials' behavior. Here, we will specially introduce the concept of surface chemistry on colloidal semiconductor nanocrystals.[5, 8]

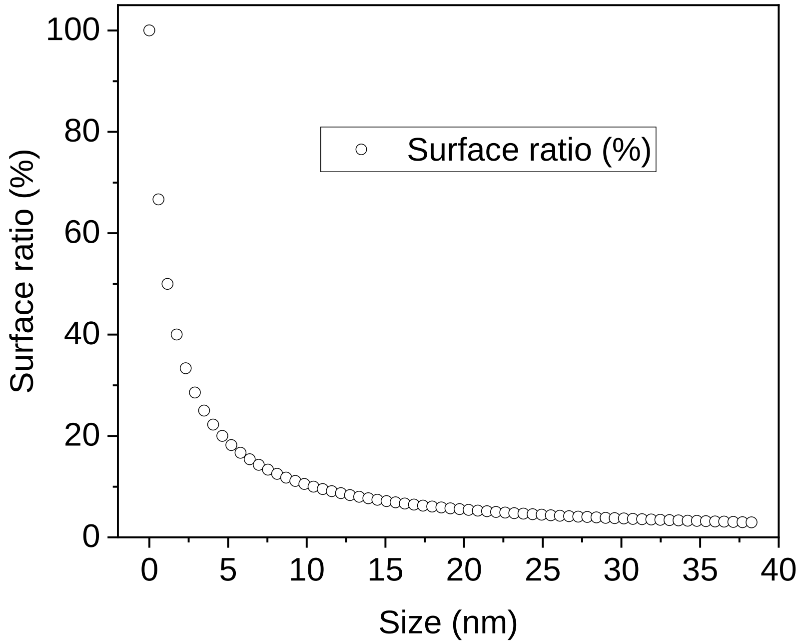

Figure 1-1. For a cubic $CsPbBr_3$ nanocrystals, the evolution of surface atomic ratio with size decreasing.

1.1 Definition of 'Surface' Concept of Colloidal Nanocrystals.

The first quantum dots could be traced to hundreds years ago. The ZnS or ZnSe doped SiO_2 matrix was used as colored glass. Until the early 90s of 20th century, By adjusting the cooling speed of melting SiO_2, the size of obtained CdSe nuclei could be adjusted. Quantum confinement effect was proposed for explaining the relation between the bandgap of CdSe embedded in SiO_2 matrix and its size.[9-10] Such size-confined CdSe or other semiconductor materials was also named as quantum dots. In the same period, the colloidal synthesis of quantum dots in solution was also developed and become the most widely used method for obtaining various type of nanocrystals (NCs) later on.[11] In the colloidal synthesis, the metal precursors, anions precursors, and long hydrocarbon surfactant were mixed into high boiling point apolar solvent. During the heating, firstly, the surfactant reacts with precursors to form monomers. In one side, the hydrocarbon part contributes mainly the solubility of monomer and keep the monomer colloidal dispersed in solution. In another side, the steric effect of the ligands slows down the aggregation rate of monomer and thus suppress the nucleation and growth. In proper condition, the nano-sized solid could be obtained in solution which confined by surface ligands. The obtained NCs could be described as composed of two parts: i) the inorganic crystalline core which contributes the intrinsic optical, magnetic properties but insoluble in apolar solvent; ii) the surface shell part, which usually the organic ligands with long hydrocarbon tail. The affinity between long hydrocarbon tail make the whole NCs well dispersed in the apolar solvent.[5] The well dispesed NCs is so called colloidal NCs. The colloidal NCs show significant advantage in various solution-based processes such as spin coating, dip coating, or inkjet printing and thus offer convienience for the fabrication of electronic and optoelectronic devices.For albeit solid-solvent system, the solid surface has a dynamic dissolution-absorption equilibrium with the solvent environment.[1] For colloidal NCs, as shown in Figure 1-2, the dynamic equilibrium usually exist between its ligands shell and free ligands in solvent. When the chemical potential of the free ligands is high in solution, ligands prefer bound to the surface of NC. When the chemical potential of the free ligands is low in solution, the ligands prefer dissolute from the NC's surface. As a result, the chemical potential of the ligands on the solid surface and in the solution would be approach to same value. The whole system reach a dynamic equilibrium by the dissolution-absorption of ligands. The dynamic ligands shell act as the interface between the solid NCs and the solution and play a key role on the colloidal stability, size, shape and electronic band structure of the NCs.[12]

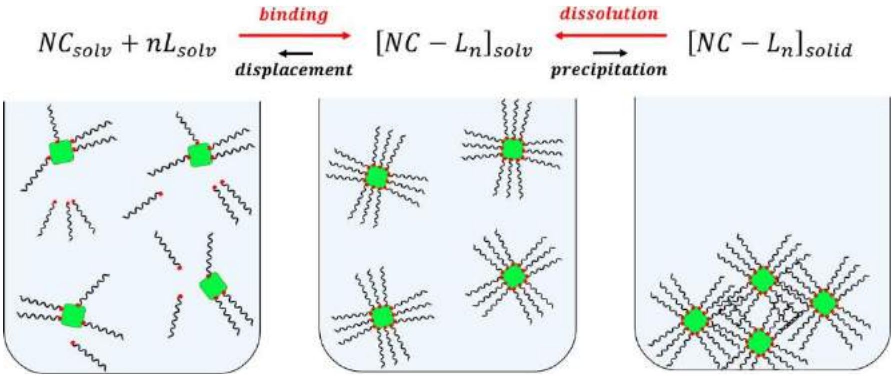

$$NC_{solv} + nL_{solv} \underset{displacement}{\overset{binding}{\rightleftharpoons}} [NC - L_n]_{solv} \underset{precipitation}{\overset{dissolution}{\rightleftharpoons}} [NC - L_n]_{solid}$$

Figure 1-2. Schematic representation of a comprehensive framework that includes (left) the binding/displacement of ligands at the nanocrystal surface in solution and (right) the precipitation/dissolution of nanocrystal–ligand complexes in organic solvents. Ideally, the first equilibrium should be pushed to the right and the second equilibrium to the left, toward the fully passivated nanocrystals in solution.[12]

1.2 Introduction of the Ligands Type.

Heritage from the concept of covalent bond classification method, ligands for colloidal nanocrystals could be sorted as X-, L- and Z-type, depending how many electrons they share in the bond of NC surface.[8, 13] As shown in Figure 1-3, X-type ligands are single-electron donors (anionic, including carboxylate acetate, phosphonate, sulfonate and various inorganic ions including Cl^-, $InCl^{4-}$, AsS_3^{3-}).[5] Some X-type ligands bound in ion pair, like tetraphenylborate cloride.[14] L-type ligands are two-electron donors (neutral Lewis bases, including various acid, amine, alcohol, thiol in their neutral form).[15] Z-type ligands are two-electron acceptors (Lewis acids, including metal halides, metal carboxylate acetate, metal thiocyanate…).[13] Ligand exchange reaction is important for altering the NCs' solubility, stability, conductivity and so on. Usually, the stronger X-type ligands (e.g., phosphonic acid, sulfonic acid) can easily replace the weaker X-type ligands (e.g., carboxylate acid).[16-17] As addition, other type ligand exchange could also happen in some special case. As X-type bound ion pair, DDABr could simultaneous exchange with CsBr on the surface of $CsPbBr_3$ NCs.[18] L-type ligands could also react with NCs to replace Z-type ligands of CdSe NCs.[13]

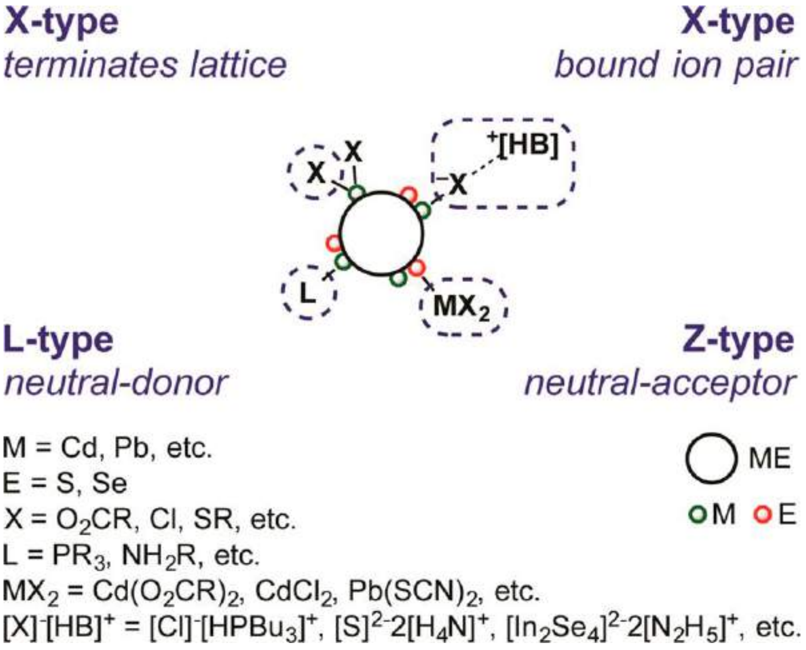

Figure 1-3. Nanocrystal Ligand Binding Motifs According to the Covalent Bond Classification Method.[8, 13]

1.3 Relationship between Surface Ligands and Physical-Chemistry Properties of Nanocrystals.

1.3.1 Correlation between surface ligands and NCs solubility.

Ligands play a key role on the solubility,[19-20] size,[21-23] morphology[24-27] and optical properties[28-29] of the colloidal nanocrystals. First, ligands solvation effect is the main driving force preventing the aggregation of colloidal NCs and thus determine their dispersibility in a given solvent.[12, 20] The solubility of the NCs in the given solvent depend on the free energy of the whole NCs dispersion system. As shown in Figure 1-4c, when the free energy of chain-solvent system is below zero, the hydrocarbon chains tend to repel each other and stabilizing NC dispersions. Conversely, when the chain–solvent has a positive energy, the solvent molecule will push the ligands chains together and cause aggregation of NCs.[12] Typically, hydrocarbon chain NCs favor in nonpolar solvent (eg. Hexane, toluene), while inorganic anions caped NCs favor polar solvent (eg. Methanol, water).[30] By changing the surface ligands from hydrocarbon (oleate) to inorganic anions (KS^-), CdSe nanocrystals can be dispersed either in toluene or formamide, respectively, as shown in Figure 1-4a, b.[31]

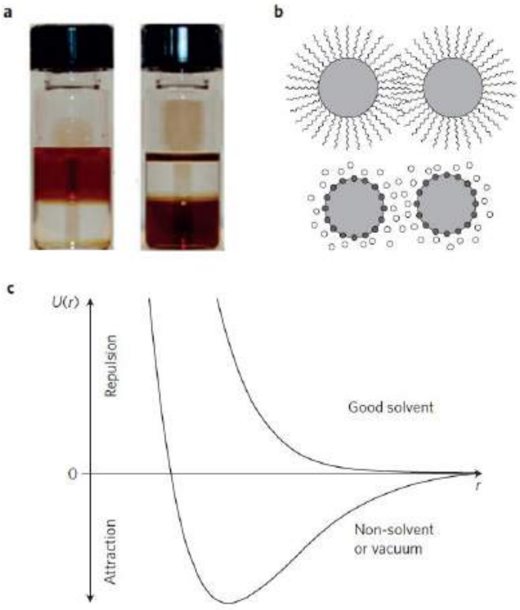

Figure 1-4. Dispersion of colloidal nanocrystals.[5] a) NCs can disperse in polar or nonpolar solvents by varying surface ligands. Eg. Oleate capped CdSe NCs disperse well in toluene, left. KS^- capped CdSe NCs disperse well in formamide, right. b) interaction between hydrocarbon capped NCs (top) and ionic ligands capped NCs (bottom). c) Evolution of interaction potential U following distance between two NCs (r) in a good solvent and non-solvent or vacuum, respectively.

Beside the enthalpy contributed by ligands-solvation interaction, the entropy of the ligands in the solvent also play a significant role on the solubility of the colloidal nanocrystals.[20] Bishop et al. have thoroughly considered all enthalpy and entropy terms for nanoparticle systems using classic colloidal models, which consider the ligands as a steric shell only. In that case, the enthalpy of ligands-ligands interaction in aggregated NCs is estimated to be below 2.5 kJ/mol, and the entropy change from aggregated NCs to dispersed NCs was below 1RT.[32] However, such model ignore the softness of ligands and its C−C σ-bond rotation and underestimate the actual enthalpy and entropy value.[20] To address such an issue, the entropy item of the rotation/bending of n-alkane chains also need to be included. Taking this parameter into account, the ligands-ligands interaction of the aggregated NCs is estimated as 80 kJ/mol, and the entropy change for NCs from aggregated to dispersed state is about 24RT. The significant entropy change attribute to the free of C−C σ-bond rotation in dispersed NCs from the restricted state in aggregated nanocrystals. The branched hydrocarbon ligands, which could maximize the free state of rotation/bend state (so called intramolecular entropy) and decrease the ligands-ligands interaction (the enthalpy item) at the same time, was so called ‘entropy ligand’. Such ‘entropy ligands’ could significantly decrease the free energy of NCs dispersion solution and thus enhance the solubility of NCs several magnitudes (10^3-10^4).[19-20] As addition, the mix of different chain length of hydrocarbon ligands could mimic the effect of branch ligands and could also be used as ‘entropy ligands’.[33-34]

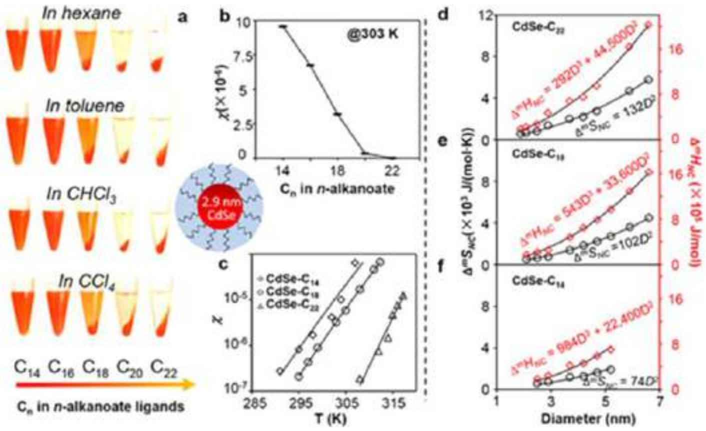

Figure 1-5. (a) Saturated CdSe NCs solutions in four common solvents with increasing carboxylate chain lendgth; (b) ligands chain length dependent solubility CdSe (2.9 nm) NCs in CCl4 at 303 K. (c) temperature-dependent solubility of CdSe (2.9 nm) NCs with three types of n-alkanoates. (d−f) Size-dependent enthalpy change ($\Delta^m H_{NC}$) and entropy change ($\Delta^m S_{NC}$) for three types of the CdSe−alkanoates complexes.[19]

1.3.2 Correlation between surface ligands and the size and morphology of colloidal nanocrystals.

Ligands also play a role on both the nucleation and growth process of nanocrystals and thus influence the final size and morphology of the nanocrystals.[21, 23] In classical nucleation theory, ligands firstly dissolve metal precursors and form metal-ligand complex. The complex release the monomers upon thermal decomposition in pre-nucleation stage. When the monomer's concentration is higher than its solubility (saturated) in given solvent, the system become unstable and have the potential to nuclei and growth solid NCs.[21, 35] For a nuclei, the formation of new phase is energy favored, so called ΔG_V, which is proportional to the volume of nuclei. As contrast, the new formed interface is not energy favored, so called $4\pi r^2\gamma$, which is proportional to the area of the nuclei. The free energy of nuclei could be described as equation (1). The saturation degree of the monomer is defined as super saturation (DS), which relate to ΔG_V. As shown in equation (2), the critical size of nuclei (r*) in a given temperature (T) is determined by the surface tension (γ) and super saturation of monomer (DS). High concentration of ligands or the strong affinity between metal and ligands could suppress the release of the monomer, and cause a slow nucleation and growth process. Such slow process usually produce smaller NCs. For example, shorter hydrocarbon ligands with less steric effect cause faster nucleation kinetic and larger NCs, as shown in Figure 1-6.[21, 35]

$$\Delta G = \frac{4}{3}\pi r^3 \Delta G_V + 4\pi r^2 \gamma \qquad (1);$$

$$r^* = -\frac{2\gamma}{\Delta G_V} = \frac{2\gamma V_m}{[RT ln(1+DS)]} \qquad (2).$$

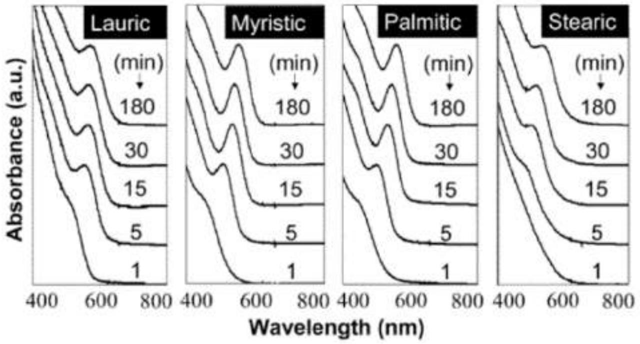

Figure 1-6. (a) Saturated CdSe NCs solutions in four common solvents with increasing carboxylate chain lendgth; (b) Ligands chain length dependent solubility CdSe (2.9 nm) NCs in CCl$_4$ at 303 K. (c) Temperature-dependent solubility of CdSe (2.9 nm) NCs with three types of n-alkanoates. (d−f) Size-dependent enthalpy change ($\Delta^m H_{NC}$) and entropy change ($\Delta^m S_{NC}$) for three types of the CdSe−alkanoates complexes.[21]

The concentration of ligands could also influence the final size of nanocrystals in a thermodynamic way.[36-38] Usually, smaller NCs due to its larger surface tension, has a higher chemical potential in its surface and thus more easy to dissolute back to monomer into solution. Such dissolution process could be suppressed, if the solution chemical potential of one part of the NCs (ligands, cations or anions) is also comparable high. As shown in Figure 1-7, small sized $CsPbBr_3$ nanocrystals is unstable and easily to grow lager in solution. By adding excess $ZnBr_2$ precursors during the synthesis, the stable small sized NCs was obtained.[37] Excess $ZnBr_2$ could release abundant Br^- and thus increase chemical potential of Br^- in solution ($\mu_{Br-,sol}$). The high $\mu_{Br-,sol}$ could balance the high $\mu_{Br-,sol}$ of small NCs and thus suppress the detachment of surface Br- ion. Additionally, high chemical potential of free ligands in solution can suppress ligands dissolution from surface and thus stabilize the NCs. Extremely concentrated ligands can capture the ultra-small clusters, which was viewed as pre-nucleation intermediate.[37]

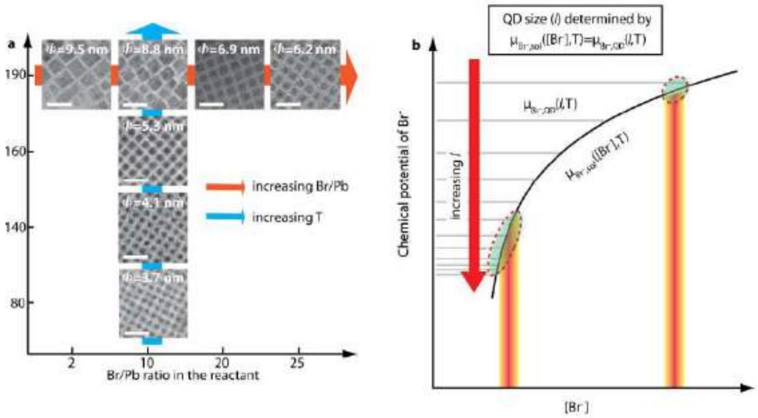

Figure 1-7. Size control via thermodynamic equilibrium in $CsPbBr_3$ QDs. a, Dependence of the QD size on Br/Pb ratio in the reactant and the reaction temperature. b, A simple model illustrating the determination of the QD size via equilibrium of Br- between the QD lattice and solution medium. The QD size (l) for a given Br- concentration ([Br-]) and temperature (T) is determined where the chemical potentials of Br- in the QD ($\mu_{Br-,sol}$, series of grey horizontal lines for different l) and in solution phase (($\mu_{Br-,sol}$, black curve) become equal.[37]

Surface ligands could also influence the morphology of nanocrystals both kinetically and thermodynamically.[24-25] The ligands could influence the free energy of facet and the growth rate, respectively. If the system grows slow enough, the final shape of NCs favor to expose the facets with lowest free energy. If the nucleation and grows rate is very quick, the shape depends on the adding rate of monomers on each specific facets. [25] For example, TOPO has a lower affinity with Cd^{2+}, while alkyl phosphonic acid has a strong affinity with Cd^{2+}. When only use TOPO as ligands, TOPO-Cd binding is too weak to avoid NCs aggregation and thus only obtained very large, insoluble CdSe nanorod as product. When add 1%-3% (weight ratio) hexalphosphonic acid (HPA) in the system, the overall growth rate became slow enough, the well-confined, thermodynamic favored spherical NCs was obtained. When increasing the HPA more to 10%-30%, the excess HPA lower down the $(0\bar{1}10)$ and $(1\bar{1}20)$ facets specifically and result in the isotropic CdSe nanorod.[25] In that case, the surface ligands influence the morphology of NCs in a thermodynamic way. There are a lot cases that the affinity between ligands and certain facets determined final shape of NCs. For example, shorter phosphonic acid like (PPA) favor in zinc blend (ZB) phase and longer phosphonic acid (ODPA) favor in wurtzite phase of CdSe.[24] by mixing the short PA and long PA in a proper ratio, we could obtain the unique tetrapod CdSe NCs, which has a zinc blend nuclei and four wurtzite branches.[24, 39] For lead halide perovskite, the alkyl ammonium cations has strong affinity with (001) facet of perovskite NCs, so we can only obtain cubic/platelet nanocrystals in oleylamine-acid environment.[14] When we avoid the use of alkyl amine, for example, using alkyl phosphonic acid as ligands or α-bromo ketone as halide reagent and under limited amount of ammonium ion, the polyhedron $CsPbBr_3$ nanocrystals exposed various facets could be obtained.[40-42] During the synthesis of CdSe nanoplatelets, introduce of several metal acetate (eg. $Zn(Ac)_2$, $Mn(Ac)_2$) in the Cd precursors is necessary.[43] The Cd precursor mixed with metal acetate salt could decrease the solubility of formed monomer in 1-ODE solvent and thus cause a significant higher chemical potential (or supersaturation) environment. Such high chemical potential environment is the key point to obtain isotropic shaped nanocrystals.[21, 43] Template effect of ligands could viewed as a special case of kinetic control of ligands on the morphology of NCs.[44-45] For example, the alkyl amine could easily form lamellar structure with metal cations. Such lamellar structure with gentle heating could transfer into nanoplatetes, as show in Figure 1-8.[45] Such template method is general method to obtain various II-VI semiconductor nanoplatelets.[46] In addition, the $CsPbBr_3$ cluster can be used as single precursors to obtain $CsPbBr_3$ NCs. The cluster itself also has a strong self-assemble tendency. With gentle heating, the cluster assemblies could transfer into various anisotropic $CsPbBr_3$ nanorod and nanoplatelets, as shown in Figure 1-9.[47]

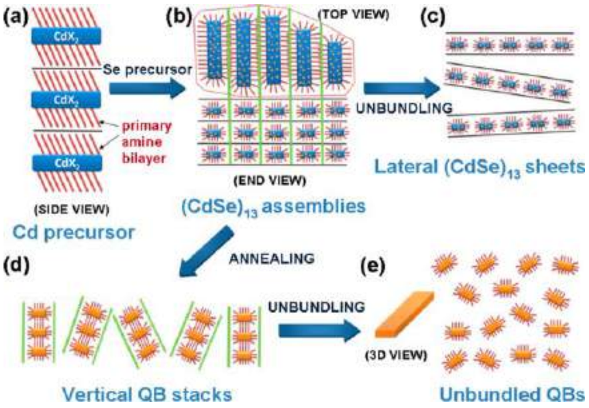

Figure 1-8. A schematic showing the conversion of the double-lamellar (CdSe)13 NC as to CdSe QBs, and the various unbundling processes that occur. The blue fields represent the host domains within the double lamellar templates. (CdSe)13 nanoclusters are represented as orange dots and CdSe QBs as orange rectangles. The short red lines depict primary-amine surfactant molecules. The black and green lines represent the orthogonal interfaces along which unbundling occurs.[45]

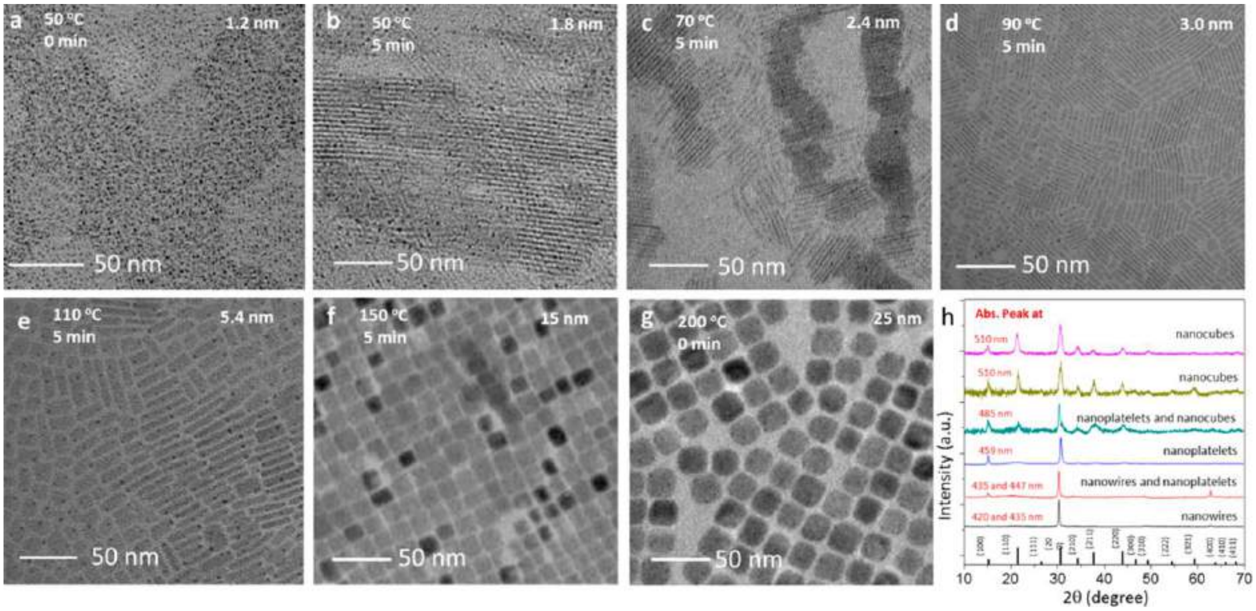

Figure 1-9. (a,b) TEM images of fragmented nanowire-like 1D structures having diameters of ∼1.2 and ∼1.8 nm. (c,d) Platelet-like nanostructures with wide distributions of their lengths. (e) TEM images of mixture of platelets and cubes at different resolutions. (f,g) TEM images of ∼15 and ∼25 nm nanocubes. The reaction conditions and size of each set of nanocrystals are depicted in the respective panels. (h) Powder XRD patterns of samples collected at different time/temperature intervals for the 50−200 °C step-rise reaction. The absorption peak positions are marked near each pattern.[47]

1.3.3 Relation between surface ligands and optical properties of nanocrystals.

Surface ligands could alter the band structure of semiconductor nanocrystals and thus influence their optical, electrical, magnetic and catalytic properties.[48-55] Surface atoms in a semiconductor NC could generate some localized states lying in the bandgap behaving as traps for electrons or holes,[50] therefore possibly leading to luminescence quenching.[48-49] As shown in Figure 1-10, three theoretical models have been proposed to describe the luminescence of core and surface of NCs.[56] In the standard energy-level model, the band of surface trap is temperature independent and thus the trap emission is temperature insensitive. The second is classical electron transfer (ET) theory which describe thermally activated population transfer from the core to the surface. The simulated spectra would show temperature dependence, but only with little broadening and red shifting. The third model is semiclassical ET theory. The dashed lines represent the quantum mode, with displacements implicit. The coupling with quantum model (dash line) gives rise to the temperature dependence of the surface PL, with abvious broadening and red-shifting. In most semiconductor, the trap emission show broadening and shift with temperature and thus could be described by the semiclassical ET theory, as shown in Figure 1-10e. Although sometimes the trap emission could be utilized directly for white LED application,[57] in most cases, surface engineering is necessary to eliminate the surface traps. As shown in Figure 1-11a, The energy band of ligands (e.g. oleate and oleylamine) could hybrid with the isolated band of the dangling metals. The hybrid orbitals were outside the bandgap and thus the trap band was eliminated. In Figure 1-11b, the CdSe NCs with higher carboxylate coverage also have a higher photoluminescence quantum yield (PLQY).[5, 13]

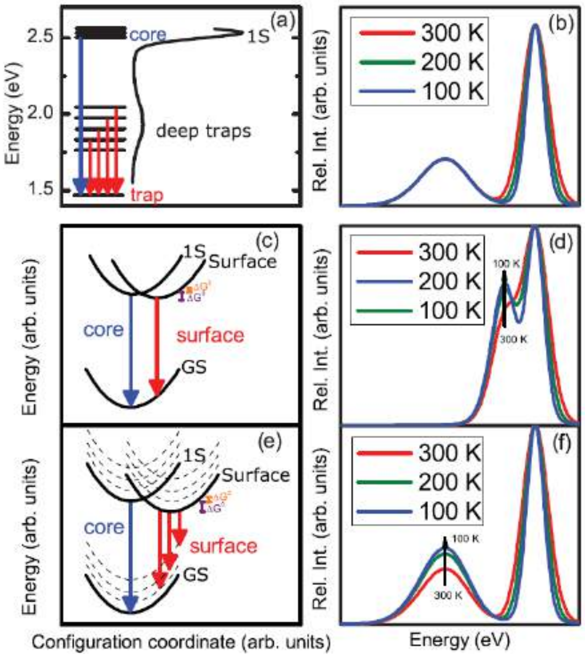

Figure 1-10. Three models for core and surface emission from NCs.[56] The standard energy-level picture of surface PL invokes a distribution of deep traps shown in the exciton representation (a). Due the depth of these traps, the relative PL spectra would exhibit no temperature dependence (b). A configuration coordinate picture using classical electron transfer (ET) theory to describe thermally activated population transfer from the core to the surface (c). The simulated spectra would show temperature dependence, but with little broadening and red shifting (d). A minimal configuration coordinate picture using a semiclassical ET theory (e). The solid line represents the classical mode and the dashed lines represent the quantum mode, with displacements implicit. The small free-energy difference along the classical bath coordinate gives rise to the temperature dependence of the surface PL, whereas the large coupling to the quantum (phonon) modes gives rise to the broadening and redshifting (f).

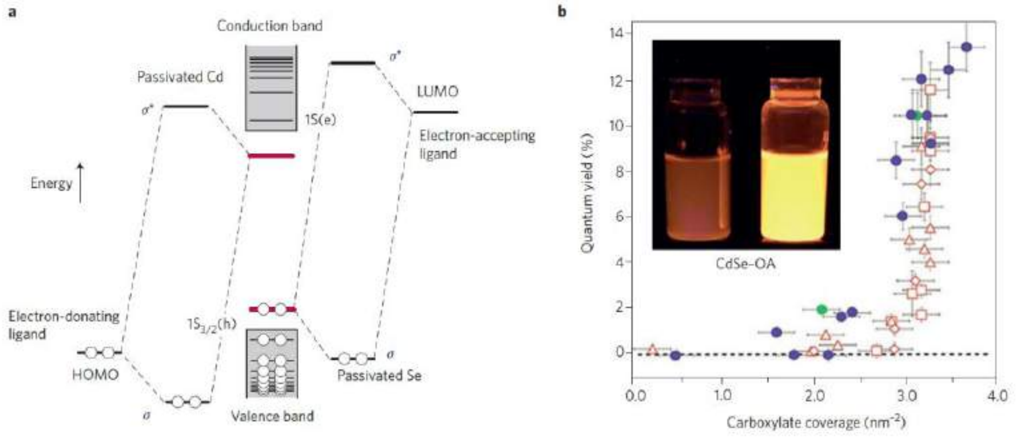

Figure 1-11. Effect of ligands on nanocrystal surface states.[5] a, Simplified molecular orbital diagram of a CdSe quantum dot showing that the energies of Cd and Se surface electronic states (red levels) are pushed outside the bandgap upon ligand binding. b, Experimental photoluminescence quantum yield of CdSe quantum dot samples with different cadmium oleate (OA) surface coverage.

In recent studies of Ivan. Et. al, L-type, X-type and Z-type ligands were found to have different passivation effect on trap level of II-VI and III-V semiconductor nanocrystals.[48] For L-type and X-type ligands, desorption in dynamic binding of these ligands does not introduce deep trap in the bandgap. However, loss of Z-type ligands, which directly generate uncoordinated surface atom, cause deep trap in the bandgap and thus has a severe impact on its bandgap emission. Correspondingly, adding excess Z-type ligands could increase the PLQY of colloidal NCs generally.[48] For classical semiconductor NCs, due to steric effect, not all surface atom could be passivated well by ligands. To achieve optimal PLQY, core-shell structure was required to passivate them all and confine the exciton (type I alignment).[58, 59] For lead halide perovskite NCs, it's less sensitive to the baring surface defects, so called 'defect tolerance' behavior. Only proper ligands passivation could already reach the optimal optical properties.[17, 60]

Ligands passivation is also import for electron/hole transfer. Surface traps could enhance recombination of electron/hole pair on the surface and thus drain carriers from the solid. Specifically, shallow traps capture the carriers in a reproducibly way, while deep traps capture both types carriers and induce its recombination. The ligands passivation is critical to eliminate the traps and suppress recombination. For example, trap concentration in QD films has been reduced using atomic ligands like halide atoms, leading to part-per-million trap concentration (of ~10^{22} surface atoms per cm^3, only ~10^{16} remain unpassivated) and improved photovoltaic performance, with PbS QD solar cells achieving over 9% PCE. [50, 61]

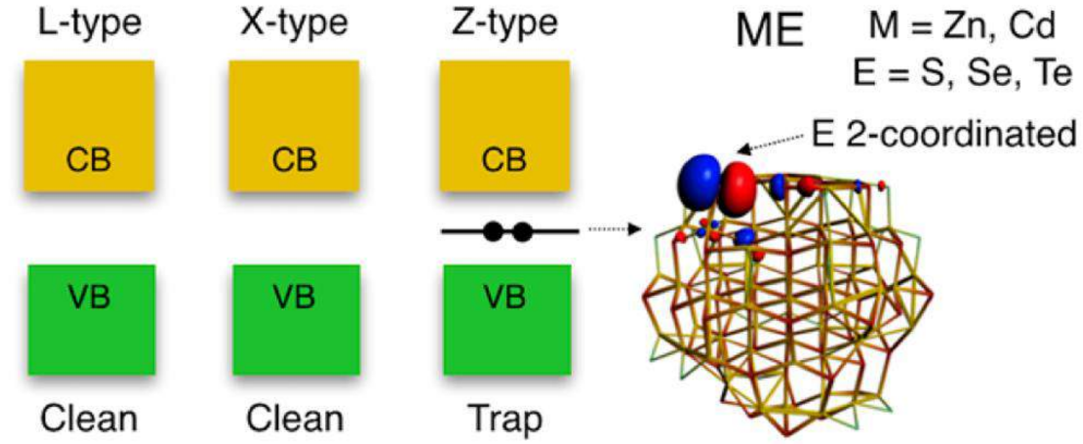

Figure 1-12. Effect on the band structure by various type ligands (L-type, X-type and Z-type).[49]

Surface ligands is also important on inducing chirality on colloidal NCs.[62-63] By chiral heritage, fluorescent NCs with chiral surface ligands could induce the strong optical activity of both circular dichroism (CD) absorption spectra and circularly polarized luminescence (CPL) at its exciton transitions wavelength. Until recently, there are three main method to construct colloidal NCs 1) Using chiral molecules as ligands in the direct synthesis of NCs; 2) Using chiral molecules to post ligands treatment of NCs; 3) creating chiral environment, which could directly interact with NCs. For example, assembly with the chiral gelators, the NCs could also show chirality.[62]

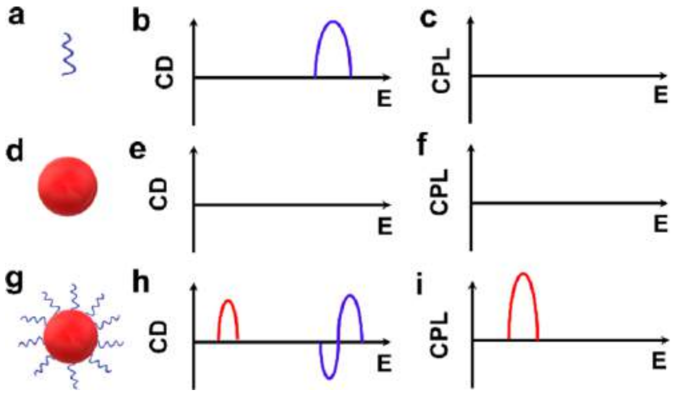

Figure 1-13. Scheme of optical activity of colloidal semiconductor NCs induced by chiral organic ligands. When chiral ligands with strong CD signal (a,b) but free of emission (c) are adsorbed on the surface of achiral semiconductor NCs (d,f), new optical activity with both absorption (h) and emission (i) appears at the characteristic wavelength corresponding to the exciton transitions in NCs (g).[62]

1.3.4 Relation between surface ligands and conductivity of nanocrystals.

Classical long chain hydrocarbon ligands usually is not conductive.[11, 22] Although such insulating surfactant is necessary in the synthesis of NCs, it would block the further performance of NCs on application of electronic devices. Indeed, semiconductor NCs are particularly appealing as they can be used as building blocks in solar cells,[64] light emitting diodes (LEDs)[65] and various film based solid devices due to its solution processability.[66] In such applications, the NC film should be conductive, which is also heavily influenced by its surface ligands.[61, 66] To address such issue, post synthesis ligand exchange with small ionic molecules or some designed conductive ligands were widely applied.[31, 61] Ligand exchange which use excess exogenous ligands to replace original ligands could be employed. It could happen in NCs solution or directly in a NCs film, so called solid-state exchange. Among various conductive ligands, DDABr and small ionic molecules ($Sn_2S_6^{4-}$, $InCl^{4-}$, Cl^-, I^-, SCN^-) are wide applied., which could improve the conductivity and meanwhile maintain the colloidal dispersion in polar solvent.[31] For example, treating the PbSe NCs film with hydrazine, increase its electron mobility close to ~1 $cm^2\ V^{-1}\ s^{-1}$. Treating a PbSe NC film with inorganic ligands (SCN^-)yielded NC films with higher mobility, ~ 7 $cm^2\ V^{-1}\ s^{-1}$.[66] Beside ligand exchange method, volatile ligands (unstable under heating) caped NCs could also be used to produce high conductivity NCs film. By thermal annealing, the volatile ligands could be removed from the film and the NCs could grow into larger crystallites. Such method could be used for solar cells and field-effect transistors.[67]

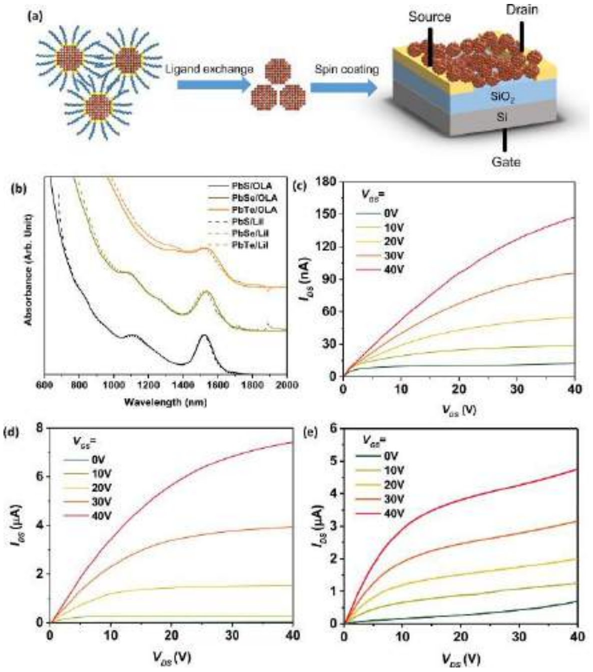

Figure 1-14. (a) Schematic of FET devices with ionic ligand passivated PbSe QDs. (b) Absorption spectra of PbS (5.8 nm, black), PbSe (5.0 nm, dark yellow), and PbTe (5.7 nm, orange) QDs with similar band gap before (solid, in TCE) and after (dashed, in DFP) ligand exchange with LiI. ISD–VSD curves of PbS/LiI QD FET (c), PbSe/LiI QD FET (d), and PbTe/LiI QD FET (e).[66]

REFERENCES:

1. Schwertmann, U., Solubility and dissolution of iron oxides. *Plant and Soil* **1991,** *130* (1), 1-25.
2. Holland, N. B.; Qiu, Y.; Ruegsegger, M.; Marchant, R. E., Biomimetic engineering of non-adhesive glycocalyx-like surfaces using oligosaccharide surfactant polymers. *Nature* **1998,** *392* (6678), 799-801.
3. von Maltzahn, G.; Vauthey, S.; Santoso, S.; Zhang, S., Positively Charged Surfactant-like Peptides Self-assemble into Nanostructures. *Langmuir* **2003,** *19* (10), 4332-4337.
4. Antolini, E., Catalysts for direct ethanol fuel cells. *Journal of Power Sources* **2007,** *170* (1), 1-12.
5. Boles, M. A.; Ling, D.; Hyeon, T.; Talapin, D. V., The surface science of nanocrystals. *Nature Materials* **2016,** *15* (2), 141-153.
6. Johnson, N. B.; Lennon, I. C.; Moran, P. H.; Ramsden, J. A., Industrial-Scale Synthesis and Applications of Asymmetric Hydrogenation Catalysts. *Accounts of Chemical Research* **2007,** *40* (12), 1291-1299.
7. Schlögl, R., Heterogeneous Catalysis. *Angewandte Chemie International Edition* **2015,** *54* (11), 3465-3520.
8. Owen, J., The coordination chemistry of nanocrystal surfaces. *Science* **2015,** *347* (6222), 615-616.
9. Schmitt-Rink, S.; Miller, D. A. B.; Chemla, D. S., Theory of the linear and nonlinear optical properties of semiconductor microcrystallites. *Physical Review B* **1987,** *35* (15), 8113-8125.
10. Fujii, M.; Hayashi, S.; Yamamoto, K., Raman scattering from quantum dots of Ge embedded in SiO2 thin films. *Applied Physics Letters* **1990,** *57* (25), 2692-2694.
11. Murray, C. B.; Norris, D. J.; Bawendi, M. G., Synthesis and characterization of nearly monodisperse CdE (E = sulfur, selenium, tellurium) semiconductor nanocrystallites. *Journal of the American Chemical Society* **1993,** *115* (19), 8706-8715.
12. Zito, J.; Infante, I., The Future of Ligand Engineering in Colloidal Semiconductor Nanocrystals. *Accounts of Chemical Research* **2021,** *54* (7), 1555-1564.
13. Anderson, N. C.; Hendricks, M. P.; Choi, J. J.; Owen, J. S., Ligand Exchange and the Stoichiometry of Metal Chalcogenide Nanocrystals: Spectroscopic Observation of Facile Metal-Carboxylate Displacement and Binding. *Journal of the American Chemical Society* **2013,** *135* (49), 18536-18548.
14. Pradhan, N., Alkylammonium Halides for Facet Reconstruction and Shape Modulation in Lead Halide Perovskite Nanocrystals. *Accounts of Chemical Research* **2021,** *54* (5), 1200-1208.
15. Zhong, Q.; Cao, M.; Xu, Y.; Li, P.; Zhang, Y.; Hu, H.; Yang, D.; Xu, Y.; Wang, L.; Li, Y.; Zhang, X.; Zhang, Q., L-Type Ligand-Assisted Acid-Free Synthesis of CsPbBr3 Nanocrystals with Near-Unity Photoluminescence Quantum Yield and High Stability. *Nano Letters* **2019,** *19* (6), 4151-4157.
16. Gomes, R.; Hassinen, A.; Szczygiel, A.; Zhao, Q.; Vantomme, A.; Martins, J. C.; Hens, Z., Binding of Phosphonic Acids to CdSe Quantum Dots: A Solution NMR Study. *The Journal of Physical Chemistry Letters* **2011,** *2* (3), 145-152.

17. Nenon, D. P.; Pressler, K.; Kang, J.; Koscher, B. A.; Olshansky, J. H.; Osowiecki, W. T.; Koc, M. A.; Wang, L.-W.; Alivisatos, A. P., Design Principles for Trap-Free CsPbX3 Nanocrystals: Enumerating and Eliminating Surface Halide Vacancies with Softer Lewis Bases. *Journal of the American Chemical Society* **2018,** *140* (50), 17760-17772.

18. Imran, M.; Ijaz, P.; Goldoni, L.; Maggioni, D.; Petralanda, U.; Prato, M.; Almeida, G.; Infante, I.; Manna, L., Simultaneous Cationic and Anionic Ligand Exchange For Colloidally Stable CsPbBr3 Nanocrystals. *ACS Energy Letters* **2019,** *4* (4), 819-824.

19. Yang, Y.; Qin, H.; Jiang, M.; Lin, L.; Fu, T.; Dai, X.; Zhang, Z.; Niu, Y.; Cao, H.; Jin, Y.; Zhao, F.; Peng, X., Entropic Ligands for Nanocrystals: From Unexpected Solution Properties to Outstanding Processability. *Nano Letters* **2016,** *16* (4), 2133-2138.

20. Yang, Y.; Qin, H.; Peng, X., Intramolecular Entropy and Size-Dependent Solution Properties of Nanocrystal–Ligands Complexes. *Nano Letters* **2016,** *16* (4), 2127-2132.

21. Yu, K., CdSe Magic-Sized Nuclei, Magic-Sized Nanoclusters and Regular Nanocrystals: Monomer Effects on Nucleation and Growth. *Advanced Materials* **2012,** *24* (8), 1123-1132.

22. Yu, W. W.; Peng, X., Formation of High-Quality CdS and Other II–VI Semiconductor Nanocrystals in Noncoordinating Solvents: Tunable Reactivity of Monomers. *Angewandte Chemie International Edition* **2002,** *41* (13), 2368-2371.

23. Yu, W. W.; Wang, Y. A.; Peng, X., Formation and Stability of Size-, Shape-, and Structure-Controlled CdTe Nanocrystals: Ligand Effects on Monomers and Nanocrystals. *Chemistry of Materials* **2003,** *15* (22), 4300-4308.

24. Manna, L.; Scher, E. C.; Alivisatos, A. P., Synthesis of Soluble and Processable Rod-, Arrow-, Teardrop-, and Tetrapod-Shaped CdSe Nanocrystals. *Journal of the American Chemical Society* **2000,** *122* (51), 12700-12706.

25. Peng, X.; Manna, L.; Yang, W.; Wickham, J.; Scher, E.; Kadavanich, A.; Alivisatos, A. P., Shape control of CdSe nanocrystals. *Nature* **2000,** *404* (6773), 59-61.

26. Almeida, G.; Goldoni, L.; Akkerman, Q.; Dang, Z.; Khan, A. H.; Marras, S.; Moreels, I.; Manna, L., Role of Acid–Base Equilibria in the Size, Shape, and Phase Control of Cesium Lead Bromide Nanocrystals. *ACS Nano* **2018,** *12* (2), 1704-1711.

27. Huang, J.; Kovalenko, M. V.; Talapin, D. V., Alkyl Chains of Surface Ligands Affect Polytypism of CdSe Nanocrystals and Play an Important Role in the Synthesis of Anisotropic Nanoheterostructures. *Journal of the American Chemical Society* **2010,** *132* (45), 15866-15868.

28. Brown, P. R.; Kim, D.; Lunt, R. R.; Zhao, N.; Bawendi, M. G.; Grossman, J. C.; Bulović, V., Energy Level Modification in Lead Sulfide Quantum Dot Thin Films through Ligand Exchange. *ACS Nano* **2014,** *8* (6), 5863-5872.

29. Frederick, M. T.; Weiss, E. A., Relaxation of Exciton Confinement in CdSe Quantum Dots by Modification with a Conjugated Dithiocarbamate Ligand. *ACS Nano* **2010,** *4* (6), 3195-3200.

30. Jing, L.; Kershaw, S. V.; Li, Y.; Huang, X.; Li, Y.; Rogach, A. L.; Gao, M., Aqueous Based Semiconductor Nanocrystals. *Chemical Reviews* **2016,** *116* (18), 10623-10730.

31. Ithurria, S.; Talapin, D. V., Colloidal Atomic Layer Deposition (c-ALD) using Self-Limiting Reactions at Nanocrystal Surface Coupled to Phase Transfer between Polar and Nonpolar Media. *Journal of the American Chemical Society* **2012,** *134* (45), 18585-18590.

32. Bishop, K. J. M.; Wilmer, C. E.; Soh, S.; Grzybowski, B. A., Nanoscale Forces and Their Uses in Self-Assembly. *Small* **2009,** *5* (14), 1600-1630.

33. Pang, Z.; Zhang, J.; Cao, W.; Kong, X.; Peng, X., Partitioning surface ligands on nanocrystals for maximal solubility. *Nature Communications* **2019,** *10* (1), 2454.

34. Zhou, J.; Zhu, M.; Meng, R.; Qin, H.; Peng, X., Ideal CdSe/CdS Core/Shell Nanocrystals Enabled by Entropic Ligands and Their Core Size-, Shell Thickness-, and Ligand-Dependent Photoluminescence Properties. *Journal of the American Chemical Society* **2017,** *139* (46), 16556-16567.

35. Erdemir, D.; Lee, A. Y.; Myerson, A. S., Nucleation of Crystals from Solution: Classical and Two-Step Models. *Accounts of Chemical Research* **2009,** *42* (5), 621-629.

36. Riedinger, A.; Ott, F. D.; Mule, A.; Mazzotti, S.; Knüsel, P. N.; Kress, Stephan J. P.; Prins, F.; Erwin, S. C.; Norris, D. J., An intrinsic growth instability in isotropic materials leads to quasi-two-dimensional nanoplatelets. *Nature Materials* **2017,** *16* (7), 743-748.

37. Dong, Y.; Qiao, T.; Kim, D.; Parobek, D.; Rossi, D.; Son, D. H., Precise Control of Quantum Confinement in Cesium Lead Halide Perovskite Quantum Dots via Thermodynamic Equilibrium. *Nano Letters* **2018,** *18* (6), 3716-3722.

38. Nevers, D. R.; Williamson, C. B.; Savitzky, B. H.; Hadar, I.; Banin, U.; Kourkoutis, L. F.; Hanrath, T.; Robinson, R. D., Mesophase Formation Stabilizes High-Purity Magic-Sized Clusters. *Journal of the American Chemical Society* **2018,** *140* (10), 3652-3662.

39. Lim, J.; Bae, W. K.; Park, K. U.; zur Borg, L.; Zentel, R.; Lee, S.; Char, K., Controlled Synthesis of CdSe Tetrapods with High Morphological Uniformity by the Persistent Kinetic Growth and the Halide-Mediated Phase Transformation. *Chemistry of Materials* **2013,** *25* (8), 1443-1449.

40. Zhang, B.; Goldoni, L.; Zito, J.; Dang, Z.; Almeida, G.; Zaccaria, F.; de Wit, J.; Infante, I.; De Trizio, L.; Manna, L., Alkyl Phosphonic Acids Deliver CsPbBr3 Nanocrystals with High Photoluminescence Quantum Yield and Truncated Octahedron Shape. *Chemistry of Materials* **2019,** *31* (21), 9140-9147.

41. Bera, S.; Behera, R. K.; Pradhan, N., α-Halo Ketone for Polyhedral Perovskite Nanocrystals: Evolutions, Shape Conversions, Ligand Chemistry, and Self-Assembly. *Journal of the American Chemical Society* **2020,** *142* (49), 20865-20874.

42. Zhang, B.; Goldoni, L.; Lambruschini, C.; Moni, L.; Imran, M.; Pianetti, A.; Pinchetti, V.; Brovelli, S.; De Trizio, L.; Manna, L., Stable and Size Tunable CsPbBr3 Nanocrystals Synthesized with Oleylphosphonic Acid. *Nano Letters* **2020,** *20* (12), 8847-8853.

43. Ithurria, S.; Dubertret, B., Quasi 2D Colloidal CdSe Platelets with Thicknesses Controlled at the Atomic Level. *Journal of the American Chemical Society* **2008,** *130* (49), 16504-16505.

44. Son, J. S.; Wen, X.-D.; Joo, J.; Chae, J.; Baek, S.-i.; Park, K.; Kim, J. H.; An, K.; Yu, J. H.; Kwon, S. G.; Choi, S.-H.; Wang, Z.; Kim, Y.-W.; Kuk, Y.; Hoffmann, R.; Hyeon, T., Large-Scale Soft Colloidal Template Synthesis of 1.4 nm Thick CdSe Nanosheets. *Angewandte Chemie International Edition* **2009,** *48* (37), 6861-6864.

45. Liu, Y.-H.; Wang, F.; Wang, Y.; Gibbons, P. C.; Buhro, W. E., Lamellar Assembly of Cadmium Selenide Nanoclusters into Quantum Belts. *Journal of the American Chemical Society* **2011,** *133* (42), 17005-17013.

46. Wang, F.; Wang, Y.; Liu, Y.-H.; Morrison, P. J.; Loomis, R. A.; Buhro, W. E., Two-Dimensional Semiconductor Nanocrystals: Properties, Templated Formation, and Magic-Size Nanocluster Intermediates. *Accounts of Chemical Research* **2015,** *48* (1), 13-21.

47. Peng, L.; Dutta, A.; Xie, R.; Yang, W.; Pradhan, N., Dot–Wire–Platelet–Cube: Step Growth and Structural Transformations in CsPbBr3 Perovskite Nanocrystals. *ACS Energy Letters* **2018,** *3* (8), 2014-2020.

48. Houtepen, A. J.; Hens, Z.; Owen, J. S.; Infante, I., On the Origin of Surface Traps in Colloidal II–VI Semiconductor Nanocrystals. *Chemistry of Materials* **2017,** *29* (2), 752-761.

49. Giansante, C.; Infante, I., Surface Traps in Colloidal Quantum Dots: A Combined Experimental and Theoretical Perspective. *The Journal of Physical Chemistry Letters* **2017,** *8* (20), 5209-5215.

50. Ip, A. H.; Thon, S. M.; Hoogland, S.; Voznyy, O.; Zhitomirsky, D.; Debnath, R.; Levina, L.; Rollny, L. R.; Carey, G. H.; Fischer, A.; Kemp, K. W.; Kramer, I. J.; Ning, Z.; Labelle, A. J.; Chou, K. W.; Amassian, A.; Sargent, E. H., Hybrid passivated colloidal quantum dot solids. *Nature Nanotechnology* **2012,** *7* (9), 577-582.

51. Chuang, C.-H. M.; Brown, P. R.; Bulović, V.; Bawendi, M. G., Improved performance and stability in quantum dot solar cells through band alignment engineering. *Nature Materials* **2014,** *13* (8), 796-801.

52. Ning, Z.; Voznyy, O.; Pan, J.; Hoogland, S.; Adinolfi, V.; Xu, J.; Li, M.; Kirmani, A. R.; Sun, J.-P.; Minor, J.; Kemp, K. W.; Dong, H.; Rollny, L.; Labelle, A.; Carey, G.; Sutherland, B.; Hill, I.; Amassian, A.; Liu, H.; Tang, J.; Bakr, O. M.; Sargent, E. H., Air-stable n-type colloidal quantum dot solids. *Nature Materials* **2014,** *13* (8), 822-828.

53. Kwon, S. G.; Krylova, G.; Sumer, A.; Schwartz, M. M.; Bunel, E. E.; Marshall, C. L.; Chattopadhyay, S.; Lee, B.; Jellinek, J.; Shevchenko, E. V., Capping Ligands as Selectivity Switchers in Hydrogenation Reactions. *Nano Letters* **2012,** *12* (10), 5382-5388.

54. Boyer, J. L.; Rochford, J.; Tsai, M.-K.; Muckerman, J. T.; Fujita, E., Ruthenium complexes with non-innocent ligands: Electron distribution and implications for catalysis. *Coordination Chemistry Reviews* **2010,** *254* (3), 309-330.

55. Xu, C.; Xu, K.; Gu, H.; Zheng, R.; Liu, H.; Zhang, X.; Guo, Z.; Xu, B., Dopamine as A Robust Anchor to Immobilize Functional Molecules on the Iron Oxide Shell of Magnetic Nanoparticles. *Journal of the American Chemical Society* **2004,** *126* (32), 9938-9939.

56. Mooney, J.; Krause, M. M.; Saari, J. I.; Kambhampati, P., Challenge to the deep-trap model of the surface in semiconductor nanocrystals. *Physical Review B* **2013,** *87* (8), 081201.

57. VanWie, T.; Wysocki, E.; McBride, J. R.; Rosenthal, S. J., Bright Cool White Emission from Ultrasmall CdSe Quantum Dots. *Chemistry of Materials* **2019,** *31* (20), 8558-8562.

58. Won, Y.-H.; Cho, O.; Kim, T.; Chung, D.-Y.; Kim, T.; Chung, H.; Jang, H.; Lee, J.; Kim, D.; Jang, E., Highly efficient and stable InP/ZnSe/ZnS quantum dot light-emitting diodes. *Nature* **2019,** *575* (7784), 634-638.

59. Vela, J.; Htoon, H.; Chen, Y.; Park, Y.-S.; Ghosh, Y.; Goodwin, P. M.; Werner, J. H.; Wells, N. P.; Casson, J. L.; Hollingsworth, J. A., Effect of shell thickness and composition on blinking suppression and the blinking mechanism in 'giant' CdSe/CdS nanocrystal quantum dots. *Journal of Biophotonics* **2010,** *3* (10-11), 706-717.

60. Ahmed, T.; Seth, S.; Samanta, A., Mechanistic Investigation of the Defect Activity Contributing to the Photoluminescence Blinking of CsPbBr3 Perovskite Nanocrystals. *ACS Nano* **2019,** *13* (11), 13537-13544.

61. Tang, J.; Kemp, K. W.; Hoogland, S.; Jeong, K. S.; Liu, H.; Levina, L.; Furukawa, M.; Wang, X.; Debnath, R.; Cha, D.; Chou, K. W.; Fischer, A.; Amassian, A.; Asbury, J. B.; Sargent, E. H., Colloidal-quantum-dot photovoltaics using atomic-ligand passivation. *Nature Materials* **2011,** *10* (10), 765-771.

62. Gao, X.; Han, B.; Yang, X.; Tang, Z., Perspective of Chiral Colloidal Semiconductor Nanocrystals: Opportunity and Challenge. *Journal of the American Chemical Society* **2019,** *141* (35), 13700-13707.

63. Ru, Y.; Ai, L.; Jia, T.; Liu, X.; Lu, S.; Tang, Z.; Yang, B., Recent advances in chiral carbonized polymer dots: From synthesis and properties to applications. *Nano Today* **2020,** *34*, 100953.

64. Ma, W.; Swisher, S. L.; Ewers, T.; Engel, J.; Ferry, V. E.; Atwater, H. A.; Alivisatos, A. P., Photovoltaic Performance of Ultrasmall PbSe Quantum Dots. *ACS Nano* **2011,** *5* (10), 8140-8147.

65. Dai, X.; Zhang, Z.; Jin, Y.; Niu, Y.; Cao, H.; Liang, X.; Chen, L.; Wang, J.; Peng, X., Solution-processed, high-performance light-emitting diodes based on quantum dots. *Nature* **2014,** *515* (7525), 96-99.

66. Lin, Q.; Yun, H. J.; Liu, W.; Song, H.-J.; Makarov, N. S.; Isaienko, O.; Nakotte, T.; Chen, G.; Luo, H.; Klimov, V. I.; Pietryga, J. M., Phase-Transfer Ligand Exchange of Lead Chalcogenide Quantum Dots for Direct Deposition of Thick, Highly Conductive Films. *Journal of the American Chemical Society* **2017,** *139* (19), 6644-6653.

67. Jiang, C.; Lee, J.-S.; Talapin, D. V., Soluble Precursors for CuInSe2, CuIn1−xGaxSe2, and Cu2ZnSn(S,Se)4 Based on Colloidal Nanocrystals and Molecular Metal Chalcogenide Surface Ligands. *Journal of the American Chemical Society* **2012,** *134* (11), 5010-5013.

Chapter 2: Surface Chemistry of Metal Halide Nanocrystals

Abstract. Metal halide NCs has recently drawn intense attention due to their excellent optical properties.[1-4] The first report of emissive metal halide NCs could traced back to the 1970s, when Pb^{2+} doped CsX matrix was found to be emissive. The breakthrough of metal halide NCs come from 2015, when the hot injection method was used to produce $CsPbX_3$ NCs with bright and adjustable emission.[2, 5] Within the huge family of metal halide materials, lead halide perovskites,[5] double perovskite[3, 6] and Sb^{3+} based metal halide are[4, 7-8]mostly studied (Figure 2-1. 1). In lead halide perovskites, corner sharing PbX_6 octahedra connect with each other forming "the skeleton" of the structure and the space in between themis filled by A^+ cations (Cs^+ or small organic cations such as methylammonium (MA^+) and Formamidinium (FA^+)). In such skeleton, the formation energy of misplacing ions is quite high and thus most of the defects exist in vacancies form. The vacancies defects only generate shallow traps or traps in the band of lead halide perovskite and don't alter the bandgap obviously. Thanks to such behaviors (so called defect tolerance), lead halide perovskites became famous for their bright and narrow band emission which can be achieved via a simple surface passivation with ligands; [1-2, 5, 9-11] 2) The Pb^{2+} ions in the perovskite lattice could be replaced by B^+ and B^{3+}, with chemical formula of $A_2B^+B^{3+}X_6$, so called double perovskite (DP). They are characterized by a 3D perovskite skeleton composed of corner-sharing $[B^+X_6]$ and $[B^{3+}X_6]$ octahedra with A^+ cations filling the voids in between. Specifically to $Cs_2AgInCl_6$ with a direct bandgap, by proper doping with other cations (eg. Bi^{3+} and Na^+), the PLQY of $Cs_2AgInCl_6$ could approach to 86% and could be ideal materials for white light;[3, 6] 3) Sb^{3+} based metal halide materials (Sb^{3+} doping or Sb^{3+} act as skeleton) which consist of $[SbX_6]^{3-}$, $[SbX_5]^{2-}$ or other Sb halide polyhedron as emit centers, is another promising metal halide materials. Some of the doped case show near unity PLQY and the emission of $[SbX_6]^{3-}$ could cover whole range of visible light by adjusting the coordination enviroenment of Sb^{3+}.[4, 7-8] Chapter 2 of this thesis deals with the surface chemistry of metal halide nanocrystals and its influence on their nucleation, band structure, and colloidal stability.

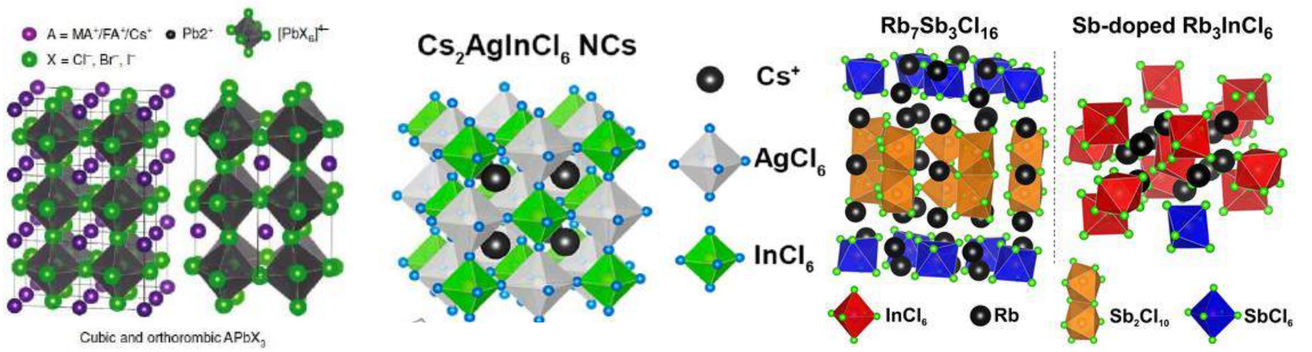

Figure 2-1. left) Structure of cubic and lead halide perovskite;[12] mid) structure of double perovskite, $Cs_2AgInCl_6$;[3] right) Sb^{3+} based materials, $Rb_7Sb_3Cl_{16}$ and Sb^{3+} doped materials, Rb_3InCl_6.[7]

2.1. Colloidal Stability of Metal Halide Nanocrystals and Surface Ligands.

The first colloidal synthesis of $CsPbX_3$ nanocrystals, developed by Protesescu et al. relies on the use of a long chain primary alkylamine (oleylamine) and a carboxylic acid (oleic acid) as ligands to dissolve metal precursors (Cs_2CO_3, $PbBr_2$, $Pb(Ac)_2$ et. al.) and to passivate the surface of the final nanocrystals.[2] The obtained CsPbX3 NC was bound with oleylammonium that occupy Cs^+ site and oleate that occupy Br^- site, respectively. The overall ligand density is around 2−3 ligands/nm^2 and here we name the oleyalammounium and oleate as standard ligands of metal halide NCs.[13] However, the binding strength of the standard ligands is weak. As shown in Figure 2-2, by ^{1}H-NMR, the bound and free part of primary ammonium was detected together with the NCs solution, adding exogenous ligands could change the fraction ratio between the bound and free part.[13] The dynamic binding of oleylammonium and oleate make them tend to desorption from surface under washing, dilution or long storage. Such desorption could cause emission quenching and aggregation of NCs. Two strategies have been devised to improve the colloidal stability: 1) post-synthesis ligand exchange;[11, 14-17] 2) devise new synthesis approaches based on ligands which strongly bound to the NCs' surface.[10, 18-19] For example, Didodecyldimethylammonium bromide (DDAB), a quaternary ammonium salt, was widely used to post treatment the oleylammonium-oleate capped NCs.[16, 20] The DDAB could exchange with cationic and anionic ligands at the same time and has a strong binding affinity with NCs surface. The addition of DDAB results in impressive colloidal stability and near-unity PLQYs of $CsPbBr_3$ NCs. As shown in Figure 2-3, DDAB capped NCs could be stored under ambient conditions over a month and show heating resistance under 50 ˚C.[16] As comparison, the standard ligands capped NCs is easy to aggregate after several day's storage or after mild heating. Wang. S. *et al.* utilized exogenous polyzwitterionic molecules to exchange the oleylammonium-oleate caped $CsPbX_3$ NCs(Figure 2-1). The polyzwitterions has a strong binding affinity with NCs surface and is soluble in apolar solvent. The NCs after ligands exchange are thus stable in apolar solvent.[14, 19, 21] The soft Lewis acid could also be used to exchange the weak oleic acid. Nenon et al. found the soft acid including alkylphosphonic acid, benzoic acid and difluoroacetate acid could fully exchange with beginning oleate ligands, as shown in Figure 2-5.[15] The added ligands show negative NOE signal with oleyammonium, which indicate the adding of soft Lewis acid only replace the oleate part but keep the oleylammonium ligands. Specifically, the addition of hexylphosphonic acid result in $CsPbBr_3$ NCs with near unity PLQY and longer emission lifetime.[17] As mentioned before, the use of ligands with stronger binding in direct synthesis is another common strategy to enhance the stability of perovskite nanocrystals. We employed alkyphosphonic acid as single ligands to dissolve metal precursors and as surfactant of $CsPbBr_3$ nanocrystals.[10] Due to the strong binding affinity between Pb^{2+} and phosphonate species, the obtained NCs were terminated by Pb rich surfaces and showed high stability against dilution. The details will be discussed in Chapter 4. Dodecylbenzene sulfonic acid (DBSA) as an even stronger Lewis acid (Pka =1.8) was also employed in the synthesis of $CsPbBr_3$ nanocrystals by Yang, D. et al.[18] The high binding strength of sulfonic acid toward Pb^{2+} was observed and it allow for the cleaning of the resulting NCs up to eight times without losing their colloidal stability. The zwitterionic ligands were also directly employed in synthesis. The zwitterionic ligands not only improve the colloidal stability and PLQY of NCs, but also increase it solubility in some cases. Some of zwitterionic ligands has a branched chain and could be viewed as 'entropy ligands'. The branched chain could increase steric effect to avoid NCs aggregation and release more entropy of C-C rotation energy in NCs' dispersion state. Such behavior make the branched ligands caped NCs has a high tendency to maintain dispersion state in solution, as discussed in Chapter 1.3.1. For example, the sulfobetaine-capped nanocrystals were found to have an high solubility on non-polar solvent (50-100 mg/ml). The soy lecithin as a natural zwitterionic ligands could push the NCs' solubility to 400 mg/ml in toluene.[21]

As regarding double perovskite NCs, its surface chemistry was less investigated. Usually, the metal halide NCs is also capped by standard oleate-oleylammonium ligands and thus has a bad colloidal stability against anti-solvent washing.[22-23] We here employed the phenylacetic acid (softer Lewis acid) to replace oleic acid in the direct synthesis, the colloidal stability of $Cs_2Ag_{0.6}Na_{0.4}InCl_6$ NCs against anti-solvent washing was significantly improved. After thorough washing, the surface chemistry of double perovskite was carefully analyzed.[23] The details would be discussed in chapter 5.

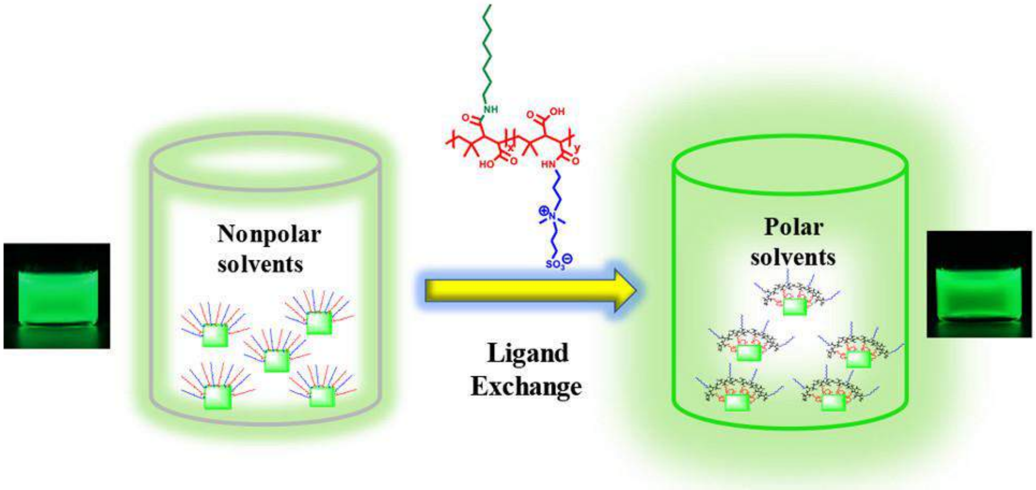

Figure 2-2. a) Dynamic binding of $CsPbBr_3$ nanocrystals passivated by standard ligands; b) $CsPbBr_3$ nanocrystals after treated with zwitterion ligands; c) stability comparison between standard $CsPbBr_3$ nanocrystals and zwitterion caped nanocrystals in various anti-solvent.[14]

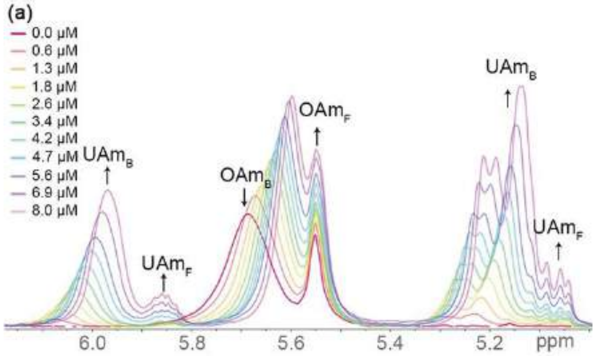

Figure 2-3. Room-temperature 1H NMR spectra of a 2.5 mm CsPbBr3 QD suspension with oleylamine (OAm) and lauric acid native ligands, titrated with increasing amounts (0–8.0 μM) of undec-10-en-1-amine (UAm) in d8-toluene, showing both free (F) and bound (B) fractions.[13]

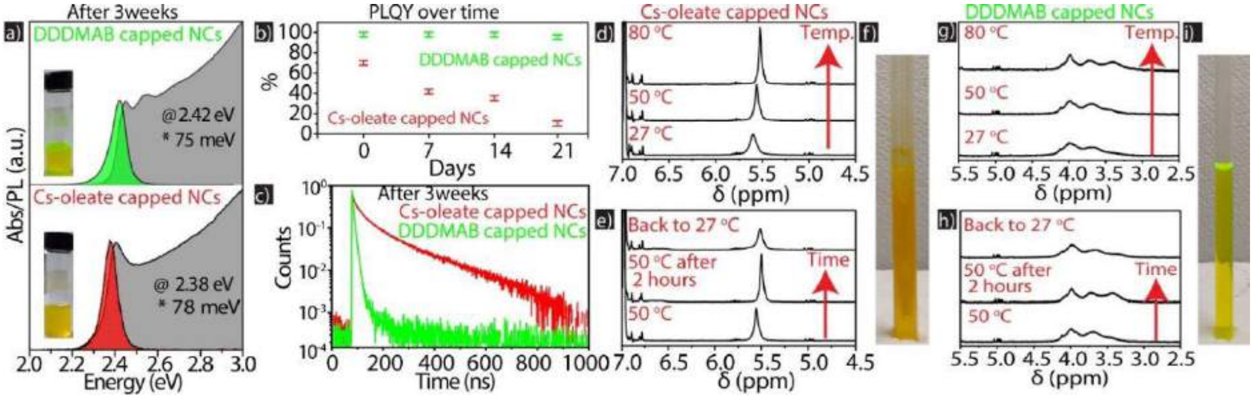

Figure 2-4. a) Absorbance and PL of Cs-oleate capped and DDAB capped $CsPbBr_3$ NCs aged for 3 weeks under air in closed vials. b) PLQY over time and c) PL decays of aged samples. d-i) Thermal stability tests on Cs-oleate capped and DDAB capped NCs by ^{1}H-NMR.[16]

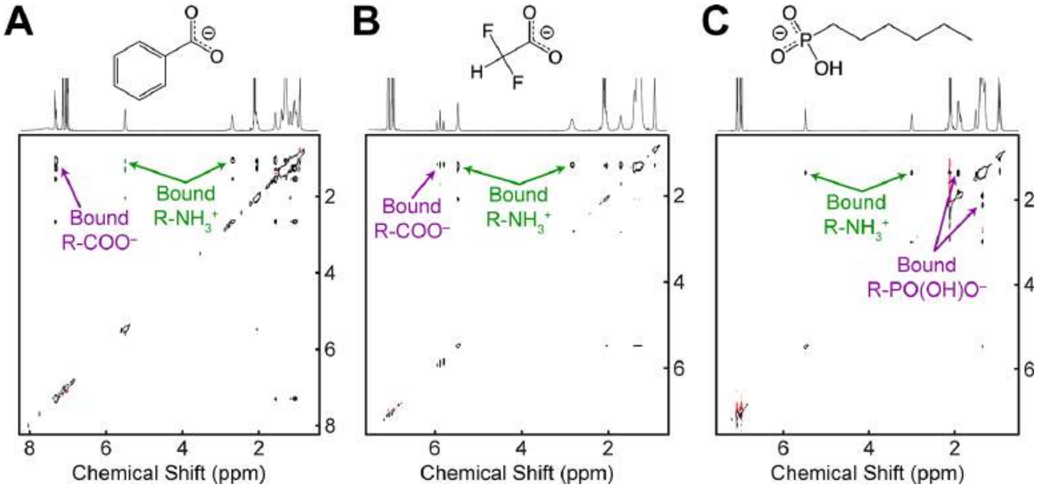

Figure 2-5. ^{1}H NOESY NMR spectra of CsPbBr3 nanocrystal samples exchanged to ligand pairs of oleylammonium and (A) benzoate, (B) difluoroacetate, and (C) hexylphosphonate.[15]

2.2. Size/Morphology of Metal Halide NCs and Surface Chemistry

The nucleation and growth of metal halide nanocrystal could be described by theclassical nucleation theory proposed by Gibbs at the end of the 19th century.[24-25] The super-saturation (DS) and the reaction temperature (T) govern the critical radius of the nuclei and, thus, influencing the final size of the NCs, as discussed in chapter 1.3.2. However, due to the fast nucleation and intrinsic instability, the size control, especially for obtaining small-sized nanocrystals is much challenged for metal halide materials.[10, 19, 26] The small-sized NCs tend to dissolve into the solution or grow into larger NCs with addition of monomers.[27] Two main strategies to obtain small-sized metal halide NCs have been reported so far: 1) the synthesis of $CsPbBr_3$ NCs in the presence of an excess of $ZnBr^{2-}$. The presence of such salt was claimed to increase the chemical potential of Br^- on the solution, which results in a low tendency of NCs to dissolve in the reaction medium[26] (see Figure 1.3.2). However, such NCs solution can’t be washed thoroughly. Once the excess precursors was washed out, the small NCs would start to dissolve into solution again. 2) Utilizing stronger ligands to block the further growth of small NCs.[10, 19] For example, using tetradecylphosphonic acid (TDPA) as sole ligands, we could obtain monodispersed 7 nm polyhedron $CsPbBr_3$ nanocrystals, which show good stability against washing and dilution. We could reduce the size to 5 nm for $CsPbBr_3$ NCs, when employed the oleyphosphonic acid (OLPA) as ligands. The detailed discussion for TDPA and OLPA case would be shown in Chapter 4. 3) Another way to stabilize the small sized NCs is to package the NCs together. The interaction between cluster-cluster would reduce the energy of whole system and thus provide extra stability for each clusters. The method is well known to stabilize II-VI nanoclusters. For example, in an extreme high concentration (1000 mM), the formation of CdS nanocluster was favored and the formation of larger CdS nanocrystals was suppressed. The CdS nanocluster stack with each other in hexagonal symmetry and the interaction reduce the free energy of whole system, as shown in Figure 2-6.[28-29] Here, such method was optimized by using aromatic ligands, which could show π-π interaction. Such aromatic ligands was then employed to stabilize the $CsPbBr_3$ nanoclusters, which would be discussed in chapter 6.

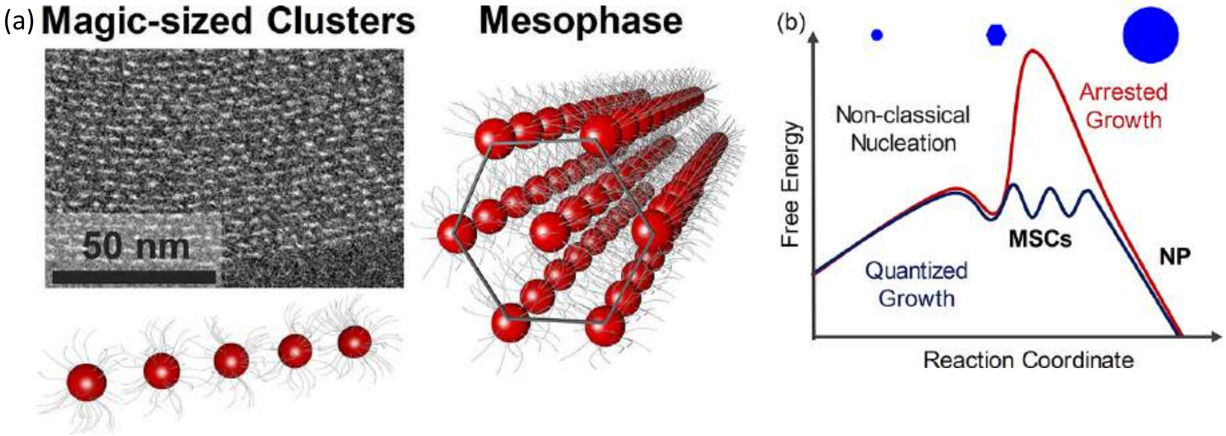

Figure 2-6. (a) The TEM image of aggregated CdS nanoclusters and its hexagonal stacking scheme. (b) How MSCs reduce the free energy of system by aggregation.[28]

Typically, the shape of metal halide colloidal nanocrystal depends on the reaction temperature, surfactants (both affecting the growth kinetics) and their intrinsic crystal structure. Among these parameters, the most effective in providing a control over the shape of the NCs is the nature and the amount of surface ligands employed in the synthesis.[2, 10, 12, 17, 19-20, 30-33] Oleylammonium, as the most common surfactant on surface halide NCs, plays a major role on the shape of obtained NCs.[20, 33] Oleylammonium binds to the surface of CsPbBr3 NCs by occupying Cs^+ sites, and thus always favor in binding with [100] facets. With such favor, when the ammonium-oleate ratio is relatively low, the shape of NCs would be standard cubic which exposed six [100] facets. [33] With the increasing amount of ammonium, the [100] facets could extend more and induce the formation of nanoplatelets shape. [12] In addition, the oleylammonium could also etch the NCs by dissolving $PbBr_2$ and thus influence the final shape of NCs. For example, with oleylammonium bromide treating at elevated temperature (250°C), the certain facets of polyhedron $CsPbBr_3$ nanocrystals were etched and thus transfer to six armed nanocrystals, as shown in Figure 2-7.[31] The high affinity between oleylammonium and [100] facets actually block the further shape control of perovskite NCs. Several studies were also aimed at studying the effect of secondary and tertiary amines on the synthesis of $CsPbBr_3$ nanocrystals.[10, 19, 30, 32] For example, Imran. et al. employed secondary amine to replace oleylamine during the synthesis.[30] The secondary amine was found almost not bound with NCs surface due to steric hindrance, while the Cs-oleate is dominated surfactant. Without ammonium ions on the surface, the formation of nanoplatelets is avoided, even at low temperature (which favor the formation of platelets in standard synthesis). The obtained shape pure, highly monodisperse cubic NCs could aggregate into cubic superlattice, as shown in Figure 2-8. Furthermore, the tertiary amine was also used to replace oleylammonium as surfactant. As shown in Figure 2-9, Bera. et al. employed α-Halo Ketone in the direct synthesis.[32] With proper heating, the α-Halo Ketone further transfer into tertiary amine, which show binding affinity to [020], [112], [200] facets and led to 12 faceted rhombic dodecahedrons $CsPbBr_3$.

Several studies also investigated the possibility of synthesizing perovskite NCs in the absence of oleylamine, thus pushing the stabilization of the system with a surface passivation alternative to that of oleylammonium-Br, and, therefore, possibly a different shape. Zhang. B. et.al employed alkylphosphonic acids as the sole ligands in the synthesis of CsPbBr3 NCs obtaining, for the first time?, nanostructures with a truncated octahedron? shape.[10, 19] The details are discussed in Chapter 4 of this thesis. As special case for amine-free system, the inorganic ionic molecules (Na^+) cause a polyhedron NCs shape also.

Moreover, templates have been also exploited to govern the morphology of metal halide NCs. For example, SiO_2 and TiO_2 were employed as templates to generate high stable perovskite emitters.[34-35] Not surprisingly, the size and shape of nanocrystals was determined by the size and morphology of parent template. For example, Dirin, D. N. et al. synthesis various $APbX_3$ in the pore of mesoporous silica. The obtained $APbX_3$ show nanowire shape and the size was adjustable by the choose of pore size of silica (from 2.5 nm to 50 nm).[34]

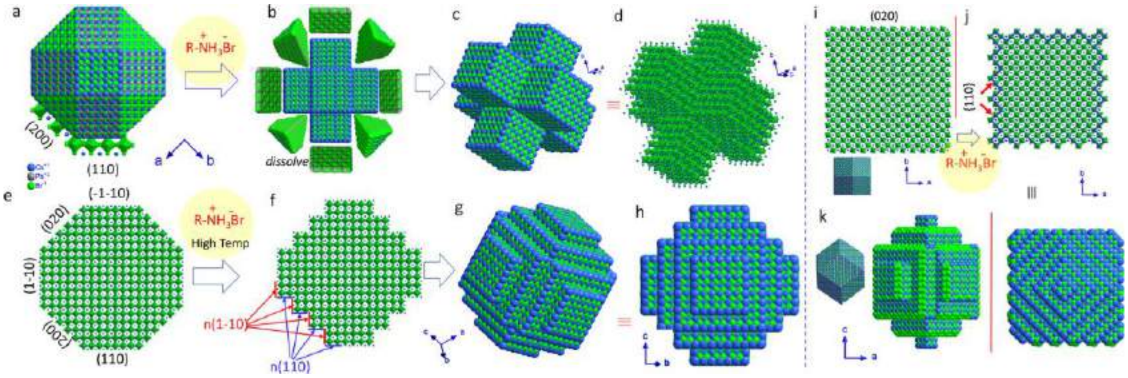

Figure 2-7. Schematic presentation of the transformation of a $CsPbBr_3$ polyhedron to armed nanostructures with a treatment of alkylammonium bromide solution.[31]

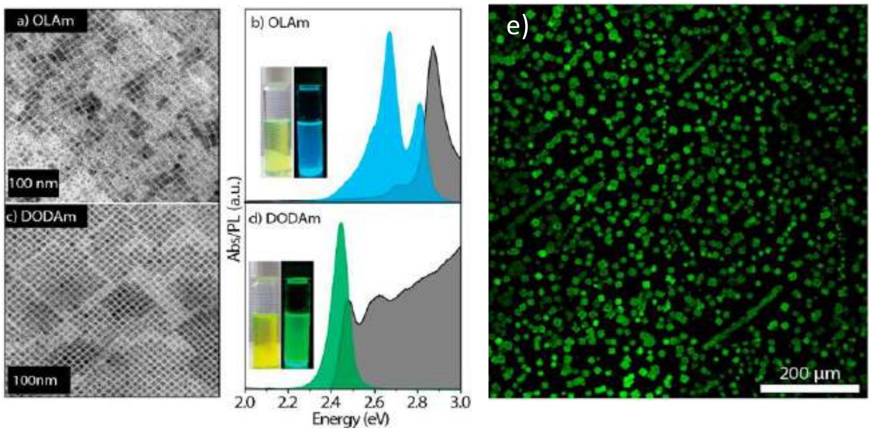

Figure 2-8. Standard synthesis using oleylamine (OLAm) to obtain mixture of nanocubic and nanoplatelets. b) Corresponding a) TEM image and b) absorption and emission spectra. Using secondary amine (dioctyldecylamine, DODAm) to replace oleylamine. Corresponding c) TEM image and d) absorption and emission spectra. e) image of superlattice aggregated by cubic nanocrystals from c).[30]

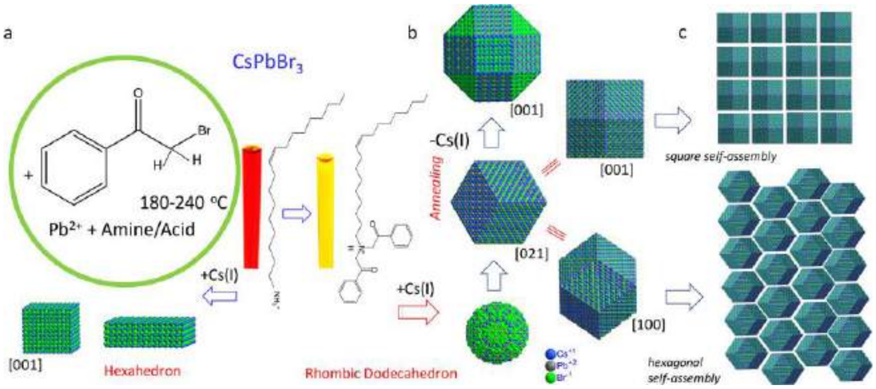

Figure 2-9. (a) Standard cubic and platelets nanocrystals was obtained when the absent of tertiary amine. (b) 12 faceted rhombic was obtained instead after the formation of tertiary amine during the pre-heating process. (c) different packing patterns (square and hexagonal) of 12 faceted NCs.[32]

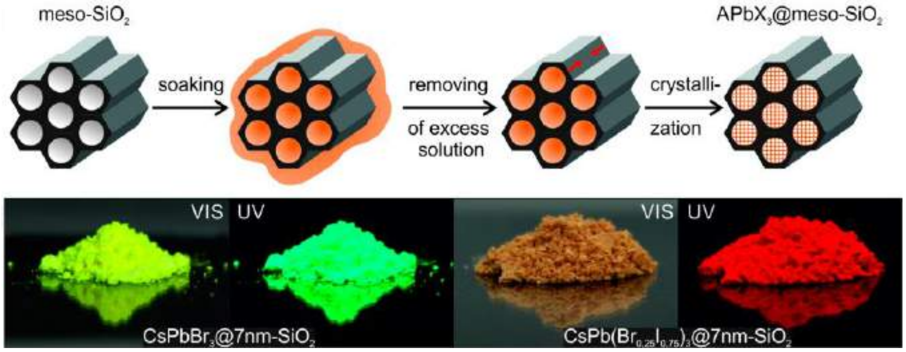

Figure 2-10. (Top) Schematic of the template-assisted synthesis of APbX3 NCs with mesoporous silica. (Bottom) corresponding product under visible light and UV light.[34]

2.3. Band-Optical Properties of Metal Halide Nanocrystals and Surface Chemistry

As shown in Figure 2-11, in the lead halide structures, the formation energy of deep traps is very high and most of the low-formation-energy defects generate shallow traps. Such defects are typically vacancies which introduce either energy levels within the bands or shallow states near the band edges. Moreover, the amount of such surface vacancies can be very high (speficy from ivan's paper) before observing a significan variation on the electronic properties of the material, behavior which has been named as defects-tolerant.[5, 95, 36] Such defect-tolerance, in turn, confers lead halide perovskite materials excellent optical properties. As shown in Figure 2-12, for classical II-VI and III-V semiconductor nanocrystals, it usually require shell coating to achieve ideal PLQY, which is time and energy cost.[37-38] In contrast, lead halide perovskites require only a "proper" ligand passivation to achieve near unity PLQY values.[10, 14-16, 19] As shown in Figure 2-13, the lead halide NCs could be divided into two types: CsX terminated and PbX_2 terminated.[39] When the crystals' surface termination is CsX, Cs^+ surface sites could be occupied by alkylammonium ions, such as oleylammonium, DDA+, benzylammonium.[13, 16, 33] Proper adding excess A ligands could thus improve the emission efficiency of lead halide NCs. The X ligands include oleate, phosphonate and Br^-. Proper adding of X ligands, like Cs-oleate, benzoic acid, hexphosphonic acid and $ZnBr_2$ could provide better passivation of X vacancies on the surface trap.[10, 15-16, 18] Specially, DDAB and zwitterion ligands could act as AX ligands pair and thus could passivate A^+ and X^- vacancies at the same time.[14, 16] The DDAB has also been used as the most common ligand to exchange the standard oleate-oleylammonium ligands and improve the brightness and stability of nanocrystals.[16, 20, 26]For the PbX_2 terminated nanocrystals, it has a rare experimental case on lead halide nanocrystals, only when employing strong Lewis acid as ligands in the direct synthesis. For example, alky phosphonic acid and dodecylbenzene sulfonic acid were employed in the direct synthesis and cause a Pb rich compostion for the $CsPbBr_3$.[10, 18-19] In such case, due to the strong binding affinity between the phosphonate (sulfonate) and Pb^{2+} rich surface, both NCs show near-unity PLQY and stability against washing. Furthermore, we here also study how the ligands stripping would influence the band and final emission of lead halide nanocrystals. The details would be discussed in Chapter 4.

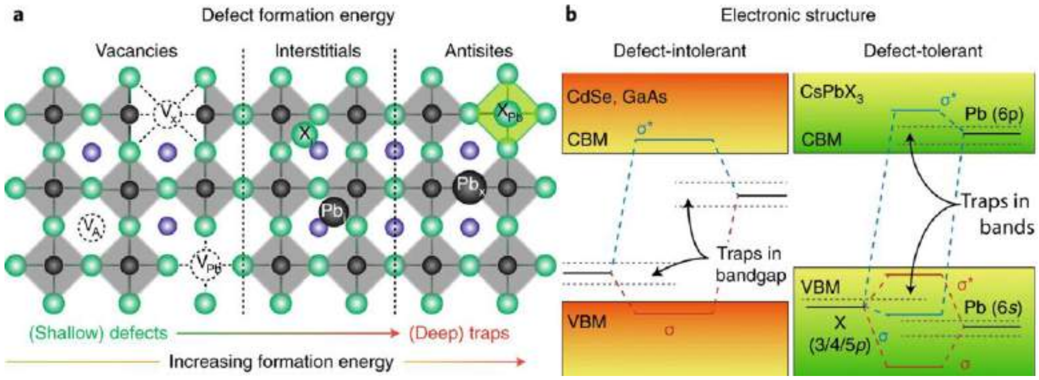

Figure 2-11. (a) Structure scheme of lead halide materials. (b) Band structure of classical II-VI, III-V semiconductors (left) and lead halide materials (right).[5]

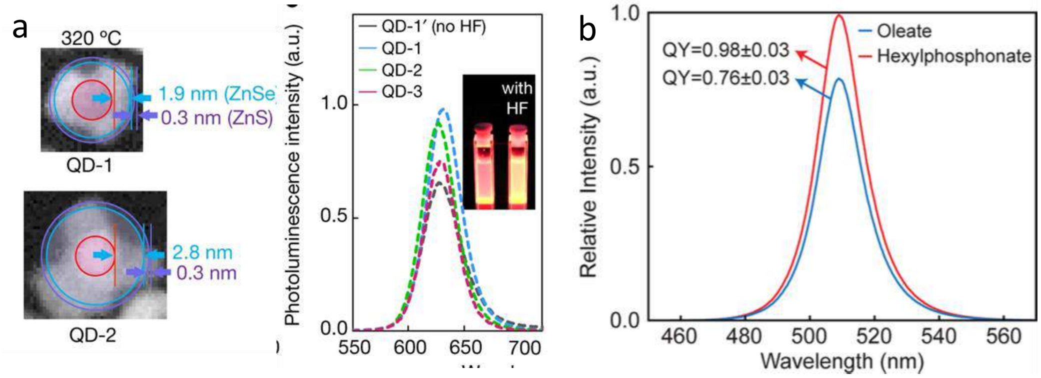

Figure 2-12. (a) Structure scheme of lead halide materials.[38] (b) Band structure of classical II-VI, III-V semiconductors (left) and lead halide materials (right).[15]

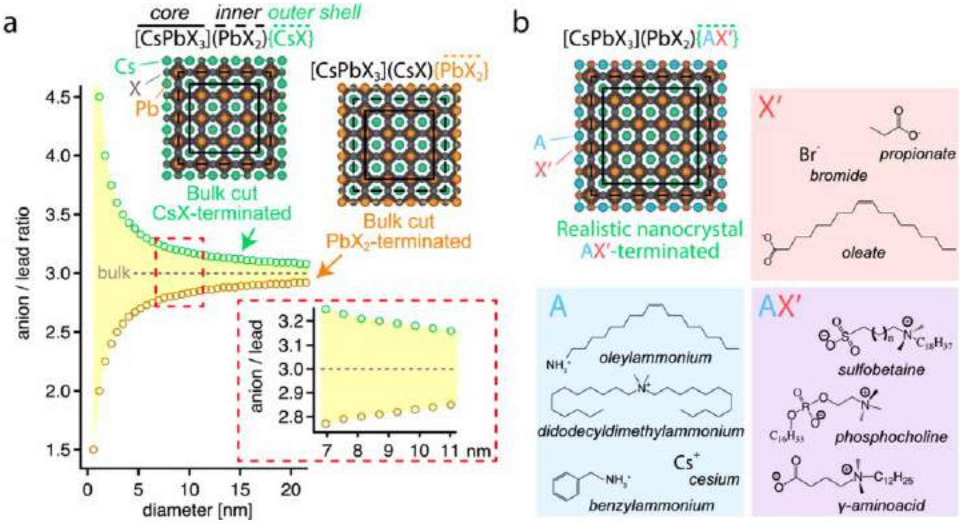

Figure 2-13. (a) Composition scheme of CsX terminated perovskite and PbX$_2$ terminated perovskite. With different termination, the mol ratio of X: Pb vary from 2.8 to 3.2. (b) Various ligands combination for AX pair. A = [oleylammonium, DDA+, benzylammonium and Cs$^+$], X = [oleate, propionate and Br$^-$]. AX pair could also replace by the various zwitterion ligands.[39]

As to double perovskite and other metal halide nanocrystals, they are not defect tolerance anymore.[23, 36] For example, with proper Bi^{3+} and Na$^+$ doping, the double perovskite Cs$_2$AgInCl$_6$ could generate bright broadband emission and its PLQY could reach to 86% in its bulk form. [6] However, for Bi^{3+}-Na$^+$ doped Cs$_2$AgInCl$_6$ nanocrystals, with standard ligands, the PLQY is only around 20%. [3] The PLQY gap between bulk and nanocrystals indicate there existing large surface trap on the nanocrystal, which finally hinder the effective radiative recombination. By varying different ligands combination, the PLQY of nanocrystals could reach to 30% but still far from the bulk materials. With quantitative NMR analysis, the surface ligands density on the Cs$_2$AgInCl$_6$ nanocrystals was determined as 4.9 ligands/nm^2. Although the ligands density is already much higher than typical CsPbBr$_3$ nanocrystals, which is around 2-3 ligands/nm^2, it was proved to still far from to reach ideal passivation for surface Cl trap. As shown in Figure 2-14, strongly localized 3p orbitals of surface Cl could form deep trap on the band structure of Cs$_2$AgInCl$_6$ nanocrystals, and thus heavily influence the emission efficiency of double perovskite.[23] Considering the steric effect of ligands, the near 100% passivation is almost impossible reached for double perovskite nanocrystals. To eliminate the PLQY gap between bulk and nanocrystals, the shell coating should be an alternative way. In addition, the 0D metal halide NCs could be a more promising emitter than the 3D double perovskite. As it's emitter center is more localized and would be less influenced by the trap on the NCs' surface.[8]

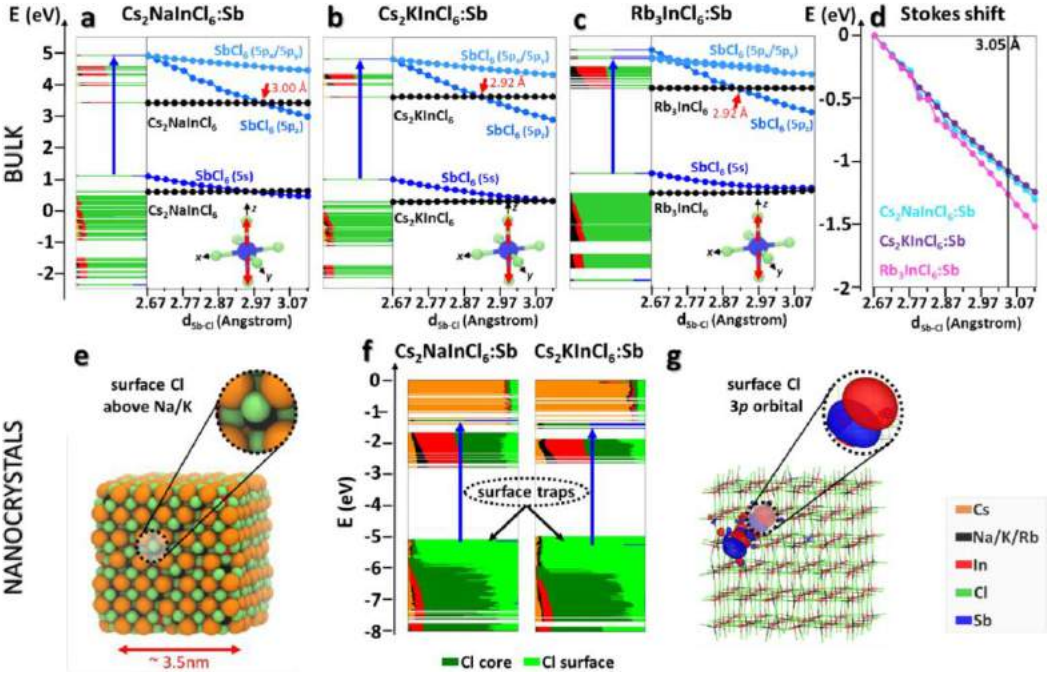

Figure 2-14. Band energy of double perovskite (a) $Cs_2NaInCl_6$, (b) Cs_2KInCl_6 and (c) Rb_3InCl_6. Both NCs was doped by Sb^{3+} and comprised by 2×2×2 supercells. (d) Energy shift of 5s orbital of $[SbCl_6]^{3-}$ following by the systematic stretching of the axial Sb−Cl bonds in different lattice environment. (e) Scheme of surface Cl on the double perovskite nanocrystals (d = 3.5 nm). (f) The trap state mainly contributed by surface Cl on the $Cs_2NaInCl_6$, and Cs_2KInCl_6 nanocrystals. (g) Strongly localized 3p orbitals of surface Cl.[8]

REFERENCES:

1. Akkerman, Q. A.; D'Innocenzo, V.; Accornero, S.; Scarpellini, A.; Petrozza, A.; Prato, M.; Manna, L., Tuning the Optical Properties of Cesium Lead Halide Perovskite Nanocrystals by Anion Exchange Reactions. *Journal of the American Chemical Society* **2015,** *137* (32), 10276-10281.
2. Protesescu, L.; Yakunin, S.; Bodnarchuk, M. I.; Krieg, F.; Caputo, R.; Hendon, C. H.; Yang, R. X.; Walsh, A.; Kovalenko, M. V., Nanocrystals of Cesium Lead Halide Perovskites (CsPbX3, X = Cl, Br, and I): Novel Optoelectronic Materials Showing Bright Emission with Wide Color Gamut. *Nano Letters* **2015,** *15* (6), 3692-3696.
3. Locardi, F.; Cirignano, M.; Baranov, D.; Dang, Z.; Prato, M.; Drago, F.; Ferretti, M.; Pinchetti, V.; Fanciulli, M.; Brovelli, S.; De Trizio, L.; Manna, L., Colloidal Synthesis of Double Perovskite Cs2AgInCl6 and Mn-Doped Cs2AgInCl6 Nanocrystals. *Journal of the American Chemical Society* **2018,** *140* (40), 12989-12995.
4. Jing, Y.; Liu, Y.; Li, M.; Xia, Z., Photoluminescence of Singlet/Triplet Self-Trapped Excitons in Sb3+-Based Metal Halides. *Advanced Optical Materials* **2021,** *9* (8), 2002213.
5. Akkerman, Q. A.; Rainò, G.; Kovalenko, M. V.; Manna, L., Genesis, challenges and opportunities for colloidal lead halide perovskite nanocrystals. *Nature Materials* **2018,** *17* (5), 394-405.
6. Luo, J.; Wang, X.; Li, S.; Liu, J.; Guo, Y.; Niu, G.; Yao, L.; Fu, Y.; Gao, L.; Dong, Q.; Zhao, C.; Leng, M.; Ma, F.; Liang, W.; Wang, L.; Jin, S.; Han, J.; Zhang, L.; Etheridge, J.; Wang, J.; Yan, Y.; Sargent, E. H.; Tang, J., Efficient and stable emission of warm-white light from lead-free halide double perovskites. *Nature* **2018,** *563* (7732), 541-545.
7. Zhang, B.; Pinchetti, V.; Zito, J.; Ray, A.; Melcherts, A. E. M.; Ghini, M.; Pianetti, A.; Infante, I.; Brovelli, S.; De Trizio, L.; Manna, L., Isolated [SbCl6]3– Octahedra Are the Only Active Emitters in Rb7Sb3Cl16 Nanocrystals. *ACS Energy Letters* **2021,** *6* (11), 3952-3959.
8. Zhu, D.; Zaffalon, M. L.; Zito, J.; Cova, F.; Meinardi, F.; De Trizio, L.; Infante, I.; Brovelli, S.; Manna, L., Sb-Doped Metal Halide Nanocrystals: A 0D versus 3D Comparison. *ACS Energy Letters* **2021,** *6* (6), 2283-2292.
9. Dirin, D. N.; Protesescu, L.; Trummer, D.; Kochetygov, I. V.; Yakunin, S.; Krumeich, F.; Stadie, N. P.; Kovalenko, M. V., Harnessing Defect-Tolerance at the Nanoscale: Highly Luminescent Lead Halide Perovskite Nanocrystals in Mesoporous Silica Matrixes. *Nano Letters* **2016,** *16* (9), 5866-5874.
10. Zhang, B.; Goldoni, L.; Zito, J.; Dang, Z.; Almeida, G.; Zaccaria, F.; de Wit, J.; Infante, I.; De Trizio, L.; Manna, L., Alkyl Phosphonic Acids Deliver CsPbBr3 Nanocrystals with High Photoluminescence Quantum Yield and Truncated Octahedron Shape. *Chemistry of Materials* **2019,** *31* (21), 9140-9147.
11. Wang, S.; Du, L.; Jin, Z.; Xin, Y.; Mattoussi, H., Enhanced Stabilization and Easy Phase Transfer of CsPbBr3 Perovskite Quantum Dots Promoted by High-Affinity Polyzwitterionic Ligands. *Journal of the American Chemical Society* **2020,** *142* (29), 12669-12680.
12. Almeida, G.; Goldoni, L.; Akkerman, Q.; Dang, Z.; Khan, A. H.; Marras, S.; Moreels, I.; Manna, L., Role of Acid–Base Equilibria in the Size, Shape, and Phase Control of Cesium Lead Bromide Nanocrystals. *ACS Nano* **2018,** *12* (2), 1704-1711.
13. Smock, S. R.; Williams, T. J.; Brutchey, R. L., Quantifying the Thermodynamics of Ligand Binding to CsPbBr3 Quantum Dots. *Angewandte Chemie International Edition* **2018,** *57* (36), 11711-11715.
14. Krieg, F.; Ochsenbein, S. T.; Yakunin, S.; ten Brinck, S.; Aellen, P.; Süess, A.; Clerc, B.; Guggisberg, D.; Nazarenko, O.; Shynkarenko, Y.; Kumar, S.; Shih, C.-J.; Infante, I.; Kovalenko, M. V., Colloidal CsPbX3 (X = Cl, Br, I) Nanocrystals 2.0: Zwitterionic Capping Ligands for Improved Durability and Stability. *ACS Energy Letters* **2018,** *3* (3), 641-646.

15. Nenon, D. P.; Pressler, K.; Kang, J.; Koscher, B. A.; Olshansky, J. H.; Osowiecki, W. T.; Koc, M. A.; Wang, L.-W.; Alivisatos, A. P., Design Principles for Trap-Free CsPbX3 Nanocrystals: Enumerating and Eliminating Surface Halide Vacancies with Softer Lewis Bases. *Journal of the American Chemical Society* **2018,** *140* (50), 17760-17772.

16. Imran, M.; Ijaz, P.; Goldoni, L.; Maggioni, D.; Petralanda, U.; Prato, M.; Almeida, G.; Infante, I.; Manna, L., Simultaneous Cationic and Anionic Ligand Exchange For Colloidally Stable CsPbBr3 Nanocrystals. *ACS Energy Letters* **2019,** *4* (4), 819-824.

17. Shamsi, J.; Kubicki, D.; Anaya, M.; Liu, Y.; Ji, K.; Frohna, K.; Grey, C. P.; Friend, R. H.; Stranks, S. D., Stable Hexylphosphonate-Capped Blue-Emitting Quantum-Confined CsPbBr3 Nanoplatelets. *ACS Energy Letters* **2020,** *5* (6), 1900-1907.

18. Yang, D.; Li, X.; Zhou, W.; Zhang, S.; Meng, C.; Wu, Y.; Wang, Y.; Zeng, H., CsPbBr3 Quantum Dots 2.0: Benzenesulfonic Acid Equivalent Ligand Awakens Complete Purification. *Advanced Materials* **2019,** *31* (30), 1900767.

19. Zhang, B.; Goldoni, L.; Lambruschini, C.; Moni, L.; Imran, M.; Pianetti, A.; Pinchetti, V.; Brovelli, S.; De Trizio, L.; Manna, L., Stable and Size Tunable CsPbBr3 Nanocrystals Synthesized with Oleylphosphonic Acid. *Nano Letters* **2020,** *20* (12), 8847-8853.

20. Stelmakh, A.; Aebli, M.; Baumketner, A.; Kovalenko, M. V., On the Mechanism of Alkylammonium Ligands Binding to the Surface of CsPbBr3 Nanocrystals. *Chemistry of Materials* **2021,** *33* (15), 5962-5973.

21. Krieg, F.; Ong, Q. K.; Burian, M.; Rainò, G.; Naumenko, D.; Amenitsch, H.; Süess, A.; Grotevent, M. J.; Krumeich, F.; Bodnarchuk, M. I.; Shorubalko, I.; Stellacci, F.; Kovalenko, M. V., Stable Ultraconcentrated and Ultradilute Colloids of CsPbX3 (X = Cl, Br) Nanocrystals Using Natural Lecithin as a Capping Ligand. *Journal of the American Chemical Society* **2019,** *141* (50), 19839-19849.

22. Zhang, Y.; Shah, T.; Deepak, F. L.; Korgel, B. A., Surface Science and Colloidal Stability of Double-Perovskite Cs2AgBiBr6 Nanocrystals and Their Superlattices. *Chemistry of Materials* **2019,** *31* (19), 7962-7969.

23. Zhang, B.; Wang, M.; Ghini, M.; Melcherts, A. E. M.; Zito, J.; Goldoni, L.; Infante, I.; Guizzardi, M.; Scotognella, F.; Kriegel, I.; De Trizio, L.; Manna, L., Colloidal Bi-Doped Cs2Ag1–xNaxInCl6 Nanocrystals: Undercoordinated Surface Cl Ions Limit their Light Emission Efficiency. *ACS Materials Letters* **2020,** *2* (11), 1442-1449.

24. Erdemir, D.; Lee, A. Y.; Myerson, A. S., Nucleation of Crystals from Solution: Classical and Two-Step Models. *Accounts of Chemical Research* **2009,** *42* (5), 621-629.

25. Yu, K., CdSe Magic-Sized Nuclei, Magic-Sized Nanoclusters and Regular Nanocrystals: Monomer Effects on Nucleation and Growth. *Advanced Materials* **2012,** *24* (8), 1123-1132.

26. Dong, Y.; Qiao, T.; Kim, D.; Parobek, D.; Rossi, D.; Son, D. H., Precise Control of Quantum Confinement in Cesium Lead Halide Perovskite Quantum Dots via Thermodynamic Equilibrium. *Nano Letters* **2018,** *18* (6), 3716-3722.

27. Peng, L.; Dutta, A.; Xie, R.; Yang, W.; Pradhan, N., Dot–Wire–Platelet–Cube: Step Growth and Structural Transformations in CsPbBr3 Perovskite Nanocrystals. *ACS Energy Letters* **2018,** *3* (8), 2014-2020.

28. Nevers, D. R.; Williamson, C. B.; Savitzky, B. H.; Hadar, I.; Banin, U.; Kourkoutis, L. F.; Hanrath, T.; Robinson, R. D., Mesophase Formation Stabilizes High-Purity Magic-Sized Clusters. *Journal of the American Chemical Society* **2018,** *140* (10), 3652-3662.

29. Zhang, B.; Zhu, T.; Ou, M.; Rowell, N.; Fan, H.; Han, J.; Tan, L.; Dove, M. T.; Ren, Y.; Zuo, X.; Han, S.; Zeng, J.; Yu, K., Thermally-induced reversible structural isomerization in colloidal semiconductor CdS magic-size clusters. *Nature Communications* **2018,** *9* (1), 2499.

30. Imran, M.; Ijaz, P.; Baranov, D.; Goldoni, L.; Petralanda, U.; Akkerman, Q.; Abdelhady, A. L.; Prato, M.; Bianchini, P.; Infante, I.; Manna, L., Shape-Pure, Nearly Monodispersed CsPbBr3 Nanocubes Prepared Using Secondary Aliphatic Amines. *Nano Letters* **2018,** *18* (12), 7822-7831.

31. Peng, L.; Dutta, S. K.; Mondal, D.; Hudait, B.; Shyamal, S.; Xie, R.; Mahadevan, P.; Pradhan, N., Arm Growth and Facet Modulation in Perovskite Nanocrystals. *Journal of the American Chemical Society* **2019,** *141* (40), 16160-16168.

32. Bera, S.; Behera, R. K.; Pradhan, N., α-Halo Ketone for Polyhedral Perovskite Nanocrystals: Evolutions, Shape Conversions, Ligand Chemistry, and Self-Assembly. *Journal of the American Chemical Society* **2020,** *142* (49), 20865-20874.

33. Pradhan, N., Alkylammonium Halides for Facet Reconstruction and Shape Modulation in Lead Halide Perovskite Nanocrystals. *Accounts of Chemical Research* **2021,** *54* (5), 1200-1208.

34. Malgras, V.; Tominaka, S.; Ryan, J. W.; Henzie, J.; Takei, T.; Ohara, K.; Yamauchi, Y., Observation of Quantum Confinement in Monodisperse Methylammonium Lead Halide Perovskite Nanocrystals Embedded in Mesoporous Silica. *Journal of the American Chemical Society* **2016,** *138* (42), 13874-13881.

35. Ji, Y.; Wang, M.; Yang, Z.; Qiu, H.; Padhiar, M. A.; Zhou, Y.; Wang, H.; Dang, J.; Gaponenko, N. V.; Bhatti, A. S., Trioctylphosphine-Assisted Pre-protection Low-Temperature Solvothermal Synthesis of Highly Stable CsPbBr3/TiO2 Nanocomposites. *The Journal of Physical Chemistry Letters* **2021,** *12* (15), 3786-3794.

36. Infante, I.; Manna, L., Are There Good Alternatives to Lead Halide Perovskite Nanocrystals? *Nano Letters* **2021,** *21* (1), 6-9.

37. Cao, H.; Ma, J.; Huang, L.; Qin, H.; Meng, R.; Li, Y.; Peng, X., Design and Synthesis of Antiblinking and Antibleaching Quantum Dots in Multiple Colors via Wave Function Confinement. *Journal of the American Chemical Society* **2016,** *138* (48), 15727-15735.

38. Won, Y.-H.; Cho, O.; Kim, T.; Chung, D.-Y.; Kim, T.; Chung, H.; Jang, H.; Lee, J.; Kim, D.; Jang, E., Highly efficient and stable InP/ZnSe/ZnS quantum dot light-emitting diodes. *Nature* **2019,** *575* (7784), 634-638.

39. Bodnarchuk, M. I.; Boehme, S. C.; ten Brinck, S.; Bernasconi, C.; Shynkarenko, Y.; Krieg, F.; Widmer, R.; Aeschlimann, B.; Günther, D.; Kovalenko, M. V.; Infante, I., Rationalizing and Controlling the Surface Structure and Electronic Passivation of Cesium Lead Halide Nanocrystals. *ACS Energy Letters* **2019,** *4* (1), 63-74.

Chapter 3: Characterization Method for Surface Chemistry of Metal Halide NCs.

Metal halide (MH) nanocrystals are big family with ~10^4 different materials. Although LHP materials has been deeply characterized, many other MH materials remain to be unexplored. Comparing with classical semiconductor NCs, the intrinsic soft lattice of MH make their characterization more challenged. To draw a complete picture of the surface chemistry of MH NCs, the combination of structure, composition, morphology and surface characterization is necessary.[1] Here we will focus on the surface analysis of MH NCs.

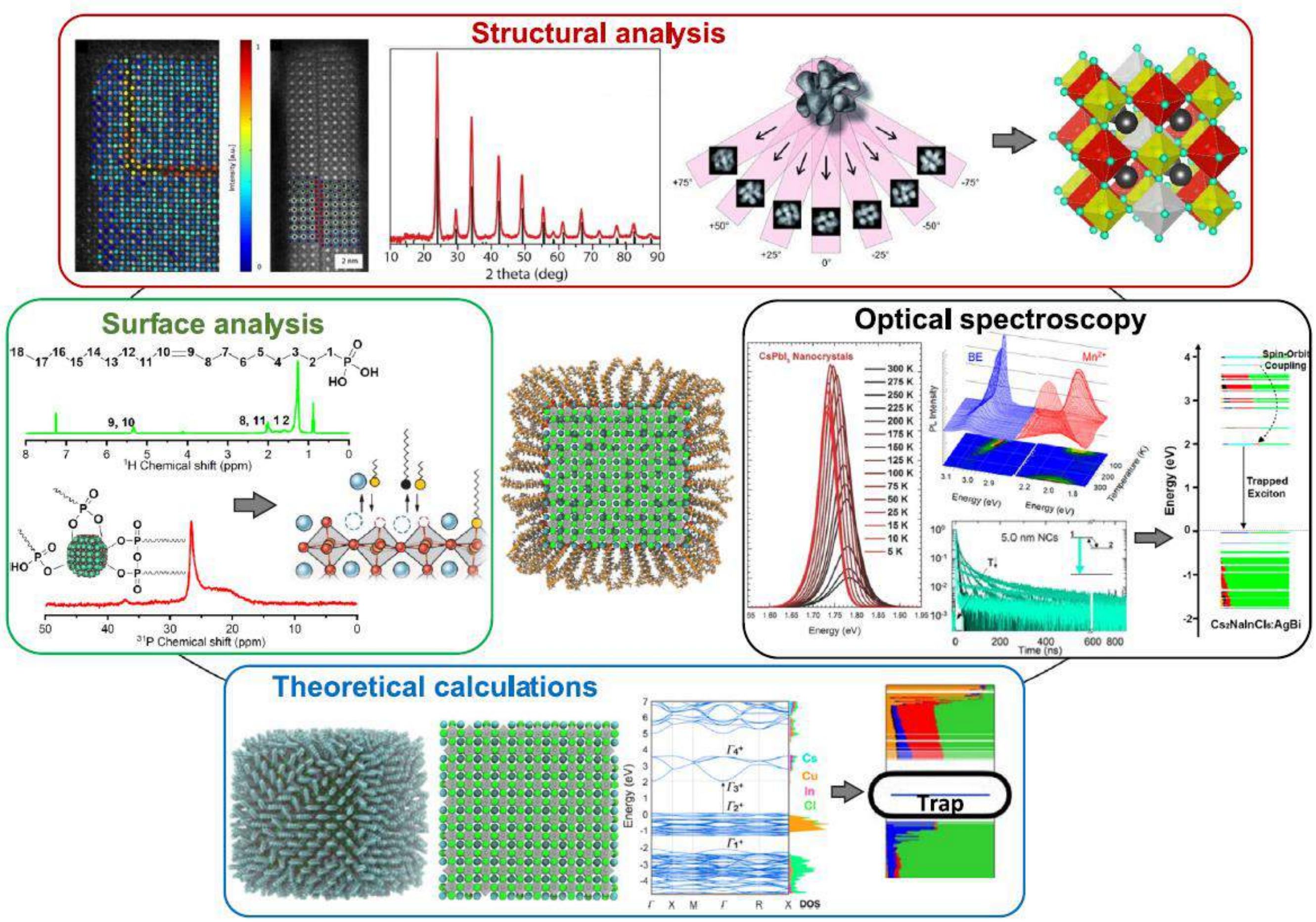

Figure 3-1. Structural characterization (TEM, XRD, 3D electron diffraction), surface analysis (ICP, TGA, EDS, NMR), optical analysis and theoretical calculations of MH NCs.[1]

3.1 Composition Characterization.

Thermogravimetric analysis (TGA).

TGA is a convenient method to evaluate the inorganic core/organic ligands mass ratio of colloidal nanocrystals, provided that they are thoroughly cleaned (i.e. no residual organic in the NCs dispersion).[2-4] TGA spectra collect the temperature dependent mass of given sample. Generally, the organic part of the NCs will evaporate and the inert inorganic core remain stable under heating. The weight fraction of bound ligands in nanocrystals can be appreciated by the study reported by Kui et al. who performed the TGA of bulk CdS, 3 nm CdS nanocrystals (RQDs) and two small (<2 nm) CdS nanocrystals (MSC-311 and MSC-322) (Figure 3-2).[4] While the mass of bulk CdS remained constant, a significant mass loss was recorded from room temperature up to 400°C for the NC samples. Such results indicate that the mass of organic ligands increases when decreasing the size of the NCs up to a value as high as 50% in the case of <2 nm NCs.[4]

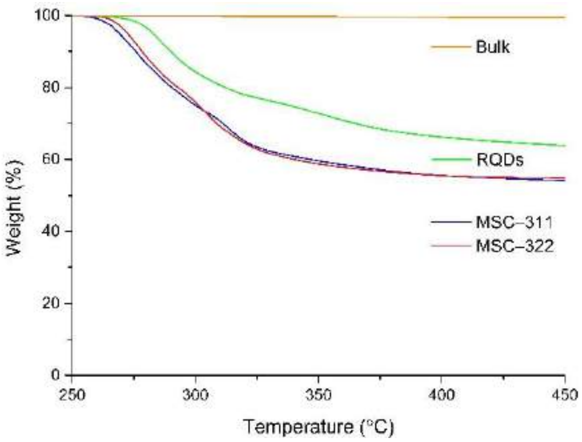

Figure 3-2. TGA spectra of two small CdS nanoclusters (named as MSC-311 and MSC-322), CdS regular quantum dot (RQDs) and bulk CdS materials. The sample was dried before test and has a mass around 10-20 mg. The TGA machine is type NETZSCH STA 449C. The test was done under N2 atmosphere, with a temperature range from 30-450°C, with a step of 15°C /min.[4]

Inductively Coupled Plasma-optical Emission Spectrometry and Inductively coupled plasma mass spectrometry (ICP-OES and ICP-MS). ICP-OES is a general method for quantitatively element analysis. The machine comprised by ionization part (ICP) and optical part (OES).[5] The given sample is ionized into atomic form and be excited under 7000 K in the ICP part. The excited atom emit light with specific energy when relax to its ground state. The specific light can be detected and analyzed by the OES part. ICP-OES analysis is typically performed to retrieve an accurate concentration of the tested element and, thus, to estimate both the NCs concentration and elemental ratios between elements, that is the composition of the NCs. However, for halide element, whose specific spectra is out of the range of OES system, can't be detected by ICP-OES properly. It limit the application of ICP-OES for the composition determination of metal halide materials.[6] ICP-MS is a similar technic with ICP-OES but using mass spectrometer (MS) to replace the OES part as detector.[5] ICP-MS could detect more element and has a much higher sensitivity (ng/ml) than ICP-OES (ug/ml). The high sensitivity is helpful to determine the concentration of doping element, even in a extreme low doping concentration.[7-8]

Energy-dispersive X-ray spectroscopy (EDS). In EDS process, high speed electrons interact with the inner layer electron of given atom in way of elastic and inelastic collision. In such process, most of the incident electron energy (~99%) is converted into heating, while 1% of the energy excites the atoms in a radiative way. As shown in Figure 3-3, when the inner electrons of an atom are kicked out by an external stimulus, the outer electrons will be also destabilized and will fill up the vacancy formed in the inner layer. Such process generates a characteristic X-rays emission, which depends on the energy difference between outer and inner electron shells of a specific atom (eg. M-K, L-K, M-L).[9-10] In this way, it is possible to investigate which atomic species are present in a given sample and to estimate their quantity. More importantly, the EDS analysis performed in a TEM could also yield the space distribution (mapping) of element in a given NC sample.[11-12] Such mapping is particularly usefull when characterizing complex structures or heterostructures, as it allows to clearly distinguish the different crystal domains (provided that they have a different composition). As an example, the EDS analysis was used to investigate $CsPbBr_3$-$Pb_4S_3Br_2$ nano heterostructures: with a ratios of Cs:Pb:Br equal to 1:1:3 for the perovskite domain, and of Pb: S: Br equal to 4:3:3 for the lead chalcohalide domain (Figure 3-4).[12]

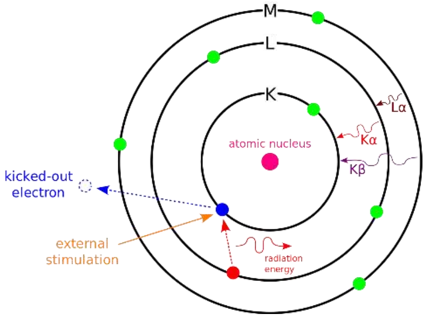

Figure 3-3. Model of interaction between external electron and atomic.

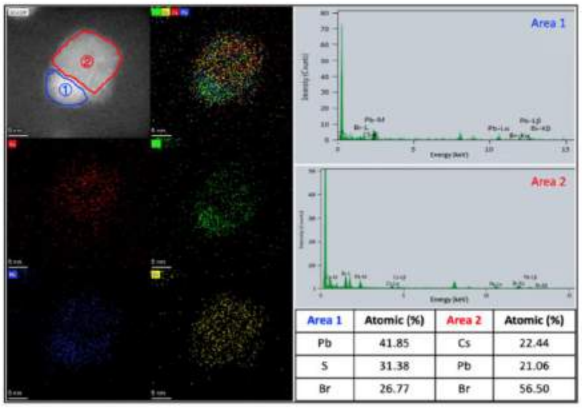

Area 1	Atomic (%)	Area 2	Atomic (%)
Pb	41.85	Cs	22.44
S	31.38	Pb	21.06
Br	26.77	Br	56.50

Figure 3-4. HAADF-STEM EDS analysis of the $CsPbBr_3$-$Pb_4S_3Br_2$ NCs.[12]

X-ray Photoelectron Spectroscopy (XPS).

When certain light react with the surface of the solid, some of electron will absorb the light and gain enough dynamic energy to release from the surface. Such process was named as photoelectric effect, as shown in Scheme 1. XPS is based on the photoelectric effect using the X-ray as incident light.[13] The inner electron could absorb the X-ray light and release from the atom. The outer electrons will fill up the vacancy formed in the inner layer. Such process generates a characteristic X-rays emission, which depends on the energy difference between outer and inner electron shells of a specific atom, as shown in Figure 3-3. XPS could generally detect all the elements except H and He. By XPS analysis, not only the composition of the sample surface can be detected, the chemical state of the element can also be determined by its characteristic binding energy spectra.[14-15] As shown in Figure 3-5, in the XPS spectra of CdSe NCs, the surface Cd which bound to O, N show different binding energy with the inner Cd which bound to Se only. Moreover, the over Cd 3d XPS spectra in zinc blend CdSe NCs is also very different with the spectra in wurtzite CdSe NCs.[14]

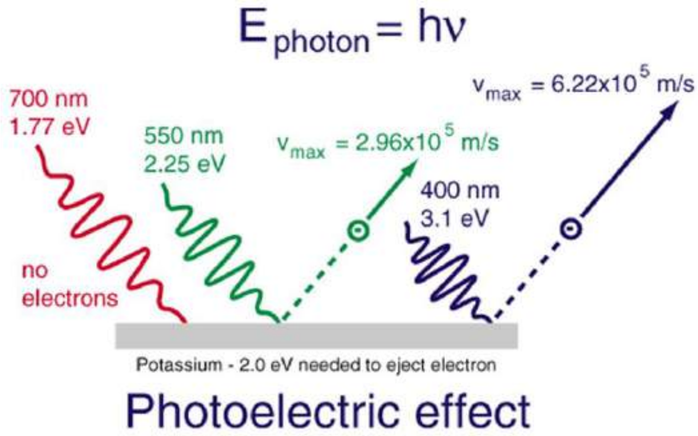

Scheme 1. Mechanism of photoelectric effect.

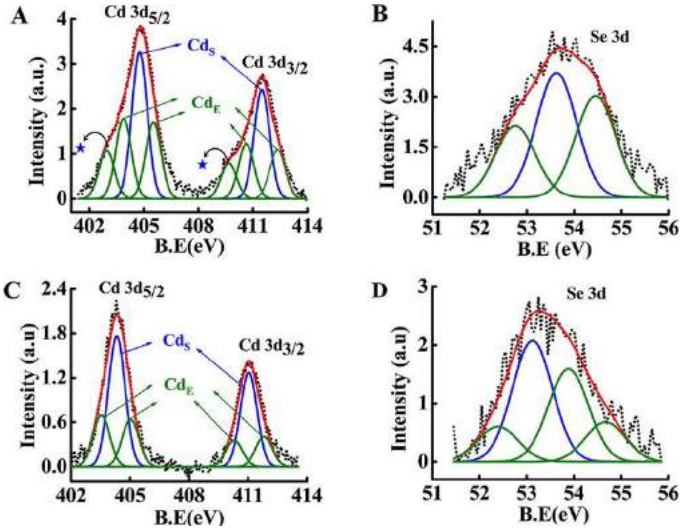

Figure 3-5. XPS spectra of A) 3d electrons of Cd in Zinc blend CdSe nanocrystals and B) corresponding 3d electrons of Se. C) 3d electrons of Cd in wurtzite CdSe nanocrystals and D) corresponding 3d electrons of Se. The peaks of Cd was separated into two part: Cd bound to Se (blue traces) and Cd bound to oxygen, nitrogen (green traces).[14]

Table 1. Summary of composition characterization technic.[1]

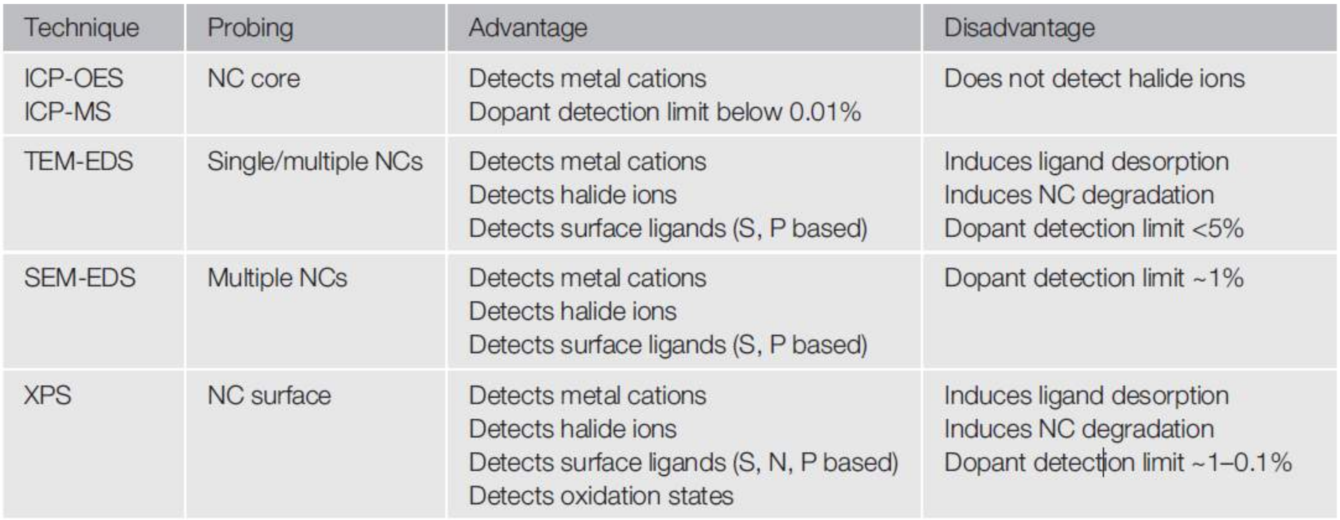

Technique	Probing	Advantage	Disadvantage
ICP-OES ICP-MS	NC core	Detects metal cations Dopant detection limit below 0.01%	Does not detect halide ions
TEM-EDS	Single/multiple NCs	Detects metal cations Detects halide ions Detects surface ligands (S, P based)	Induces ligand desorption Induces NC degradation Dopant detection limit <5%
SEM-EDS	Multiple NCs	Detects metal cations Detects halide ions Detects surface ligands (S, P based)	Dopant detection limit ~1%
XPS	NC surface	Detects metal cations Detects halide ions Detects surface ligands (S, N, P based) Detects oxidation states	Induces ligand desorption Induces NC degradation Dopant detection limit ~1–0.1%

3.2 Shape and morphology characterization.

Transmission electron microscop (TEM). The minimum distance (r_{min}) between two points that can be resolved with a microscope can be expressed as: $r_{min} = 0.61\lambda/n\sin\alpha$, with n = refractive index of sample, α = semi-angle of collection of magnifying lens ($n\cdot\sin\alpha$=numerical aperture~1).[16-17] The final resolution is limited by the wavelength of light. TEM has a much higher resolution than normal light microscopes, because electron has a much smaller de Broglie wavelength (1.23 nm). The TEM analysis is the most powerful tool to characterize the size, size distribution and morphology of NCs.[11-12, 18-24] As shown in Figure 3-6a-c, the size evolution of $CsPbBr_3$ nanocrystals could be clearly characterized by low resolution TEM. [20] As shown in Figure 3-6d-f, TEM images show different size and morphology the $CsPbBr_3$ NCs.[18-19, 21] Moreover, with higher energy of electron beam, the high resolution TEM (HRTEM) image could be collected. In HRTEM, the lattice parameters of given NCs could be detected. The lattice parameter is related to different exposed facets. As shown in Figure 3-6g, the HRTEM of phosphonate capped $CsPbBr_3$ nanocrystals indicate it expose uncommon facets comparing with standard cubic $CsPbBr_3$ nanocrystals (only six [001] facets). [25] Beside direct image of individual nanocrystals, the super-structure of the self-assembled nanocrystals could also be visualized in TEM. As shown in Figure 3-6h, the spiral nanorod which comprised by the polyhedron nanocrytsals was shown in inverted TEM.[23] As shown in Figure 3-6i, the superlattice of $CsPbBr_3$ NCs in hexagonal stacking was clearly visualized.[22] The interaction between electron and sample could also generate side reaction, which result in the damage of the specimen. As shown in Figure 3-7a-c, under the irradiation of electron beam, the Pb element which escape from Cs_4PbBr_6 NCs, was gradually reduced into Pb^0. When the concentration is enough high, the Pb^0 start to nucleate and grow into large nanocrystals.[24] For $CsPbBr_3$ NCs, it's also common that the electron reduced Pb^0 crystal appear as black dot on the TEM image of NCs. As shown in Figure 3-7d-e, the Ag^+ in the lattice of $Cs_2AgInCl_6$ nanocrystals was reduced by long electron irradiation and nucleate into Ag^0 particle on the surface.[26] Operating the TEM at lower energy (200 keV) and at low temperatures or better surface passivation of NCs could reduce such side reaction.[1, 27-28]

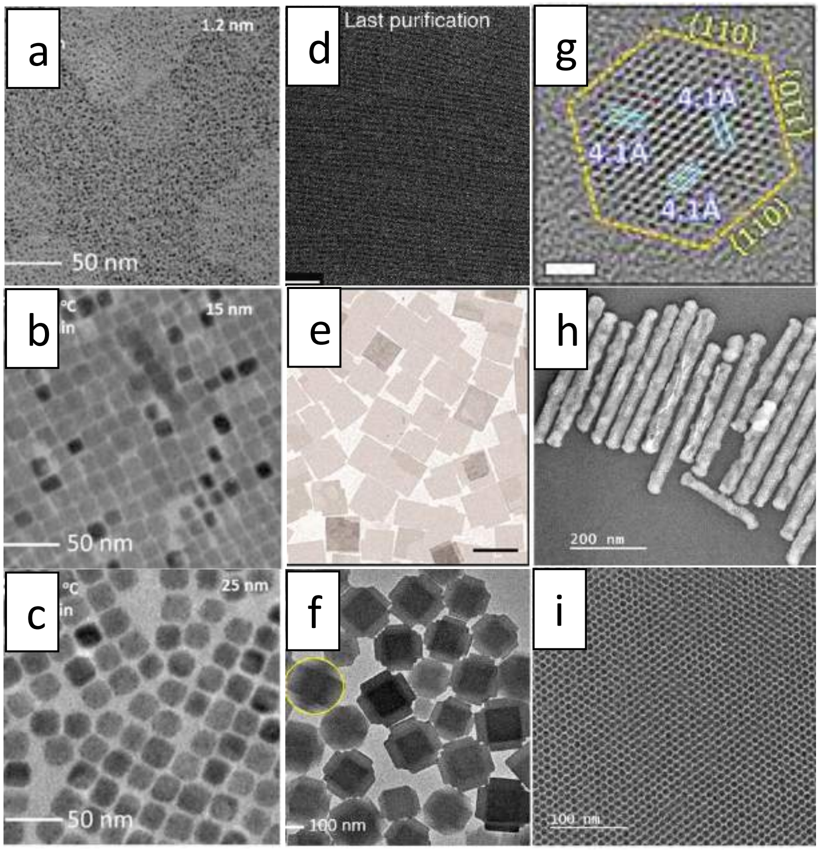

Figure 3-6. TEM image of a) small b) middle and c) large $CsPbBr_3$ nanocrystals;[20] TEM image of d) $CsPbBr_3$ nanowire,[19] e) $CsPbBr_3$ nanoplatelets[18] and f) $CsPbBr_3$ cubic with six-arm;[21] g) HRTEM of polyhedron $CsPbBr_3$ exposing different facets;[25] h) self-assembled spiral $CsPbBr_3$ nanorod;[23] i) self-assembled superlattice of polyhedron $CsPbBr_3$ nanocrystals.[22]

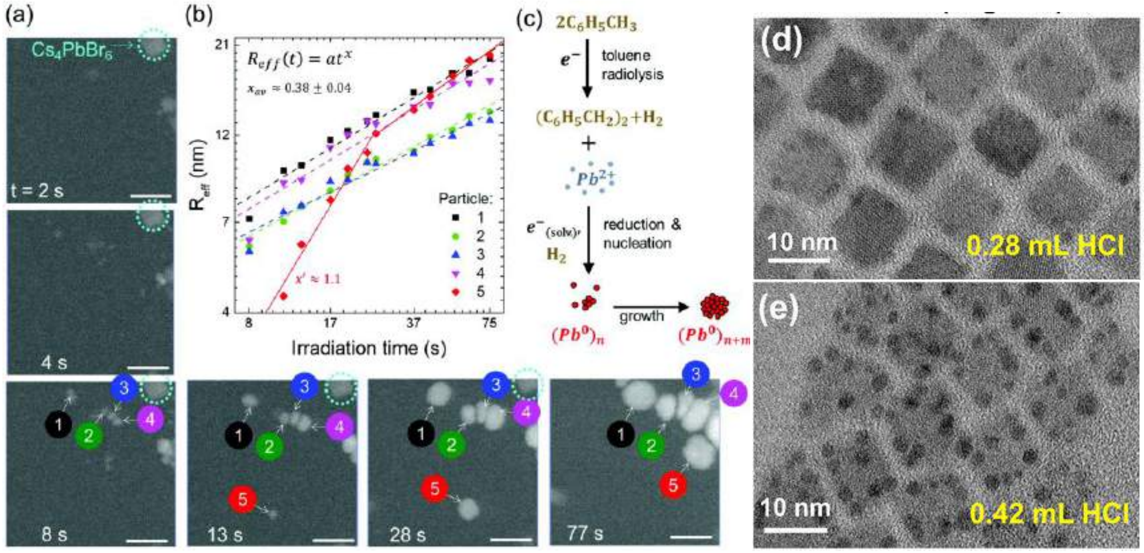

Figure 3-7. The nucleation of Pb^0 particles in Cs_4PbBr_6 NC solution: (a) Time evolution of Pb^0 particles (scale bar: 50 nm), (b) the log–log plot of the size evolution of 5 different Pb^0 particles ($R_{eff} \sim t^x$), and (c) proposed mechanism of electron reduced Pb^0 particles,[24] (d) and (e) TEM image of Bi^{3+} doped $Cs_2AgInCl_6$ nanocrystals.[26]

Dynamic light scattering (DLS). The scattering interaction between laser and solution sample could provide hydrodynamic size of dispersed sample. It is worth to notice, the organic ligands is usually invisible in TEM image due to its low crystallization degree. In practice, size measured by TEM is usually smaller than the size measured by DLS. The difference is dependent on the length of surface ligands.[25] For example, the common oleylamine or oleic acid has a length around 2 nm.[29]

Small-angle X-ray scattering (SAXS). When X-rays interact with a specimen, their diffraction obeys the Bragg equation, $2d\sin\theta = n\lambda$. In the equation, d represent the lattice distance, θ represent the angle between incident light and sample, λ represent the wavelength of light and n represent arbitrary positive integer. Large θ (>5°) correspond to the sub-nano distance, which in the range of normal chemical bonding. The wide angle X-ray scattering (WAXS) thus represent the information of periodic atomic structure. On the other hand, the small θ (<5°) correspond to the d of several nanometers. The SAXS thus contain the information of the periodic aggregation of NCs and its size, shape.[30-32] Using synchrotron X-ray as brighter lights source, the resolution of SAXS is much improved and become a popular technic on size-determined technic in recent years.[33] SAXS technic could adopt sample both in solid and dispersion state. [31] SAXS usually collect the overall signal of large bundle sample, which represent the sample information more averagely comparing TEM. In contrast, SAXS test is also non-destructive and thus play a important role on observing in-situ size evolution of given samples It is generally applied in the study of NCs' nucleation and growth process.[30, 32] As shown in Figure 3-8a, by proper fitting of SAXS data, multi-level structure of NCs aggregations could be analysised..[31] The in-situ SAXS investigation on the Cd(Myristate)$_2$ precursors in the heating process was shown in Figure 3-8c. It indicates that the initial Cd(Myristic)$_2$ has a lamellar structure, which gradually dissolve when increasing the temperature. Such lamellar structure of Cd precursors play a templet effect in the formation of CdSe nanocluster and nanoplatelet in low temperature (30 to 70°C).[30]

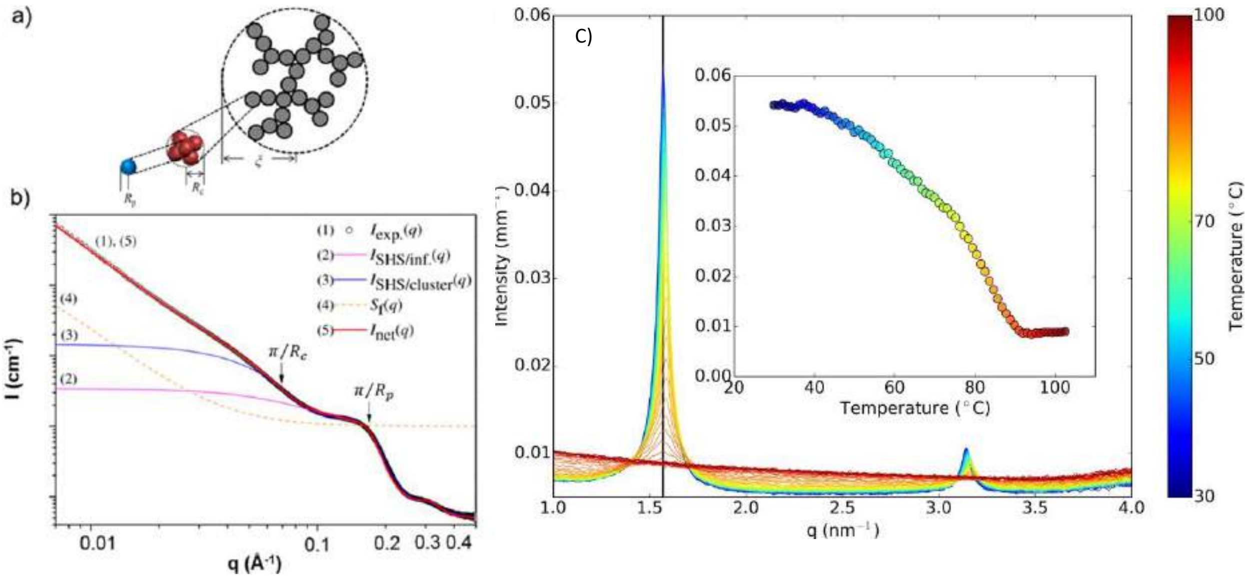

Figure 3-8. a) Tertiary structure of aggregated sample. Individual particles (blue ball, R_p), aggregated individual particles (red ball, R_c) and higher grade aggregation ξ.b) SAXS data of the aggregated sample. and fitting for each parameters (R_p, R_c).[31] c) in-situ SAXS characterization of Cd(Myristic)$_2$ precursors under heating process in the formation of CdSe nanocrystals.[30]

3.3 Binding Motif Characterization.

Fourier-transform infrared spectroscopy (FTIR). Molecules can absorb light which can promote vibrational or rotational modes. The energies of such modes fall in the IR. Every molecule is characterized by its specific vibrational/rotational modes so the IR absorption of molecules can be used as its fingerprint.[34] [35] With different functional group of the molecules, it show different character peaks in FTIR spectra, as shown in Figure 3-9.[36] It's easy to tell the bound ligands types on the surface of colloidal NCs. The vibrational and rotational energies of ligands change when they are bound to the surface of NCs in certain binding motif. we could also deduce the binding motif of ligands by analysising the FTIR spectra of NCs. The FTIR technic is generally applied on the study of ligands exchange process. As shown in Figure 3-10, after adding alkylthiolate on the oleate caped CdSe NCs, the treated NCs was characterized by FTIR spectra. At first, The C═O stretching peak at 1534 cm^{-1}, indicative of surface-bound oleate, vanishes, while the free oleic acid (OA) peak at 1707 cm^{-1} appears and disappears upon further purification, indicating complete ligand exchange with octanethiol. This is also inferred by following the weak stretching peak of the olefin proton (═C—H, around 3000 cm^{-1}) that is seen only for the free OA ligands and the oleate bound ligands. Similar results were observed for the entire series of R–SH ligands.[37]

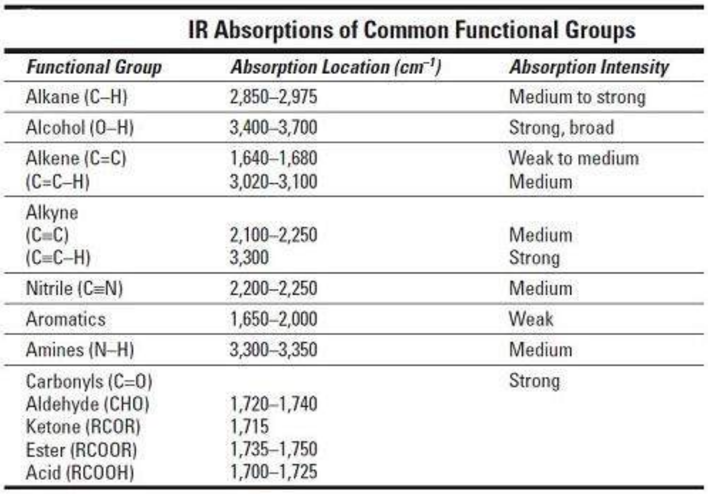

IR Absorptions of Common Functional Groups

Functional Group	Absorption Location (cm^{-1})	Absorption Intensity
Alkane (C–H)	2,850–2,975	Medium to strong
Alcohol (O–H)	3,400–3,700	Strong, broad
Alkene (C=C) (C=C–H)	1,640–1,680 3,020–3,100	Weak to medium Medium
Alkyne (C≡C) (C≡C–H)	 2,100–2,250 3,300	 Medium Strong
Nitrile (C≡N)	2,200–2,250	Medium
Aromatics	1,650–2,000	Weak
Amines (N–H)	3,300–3,350	Medium
Carbonyls (C=O) Aldehyde (CHO) Ketone (RCOR) Ester (RCOOR) Acid (RCOOH)	 1,720–1,740 1,715 1,735–1,750 1,700–1,725	Strong

Figure 3-9. The feature FTIR peaks of various function group.[36]

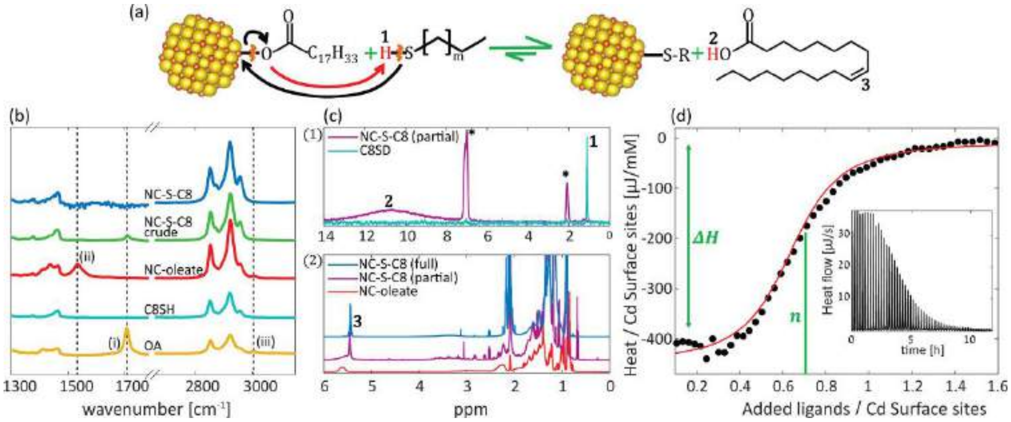

Figure 3-10. (a) Scheme of ligand exchange reaction by adding alkylthiolate on the oleate caped CdSe NCs. (b) FTIR spectra of CdSe NCs before (red), in (green) and after ligands exchange (blue). The FTIR of two free ligands (yellow and blue) was also presented. (c) 1H NMR. (d) Theoretical fitting of the ligands exchange process.[37]

Nuclear magnetic resonance spectroscopy (NMR).

As shown in Figure 3-11, the nuclei's energy levels split under strong magnetic field. The nuclei in the ground state cantransfer into excited state after absorbing corresponding energy. During the relaxation of excited nuclei transfer, the energy will be released as light and thus can be detected as specific signal of certain nuclei. The chemical environment surrounding nuclei comprise its local magnetic fields and it influences the required external magnetic field. When the density of electron cloud surrounding the nuclei is high, the required external magnetic field to excite the nuclei is also high, vice versa. The difference intensity of required external magnetic field represent the chemical environment of the nuclei (or named as chemical shift). The chemical environment give access to the details of the electronic structure of functional groups. As the chemical shift is highly characteristic and high resolution, the NMR spectroscopy is most important method to exactly character molecules in chemistry field.[38]

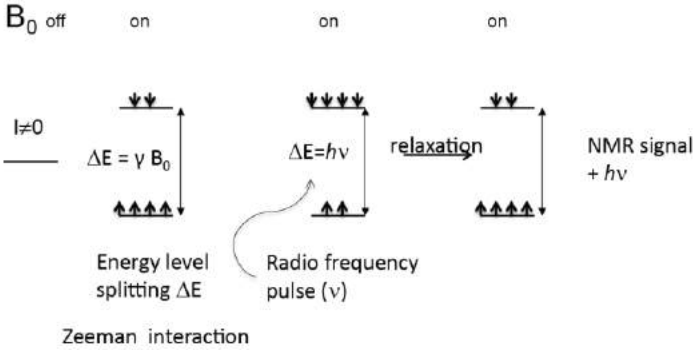

Figure 3-11. Scheme of NMR mechanism.

Solution NMR plays a key role in identifying the binding motif of ligands on the NCs' surface.[25, 39-40] Utilizing solution NMR technique, we could 1) employ non-destructive analysis for the well-dispersed NCs; 2) Distinguish free species from bound ones in the solution system; 3) estimate the amount of surface ligands present in a NCs dispersion (and, from there, the surface ligands density); 4) in-situ observation the surface change of NCs.[41] As shown in Figure 3-12, the ^{1}H NMR spectra of free oleic acid and well purified oleic acid capped CdSe NCs was presented. In both spectra, the oleic acid shows the same characteristic peaks at 5.4-5.8 ppm, belonging to the alkene protons, and the multiplets at ~0.9 ppm, belonging to methyl protons resonance. However, for the bound oleate, the peaks are broadened and show a downfield shift. The broadness indicate the restricted rotational mobility of the ligands, which usually caused by ligands aggregation (micelles) and binding with NCs. Such broadening is more pronounced for the protons which are closer to the NCs's surface (i.e. closer to the anchoring group), since their mobility is more restricted than that of protons in the alkyl chain.[41] The downfield shift is caused by the electron-draw effect of the surface metal cations which reduce the electron density of the ligands species. Quantitatively analysis of ligands could also be achieved by integrating the peaks area of ligands, after dissolving the NCs in DMSO and release the ligands in free state.[7] The result of the quantitative NMR analysis can be used to calculate the surface ligands density bound to the colloidal NCs (n.b. that to estimate the total surface area of the NCs one has to know the size, shape and concentration of the NCs in solution).

When P-based ligands (e.g. TOPO, TOP, phosphonic acid) are employed in the synthesis/passivation of colloidal NCs, ^{31}P NMR spectroscopy can be employed to probe the ligand-NC's surface interactions.[25, 39, 42] As shown in Figure 3-13a, the octyldecylphosphonic acid (ODPA) capped CdSe NCs show very broad multi peaks in ^{31}P NMR spectra. Such multiple broad 31P NMR peaks indicate that ODPA is bound to the NCs' surface via different binding motifs. To have a more clear investigation, we need release the bound ligands to its free states. Trimethylsilyl selenide (TMS-Se) was added into the CdSe-PA NCs to strip out the phosphonate molecules while maintaining its binding motif, as shown in Figure 3-13c. After reaction, the broad signal was transferred into three sharp individual peaks, which is easier to identify. The three sharp peaks were identified as single protonated phosphonate and one pair isomer of phosphonate anhydride. The result indicated that there were dehydration reaction of ODPA during the reaction.[7, 25]

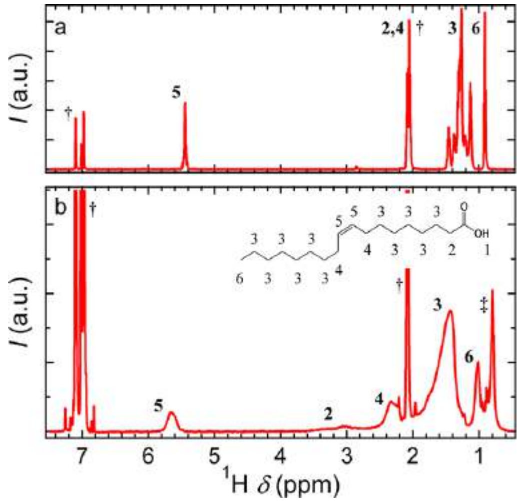

Figure 3-12. (a) 1D ^{1}H NMR spectrum of free oleic acid (OA) and (b) OA caped CdSe NCs dispersion in d_8-toluene.[41]

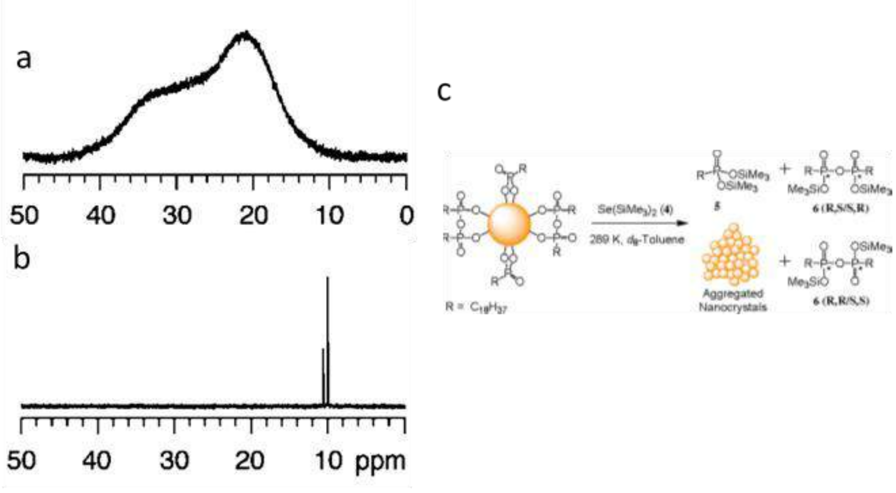

Figure 3-13. (a) 1D ^{31}P NMR spectrum of n-octadecylphosphonic acid (ODPA) caped CdSe NCs and (b) solution after reaction between CdSe NCs and TMS-Se in d_8-toluene. (c) Reaction scheme between ODPA caped NCs and TMS-Se.[39]

2D NMR: Diffusion ordered (DOSY) and Nuclear Overhauser effect (NOESY) spectroscopies. DOSY is a 2D NMR technique that measures the diffusion coefficients and 1D ^{1}H NMR at the same time. 1H-DOSY NMR can be used to obtain the hydrodynamic radius and formula weight of the given molecule.[41] Free ligands will yield a small radius and weight. Bound ligands yield diffusion coefficients ascribable to roughly the size of the NCs. It is especially powerful on determining the size and ligands binding state of II–VI and III–V nanocrystals.[43-44] As shown in Figure 3-14, the ^{1}H and ^{113}Cd DOSY spectra of $Cd(OAc)_2$ was presented.[43] The diffusion coefficients resulting from the two analyses match ($1.78x10^{-10}$ m^2 s^{-1}), indicating the consistence of the diffusion coefficient test.

^{1}H-^{1}H NOESY. NOESY signal will be generated when two proton is close enough (the distance is smallerthan 5 Å). NOESY cross peaks sign are opposite for free and bound ligands. For free ligands, the sign of NOESY cross peaks is opposite to the sign of the diagonal. For bound ligands NOESY cross peaks have the same sign with diagonal peaks, due to a long correlation time (τ_c).[41] ^{1}H-^{1}H NOESY could provide information about the ligands distribution, interaction and the bound state of ligands on surface. As shown in Figure 3-15, the alkene proton of oleylamine (OLAm) and aromatic proton of phenylacetic acid (PhAc), show same signal (red) with diagonal peaks. It indicate the OLAm and PhAc are dynamically interacting with NCs. The PhAc-OAm amide returns positive sign (blue) cross peak, similar to that of free molecules in solution and therefore is not bound.[7]

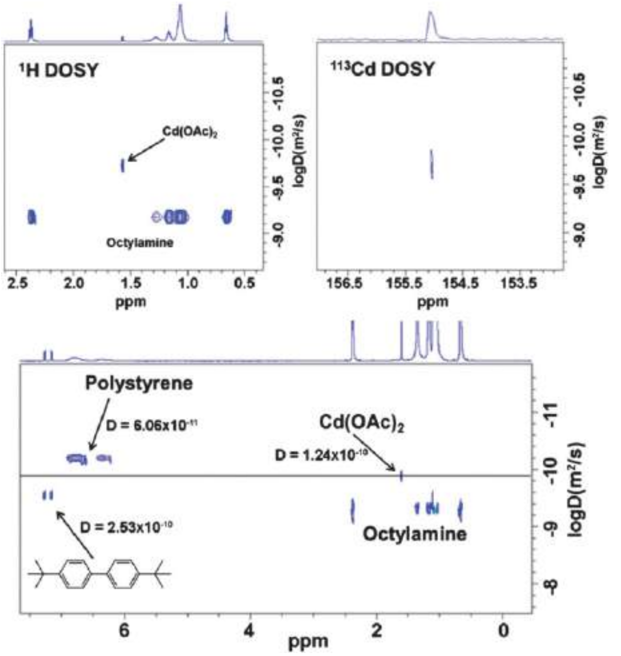

Figure 3-14. (Above) ^{1}H DOSY and ^{113}Cd DOSY of $Cd(OAc)_2*2H_2O$ dissolved in octylamine. (Below) 1H DOSY of $Cd(OAc)_2*2H_2O$ dissolved in octylamine in the presence of polystyrene (Mw = 2400) and di-tert-butylbiphenyl (Mw = 266.42) added as two inert internal references.[43]

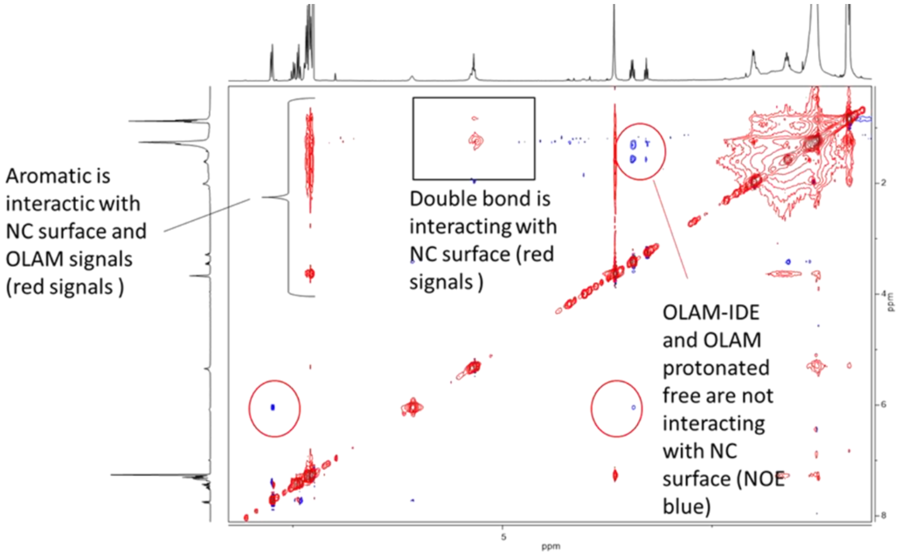

Figure 3-15. ^{1}H-^{1}H 2D NOESY spectrum in $CDCl_3$ of PhAc-OAm batch NCs and residual free PhAc-OLAm amide molecule.

Solid-state nuclear magnetic resonance (NMR) spectroscopy. While solution NMR target on the organic molecules on the surface, solid NMR reveal the information of the inorganic atom in the lattice.[45-46] The surrounding environment information (e.g. geometry, topology and structure dynamic) of the certain atom in the lattice could be provided without solubility requirement as solution NMR. Almost all important elements for metal halide materials could have effective NMR isotopes, like ^{133}Cs, ^{207}Pb, $^{35/37}$Cl, $^{79/81}$Br,

^{127}I, $^{85/87}$Rb, $^{107/109}$Ag, ^{119}Sn, $^{121/123}$Sb, ^{209}Bi, ^{55}Mn, and $^{63/65}$Cu.[46] Each element isotope has a special frequency range in NMR spectra and thus could easily avoid signal overlap with other element. For solid NMR, the different crystallinity, static and dynamic structural disorder, concomitant phases, and impurities could be clearly presented and provide extra information comparing with X-ray related technic. As shown in Figure 3-16, the surface-selective ^{133}Cs and ^{207}Pb solid-state NMR experiments suggest that the surface of the cuboidal $CsPbBr_3$ particles are terminated by a CsBr shell. ^{1}H[^{133}Cs] RESPDOR and ^{1}H[^{207}Pb] S-REDOR measurements confirm this proposition and further suggest that alkylammonium ligands substitute into Cs sites at the surface of the particles.[45]

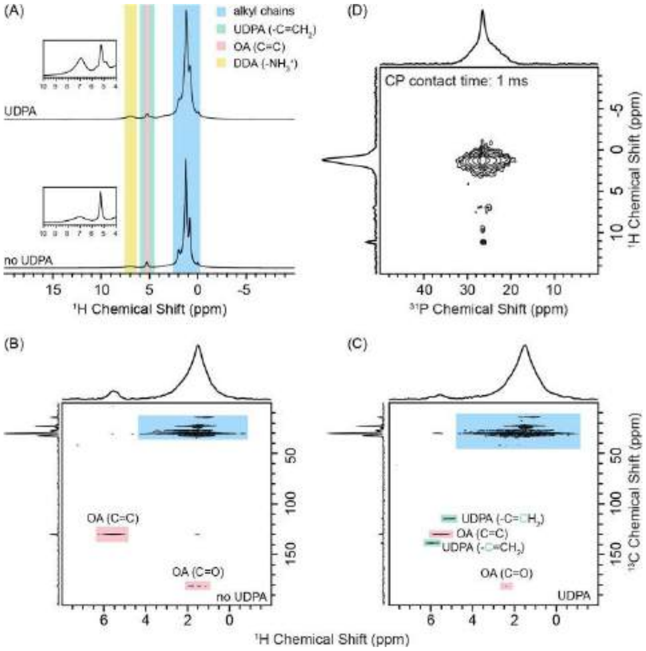

Figure 3-16. (A) MAS ^{1}H spin echo solid-state NMR spectra of CsPbBr3 QDs with and without UDPA. The insets show the diagnostic high frequency chemical shifts of the vinyl functional groups of UDPA, alkenyl protons of oleate (OA), and the ammonium group of dodecylammonium (DDA). ^{1}H detected 2D dipolar ^{1}H−^{13}C CP-HETCOR spectra of $CsPbBr_3$ QDs (B) without and (C) with UDPA. (D) 2D dipolar $^{1}H \rightarrow {}^{31}P$ CP HETCOR of $CsPbBr_3$ QDs with UDPA. The CP contact time is indicated. All spectra were obtained with a 25 kHz MAS frequency.[45]

REFERENCES:

1. De Trizio, L.; Infante, I.; Abdelhady, A. L.; Brovelli, S.; Manna, L., Guidelines for the characterization of metal halide nanocrystals. *Trends in Chemistry* **2021,** *3* (8), 631-644.
2. Hoffman, J. B.; Zaiats, G.; Wappes, I.; Kamat, P. V., CsPbBr3 Solar Cells: Controlled Film Growth through Layer-by-Layer Quantum Dot Deposition. *Chemistry of Materials* **2017,** *29* (22), 9767-9774.
3. Li, Z.-J.; Hofman, E.; Li, J.; Davis, A. H.; Tung, C.-H.; Wu, L.-Z.; Zheng, W., Photoelectrochemically Active and Environmentally Stable CsPbBr3/TiO2 Core/Shell Nanocrystals. *Advanced Functional Materials* **2018,** *28* (1), 1704288.
4. Zhang, B.; Zhu, T.; Ou, M.; Rowell, N.; Fan, H.; Han, J.; Tan, L.; Dove, M. T.; Ren, Y.; Zuo, X.; Han, S.; Zeng, J.; Yu, K., Thermally-induced reversible structural isomerization in colloidal semiconductor CdS magic-size clusters. *Nature Communications* **2018,** *9* (1), 2499.
5. Olesik, J. W., Elemental analysis using icp-oes and icp/ms. *Analytical Chemistry* **1991,** *63* (1), 12A-21A.
6. Almeida, G.; Ashton, O. J.; Goldoni, L.; Maggioni, D.; Petralanda, U.; Mishra, N.; Akkerman, Q. A.; Infante, I.; Snaith, H. J.; Manna, L., The Phosphine Oxide Route toward Lead Halide Perovskite Nanocrystals. *Journal of the American Chemical Society* **2018,** *140* (44), 14878-14886.
7. Zhang, B.; Wang, M.; Ghini, M.; Melcherts, A. E. M.; Zito, J.; Goldoni, L.; Infante, I.; Guizzardi, M.; Scotognella, F.; Kriegel, I.; De Trizio, L.; Manna, L., Colloidal Bi-Doped Cs2Ag1–xNaxInCl6 Nanocrystals: Undercoordinated Surface Cl Ions Limit their Light Emission Efficiency. *ACS Materials Letters* **2020,** *2* (11), 1442-1449.
8. Locardi, F.; Sartori, E.; Buha, J.; Zito, J.; Prato, M.; Pinchetti, V.; Zaffalon, M. L.; Ferretti, M.; Brovelli, S.; Infante, I.; De Trizio, L.; Manna, L., Emissive Bi-Doped Double Perovskite Cs2Ag1–xNaxInCl6 Nanocrystals. *ACS Energy Letters* **2019,** *4* (8), 1976-1982.
9. D'Alfonso, A. J.; Freitag, B.; Klenov, D.; Allen, L. J., Atomic-resolution chemical mapping using energy-dispersive x-ray spectroscopy. *Physical Review B* **2010,** *81* (10), 100101.
10. Shindo, D.; Oikawa, T., Energy dispersive x-ray spectroscopy. In *Analytical electron microscopy for materials science*, Springer: 2002; pp 81-102.

11. Shamsi, J.; Dang, Z.; Ijaz, P.; Abdelhady, A. L.; Bertoni, G.; Moreels, I.; Manna, L., Colloidal CsX (X = Cl, Br, I) Nanocrystals and Their Transformation to CsPbX3 Nanocrystals by Cation Exchange. *Chemistry of Materials* **2018,** *30* (1), 79-83.
12. Imran, M.; Peng, L.; Pianetti, A.; Pinchetti, V.; Ramade, J.; Zito, J.; Di Stasio, F.; Buha, J.; Toso, S.; Song, J.; Infante, I.; Bals, S.; Brovelli, S.; Manna, L., Halide Perovskite–Lead Chalcohalide Nanocrystal Heterostructures. *Journal of the American Chemical Society* **2021,** *143* (3), 1435-1446.
13. Fadley, C. S., X-ray photoelectron spectroscopy: Progress and perspectives. *Journal of Electron Spectroscopy and Related Phenomena* **2010,** *178-179*, 2-32.
14. Subila, K. B.; Kishore Kumar, G.; Shivaprasad, S. M.; George Thomas, K., Luminescence Properties of CdSe Quantum Dots: Role of Crystal Structure and Surface Composition. *The Journal of Physical Chemistry Letters* **2013,** *4* (16), 2774-2779.
15. Liu, Y.; Zai, H.; Xie, H.; Liu, B.; Wang, S.; Zhao, Y.; Niu, D.; Huang, H.; Chen, Q.; Gao, Y., Effects of CsPbBr3 nanocrystals concentration on electronic structure and surface composition of perovskite films. *Organic Electronics* **2019,** *73*, 327-331.
16. Müller, S. A.; Aebi, U.; Engel, A., What transmission electron microscopes can visualize now and in the future. *Journal of Structural Biology* **2008,** *163* (3), 235-245.
17. Barthel, J.; Thust, A., Quantification of the Information Limit of Transmission Electron Microscopes. *Physical Review Letters* **2008,** *101* (20), 200801.
18. Shamsi, J.; Dang, Z.; Bianchini, P.; Canale, C.; Di Stasio, F.; Brescia, R.; Prato, M.; Manna, L., Colloidal Synthesis of Quantum Confined Single Crystal CsPbBr3 Nanosheets with Lateral Size Control up to the Micrometer Range. *Journal of the American Chemical Society* **2016,** *138* (23), 7240-7243.
19. Zhang, D.; Yu, Y.; Bekenstein, Y.; Wong, A. B.; Alivisatos, A. P.; Yang, P., Ultrathin Colloidal Cesium Lead Halide Perovskite Nanowires. *Journal of the American Chemical Society* **2016,** *138* (40), 13155-13158.
20. Peng, L.; Dutta, A.; Xie, R.; Yang, W.; Pradhan, N., Dot–Wire–Platelet–Cube: Step Growth and Structural Transformations in CsPbBr3 Perovskite Nanocrystals. *ACS Energy Letters* **2018,** *3* (8), 2014-2020.
21. Peng, L.; Dutta, S. K.; Mondal, D.; Hudait, B.; Shyamal, S.; Xie, R.; Mahadevan, P.; Pradhan, N., Arm Growth and Facet Modulation in Perovskite Nanocrystals. *Journal of the American Chemical Society* **2019,** *141* (40), 16160-16168.
22. Bera, S.; Behera, R. K.; Pradhan, N., α-Halo Ketone for Polyhedral Perovskite Nanocrystals: Evolutions, Shape Conversions, Ligand Chemistry, and Self-Assembly. *Journal of the American Chemical Society* **2020,** *142* (49), 20865-20874.
23. Bera, S.; Shyamal, S.; Pradhan, N., Chemically Spiraling CsPbBr3 Perovskite Nanorods. *Journal of the American Chemical Society* **2021,** *143* (36), 14895-14906.
24. Dang, Z.; Manna, L.; Baranov, D., Detection of Pb2+ traces in dispersion of Cs4PbBr6 nanocrystals by in situ liquid cell transmission electron microscopy. *Nanoscale* **2021,** *13* (4), 2317-2323.
25. Zhang, B.; Goldoni, L.; Zito, J.; Dang, Z.; Almeida, G.; Zaccaria, F.; de Wit, J.; Infante, I.; De Trizio, L.; Manna, L., Alkyl Phosphonic Acids Deliver CsPbBr3 Nanocrystals with High Photoluminescence Quantum Yield and Truncated Octahedron Shape. *Chemistry of Materials* **2019,** *31* (21), 9140-9147.
26. Liu, Y.; Jing, Y.; Zhao, J.; Liu, Q.; Xia, Z., Design Optimization of Lead-Free Perovskite Cs2AgInCl6:Bi Nanocrystals with 11.4% Photoluminescence Quantum Yield. *Chemistry of Materials* **2019,** *31* (9), 3333-3339.
27. Imran, M.; Ramade, J.; Di Stasio, F.; De Franco, M.; Buha, J.; Van Aert, S.; Goldoni, L.; Lauciello, S.; Prato, M.; Infante, I.; Bals, S.; Manna, L., Alloy CsCdxPb1–xBr3 Perovskite Nanocrystals: The Role of Surface Passivation in Preserving Composition and Blue Emission. *Chemistry of Materials* **2020,** *32* (24), 10641-10652.
28. Li, F.; Liu, Y.; Wang, H.; Zhan, Q.; Liu, Q.; Xia, Z., Postsynthetic Surface Trap Removal of CsPbX3 (X = Cl, Br, or I) Quantum Dots via a ZnX2/Hexane Solution toward an Enhanced Luminescence Quantum Yield. *Chemistry of Materials* **2018,** *30* (23), 8546-8554.
29. Wang, Z.; Wen, X.-D.; Hoffmann, R.; Son, J. S.; Li, R.; Fang, C.-C.; Smilgies, D.-M.; Hyeon, T., Reconstructing a solid-solid phase transformation pathway in CdSe nanosheets with associated soft ligands. *Proceedings of the National Academy of Sciences* **2010,** *107* (40), 17119.
30. Abécassis, B.; Bouet, C.; Garnero, C.; Constantin, D.; Lequeux, N.; Ithurria, S.; Dubertret, B.; Pauw, B. R.; Pontoni, D., Real-Time in Situ Probing of High-Temperature Quantum Dots Solution Synthesis. *Nano Letters* **2015,** *15* (4), 2620-2626.
31. Li, T.; Senesi, A. J.; Lee, B., Small Angle X-ray Scattering for Nanoparticle Research. *Chemical Reviews* **2016,** *116* (18), 11128-11180.
32. Huang, H.; Feil, M. W.; Fuchs, S.; Debnath, T.; Richter, A. F.; Tong, Y.; Wu, L.; Wang, Y.; Döblinger, M.; Nickel, B., Growth of Perovskite CsPbBr3 Nanocrystals and Their Formed Superstructures Revealed by In Situ Spectroscopy. *Chemistry of Materials* **2020,** *32* (20), 8877-8884.
33. Zhang, W.-Z.; Tang, J.-C.; Wang, S.-S.; Wang, Z.-J.; Qin, W.-M.; He, J.-H., The protein complex crystallography beamline (BL19U1) at the Shanghai Synchrotron Radiation Facility. *Nuclear Science and Techniques* **2019,** *30* (11), 170.
34. Faix, O., Fourier Transform Infrared Spectroscopy. In *Methods in Lignin Chemistry*, Lin, S. Y.; Dence, C. W., Eds. Springer Berlin Heidelberg: Berlin, Heidelberg, 1992; pp 83-109.
35. Gan, Z.; Yu, Z.; Meng, M.; Xia, W.; Zhang, X., Hydration of mixed halide perovskites investigated by Fourier transform infrared spectroscopy. *APL Materials* **2019,** *7* (3), 031107.
36. Ragavendran, P.; Sophia, D.; Arul Raj, C.; Gopalakrishnan, V., Functional group analysis of various extracts of Aerva lanata (L.,) by FTIR spectrum. *Pharmacologyonline* **2011,** *1*, 358-364.
37. Elimelech, O.; Aviv, O.; Oded, M.; Banin, U., A Tale of Tails: Thermodynamics of CdSe Nanocrystal Surface Ligand Exchange. *Nano Letters* **2020,** *20* (9), 6396-6403.

38. Lambert, J. B.; Mazzola, E. P.; Ridge, C. D., *Nuclear magnetic resonance spectroscopy: an introduction to principles, applications, and experimental methods*. John Wiley & Sons: 2019.

39. Gomes, R.; Hassinen, A.; Szczygiel, A.; Zhao, Q.; Vantomme, A.; Martins, J. C.; Hens, Z., Binding of Phosphonic Acids to CdSe Quantum Dots: A Solution NMR Study. *The Journal of Physical Chemistry Letters* **2011,** *2* (3), 145-152.

40. Smock, S. R.; Williams, T. J.; Brutchey, R. L., Quantifying the Thermodynamics of Ligand Binding to CsPbBr3 Quantum Dots. *Angewandte Chemie International Edition* **2018,** *57* (36), 11711-11715.

41. Hens, Z.; Martins, J. C., A Solution NMR Toolbox for Characterizing the Surface Chemistry of Colloidal Nanocrystals. *Chemistry of Materials* **2013,** *25* (8), 1211-1221.

42. Peng, X.; Manna, L.; Yang, W.; Wickham, J.; Scher, E.; Kadavanich, A.; Alivisatos, A. P., Shape control of CdSe nanocrystals. *Nature* **2000,** *404* (6773), 59-61.

43. García-Rodríguez, R.; Liu, H., Solution structure of cadmium carboxylate and its implications for the synthesis of cadmium chalcogenide nanocrystals. *Chemical Communications* **2013,** *49* (71), 7857-7859.

44. Li, D.; Keresztes, I.; Hopson, R.; Williard, P. G., Characterization of Reactive Intermediates by Multinuclear Diffusion-Ordered NMR Spectroscopy (DOSY). *Accounts of Chemical Research* **2009,** *42* (2), 270-280.

45. Chen, Y.; Smock, S. R.; Flintgruber, A. H.; Perras, F. A.; Brutchey, R. L.; Rossini, A. J., Surface Termination of CsPbBr3 Perovskite Quantum Dots Determined by Solid-State NMR Spectroscopy. *Journal of the American Chemical Society* **2020,** *142* (13), 6117-6127.

46. Piveteau, L.; Morad, V.; Kovalenko, M. V., Solid-State NMR and NQR Spectroscopy of Lead-Halide Perovskite Materials. *Journal of the American Chemical Society* **2020,** *142* (46), 19413-19437.

Chapter 4: Surface Chemistry of Lead Halide Nanocrystals.

ABSTRACT. In this chapter, using CsPbBr3 NCs as study object, the surface chemistry of lead halide materials was investigated. The chapter was divided into three part: (1) I A synthesis method was developed to produce alkyphosphonic acid-capped CsPbBr3 NCs. Several alkyphosphonic acids were tested, namely methylphosphonic acid (MPA), hexylphosphonic acid (HPA), tetradecylphosphonic acid (TDPA), octadecylphosphonic acid (ODPA) , and the corresponding NCs were studied in order to shed light onto their ligand shell. The size of NCs was well controlled by adjusting the length of alkyl chain of ligands. Absence of ammonium halide surfactant induce some new facets and polyhedron shape of lead halide NCs. With strong binding affinity of phosphonic acid to NCs surface, the stability against dilution of CsPbBr3 NCs improved and its PLQY approach to near unity. (2)

Softer phosphonic ligands, namely oleylphsophonic acid was used to extend the low temperature window for synthesis. In lower temperature (~100 ℃), stable small sized (~5 nm) CsPbBr3 NCs was obtained. The 5 nm CsPbBr3 NCs show strong quantum confinement effect. (3) In the next part, we also used oleylphosphonic acid in its neutral state to strip the ligands of DDAB capped NCs. With 40% stripping ratio, the obtained NCs still maintain its original optical properties. It quantitatively revealed the defect-tolerance behavior of lead halide NCs.

4.1. Alkyl Phosphonic Acids Deliver CsPbBr3 Nanocrystals with High Photoluminescence Quantum Yield and Truncated Octahedron Shape.

INTRODUCTION. Lead halide perovskite (LHP) nanocrystals (NCs) have drawn intense attention due to their excellent optoelectronic properties. Such NCs have been widely applied for bio-imaging,[1] liquid crystal displays,[2] light emitting diodes (LEDs)[3-4] and solar concentrators.[5-7] The standard surfactants employed in the LHP NCs synthesis are, tipically, oleic acid and oleyamine. Standard LHP NCs show poor colloidal stability and limited photoluminescence quantum yield (PLQY),[8-11] features caused by the lability of the aforementioned ligands (oleylammonium-halide or Cs-oleate species).[11-12] Indeed, the alkylammonium (oleate) ions can easily loose (gain) a proton and thus being dissolved by the solvent. To solve this problem, other alternative ligands (including the use of stronger Lewis acids[13] and quaternary ammonium salts (DDAB)[10, 14-15]) have been tested in either post-synthesis ligand exchange procedures or directly during the synthesis of perovskite NCs.[16-17] For example, by replacing oleylamine and oleic acid with zwitterionic molecules, the resulting $CsPbX_3$ NCs exhibited a higher stability and PLQY. These features are due to the fact that zwitterionic molecules can coordinate to both surface cations and anions and they do not desorb from the NCs' surface upon protonation/deprotonation. Sulfonic acids was employed in the direct synthesis of $CsPbBr_3$. Due to its strong binding affinity with surface, the obtained NCs show high stability and can be washed multi times by polar solvents.[17]

Similar to sulfonic acids, alkyl phosphonic acids (PAs) have a strong affinity toward Pb^{2+} ions.[18] These acids have been widely employed as surfactants (as additional ligands in the synthesis or during post-synthesis treatments) for LHP NCs to improve their PLQY and stability.[13, 19-20] However, a clear understanding of the role of phosphonic acids/phosphonates on the NCs' structural and optical properties has not been achieved so far.

In this work, we employed PAs as the only ligand (see Scheme 1) for the colloidal synthesis of $CsPbBr_3$ NCs. The obtained NCs had a near unity PLQY and their PL lifetime decay was single exponential. The NMR analysis indicated that the surface of our NCs was passivated by hydrogen phosphonates and phosphonic acid anhydrides. The NCs show a truncated octahedron shape and expose (110) and (111) facets, which have never been observed before. Density functional theory (DFT) calculations indicate that the phosphonate ligands could efficiently suppress the surface trap states and equally favor the (001) and (110) facets. It well explain the high PLQY and the truncated octahedron shape.

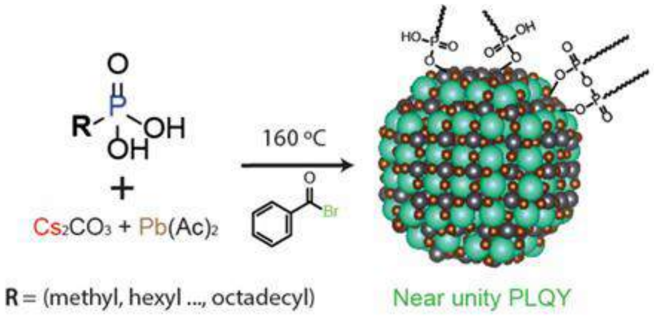

Scheme 1. Colloidal synthesis approach of $CsPbBr_3$ NCs employing only PA surfactant.

EXPERIMENTAL PART

Chemicals. Cesium carbonate (Cs_2CO_3, reagent Plus, 99%), lead acetate trihydrate ($Pb(CH_3COO)_2$-$3H_2O$, 99.99%), benzoyl bromide (C_6H_5COBr, 97%), toluene (anhydrous, 99.5%) and 1-octadecene (1-ODE, technical grade, 90%) were purchased from Sigma-Aldrich. Meth-yphosphonic acid (MPA), hexylphosphonic acid (HPA), octylphosphonic acid (OPA), tetradecylphosphonic acid (TDPA) and octyldecylphosphonic acid (ODPA) were pur-chased from PCI synthesis. All chemicals were used without further purification.

Synthesis of $CsPbBr_3$ NCs. 76 mg (0.2 mmol) of $Pb(CH_3COO)_2$-$3H_2O$, 16 mg (0.1 mmol) of Cs_2CO_3, 0.6 mmol of phosphonic acid and 10 mL of 1- ODE were mixed in a 25 mL 3-neck flask. The reac-tion mixture was degassed for 1 h at 110 °C and then the temperature was raised to 220 °C under a N_2 flux to achieve a full dissolution of the precursors. Subsequently, the precursors solution was cooled down to 105 °C and degassed at that temperature for one additional hour. 50 µL of benzoyl bromide diluted in 500 µL of degassed ODE was then injected into the mixture at 160 °C. Immediately after the injection, the reaction was quenched by immersing the flask in an ice-water bath. Ethyl acetate, at a volume ratio of 3.5:1 with crude NCs solution, was used to wash the samples. After centrifuging at 6000 rpm for 10 min, the supernatant was discarded, and the NCs were dispersed in toluene (1 ml). The NCs were washed a second time by adding 3.5 ml of ethyl ace-tate followed by centrifugation at 6000 rpm for 10 min. Eventually, the precipitated NCs were redispersed in tol-uene and kept in a N2 filled glovebox for further charac-terizations.

Optical Characterizations. The UV-Visible absorption spectra were recorded using a Varian Cary 300 UV-VIS absorption spectrophotometer. The PL spectra were measured on a Varian Cary Eclipse spectrophotometer using an excitation wavelength (λex) of 350 nm. Samples were prepared by diluting NC solutions in toluene, in quartz cuvettes with a path length of 1 cm. Photolumines-cence decays of dilute NC solutions (OD400nm = 0.15) were measured by time-correlated single-photon counting on a Edinburgh Instruments FLS920 spectrofluorometer equipped with a 405 nm laser diode (50 ps pulses) used to excite the NCs. The photoluminescence quantum yields of dilute NC solutions (OD400nm = 0.3 ± 0.1) were meas-ured using an integrating sphere, exciting the samples with a 400 nm continuous wave Laser diode and the emitted light was collected with a TM-C10083CA Hama-matsu Mini-Spectrometer.

Transmission Electron Microscopy (TEM). A JEOL JEM-1011 microscope at an accelerating voltage of 100 kV, was used to acquire bright field TEM images. The samples were prepared by dropping diluted nanocrystal solution on carbon-coated 200 mesh copper grids. High-resolution TEM (HRTEM) imaging, high-angle annular dark field (HAADF) scanning TEM (STEM) imaging, and energy-dispersive X-ray spectroscopy (EDS) analyses were carried out on a JEOL JEM-2200FS microscope equipped with a Schottky emitter working at an accelerat-ing voltage of 200 kV, a CEOS spherical aberration correc-tor for the objective lens, and a Bruker Quantax 400 sys-tem with a 60 mm^2 XFlash 5060 silicon drift detector (SDD). For HRTEM analyses, the same diluted NCs were drop-cast onto ultrathin carbon/holey carbon-coated 400 mesh copper grids. The EDS spectra were quantified us-ing the Cliff-Lorimer method for Cs Lα, Pb Lα, Br Kα, and P peaks, and the reported STEM-EDS maps were obtained by integrating the intensities over the same peaks.

Dynamic Light Scattering (DLS) Measurements. The solvodynamic diameter of the NCs was determined by Malvern Zetasizer (Nano Series, Nano ZS) instrument. For each sample, three measurements were taken with 10−20 acquisitions.

X-ray Diffraction (XRD). XRD measurements were performed on a PANalytical Empyrean X-ray diffractome-ter, with a 1.8 kW Cu Kα ceramic X-ray tube and PIXcel3D 2 ×2 area detector, operating at 45 kV and 40 mA. The samples were prepared by dropcasting onto a zero dif-fraction silicon substrate.

X-ray Photoelectron Spectroscopy (XPS). This was performed on a Kratos Axis UltraDLD spectrometer, equipped with a monochromatic Al Kα source, which was operated at 20 mA and 15 kV. Concentrated solutions of NCs were dropcast onto freshly cleaved highly oriented pyrolytic graphite substrates. Survey scans were carried out using an analysis area of 300 × 700 μm and a pass energy of 160 eV. High resolution scans were performed on the same analysis area, but with a pass energy of 10 eV. The Kratos charge neutralizer system was used on all specimens. Spectra were charge corrected to the main line of the carbon 1s spectrum (adventitious carbon) set to 284.8 eV. Spectra were analyzed using CasaXPS soft-ware (version 2.3.17).

Nuclear Magnetic Resonance (NMR). NMR spectra were acquired on a Bruker Avance III 400 MHz spec-trometer, equipped with a Broad Band Inverse probe (BBI). 31P spectra were performed at 300 K, in chloro-form-d, by using inverse gated 1H decoupled 31P NMR se-quence (Bruker library). Main acquisition parameters employed were: 64-2048 transients (depending on sam-ple concentration), 64K data points, 4 steady scans and an inter-pulses delay of 2 s, over a spectral width of 200.45 ppm, (offset at 0.00 ppm), at a fixed receiver gain (2050). NMR experiments at different temperatures (from 300 to 323 K) were performed in toluene-d8. At each desired temperature, the samples were let equili-brate inside the probe for at least 5 min before acquiring the spectra keeping the acquisition parameters fixed. All the NMR chemical shifts were referred to a TEP (triethyl phosphate) 10 mM solution in CDCl3, setting at 0.0 ppm its 31P signal.

DFT Calculations. We have carried out atomistic simulations at the density functional theory level using the PBE exchange−correlation functional[22] and a double-ζ basis set plus polarization functions[23-24] on all atoms as implemented in the CP2K 5.1. All structures have been optimized in vacuum. Scalar relativistic effects were incorporated as effective core potential functions in the basis set. Spin−orbit coupling effects were not included but their impact on the relaxed structural properties was demonstrated to be negligible for similar systems. More details on how the models were built can be found in the main text and in refs.[15, 25]

RESULTS AND DISCUSSION

Synthesis and Structural Characterization. The synthesis of PA-capped $CsPbBr_3$ NCs was carried out by modifying benzoyl halide injection method. In such method, $Pb(ac)_2$ and benzoyl halides are employed as two individual precursors to replace standard $PbBr_2$ precursors. In details, metal cation precursors (Cs_2CO_3 and $Pb(ac)_2$) were dissolved in 1-octadecene together with the desired alkyl phosphonic acid(s) at 220°C. Subsequently, the nucleation and growth of the NCs was triggered by the swift injection of benzoyl bromide at 160°C (see the Experiment Section for details). It is important to highlight that the “pre-heating step” at 220°C was necessary to obtain a complete solubilization and fully transparent metal-ligands precursors solutions. Various PAs having different alkyl chain lengths or combinations of PAs was used as desired ligands (see Table 1). If the chain length of PA is too short such as octylphsphonic acid (OPA, C8) or too long such as octadecyl phos-phonic acid (ODPA, C18), they couldn't yield colloidally stable $CsPbBr_3$ NCs (see Figure S1 of the Supporting Infor-mation (SI) and Table 1). On the other hand, by using tetradecyl phosphonic acid (TDPA, C14), or a combination of a long chain and a short chain PAs (see Table 1 and Figure 1), the colloidal stable NC dispersions were obtained. TEM revealed that the size of $CsPbBr_3$ NCs could be tuned from ~7 to ~17 nm by changing the chain length of the PAs (Figure 1 a-e) with no presence of aggregates. DLS show similar size result which indicate the NCs is well dispersed. All the NC samples had an pure orthorhombic $CsPbBr_3$ perovskite structure (ICSD: 98751) as evidenced by our XRD analysis (Figure 1f and Figure S2).

Table 1. Different PAs combination employed in the synthesis and the corresponding optical properties.

PAs Employed (ratio)	Colloidal Stability	Size (nm)	PL Peak (nm)	FWHM (meV)	PLQY (%)	τ_1 (ns)	τ_1 %
TDPA	✓	7.1±1.4	498	125	95.3	4.3	99.1
MPA-ODPA (1:3)	✓	16.7±1.6	518	83	72.4	24.4	57.1
HPA-ODPA (1:3)	✓	9.4±1.1	508	116	92.9	4.1	99.7
TDPA-ODPA (3:1)	✓	7.4±1.0	499	123	96.8	4.4	98.1
OPA	×	> 200	522	87	-	-	-
ODPA	×	8.5±1.0	511	94	-	-	-

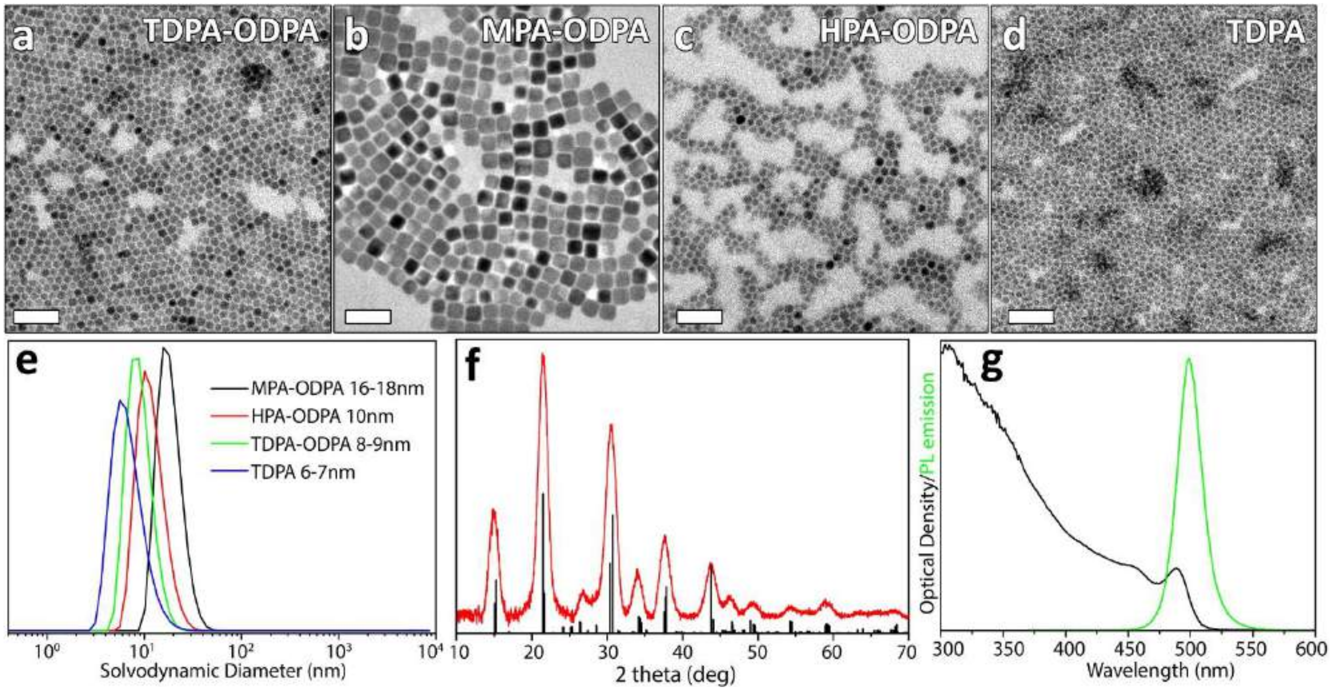

Figure 1. TEM images of $CsPbBr_3$ NCs prepared by using different combinations of PAs: (a) TDPA-ODPA (ratio 3:1), (b) MPA-ODPA (ratio 1:3), (c) HPA-ODPA (ratio 1:3) and (d) TDPA only. The scale bars are 50 nm. (e) DLS spectra of the PA capped NC show solvodynamic radius. (f) XRD pattern of NCs and orthorhombic CsPbBr3 bulk, (g) optical absorbance and PL emission of a TDPA-ODPA capped NCs.

The TEM images showed that PA capped NCs had an uncommon truncated octahedron shape (Figure 1 and 2), which has never been previously observed in "traditional" colloidal synthesis methods (i.e. ligand assisted reprecipitation and hot-injection routes).[3, 8-10, 13, 16, 20, 26-27] In some region of TEM image, the hexagonal self-assembly patterns of NCs was formed (Figure 1a, d and Figure S4). To further investigate NCs' morphology and faceting, the high-resolution (HR) TEM analysis was employed. The picked NCs has a size of 10 nm (Figure 1c), whereas smaller NCs degraded quickly under the electron beam (Figure S5). Figure 2a-c reports representative HRTEM images of NCs with [110], [111], and [001] zone axes, respectively. The corresponding atomic models are shown in Figure 2d-f. In addition to the three equivalent (010), (100) and (001) facets, the NCs also exposed several new types of facets for lead halide NCs, namely (110) and (111) ones (Figure 2g-i and Figure S6). As mentioned earlier, the faceting of our NC samples is different from that of NCs synthesized by conventional routes, which are known to be enclosed by the equivalent (100), (010) and (001) facets of the cubic phase (ICSD: 98751).[28] We ascribe this unusual faceting to PAs' passivating and the absence of oleylammonium halide surfactant in the NCs surface, as discussed in the DFT section below.

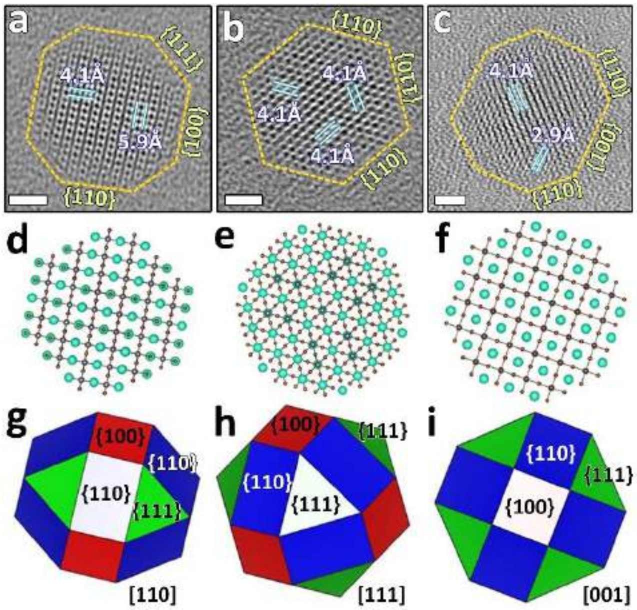

Figure 2. HRTEM images of $CsPbBr_3$ NCs oriented in different zone axes: (a) [110], (b) [111], (c) [001]. The corresponding atomic models (d-f) built by VESTA[29] (containing Cs (cyan) and Pb (grey) and Br (brown) atoms) and (g-i) polyhedron models with exposed facets. The scale bars are 2 nm.

Surface characterization. To investigate the surface of our NCs, we picked up the TDPA-capped $CsPbBr_3$ NCs as study case. We initially performed XPS, FTIR and STEM-EDS analyses as composition anaslysis. According to STEM-EDS elemental maps, phosphorous was distributed the surface of NCs (Figure S7); FTIR spectra the presence of bound alkylphosponic acids (Figure S8);[30-31] the XPS analysis revealed a Cs/Pb/Br/P molar ratio of 1/1.06/2.19/0.77, which suggested, following the requirements of charge balance, that alkylphosphonates replaced most of Br^- anions one by one on the surface of the NCs.

To better elucidate the binding motifs of PAs, we also performed an in depth ^{31}P NMR analysis.[32-33] The NMR spectrum of TDPA-capped $CsPbBr_3$ NCs evidenced multiple broad ^{31}P peaks in the range of 15-30 ppm (Figure 3a). If compared to the sharp ^{31}P singlet of the "free" TDPA (**1**) NMR spectrum (Figure 3b), the broad peaks characterizing PA capped LHP NCs indicated that TDPA species were bound to the surface of the NCs. Moreover, the presence of multiple signals suggested multiple binding motifs of TDPA to the surface.

To better elucidate the exact binding way of TDPA molecules cholortrimethylsilane (TMS-Cl) was reacted with TDPA molecules (Figure 3c) and with the NCs themselves (Figure 3d). Such method has been previously employed to reveal the binding motifs of aklylphosphonate species on the surface of CdSe and PbSe quantum dots.[18, 32-33] That is because TMS -halides and -chalcogenides (*i.e.* TMS-Se or –S) are able to react with alkylphosphonate species bound to thesurface of NCs, forming the corresponding TMS-substituted counterparts (see Figure 3d and Scheme 2) and precipitating the NCs. The free TMS-PA specices formed upon this reaction can be readily detected by ^{31}P NMR analysis. Upon reaction of TDPA with TMS-Cl we observed two individual ^{31}P NMR peaks which could be assigned to (**2**) mono- and (**3**) di- TMS substituted TDPA species (see Figure 3c). Namely, these are TMS hydrogen tetradecylphosphonic acid (**2**) and O, O′-bis(TMS)tetradecylphosphonic acid (**3**), which are the only expected products of this reaction, as also pointed out by Owen *et al*.[32] On the other hand, after the reaction of TMS-Cl with our perovskite NCs, we observed the formation of three ^{31}P NMR sharp peaks (Figure 3d). In analogy to what reported by Owen *et al.*, one pair of sharp peaks (13.83 and 14.43 ppm) with similar intensities could be assigned to one pair of isomers of *O,O'*-bis(trimethylsilyl)tetradecylphosphonic acid anhydride (**4**, **5**, see Scheme 2 and Figure 3d).[32] The third peak, at 33.10 ppm, was assigned to (**2**) corresponding to the ^{31}P NMR peak when reacting TMS-Cl with TDPA only. The broad shoulder signal around 15 ppm (Figure 3d) might belong to polyphosphonic anhydrides which was formed by condensation of phosphonic acids during the synthesis.

Overall, the ^{31}P NMR experiments indicated that TDPA-capped $CsPbB_3$ NCs were passivated mainly by phosphonic acid anhydride and hydrogen phosphonate.

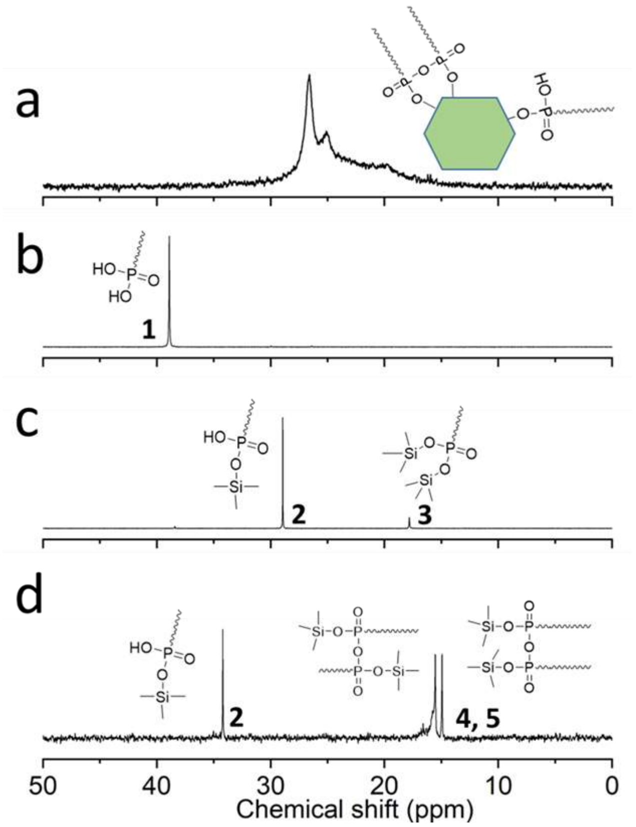

Figure 3. ^{31}P NMR spectra of (a) TDPA capped CsPbBr$_3$ NCs, (b) free TDPA ligand, (c) TDPA ligands after reacting with chlorotrimethylsilane (TMS-Cl), (d) TDPA capped CsPbBr$_3$ NCs after the reacting with TMS-Cl. All test was in CDCl$_3$.

Scheme 2. Stripping effect of TMS-Cl on the alkylphosphonate ligands bound to the surface of CsPbBr$_3$ NCs.

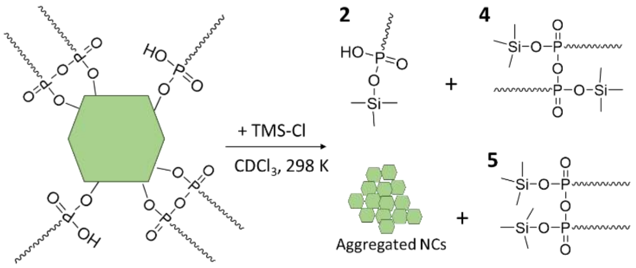

DFT calculations. To reveal how the PA ligands are able to provide an efficient passivation of CsPbBr$_3$ NCs and, at the same time, to induce a truncated octahedron shape, we performed DFT calculations. The CsPbBr$_3$ NCs were modelled as having a 2.5 nm-sided cubic shape presenting two equivalent (001) and four equivalent (110) facets in the cubic representation (Figure S9). This model is slightly different from the observed truncated octahedron shape, but it is computationally more affordable and includes the same facets relevant for our analysis. The (110) facet is terminated by both Cs and Pb ions lying on the same plane, while the (001) type can be either Cs- or Pb- rich terminated. In our calculations we employed a simplified version of the PA ligands by replacing TDPA with a shorter alkyl chain ligand, namely butyl phosphonate. In these simulations we considered the presence of both hydrogen phosphonate (HPA)$^-$, phosphonic acid anhydride (anhy)$^{2-}$, which carries two anchoring groups, and, although not experimentally detected, also phosphonate (PA)$^{2-}$ ligands. The binding affinity (BDE) of the ligands to the NC surface was computed as:

$$\mathrm{BDE} = E[\mathrm{NC}] - (E[\mathrm{NC(o)}] + E[\mathrm{BX}_n]) \qquad (1)$$

where NC is the core with one facet capped with ligands, NC(o) is the NC with a BX$_n$ vacancy, and BX$_n$ is the dissociated ligand. Here B can be either Cs$^+$ or Pb^{2+}, and X is the alkylphosphonate counterion. The calculated values of BDE per ligand are reported in Table 2, while the corresponding binding sites are depicted in Figure S10.

What emerged from our calculations is that the passivation of a Pb-rich (001) surface with either Pb(HPA)$_2$ or Pb(anhy) moieties is energetically more favorable than passivating a Cs-rich (110) surface with Cs(HPA). This indicates that Pb-rich surfaces are more likely to be stabilized. In addition, both $Pb(HPA)_2$ and Pb(anhy) have similar binding affinities for the (001) and (110) facets, suggesting that the grow rate along these two axes should be equal, and explaining the experimental observation of the formation of truncated octahedra. It is interesting to note that the two phosphonate anchoring groups of a single anhydride molecule are expected to occupy two adjacent anion sites at the NC surface. It is apparent from our calculations that this configuration is allowed on both Pb-terminated (001) facets and (110) facets, but less on the Cs-terminated (001) facets, since on the latter facets the anion sites are too far apart. The formation of truncated octahedra NCs could then be explained by considering the presence of Pb(anhy) species which form during the preparation of the precursors, and before the hot-injection.

The binding of the $Pb(HPA)_2$ on both (001) and (110) facets should be further stabilized by the presence of hydrogen bonds between the phosphonate units (see Table 2, first two rows, and Figure S11). The presence of a network of hydrogen bonds, which does not form at the high temperatures used during the synthesis, but most likely after the growth of the NCs, may increase the ligands binding affinity and can explain the evidence (see below and also Table 2) that the ligands do not detach from the NCs' surface at high dilutions.

To demonstrate the tolerance of our NCs to the formation of defect states, we have computed the electronic structure of a fully passivated NC with a truncated octahedron shape, exposing all facets as in the experiments (Figure 4a). To simplify the model, we have employed only hydrogen phosphonates (*i.e.* HPA species). The Cs/Pb/Br/P atomic ratio employed in the model was 1/1.12/2.14/1.09, as close as possible to that experimentally measured by XPS (that is 1/1.06/2.19/0.77). In Figure 4a we show the NC core after relaxing the full structure, whereas in Figure 4b we present the full structure including the phosphonate ligands. In this case, for computational efficiency, we use methylphosphonates (MPA) ligands. What we can observe is that the electronic structure and the geometry of the NC remains substantially intact, even after reconstructing the surface. In Figure 4c we show the electronic structure of this system. Here the VB edge, which is more sensitive to the formation of localized trap states, is fully delocalized (see also Figure S12). Unlike the Cs-oleate case,[20] we observed that an excess of phosphonate ligands introduced sub-valence, and thus shallow, localized states, which do not affect the emission efficiency of these NCs.

Table 2: Computed BDE value between different metal (Pb or Cs) phosphonate groups and the NC surface, in kcal/mol.

	Pb-rich(001)	**Cs-rich(001)**	**(110)**
$Pb(HPA)_2$ (no H-bonded)	52.2	//	44.4
$Pb(HPA)_2$ (H-bonded)	53.2	//	55.1
Cs(HPA)	//	48.5	54.4
Pb(PA)	47.9	//	47.5
Pb(anhy)	68.5	//	65.4

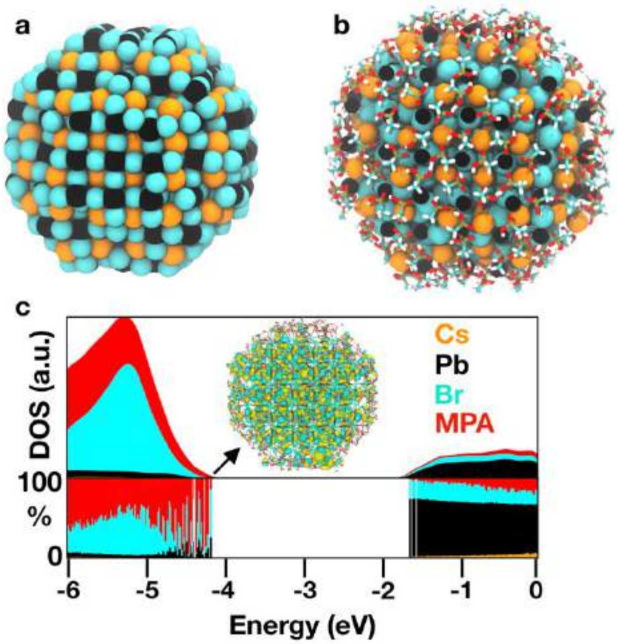

Figure 4. (a) Relaxed $CsPbBr_3$ NC model of 3.0 nm diameter computed at the DFT/PBE level of theory. The ligands shell was not shown only for pictorial reason. (b) Same NC model as (a) where the MPA ligands have been visually included. (c) (top) Projected density of states (PDOS) on each atom and ligand type of the NC model: Cs, orange; Pb, black; Br, turquoise; methylphosphonate, red. Electronic structure of MPA capped NCs is shown (bottom).

Stability test. In order to assess the colloidal stability of our NC systems, the PL emission of both “standard” oleylammonium-Br passivated NCs[8] and TDPA-ODPA capped $CsPbBr_3$ NCs was recorded as a function of their concentration in toluene (Figure 5a-b). This testcan be used to assess the dynamic binding of ligands on the surface $CsPbBr_3$ NCs.[13] Weakly bound ligands, such as oleylammonium-halide ligand pairs, desorb from the surface of the NCs upon dilution, leaving behind halide vacancies, and thus lowering the PLQY.[13] Our result indicated that: i) at high NC concentrations (100-10 nM), the relative PL intensity of both samples increased by dilution. The dilution in this range reduce the self-absorption effect; ii) at low NC concentrations (10-1 nM), the PL intensity of standard NCs was observed to decrease by dilution, while that of TDPA-ODPA capped $CsPbBr_3$ NCs remained almost constant, as shown in Figure 5a-b. These results confirmedthat alkyl phosphonates ligands were strongly bound to the surface of $CsPbBr_3$ NCs.[33-34]

Thermal stability of our PA capped NCs was also assessed. The TDPA capped $CsPbBr_3$ NCs, dispersed in toluene-d_8, were heated up to 323K, and then cooled down to 300K (room temperature) while recording its ^{31}P NMR spectrum.[14] Upon heating, the broad ^{31}P signals (Figure 3a) evolved into a single sharper peak at about 26 ppm (Figure 5c), which could be assigned to free metal-TDPA species. Furthermore, when cooling the solution back to 300 K the peak at 26 ppm became sharper and a second sharp peak appeared at 37 ppm, which could be assigned to free TDPA (Figure 5d). These results suggested that the heating step led to the irreversible detachment of metal phosphonate ligands (Z-type) from the surface of NCs. Part of the NCs precipitated at the bottom of the NMR tube after thermal stability test. Overall our stability tests evidenced that alkylphosphonates are strongly bound to the surface of $CsPbBr_3$ NCs providing a high colloidal stability, but at the same time they have a low thermal stability. Such a low thermal stability is most likely a consequence of the marked ionic character of the NCs: ligands that are strongly bound to the surface of these ionic NCs (as in the present case) can effectively detach surface atoms upon heating as Z-type ligands.

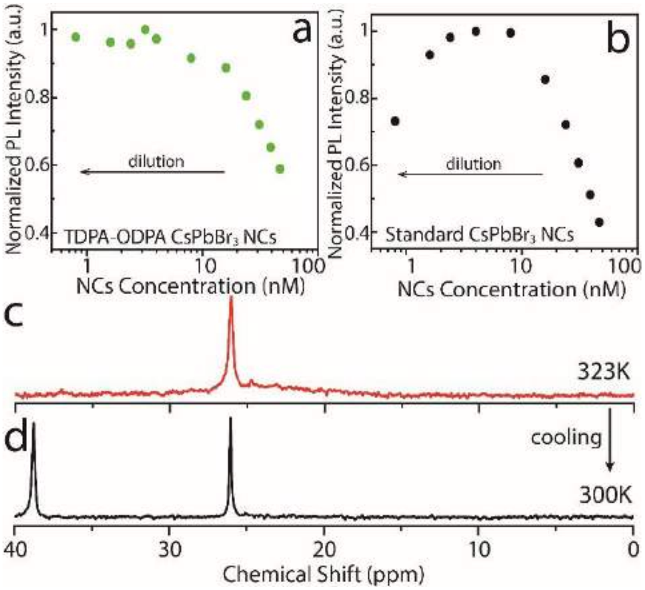

Figure 5. Normalized relative PL intensity as a function of the NCs concentration in toluene for (a) PA NCs and (b) “standard” NC samples. ^{31}P NMR spectra in toluene-d$_8$ of PA capped CsPbBr$_3$ NCs (c) heated up to 323 K, and (d) subsequently cooled to room temperature.

Conclusions. We have developed a colloidal route to produce CsPbBr$_3$ NCs by employing alkyl phosphonic acids as the only surfactants. The resulting NCs exhibited an uncommon truncated octahedron shape with new facets exposed. These NCs were characterized by near unity PLQY. Our NMR analysis revealed the presence of both phosphonic acid anhydride and hydrogen phosphonate species passivating the NCs surface. These ligands were found to provide a high colloidal stability, but a low thermal stability (with metal phosphonate species leaving the NCs surface upon heating). DFT calculations corroborated the experimental data by demonstrating the high affinity of phosphonate ligands to the NC surface and by showing a similar stabilization energy of the (001) and (110) facets, explaining the formation of a truncated octahedron shape.

Our results, thus, further enrich the knowledge on this class of materials offering a new tool to tune both the morphology and the surface chemistry of LHP NCs.

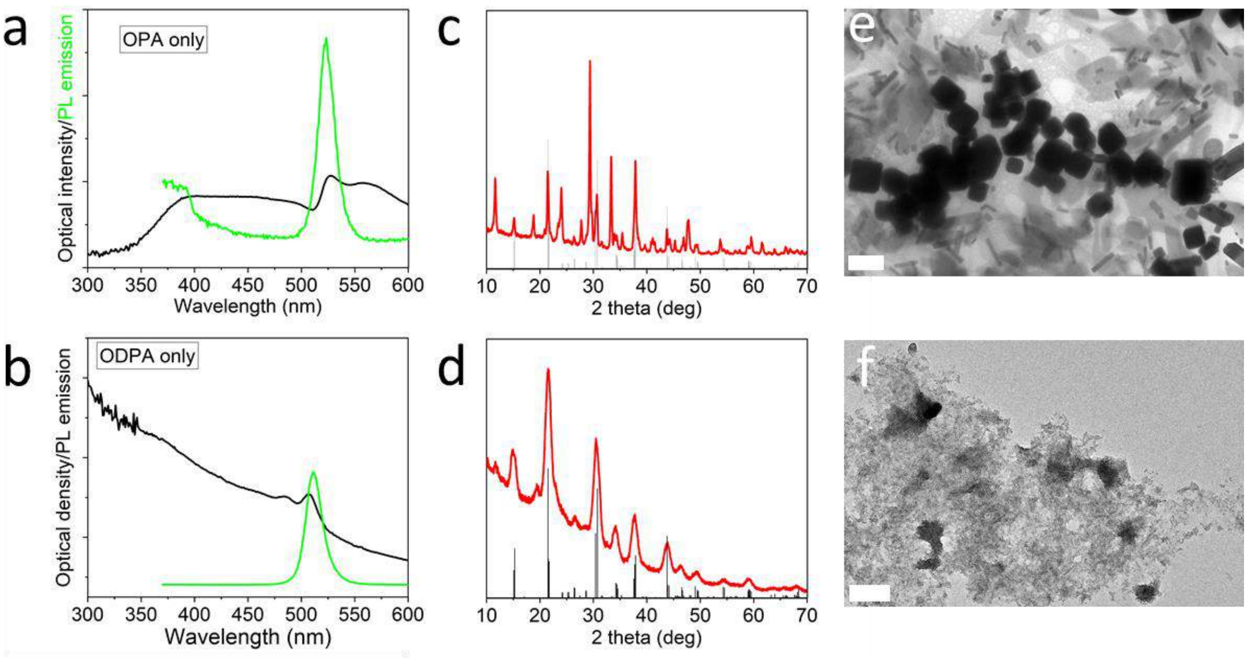

Figure S1. (a-b) Optical absorbance and PL emission of the samples synthesized using either (a) OPA or (b) ODPA as the only surfactant. XRD patterns of the samples prepared using either (c) OPA or (d) ODPA, together with the bulk reflections of CsPbBr$_3$ (ICSD number 98751), which are represented by means of gray bars. TEM images of the samples made using (e) OPA or (f) ODPA. The scale bars are 200 nm.

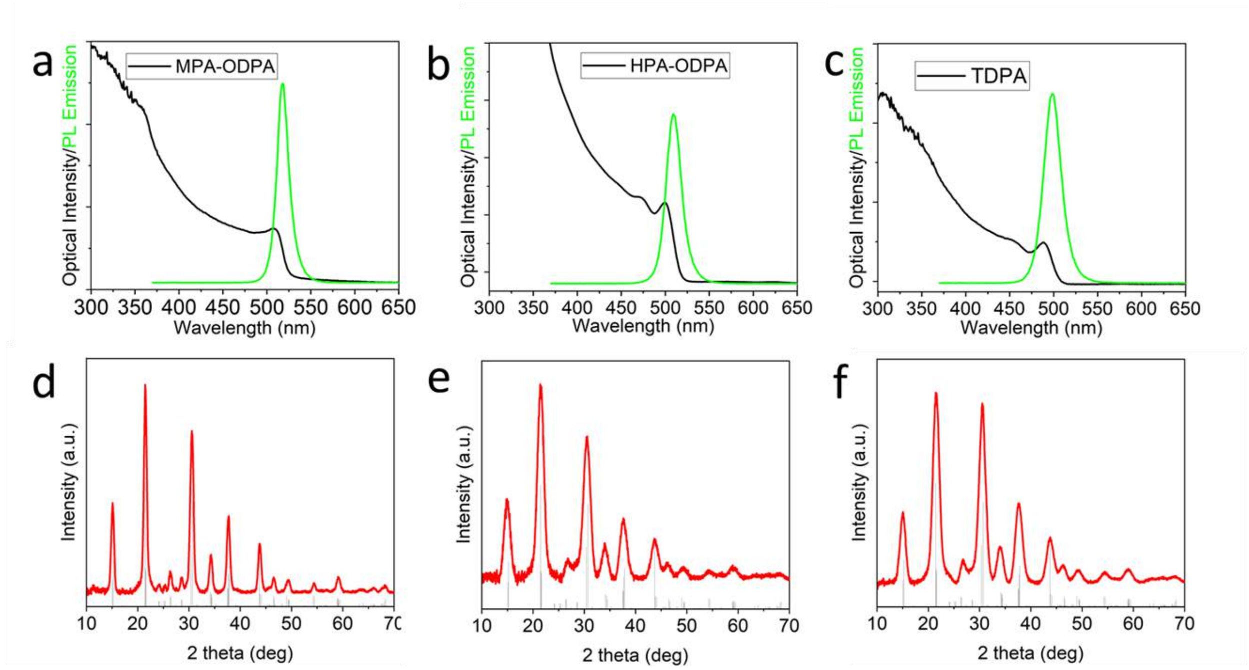

Figure S2. Optical absorbance and PL emission of samples synthesized using (a) MPA-ODPA (ratio 1:3), (b) HPA-ODPA (ratio 1:3) and (c) TDPA only. Corresponding XRD patterns of (d) MPA-ODPA (ratio 1:3), (e) HPA-ODPA (ratio 1:3) and (f) TDPA only. The bulk reflections of CsPbBr3 (ICSD number 98751) are represented by means of gray bars.

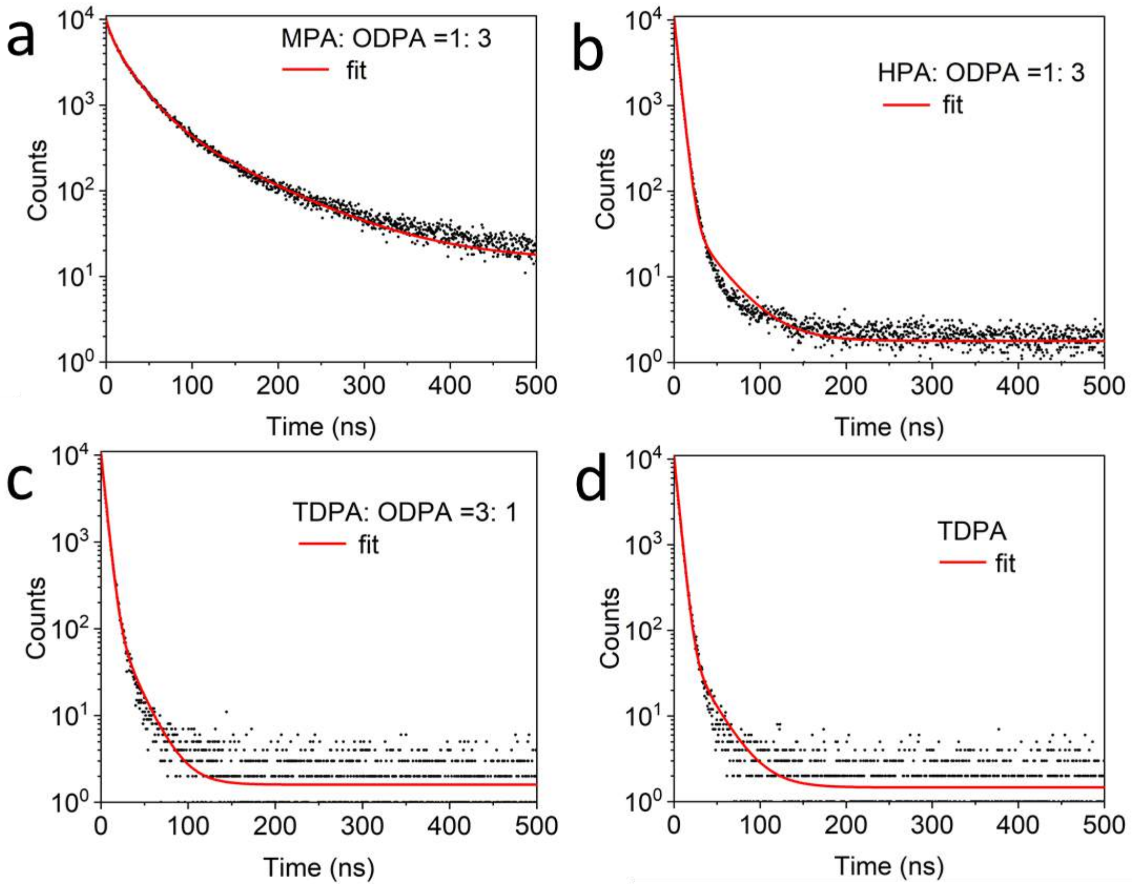

Figure S3. Time-resolved PL decay traces measured for the samples synthesized using (a) MPA-ODPA (ratio 1:3), (b) HPA-ODPA (ratio 1:3) and (c) TDPA only.

Table S1. Fitting result of PL lifetime decay. Tri-exponential decay functions were used to fit decay curve of MPA: ODPA = 1: 3 batch; Bi-exponential decay function were used to fit decay curve of TDPA and TDPA: ODPA = 3: 1 batch.

	MPA: ODPA =1: 3	HPA: ODPA =1: 3	TDPA: ODPA =3: 1	TDPA only
τ_1 (ns)	24.4	4.1	4.4	4.3
τ_1%	57.1%	99.7%	98.1%	99.1%
τ_2 (ns)	6.15	31.6	19.3	23.8
τ_2%	31.9%	0.3%	1.9%	0.9%
τ_3 (ns)	83.3			
τ_3%	11.0%			

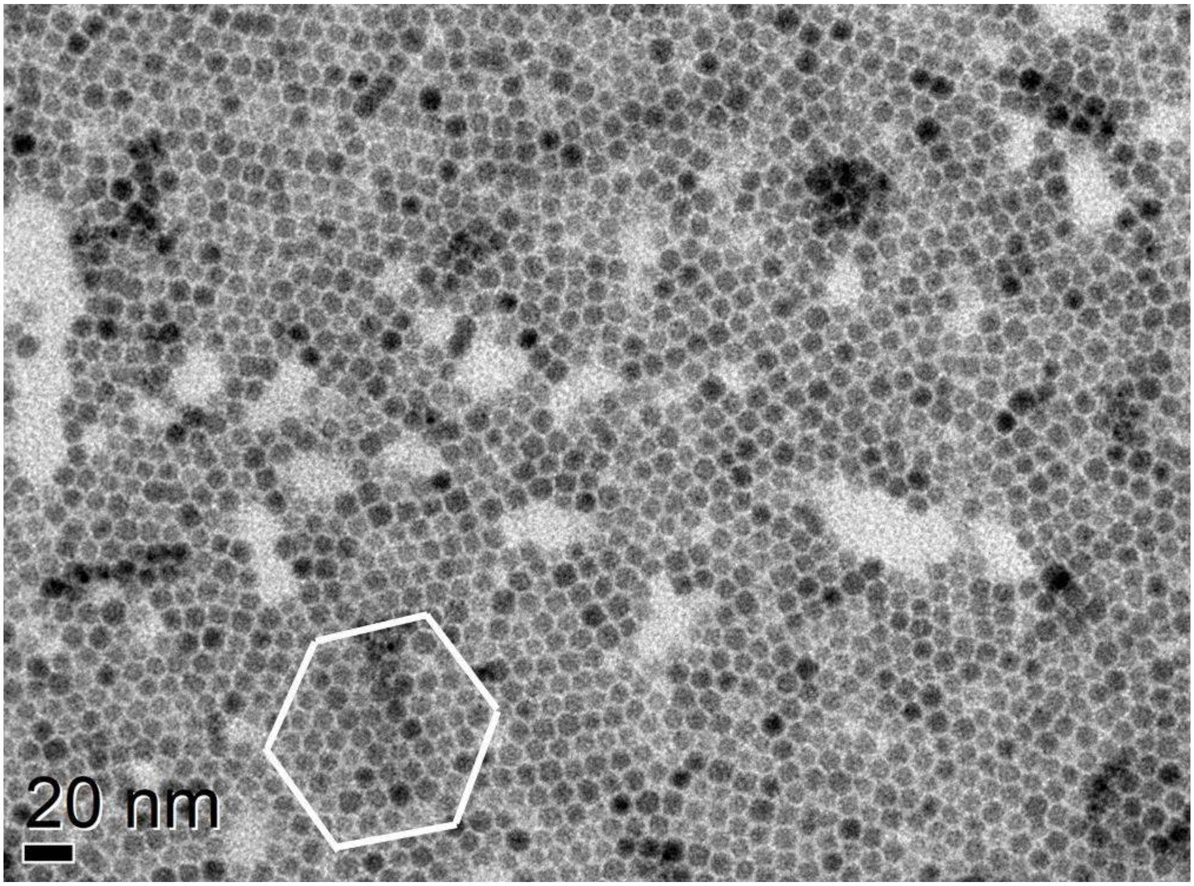

Figure S4. Region (circled by white lines) following Hexagonal self-assembly patterns of Figure 1a.

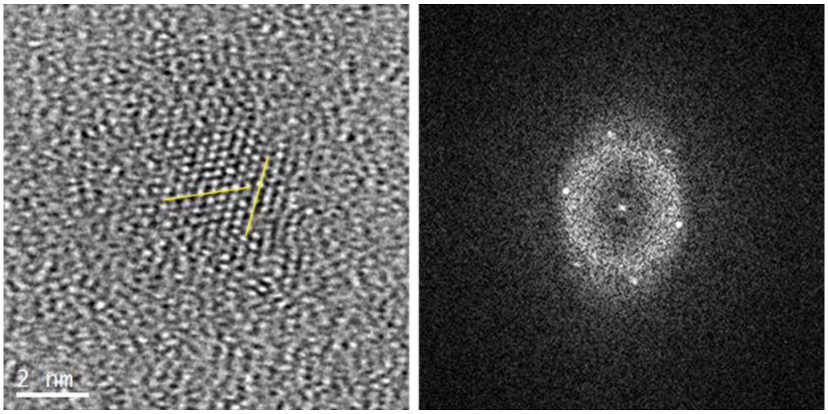

Figure S5. Small $CsPbBr_3$ NCs (prepared employing a TDPA: ODPA ratio of 1: 3) degraded into 3 nm NCs as soon as exposed to the electron beam in HRTEM mode.

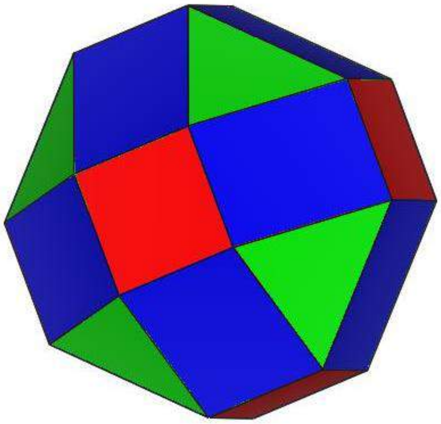

Figure S6. Polyhedron model of a truncated octhaedron $CsPbBr_3$ NC.

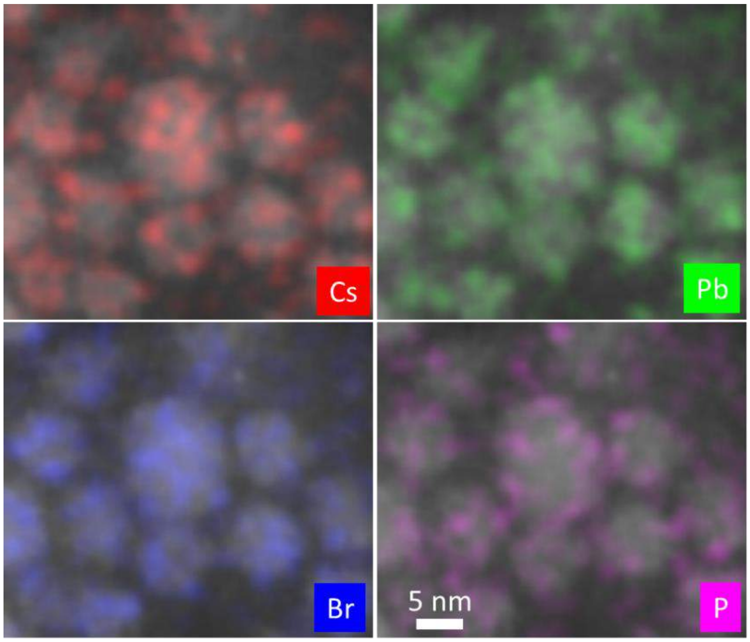

Figure S7. HAADF-STEM-EDS elemental maps of the $CsPbBr_3$ NCs revealing the presence of phosphorus on the NCs.

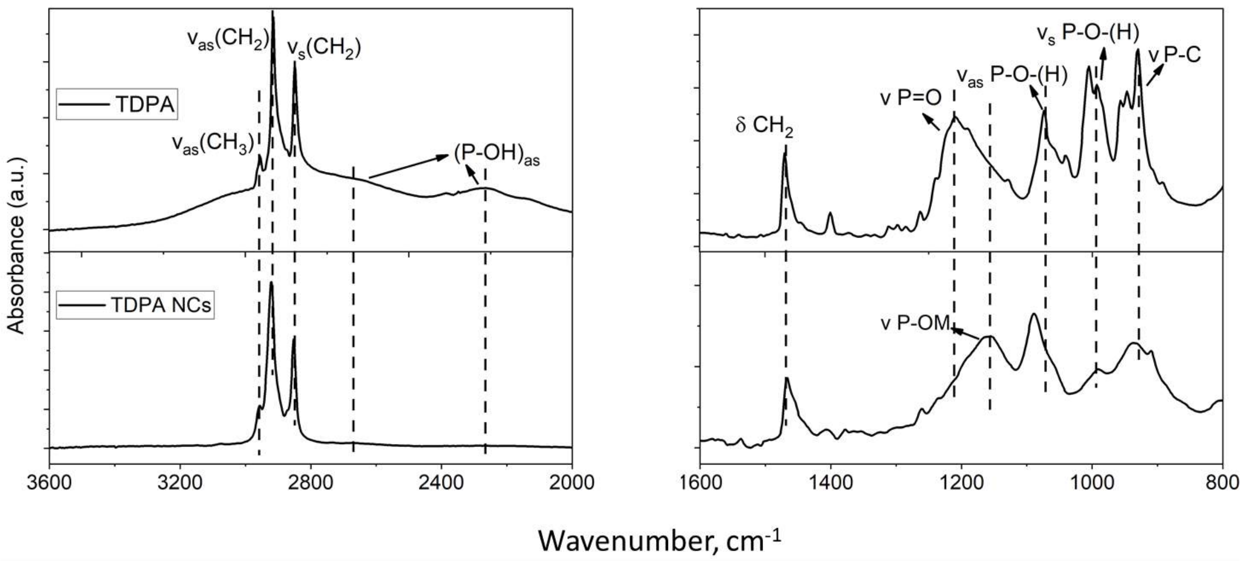

Figure S8. FT-IR spectra obtained from (upper panels) free TDPA ligands and (lower panels) CsPbBr$_3$ NCs synthesized using TDPA only. TDPA is characterized by a series of characteristic peaks which can be assigned the stretching modes of: P-OH ((P-OH)$_{as}$) from 2669 cm^{-1} to 2264 cm^{-1}; P=O (*v* P=O) at 1209 cm^{-1}; asymmetric and symmetric P-O-(H) (v_{as} P-O-(H) and v_s P-O-(H), respectively) at 1074 cm^{-1} 993 cm^{-1}, respectively.[1] In TDPA capped NCs the (P-OH)$_{as}$, v_{as} P-O-(H) and v_s P-O-(H) peaks became very weak, the *v* P=O signal totally disappeared. On the other hand a new peak at 1157 cm-^{1} appeared, which was ascribed with the P-OM stretching mode (*v* P-OM).[2]

These results indicate that no free TDPA molecules are present in the NC sample. Also, CsPbBr$_3$ NCs are covered by bound TDPA molecules which form P-OM bonds. The disappearance of the P=O stretching mode suggest that TDPA molecules are chelating the surface of the NCs.[2]

[1] Luschtinetz, R. , Seifert, G. , Jaehne, E. and Adler, H. P. *Macromol. Symp*. 2007, **254,** 248–253;

[2] Son J.G., Choi E., Piao Y., Han S.W. and Lee T.G. *Nanoscale*, 2016, **8,** 4573-4578.

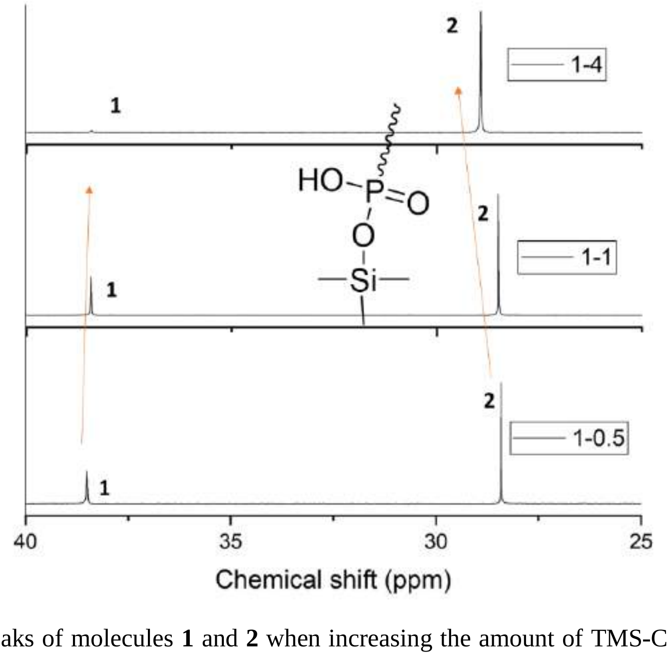

Figure S9. Shift of the NMR peaks of molecules **1** and **2** when increasing the amount of TMS-Cl that is employed in the reaction with TDPA molecules. The TDPA:TMS-Cl ratios employed in the experiments are 1:4 (top panel), 1:1 (middle panel) and 1:05 (bottom panel).

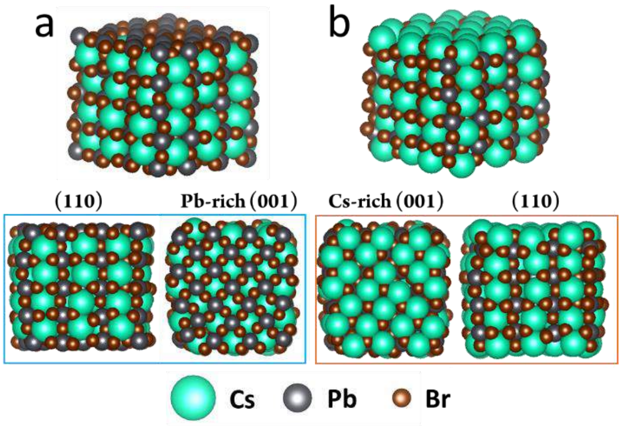

Figure S10. Cubic $CsPbBr_3$ NC model of 2.5 nm in diameter that present two equivalent (001) and four equivalent (110) facets (in the cubic representation). The (001) type can be terminated either by (a) Pb and Br or (b) Cs and Br ions, while the (110) facet is the same in both NCs. At the bottom, we show the projections of both types of NCs along the [001] and [110] directions.

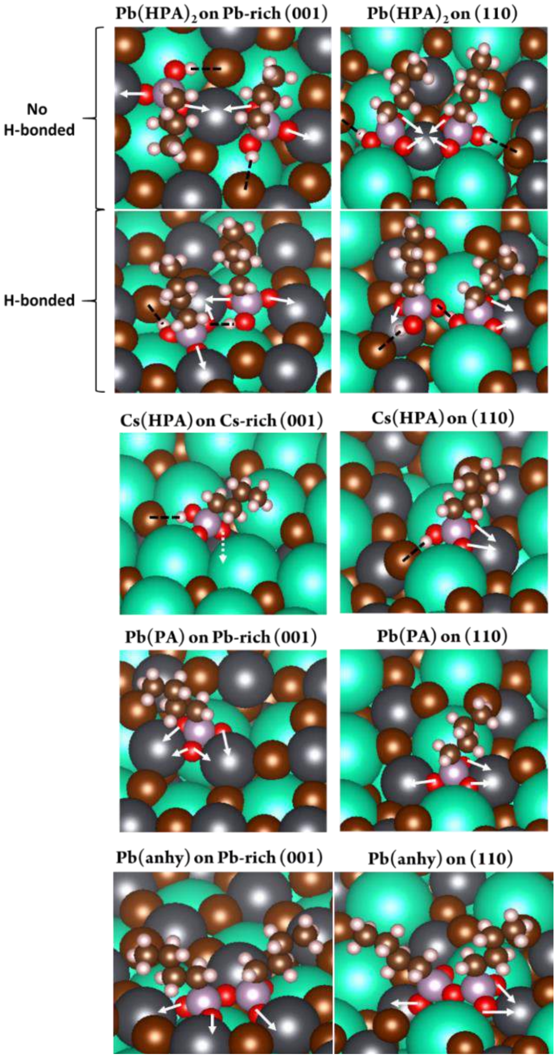

Figure S11. Detailed view of the binding sites for the different butylphosphonate groups presented in Table 2 of the main text. The black dashed lines represent the hydrogen bonds and the white arrows indicate the coordination of oxygen atoms of the ligand with the Pb ions. For Pb-rich (001) facets, two oxygen atoms are bridging two adjacent Pb ions, while on the (110) two oxygen atoms are chelating the same Pb ion. On Cs-rich (001) planes, one oxygen atom coordinates the underlying Pb in a monodentate way.

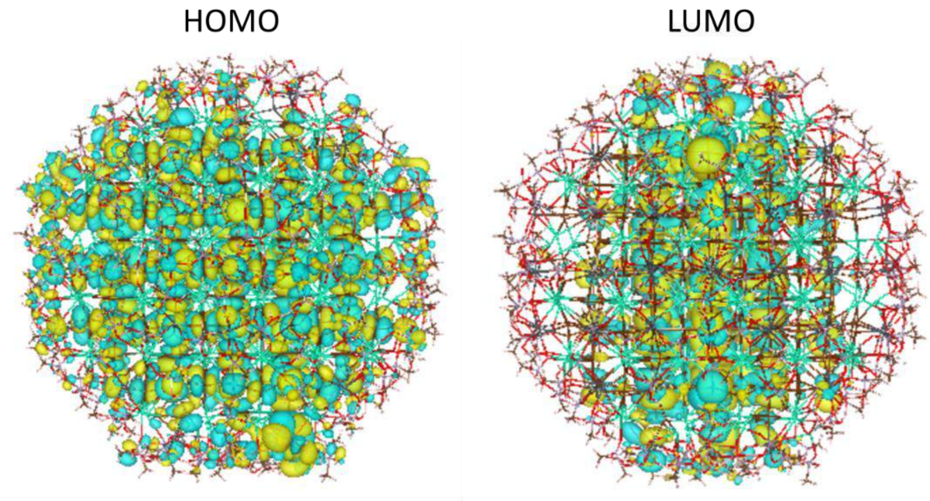

Figure S12. Molecular orbital plots of the HOMO and LUMO states for the truncated octahedron model of $CsPbBr_3$ NC fully capped with the metylphosphonates. Both are delocalized inside the NC core and free of traps.

REFERENCES:

(1) Zhang, H.; Wang, X.; Liao, Q.; Xu, Z.; Li, H.; Zheng, L.; Fu, H., Embedding Perovskite Nanocrystals into a Polymer Matrix for Tunable Luminescence Probes in Cell Imaging. *Adv. Funct. Mater.* **2017,** *27*, 1604382.

(2) Chen, X.; Zhang, F.; Ge, Y.; Shi, L.; Huang, S.; Tang, J.; Lv, Z.; Zhang, L.; Zou, B.; Zhong, H., Centimeter-Sized Cs_4PbBr_6 Crystals with Embedded $CsPbBr_3$ Nanocrystals Showing Superior Photoluminescence: Nonstoichiometry Induced Transformation and Light-Emitting Applications. *Adv. Funct. Mater.* **2018,** *28*, 1706567.

(3) D'Innocenzo, V.; Srimath Kandada, A. R.; De Bastiani, M.; Gandini, M.; Petrozza, A., Tuning the Light Emission Properties by Band Gap Engineering in Hybrid Lead Halide Perovskite. *J. Am. Chem. Soc.* **2014,** *136*, 17730-17733.

(4) Stranks, S. D.; Snaith, H. J., Metal-halide perovskites for photovoltaic and light-emitting devices. *Nat. Nanotechnol.* **2015,** *10*, 391.

(5) Luo, X.; Ding, T.; Liu, X.; Liu, Y.; Wu, K., Quantum-Cutting Luminescent Solar Concentrators Using Ytterbium-Doped Perovskite Nanocrystals. *Nano Lett.* **2019,** *19*, 338-341.

(6) Akkerman, Q. A.; Rainò, G.; Kovalenko, M. V.; Manna, L., Genesis, challenges and opportunities for colloidal lead halide perovskite nanocrystals. *Nat. Mater.* **2018,** *17*, 394-405.

(7) Meinardi, F.; Akkerman, Q. A.; Bruni, F.; Park, S.; Mauri, M.; Dang, Z.; Manna, L.; Brovelli, S., Doped Halide Perovskite Nanocrystals for Reabsorption-Free Luminescent Solar Concentrators. *ACS Energy Lett.* **2017,** *2*, 2368-2377.

(8) Protesescu, L.; Yakunin, S.; Bodnarchuk, M. I.; Krieg, F.; Caputo, R.; Hendon, C. H.; Yang, R. X.; Walsh, A.; Kovalenko, M. V., Nanocrystals of Cesium Lead Halide Perovskites ($CsPbX_3$, X = Cl, Br, and I): Novel Optoelectronic Materials Showing Bright Emission with Wide Color Gamut. *Nano Lett.* **2015,** *15*, 3692-3696.

(9) Imran, M.; Caligiuri, V.; Wang, M.; Goldoni, L.; Prato, M.; Krahne, R.; De Trizio, L.; Manna, L., Benzoyl Halides as Alternative Precursors for the Colloidal Synthesis of Lead-Based Halide Perovskite Nanocrystals. *J. Am. Chem. Soc.* **2018,** *140*, 2656-2664.

(10) Shamsi, J.; Urban, A. S.; Imran, M.; De Trizio, L.; Manna, L., Metal Halide Perovskite Nanocrystals: Synthesis, Post-Synthesis Modifications, and Their Optical Properties. *Chem. Rev.* **2019,** *119*, 3296-3348.

(11) Quarta, D.; Imran, M.; Capodilupo, A.-L.; Petralanda, U.; van Beek, B.; De Angelis, F.; Manna, L.; Infante, I.; De Trizio, L.; Giansante, C., Stable Ligand Coordination at the Surface of Colloidal $CsPbBr_3$ Nanocrystals. *J. Phys. Chem. Lett.* **2019**, 3715-3726.

(12) De Roo, J.; Ibáñez, M.; Geiregat, P.; Nedelcu, G.; Walravens, W.; Maes, J.; Martins, J. C.; Van Driessche, I.; Kovalenko, M. V.; Hens, Z., Highly Dynamic Ligand Binding and Light Absorption Coefficient of Cesium Lead Bromide Perovskite Nanocrystals. *ACS Nano* **2016,** *10*, 2071-2081.

(13) Nenon, D. P.; Pressler, K.; Kang, J.; Koscher, B. A.; Olshansky, J. H.; Osowiecki, W. T.; Koc, M. A.; Wang, L.-W.; Alivisatos, A. P., Design Principles for Trap-Free $CsPbX_3$ Nanocrystals: Enumerating and Eliminating Surface Halide Vacancies with Softer Lewis Bases. *J. Am. Chem. Soc.* **2018,** *140*, 17760-17772.

(14) Imran, M.; Ijaz, P.; Goldoni, L.; Maggioni, D.; Petralanda, U.; Prato, M.; Almeida, G.; Infante, I.; Manna, L., Simultaneous Cationic and Anionic Ligand Exchange For Colloidally Stable $CsPbBr_3$ Nanocrystals. *ACS Energy Lett.* **2019,** *4*, 819-824.

(15) Bodnarchuk, M. I.; Boehme, S. C.; ten Brinck, S.; Bernasconi, C.; Shynkarenko, Y.; Krieg, F.; Widmer, R.; Aeschlimann, B.; Günther, D.; Kovalenko, M. V.; Infante, I., Rationalizing and Controlling the Surface Structure and Electronic Passivation of Cesium Lead Halide Nanocrystals. *ACS Energy Lett.* **2019,** *4*, 63-74.

(16) Krieg, F.; Ochsenbein, S. T.; Yakunin, S.; ten Brinck, S.; Aellen, P.; Süess, A.; Clerc, B.; Guggisberg, D.; Nazarenko, O.; Shynkarenko, Y.; Kumar, S.; Shih, C.-J.; Infante, I.; Kovalenko, M. V., Colloidal $CsPbX_3$ (X = Cl, Br, I) Nanocrystals 2.0: Zwitterionic Capping Ligands for Improved Durability and Stability. *ACS Energy Lett.* **2018,** *3*, 641-646.

(17) Yang, D.; Li, X.; Zhou, W.; Zhang, S.; Meng, C.; Wu, Y.; Wang, Y.; Zeng, H., $CsPbBr_3$ Quantum Dots 2.0: Benzenesulfonic Acid Equivalent Ligand Awakens Complete Purification. *Adv. Mater.* **2019,** *0*, 1900767.

(18) Woo, J. Y.; Lee, S.; Lee, S.; Kim, W. D.; Lee, K.; Kim, K.; An, H. J.; Lee, D. C.; Jeong, S., Air-Stable PbSe Nanocrystals Passivated by Phosphonic Acids. *J. Am. Chem. Soc.* **2016,** *138*, 876-883.

(19) Tan, Y.; Zou, Y.; Wu, L.; Huang, Q.; Yang, D.; Chen, M.; Ban, M.; Wu, C.; Wu, T.; Bai, S.; Song, T.; Zhang, Q.; Sun, B., Highly Luminescent and Stable Perovskite Nanocrystals with Octylphosphonic Acid as a Ligand for Efficient Light-Emitting Diodes. *ACS Appl. Mater. Interfaces* **2018,** *10*, 3784-3792.

(20) Almeida, G.; Ashton, O. J.; Goldoni, L.; Maggioni, D.; Petralanda, U.; Mishra, N.; Akkerman, Q. A.; Infante, I.; Snaith, H. J.; Manna, L., The Phosphine Oxide Route toward Lead Halide Perovskite Nanocrystals. *J. Am. Chem. Soc.* **2018,** *140*, 14878-14886.

(21) Yang, X.; Zhang, X.; Deng, J.; Chu, Z.; Jiang, Q.; Meng, J.; Wang, P.; Zhang, L.; Yin, Z.; You, J., Efficient green light-emitting diodes based on quasi-two-dimensional composition and phase engineered perovskite with surface passivation. *Nat. Commun.* **2018,** *9*, 570.

(22) Perdew, J. P.; Burke, K.; Ernzerhof, M., Generalized Gradient Approximation Made Simple. *Phys. Rev. Lett.* **1996,** *77*, 3865-3868.

(23) VandeVondele, J.; Hutter, J., Gaussian basis sets for accurate calculations on molecular systems in gas and condensed phases. *J. Chem. Phys.* **2007,** *127*, 114105.

(24) Hutter, J.; Iannuzzi, M.; Schiffmann, F.; VandeVondele, J., cp2k: atomistic simulations of condensed matter systems. *Wiley Interdiscip. Rev.: Comput. Mol. Sci.* **2014,** *4*, 15-25.

(25) ten Brinck, S.; Infante, I., Surface Termination, Morphology, and Bright Photoluminescence of Cesium Lead Halide Perovskite Nanocrystals. *ACS Energy Lett.* **2016,** *1*, 1266-1272.

(26) Nedelcu, G.; Protesescu, L.; Yakunin, S.; Bodnarchuk, M. I.; Grotevent, M. J.; Kovalenko, M. V., Fast Anion-Exchange in Highly Luminescent Nanocrystals of Cesium Lead Halide Perovskites ($CsPbX_3$, X = Cl, Br, I). *Nano Lett.* **2015,** *15*, 5635-5640.

(27) Imran, M.; Ijaz, P.; Baranov, D.; Goldoni, L.; Petralanda, U.; Akkerman, Q.; Abdelhady, A. L.; Prato, M.; Bianchini, P.; Infante, I.; Manna, L., Shape-Pure, Nearly Monodispersed $CsPbBr_3$ Nanocubes Prepared Using Secondary Aliphatic Amines. *Nano Lett.* **2018,** *18*, 7822-7831.

(28) Cottingham, P.; Brutchey, R. L., On the crystal structure of colloidally prepared $CsPbBr_3$ quantum dots. *Chem. Commun.* **2016,** *52*, 5246-5249.

(29) Momma, K.; Izumi, F., VESTA 3 for three-dimensional visualization of crystal, volumetric and morphology data. *J. Appl. Cryst.* **2011,** *44*, 1272-1276.

(30) Luschtinetz, R.; Seifert, G.; Jaehne, E.; Adler, H.-J. P., Infrared Spectra of Alkylphosphonic Acid Bound to Aluminium Surfaces. *Macromol. Symp.* **2007,** *254*, 248-253.

(31) Son, J. G.; Choi, E.; Piao, Y.; Han, S. W.; Lee, T. G., Probing organic ligands and their binding schemes on nanocrystals by mass spectrometric and FT-IR spectroscopic imaging. *Nanoscale* **2016,** *8*, 4573-4578.

(32) Owen, J. S.; Park, J.; Trudeau, P.-E.; Alivisatos, A. P., Reaction Chemistry and Ligand Exchange at Cadmium−Selenide Nanocrystal Surfaces. *J. Am. Chem. Soc.* **2008,** *130*, 12279-12281.

(33) Gomes, R.; Hassinen, A.; Szczygiel, A.; Zhao, Q.; Vantomme, A.; Martins, J. C.; Hens, Z., Binding of Phosphonic Acids to CdSe Quantum Dots: A Solution NMR Study. *J. Phys. Chem. Lett.* **2011,** *2*, 145-152.

(34) Smock, S. R.; Williams, T. J.; Brutchey, R. L., Quantifying the Thermodynamics of Ligand Binding to $CsPbBr_3$ Quantum Dots. *Angew. Chem.* **2018,** *130*, 11885-11889.

4.2. Stable and Size Tunable CsPbBr3 Nanocrystals Synthesized with Oleylphosphonic Acid

ABSTRACT: we employed oleylphosphonic acid (OLPA) to replace the alkyl phosphonic acid in the synthesis of colloidal $CsPbBr_3$ NCs. Compared to alkyl phosphonic acid having a linear chain, OLPA has a softer chain and thus features a higher solubility in apolar solvents. Comparing with alkyl phosphonic acid, OLPA can dissolve the metal precursors at mild temperatures (80-120°C). Low reaction temperatures offer a good control over the NCs' size, allowing for the synthesis of very small (5.0 nm) NCs, which show strong quantum confinement . By NMR analysis, the OLPA-based NCs were terminated by hydrogen phosphonates and phosphonic acid anhydrides. OLPA-based NCs was show resistance against dilution, while and more stable under air comparing with alkyl phosphonate caped NCs. Such stability under air could come from the dynamic binding between NCs surface and free OLPA in solution, which stems from the high solubility of OLPA in apolar solvents. The high stability of our small sized NCs give the opportunity to investigate the optical properties of these materials in the quantum confined regime. Small NCs featured an ultra-slow emission kinetics at cryogenic temperature, in striking difference to the fast decay of larger particles. It suggested size-related exciton structure or the thermal equilibrium between coexisting radiative processes determined by trapping/detrapping dynamic.

INTRODUCTION. LHPs nanocrystals (NCs) have drawn attention due to their ideal optical properties which make them as potential candidates in various applications.[1-6] The efficient photoluminescence (PL) emission of LHP NCs stems from their intrinsic defect tolerant nature.[3, 7-8] In these systems, various works have shown that the surface passivation plays a fundamental role in achieving both colloidally stable and strongly emissive LHP NCs.[7, 9] As mentioned in Chapter 4.1., the standard ammonium and carboxylate ions are easily to detach from the surface, which is deleterious for both colloidal stability and PLQY.[7, 10] Consequently, these types of ligands are weakly bound to the NCs surface, and a highly dynamic equilibrium exists between free and bound ligands.[7, 11-13] In order to optimize the surface passivation of LHP NCs, various alternative surfactants such as zwitterionic molecules, quaternary alkyl ammonium ions, sulfonic and alkyl phosphonic acids could be the most promising ones.[3, 7, 10, 14-15]

In Chapter 4.1., we demonstrated that $CsPbBr_3$ NCs, synthesized in the presence of alkyl phosphonic acids as the only ligands in the reaction environment, are very stable against dilution, maintaining ~100% PLQY even at concentrations as low as ~1 nM.[10] However, that synthesis approach has two major limitations: i) the NC dispersions turned out to be unstable in air; ii) the alkyl phosphonic acids employed require high temperatures (at least 220 °C or above) to solubilize the metal cation precursors and this prevents the synthesis of small NCs.[10] As a matter of fact, with that method we could not grow NCs with sizes smaller than ~7 nm.

To overcome these issues, in this work the cis-oleylphosphonic acid (OLPA) as the sole surfactant in the synthesis of $CsPbBr_3$ NCs. Due to the bent chain, OLPA molecules has a lower intermolecular London forces and lower melting point comparing with linear alkyl chain PA.[16] Consequently, while TDPA and ODPAare substantially insoluble in common apolar solvents, such as hexane, toluene and octadecene (ODE),[17] OLPA has a much better solubility (>10 mg/ml at room temperature).[18] As a result, the OLPA allow the hot injection at lower temperatures (as low as 120 °C). The homogeneous small sized (< 5 nm) NCs was obtained in such low temperature(Scheme 1). Our NMR studies indicate that the surface of OLPA-based $CsPbBr_3$ NCs is passivated phosphonate species, hydrogen phosphonates and phosphonic acid anhydrides (Scheme 1). Such small NCs enabled us to access easily the strong quantum confinement regime (the exciton Bohr diameter of $CsPbBr_3$ is 7 nm),[19-20] with no need for cleaning procedures or post-synthesis ligand exchange treatments to prevent size evolution, as done in previous works in which small $CsPbBr_3$ NCs were prepared and studied optically.[20-21] The obtained NCs (including small sized one) exhibit a high colloidal stability even when exposed to air. Our PL measurements at cryogenic temperature evidenced that strongly quantum confined NCs feature an ultra-slow emission kinetics which is different from the fast decay of larger NCs. The phenomenon match with recently invoked size-dependent excitonic fine structure effects,[21] suggesting the presence of thermal equilibria between competitive radiative processes.

EXPERIMENTAL SECTION

Chemicals. Oleyl alcohol (technical grade, 85%), carbon tetrabromide (CBr_4, 99%), triphenylphosphine (PPh_3, 99%), sodium hydride (NaH, 60% dispersion in mineral oil), diethyl phosphite (98%), trimethylsilyl bromide (TMSBr, 97%), Trimethylchlorosilane (TMS-Cl, 97%), dichloromethane (DCM, anhydrous, 99.8%), 1,2,4,5-tetrachloro-3-nitrobenzene (TCNB, standard for quantitative NMR, TraceCERT®, 99.82%), *N*,*N*-dimethylformamide (DMF, anhydrous, 99.8%), methanol (MeOH, HPLC grade, ≥99.9%), ethyl acetate (AcOEt, ACS reagent, ≥99.5%), diethyl ether (Et_2O, ACS reagent, ≥99.8%) and petroleum ether (PE, 40-60 °C, ACS reagent, ≥90%) were purchased from Sigma-Aldrich. All chemicals were used without further purification except for diethyl phosphite that was distilled over $CaCl_2$ (10% w/v) under vacuum (b.p. 108 °C, 90 mbar) and stored under Ar.

Synthesis of oleylphosphonic acid (OLPA). OLPA was prepared according to a reported literature procedure (Scheme S1 in the Supporting Information, SI) with minor modifications aimed at enhancing the purity, that was calculated by quantitative NMR.[18] Diethyl oleylphosphonate (3.8 g, 9.79 mmol) was dissolved in dry DCM (8 mL) under Ar and cooled to 0 °C. TMSBr (3.0 mL, 22.5 mmol) was added drop-wise and, after stirring in the dark at room temperature overnight, the volatile components were removed by evaporation (see SI for details on the synthesis of diethyl oleylphosphonate). The residue was dissolved in MeOH and the solution was stirred at 40 °C for 3 h. The volatile components were removed by evaporation and the residue was washed with DCM (3 × 5 mL, evaporation after each step). The solid was further dried under high vacuum at 50 °C overnight in order to remove any traces of solvents (as confirmed by ^1H NMR), to give OLPA (3.25 g, yield 99%) in the form of a waxy solid. The purity, as assessed by quantitative NMR was 94% (see Figure S4 and SI for further details).

Synthesis of $CsPbBr_3$ NCs. 76 mg (0.2 mmol) of lead (II) acetate trihydrate, 16 mg (0.1 mmol) of cesium carbonate, 0.6 mmol of OLPA and 10 mL of 1-octadecene were mixed in a 25 mL 3-neck flask. The re-action mixture was degassed for 0.5 hour at room temperature and then the temperature was raised to 120 °C to achieve a full dissolution of the precursors. The whole dissolution process requires 2 hours. Subsequently, the precursors solution was cooled down to 100 °C and 50 μL of benzoyl bromide diluted in 500 μL of degassed ODE was then injected into the reaction flask. The reaction was quenched by immersing the flask in an ice-water bath. In details, 5.0nm, 6.8nm and 9.2nm NCs were prepared by quenching the reaction after 45, 120 and 600 seconds, respectively. Ethyl acetate, at a volume ratio of 8:1 with the crude NCs solution, was used to wash the samples. After centrifuging at 6000 rpm for 5 min, the supernatant was discarded and the NCs were dispersed in either hexane or toluene (1 ml). The NCs were washed a second time by adding 6 ml of ethyl acetate followed by centrifugation at 6000 rpm for 5 min. Eventually, the precipitated NCs could be redispersed in various solvents (hexane, toluene, or $CDCl_3$) for further characterizations.

PL lifetime test. Temperature-dependent steady-state and time-resolved PL spectra were obtained using excitation from a pulsed diode laser with the 3.06 eV photon energy (Edinburgh Inst. EPL 405, 40 ps pulse width) and a variable pulse repetition rate. The OLPA-based LHP NC samples were prepared as drop-cast films on glass substrates. They were placed in a variable-temperature insert of a closed-cycle helium cryostat (T = 5 – 300 K). The emitted light was coupled into a 600 µm optical fiber and the PL signal was spectrally resolved with a TM-C10083CA Hamamatsu Mini-Spectrometer. The PL dynamics were studied with a Hamamatsu R943-02 time-correlated single-photon counting unit coupled to an Oriel Instruments Cornerstone 260 monochromator.

Nuclear Magnetic Resonance (NMR) measurements. Same with Chapter 4.1.

Transmission Electron microscopy (TEM). Same with Chapter 4.1.

X-ray diffraction (XRD). Same with Chapter 4.1.

X-ray Photoelectron Spectroscopy (XPS). Same with Chapter 4.1.

UV−vis Absorption, Photoluminescence (PL), PL Quantum Yield (QY) Measurements and temperature dependent PL. Same with Chapter 4.1.

RESULTS AND DISCUSSION

Synthesis and structural characterization of OLPA-based NCs. The synthesis method is similar with the colloidal approach described in Chapter 4.1 .[10] In the present case, the use of OLPA drastically reduced the dissolving temperature of metal cation precursors in ODE. As a comparison, a complete dissolution of metal precursors was achieved only at 220 °C when working with TDPA and ODPA, while in the case of OLPA this was achieved at 120 °C. Moreover, the metal-OLPA complexes were soluble in ODE at temperatures as low as 80°C, while those metal-TDPA complex required at least 160°C.[10] Three NC samples were prepared by performing the synthesis at 100°C with different reaction time (see the experimental section for details). The XRD analysis confirmed that all the NC products have a pure orthorhombic $CsPbBr_3$ phase (ICSD number 98751).

The TEM images indicated that the increase in reaction time tune the size of NCs from ~5.0 to ~9.2 nm (Figure 1a-c) with a narrow size distribution (Figure S5). These OLPA-based NCs have a truncated octahedron shape, similarly to what we reported in Chapter 4.1.[10] This shape originates from the preferential binding affinity of alkylphosphonates to both (001) and (110) Pb-terminated facets.[10] The absorption and photoluminescence spectra of these samples can be tuned from 503 nm (PL maximum at 509 nm) in the case of 9.2 nm NCs to 482 nm (PL maximum at 491 nm) for 5.0nm NCs (Figure 1e). The PLQYs of 5.0, 6.8 and 9.2 nm NC samples are 90.9%, 83.6% and 81.0%, respectively, indicating an efficient passivation. Moreover, such high PL emission is retained even when diluting the NCs dispersions down to 1-10 nM (Figure S6). Such experiments highlight that OLPA-based NC exhibit a high colloidal stability with ligands being strongly bound to the surface.[7, 17, 22] Another important feature of OLPA-based samples is that the colloidal dispersions of NCs are stable in air up to 2 weeks (Figure S7). This is a relevant improvement, considering that colloidal suspensions of NCs prepared with TDPA and ODPA are not stable at all in air: upon air exposure, the precipitation of NCs is observed (Figure S7). These results point to an improved stability of OLPA-based NCs, which is remarkable in the case of quantum confined ones (i.e. 5.0nm).

Scheme 1. Colloidal approach to obtain $CsPbBr_3$ NCs employing oleylphosphonic acid.

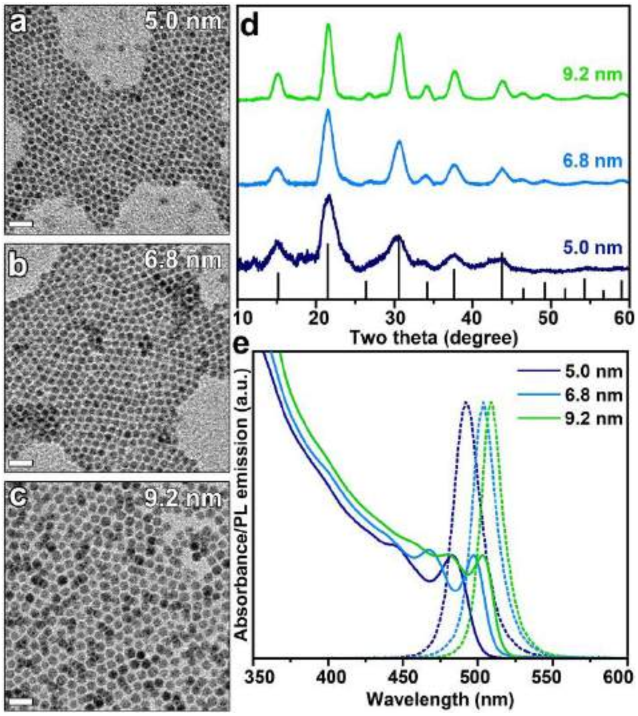

Figure 1. TEM images of (a) 5.0 nm, (b) 6.8 nm and (c) 9.2 nm $CsPbBr_3$ NCs. The scale bars are 50 nm. (d) XRD patterns. (e) Absorption and PL spectra of OLPA-based NCs with different size.

Surface characterization of OLPA-based NCs. With the aim of explaining the improved stability of OLPA-based NCs, the ligands shell of NCs was thoroughly characterized via NMR analysis Both ^1H and ^{31}P NMR spectra of NCs solution evidence the presence of OLPA based molecules bound to the surface of the NCs: both alkenyl protons (**9,10**) at 5.3 ppm (Figure 2a) and phosphorous signals in the range of 15-40 ppm (Figure 2b) are broadened with respect to those of free OLPA ligands (Figure S3 and S8), indicating that these P-based molecules bind to NCs' surface.[18] Also, the presence of multiple ^{31}P signals indicates that surface ligands adopt different binding motifs.

To reveal how OLPA molecules are anchored to the surface of perovskite NCs, we treated our NCs with trimethylchlorosilane (TMS-Cl).[10, 17, 23-24] Upon reaction of OLPA-based NCs with TMS-Cl, OLPA related species were striped out and were characterized as four individual ^{31}P NMR peaks (Figure 3c): one pair of sharp peaks at 14.92 and 15.52 ppm with similar intensities were assigned to *O,O'*-bis(trimethylsilyl)oleylphosphonic acid anhydride diastereoisomers; the peaks at 33.95 and 16.65 ppm could be ascribed to mono- and di-TMS substituted OLPA, respectively (see also Figure S8).[10, 23]

These results indicate that the surface of the NCs is passivated by phosphonates (PA^{2-}), hydrogen phosphonates (PA^-) and phosphonic acid anhydrides [PA(anhy)] (see the sketch in Figure 2b). Interestingly, PA^{2-} species were not observed when TDPA molecules were employed for the synthesis of LHP NCs at higher temperatures (180°C) (Figure S9). Overall, our NMR studies suggests that low synthesis temperatures (i.e. 100°C) suppress the formation of PA(anhy) ones (Figure S10). As contrast, when synthesis LHP NCs by OLPA at 160°C, more PA(anhy) was formed(Figures S11-13). Our results highlight that the reaction temperature plays a key role in the binding motif of phosphonic acids on the surface of $CsPbBr_3$, and, presumably, semiconductor NCs in general. As we previously calculated, the binding energies of PA^{2-} and PA^- species with surface Pb^{2+} cations are close (47.9 and 52.2 kcal/mol, respectively),[10] so the different binding motif is not sufficient to explain the improved stability of OLPA based NCs under air. We attributed the improved stability to the high solubility of OLPA molecules (and anhydrides) in toluene or other apolar solvent. After the exposure to air, oleylphosphonates (and anhydrides) can be protonated by water molecules and, thus, partially released from the NC surface and solubilized by the solvent. Being still in solution they can dynamic binding to the surface of the NCs. Conversely, TDPA and ODPA, once protonated are not soluble in apolar solvent, , hence they cannot re-bind to the surface passivation of the NCs anymore.

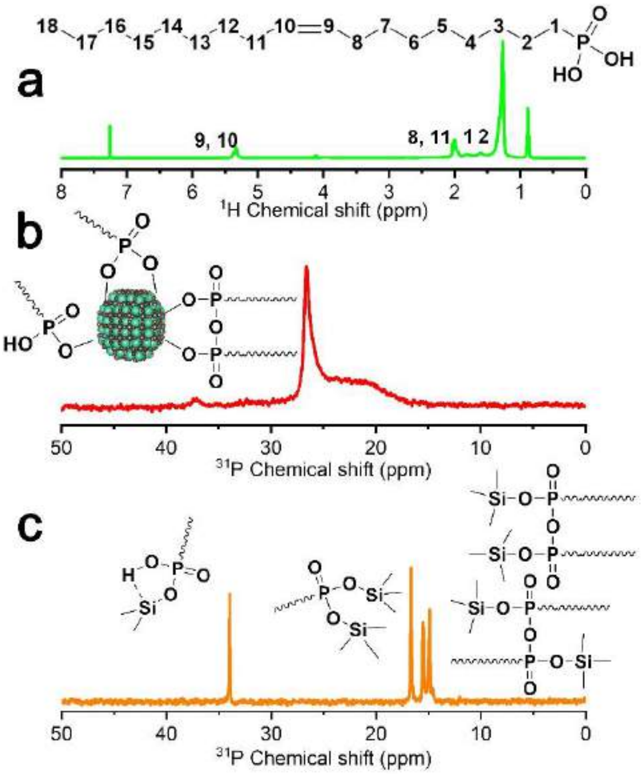

Figure 2. (a) ^{1}H NMR and (b) ^{31}P NMR characterization of 5.0 nm $CsPbBr_3$ NCs dispersed in $CDCl_3$. (c) ^{31}P NMR spectrum of the products of OLPA-based NCs after reacting with TMS-Cl in $CDCl_3$.

Optical analyses. Our method enables to synthesize strongly quantum confined and stable $CsPbBr_3$ NCsand this open a window to study the optical properties of the LHP materials in such confinement regime. We therefore proceeded to investigate the optical properties of both weak (9.2 nm) and strong (5.0 nm) quantum confined OLPA-based NCs via side-by-side PL measurements as a function of the temperature. Upon lowering the temperature, the PL spectra of both samples progressively red-shifted (Figure 3a,b), as expected due to bandgap renormalization[25-30] and their PL intensity remained essentially constant (Figure 3c), in agreement with the near-unity PLQY measured at room temperature. Consistent with the smaller number of atoms involved in the thermal expansion of the perovskite crystal lattice upon lowering the temperature, The red shift of the PL maximum was smaller for the 5.0 nm NCs than for the 9.2 nm ones (~30 meV vs. ~80 meV, respectively, Figures 3a,b and 3d). Such difference was caused by that 5.0 nm NCs has smaller number of atoms involving in the thermal expansion of crystal lattice upon cooling. The temperature dependence of the full width at half maximum (FWHM) of either systems was similar (Figure S14), suggesting that exciton-phonon coupling is almost independent on the size of the NCs.

The most striking difference between the optical properties of small vs. large NCs was the respective PL kinetics at low temperature, as reported in Figures 3e,f. At room temperature, both systems show a nearly single-exponential dynamics with lifetime (τ) of ~5 ns. Upon lowering the temperature, the PL dynamics of the 9.2 nm NCs progressively accelerate, reaching τ ~2.5 ns at T=5K (Figures 3e and 3g). This effect is typical of weak quantum confinement LHP NCs (8-15 nm) and has been ascribed to the radiative decay of bright triplet excitons becoming dominant at cryogenic temperatures.[30-32] On the other hand, the evolution of the PL kinetics of the 5.0 nm NCs is more striking: for 300K < T < 50K, the PL lifetime gradually lengthens, reaching τ ~13 ns at 50K; at lower temperatures (i.e. <50 K), the PL decay slow to τ ~700 ns (at 5K), over two orders of magnitude longer than that at RT (Figure 3f). The PL decay follow a double exponential kinetics. Importantly, the PL intensity maintain near unity at such process (Figure 3c), indicating that such a double exponential decay kinetics is purely radiative. As sketched in the inset of Figure 3f, this behavior can be described by the thermal equilibrium between two states: a higher energy excitonic state (labeled as **1**) with a large oscillator strength responsible for the fast decay at RT and a lower lying state (labeled as **2**) weakly optically coupled to the ground state that determines the slow PL kinetics below 20K. At high temperatures, state **1** is thermally populated, and the respective fast PL dominates the emission. At low temperature (<20K), excitons thermalized into state **2** could no longer be promoted to state **1**, resulting in the very slow PL tail. Consistent with this picture, we adequately fitted the trend of τ as a function of temperature with the equation:

$$\tau(\mathrm{T}) = (1 + \exp(-\Delta_{1,2}/k_B\mathrm{T}))/(\tau_1^{-1} + \tau_2^{-1}{*}\exp(-\Delta_{1,2}/k_B\mathrm{T})) \quad \text{Eq.(1)}$$

where k_B is the Boltzmann constant, τ_1 and τ_2 are the PL lifetimes of state **1** and **2**, respectively, and $\Delta_{1,2}$ is the energy separation between these two states (Figure 3g). By fitting the equation, the $\Delta_{1,2}$ is ~12 meV, which is significantly smaller than the PL linewidth of the NC ensemble. Consistently, the contour plot of the time-resolved PL of the quantum confined NCs shows no spectral evolution over time at 5K. By integrating the contour plot of PL spectra in the 0-5 ns (which is dominated by the resolution-limited component), 5-500 ns and 500-900 ns time ranges, all of them has the same PL profile (Figure 3h**)**. All such observations, including comparable value for $\Delta_{1,2}$, agree with recent results on small $CsPbBr_3$ NCs, ascribing the long-lived PL tail at cryogenic temperatures to the radiative decay of a non-emissive or 'dark' exciton state.[21] To date, such an interpretation is similar with the exciton fine structure effects commonly observed for strongly confined CdSe NCs. Therefore, our results could be of interest to extend the theoretical framework currently available for larger NCs (lateral size of 8-15 nm) through the above-mentioned bright-triplet model,[32] to more strongly confined NCs where the exciton fine structure could be substantially different.

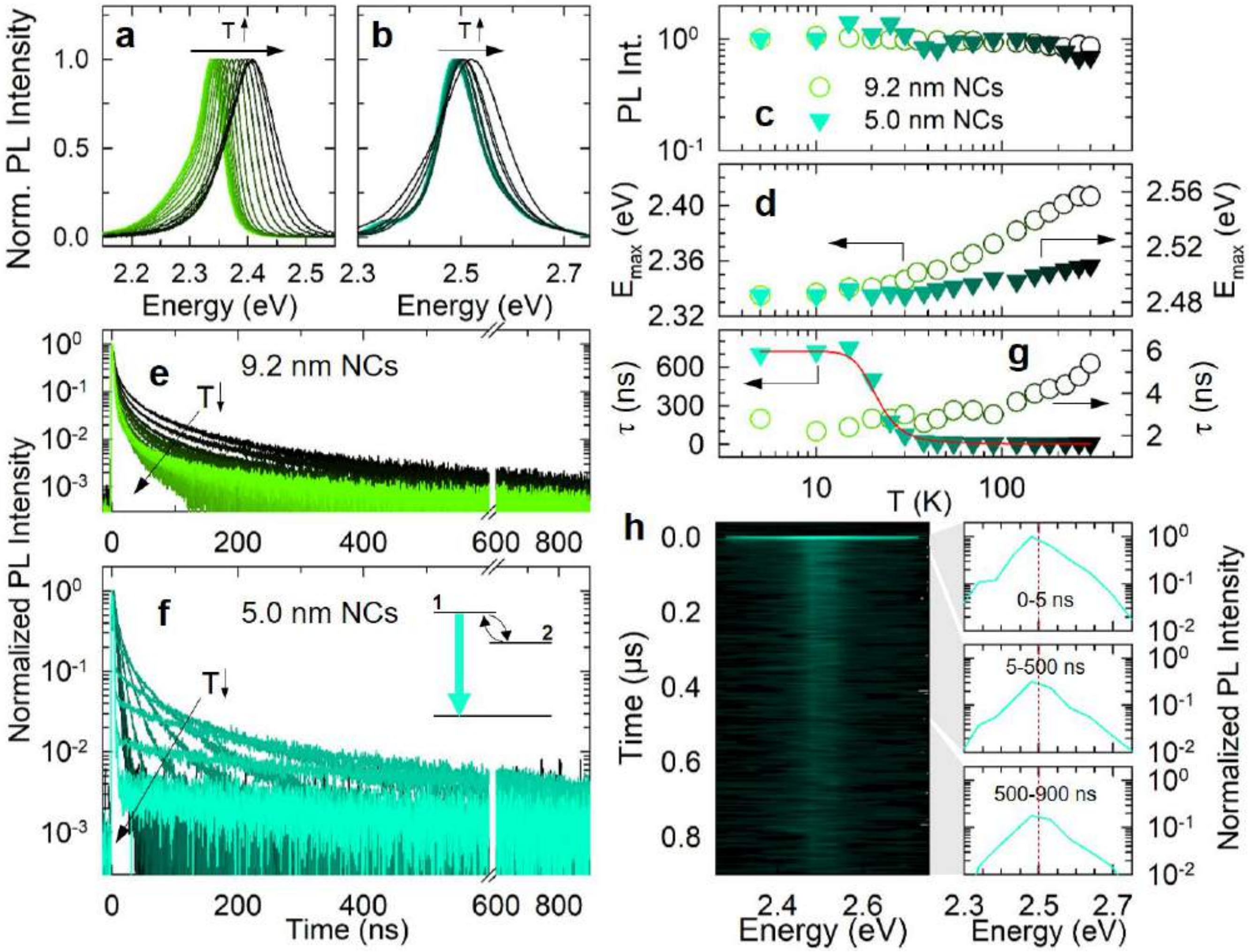

Figure 3. Normalized PL spectra of (a) 9.2 nm and (b) 5.0 nm $CsPbBr_3$ NCs as a function of the temperature (from 5K to 300K). (c) Temperature dependent PL intensity and (d) temperature dependent PL peak position of the 9.2 nm and 5.0 nm NCs (circles and triangles, respectively). (e) and (f). Temperature dependent PL decay of 9.2 nm and 5.0 nm NCs. Inset in (f): Sketch of the thermal equilibrium between two energy state (2). (g) PL lifetimes as a function of temperature. (h) Contour plot of the PL emission of 5.0 nm NCs together with the respective PL spectra by integrating in the 0-5 ns (top panel), 5-500 ns (middle panel) and 500-900 ns (bottom panel) ranges, at T = 5K.

CONCLUSIONS

In summary, we synthesized $CsPbBr_3$ NCs using oleylphosphonic acid (OLPA) as the only surfactant. Being OLPA molecules more soluble than standard phosphonic acids with linear alkyl chains (such as TDPA and ODPA) in apolar solvents, it allows for the synthesis of $CsPbBr_3$ NCs at low temperatures (100°C) with a fine control over their size down to 5.0nm, which is strongly quantum confined.OLPA-based NCs have a truncated octahedron shape with Pb-terminated facets passivated by phosphonates, hydrogen phosphonates and phosphonic acid anhydrides, as revealed by NMR analysis. OLPA-based NCs show improved stability when exposed to air. We hypothesize that such stability, which characterize also quantum confined (i.e. 5.0nm) NCs, stems from the high solubility of OLPA in apolar solvents which allows dynamically binding with the NCs surface and apolar solution.

The high stability of our small sized NCs give the opportunity to investigate the optical properties of these materials in the quantum confined regime. Small NCs featured an ultra-slow emission kinetics at cryogenic temperature, in striking difference to the fast decay of larger particles. It suggested size-related exciton structure or the thermal equilibrium between coexisting radiative processes determined by trapping/detrapping dynamic.

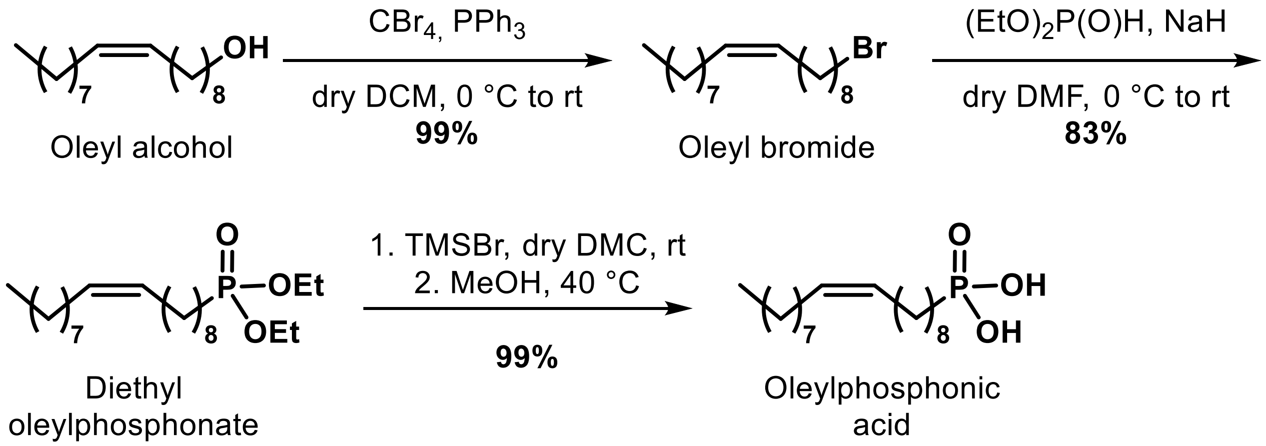

Scheme S1. Synthesis of OLPA.

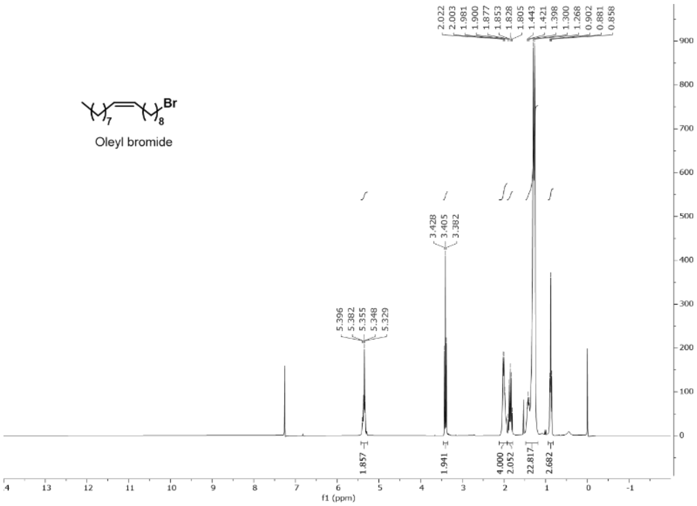

Figure S1. ^{1}H NMR spectrum of oleyl bromide

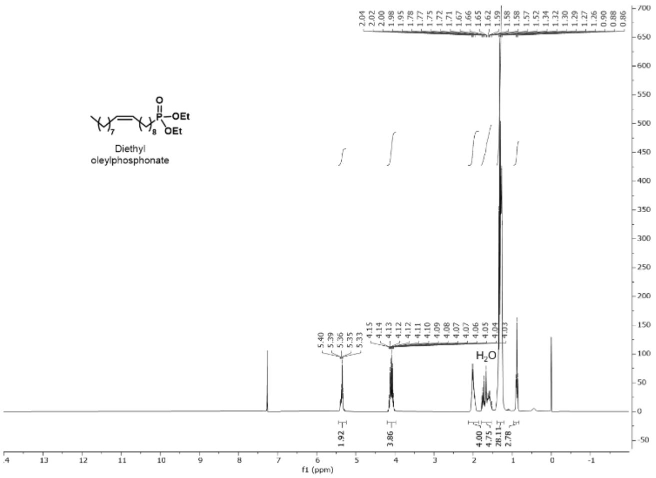

Figure S2. ^{1}H NMR spectrum of diethyl oleylphosphonate

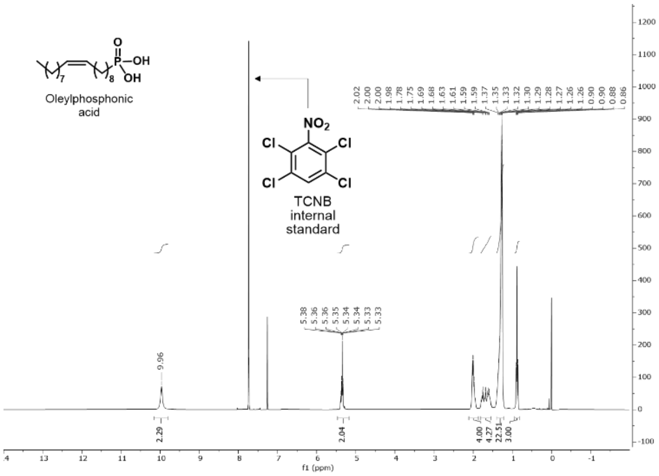

Figure S3. ^{1}H NMR spectrum of oleylphosphonic acid

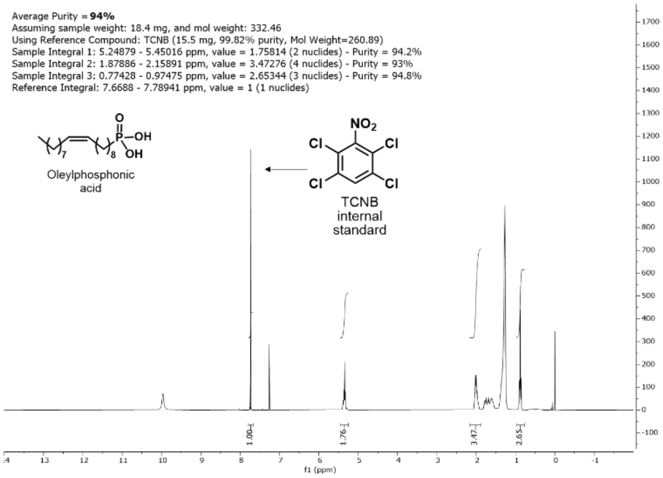

```
Average Purity = 94%
Assuming sample weight: 18.4 mg, and mol weight: 332.46
Using Reference Compound: TCNB (15.5 mg, 99.82% purity, Mol Weight=260.89)
Sample Integral 1: 5.24879 - 5.45016 ppm, value = 1.75814 (2 nuclides) - Purity = 94.2%
Sample Integral 2: 1.87886 - 2.15891 ppm, value = 3.47276 (4 nuclides) - Purity = 93%
Sample Integral 3: 0.77428 - 0.97475 ppm, value = 2.65344 (3 nuclides) - Purity = 94.8%
Reference Integral: 7.6688 - 7.78941 ppm, value = 1 (1 nuclides)
```

Figure S4. Determination of the purity of OLPA by qNMR

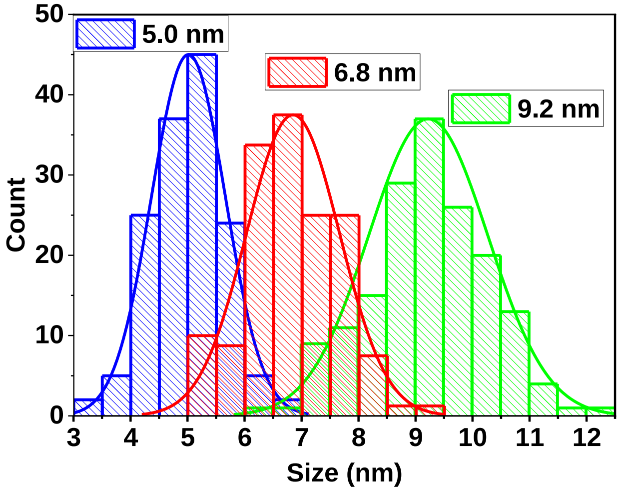

Figure S5. Size distribution histograms determined from the TEM images reported in Figure 1a-c of the main text. Sample 1 (blue): D_{mean} = 5.0 ± 0.7 nm; Sample 2 (red): D_{mean} = 6.8 ± 0.8 nm; sample 3 (green): D_{mean} = 9.2 ± 1.1 nm.

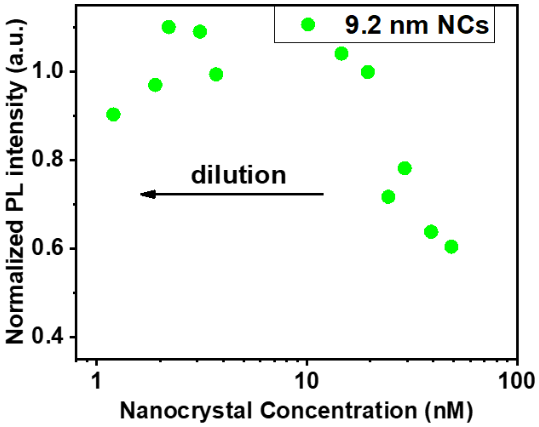

Figure S6. Variation of the PL emission intensity with dilution in case of OLPA-based NCs

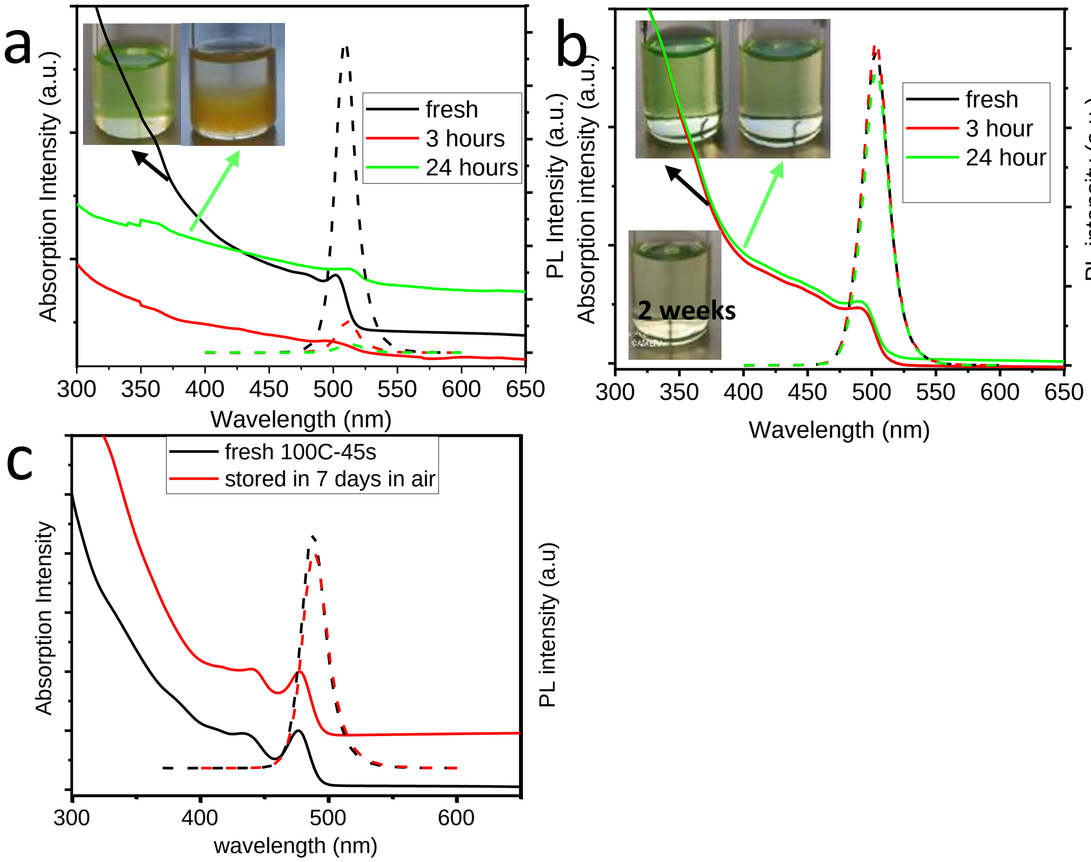

Figure S7. Absorption and PL emission curves of (a) TDPA $CsPbBr_3$ NCs (PL peak maximum at 507nm) and (b) OLPA $CsPbBr_3$ NCs (PL peak maximum at 507nm) as a function of their storage time in air. The pictures of corresponding solution are shown in the inset of panels (a) and (b). (c) Absorption (solid) and PL emission (dashed) curves of quantum confined $CsPbBr_3$ NCs (~5nm) before and after their exposure to air for 7 days.

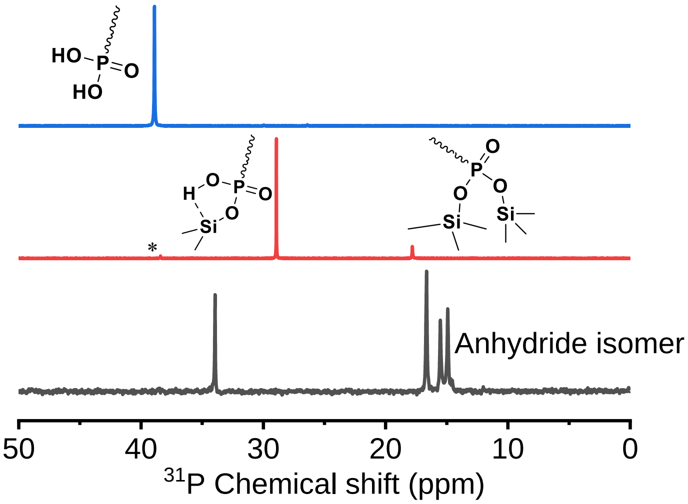

Figure S8. ^{31}P spectra in $CDCl_3$ of free OLPA molecules (blue line), the product of the reaction between TMS-Cl and OLPA molecules (employing a TMS-Cl: PA ratio of 4: 1) (red curve) or TMS-Cl and OLPA-capped NCs (black curve).The three peaks observed when reacting TMS-Cl with OLPA-molecules were assigned to: free unreacted OLPA(marked with *, at 38.4 ppm), mono-TMS substituted OLP (28.9 ppm) and di-substituted OLPA (17.8 ppm). The two peaks around 15ppm in the NMR spectrum of OLPA-capped NCs reacted with TMS-Cl were assigned to anhydride PA isomers, which has been already found in similar systems(put references).

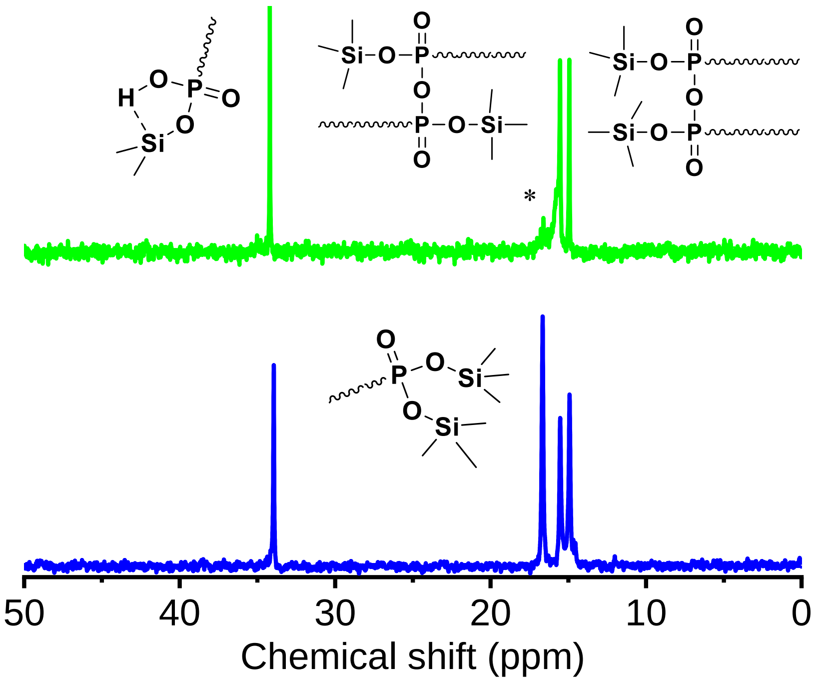

Figure S9. ^{31}P spectra in $CDCl_3$ of TDPA-capped NCs (green curve) and OLPA-capped NCs (blue curve) after being reacted with TMS-Cl. Beside hydrogen phosphonates and phosphonic acid anhydrides species, TMS-Cl treated OLPA-capped NCs also include a large amount of phosphonates species (peak at ~17ppm), which appear in a very small amount in TMS-Cl treated TDPA-capped NCs NCs (*, at 16.6 ppm).

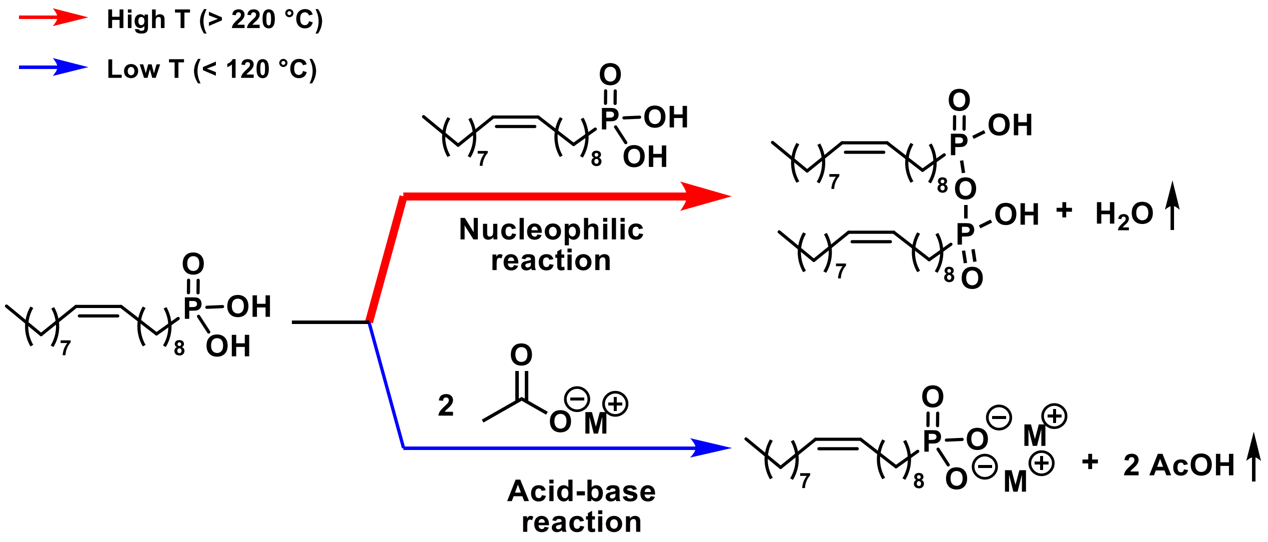

Figure S10. Competition formation pathway between PA anhydride and di-deprotonated PA. High temperature favor the nucleophilic reaction and thus produce more PA anhydride.

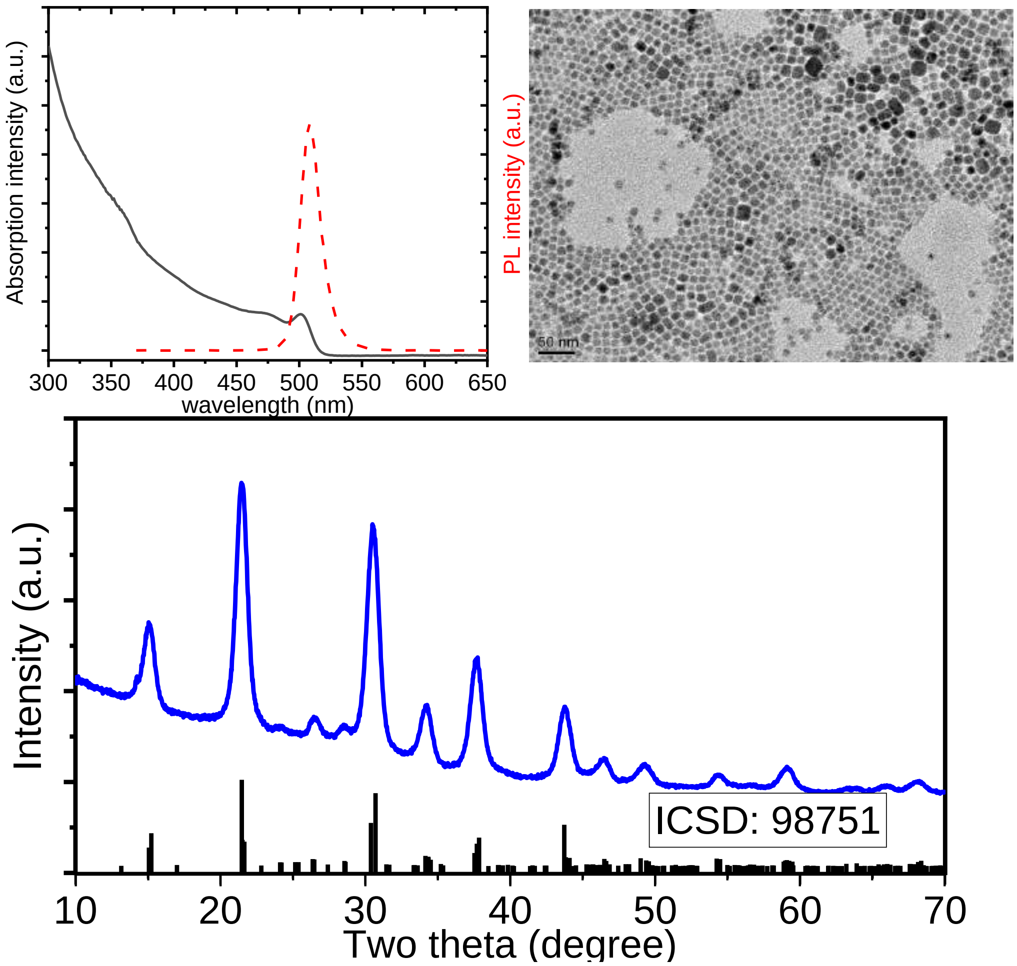

Figure S11. $CsPbBr_3$ NCs synthesized with OLPA ligands at 160°C quenching the reaction 0s after the injection of the Br precursor: (a) absorption (dark line) and photoluminescence spectra (red dashed line); (b) TEM picture, the scale bar is 50 nm; (c) XRD pattern with the corresponding bulk reflections of orthorhombic CsPbBr3 crystal structure.

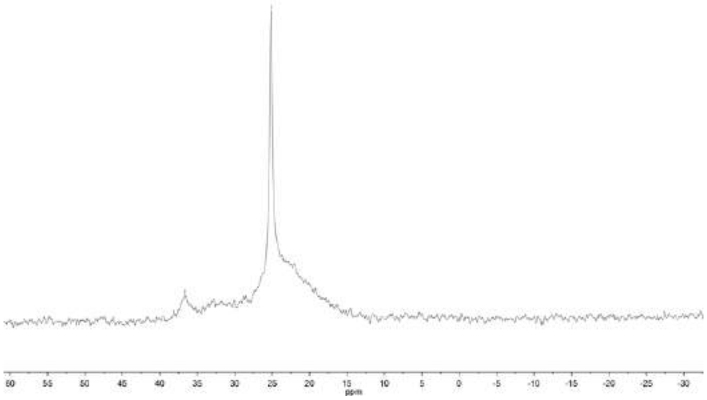

Figure S12. ^{1}H NMR (upper panel) and ^{31}P NMR (lower panel) spectra of $CsPbBr_3$ NCs synthesized in 160°C with OLPA ligands and dispersed in d8-toluene.

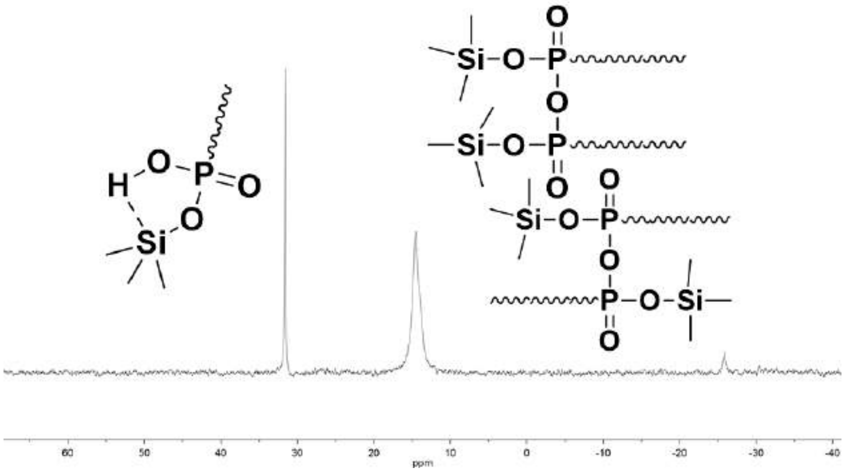

Figure S13. ^{31}P NMR of of $CsPbBr_3$ synthesized in 160C-0s with OLPA ligands in d_8-toluene after TMS-Cl addition. The sharp peak at 31.6ppm is assigned to TMS hydrogen oleylphosphonic acid and the broader peak at 14.4 ppm was assigned as O,O'-bis(trimethylsilyl)oleylphosphonic acid anhydride isomers. No O, O′-bis(TMS)oleylphosphonic acid which should has a peak at 18 ppm was found.

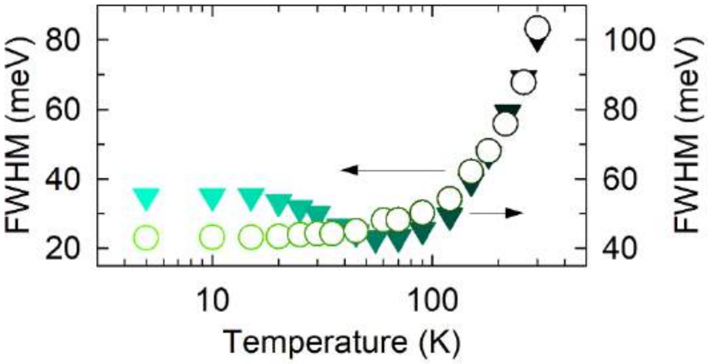

Figure S14. Temperature dependence of the PL full width at half maximum (FWHM) of 5.0 nm and 9.2 nm OLPA capped $CsPbBr_3$ NCs (triangles and circles, respectively).

REFERENCES:

(1) Luo, X.; Ding, T.; Liu, X.; Liu, Y.; Wu, K., Quantum-Cutting Luminescent Solar Concentrators Using Ytterbium-Doped Perovskite Nanocrystals. *Nano Letters* **2019,** *19*, 338-341.

(2) Akkerman, Q. A.; Rainò, G.; Kovalenko, M. V.; Manna, L., Genesis, Challenges and Opportunities for Colloidal Lead Halide Perovskite Nanocrystals. *Nature Materials* **2018,** *17*, 394-405.

(3) Shamsi, J.; Urban, A. S.; Imran, M.; De Trizio, L.; Manna, L., Metal Halide Perovskite Nanocrystals: Synthesis, Post-Synthesis Modifications, and Their Optical Properties. *Chemical Reviews* **2019,** *119*, 3296-3348.

(4) Dong, Y.; Wang, Y.-K.; Yuan, F.; Johnston, A.; Liu, Y.; Ma, D.; Choi, M.-J.; Chen, B.; Chekini, M.; Baek, S.-W.; Sagar, L. K.; Fan, J.; Hou, Y.; Wu, M.; Lee, S.; Sun, B.; Hoogland, S.; Quintero-Bermudez, R.; Ebe, H.; Todorovic, P.; Dinic, F.; Li, P.; Kung, H. T.; Saidaminov, M. I.; Kumacheva, E.; Spiecker, E.; Liao, L.-S.; Voznyy, O.; Lu, Z.-H.; Sargent, E. H., Bipolar-Shell Resurfacing for Blue Leds Based on Strongly Confined Perovskite Quantum Dots. *Nature Nanotechnology* **2020**.

(5) Liu, Y.; Cui, J.; Du, K.; Tian, H.; He, Z.; Zhou, Q.; Yang, Z.; Deng, Y.; Chen, D.; Zuo, X.; Ren, Y.; Wang, L.; Zhu, H.; Zhao, B.; Di, D.; Wang, J.; Friend, R. H.; Jin, Y., Efficient Blue Light-Emitting Diodes Based on Quantum-Confined Bromide Perovskite Nanostructures. *Nature Photonics* **2019,** *13*, 760-764.

(6) Li, Z.; Johnston, A.; Wei, M.; Saidaminov, M. I.; Martins de Pina, J.; Zheng, X.; Liu, J.; Liu, Y.; Bakr, O. M.; Sargent, E. H., Solvent-Solute Coordination Engineering for Efficient Perovskite Luminescent Solar Concentrators. *Joule* **2020,** *4*, 631-643.

(7) Nenon, D. P.; Pressler, K.; Kang, J.; Koscher, B. A.; Olshansky, J. H.; Osowiecki, W. T.; Koc, M. A.; Wang, L.-W.; Alivisatos, A. P., Design Principles for Trap-Free $Cspbx_3$ Nanocrystals: Enumerating and Eliminating Surface Halide Vacancies with Softer Lewis Bases. *Journal of the American Chemical Society* **2018,** *140*, 17760-17772.

(8) ten Brinck, S.; Zaccaria, F.; Infante, I., Defects in Lead Halide Perovskite Nanocrystals: Analogies and (Many) Differences with the Bulk. *ACS Energy Letters* **2019,** *4*, 2739-2747.

(9) Zhang, Y.; Siegler, T. D.; Thomas, C. J.; Abney, M. K.; Shah, T.; De Gorostiza, A.; Greene, R. M.; Korgel, B. A., A "Tips and Tricks" Practical Guide to the Synthesis of Metal Halide Perovskite Nanocrystals. *Chemistry of Materials* **2020,** *32*, 5410-5423.

(10) Zhang, B.; Goldoni, L.; Zito, J.; Dang, Z.; Almeida, G.; Zaccaria, F.; de Wit, J.; Infante, I.; De Trizio, L.; Manna, L., Alkyl Phosphonic Acids Deliver $Cspbbr_3$ Nanocrystals with High Photoluminescence Quantum Yield and Truncated Octahedron Shape. *Chemistry of Materials* **2019,** *31*, 9140-9147.

(11) ten Brinck, S.; Infante, I., Surface Termination, Morphology, and Bright Photoluminescence of Cesium Lead Halide Perovskite Nanocrystals. *ACS Energy Letters* **2016,** *1*, 1266-1272.

(12) Grisorio, R.; Di Clemente, M. E.; Fanizza, E.; Allegretta, I.; Altamura, D.; Striccoli, M.; Terzano, R.; Giannini, C.; Irimia-Vladu, M.; Suranna, G. P., Exploring the Surface Chemistry of Cesium Lead Halide Perovskite Nanocrystals. *Nanoscale* **2019,** *11*, 986-999.

(13) Ravi, V. K.; Santra, P. K.; Joshi, N.; Chugh, J.; Singh, S. K.; Rensmo, H.; Ghosh, P.; Nag, A., Origin of the Substitution Mechanism for the Binding of Organic Ligands on the Surface of $Cspbbr_3$ Perovskite Nanocubes. *The Journal of Physical Chemistry Letters* **2017,** *8*, 4988-4994.

(14) Imran, M.; Ijaz, P.; Goldoni, L.; Maggioni, D.; Petralanda, U.; Prato, M.; Almeida, G.; Infante, I.; Manna, L., Simultaneous Cationic and Anionic Ligand Exchange for Colloidally Stable $Cspbbr_3$ Nanocrystals. *ACS Energy Letters* **2019,** *4*, 819-824.

(15) Krieg, F.; Ochsenbein, S. T.; Yakunin, S.; ten Brinck, S.; Aellen, P.; Süess, A.; Clerc, B.; Guggisberg, D.; Nazarenko, O.; Shynkarenko, Y.; Kumar, S.; Shih, C.-J.; Infante, I.; Kovalenko, M. V., Colloidal $Cspbx_3$ (X = Cl, Br, I) Nanocrystals 2.0: Zwitterionic Capping Ligands for Improved Durability and Stability. *ACS Energy Letters* **2018,** *3*, 641-646.

(16) Rawn, J. D.; Ouellette, R. J., *Organic Chemistry: Structure, Mechanism, Synthesis*. Elsevier Science: 2018.

(17) Gomes, R.; Hassinen, A.; Szczygiel, A.; Zhao, Q.; Vantomme, A.; Martins, J. C.; Hens, Z., Binding of Phosphonic Acids to Cdse Quantum Dots: A Solution Nmr Study. *The Journal of Physical Chemistry Letters* **2011,** *2*, 145-152.

(18) De Roo, J.; Zhou, Z.; Wang, J.; Deblock, L.; Crosby, A. J.; Owen, J. S.; Nonnenmann, S. S., Synthesis of Phosphonic Acid Ligands for Nanocrystal Surface Functionalization and Solution Processed Memristors. *Chemistry of Materials* **2018,** *30*, 8034-8039.

(19) Protesescu, L.; Yakunin, S.; Bodnarchuk, M. I.; Krieg, F.; Caputo, R.; Hendon, C. H.; Yang, R. X.; Walsh, A.; Kovalenko, M. V., Nanocrystals of Cesium Lead Halide Perovskites ($Cspbx_3$, X = Cl, Br, and I): Novel Optoelectronic Materials Showing Bright Emission with Wide Color Gamut. *Nano Letters* **2015,** *15*, 3692-3696.

(20) Butkus, J.; Vashishtha, P.; Chen, K.; Gallaher, J. K.; Prasad, S. K. K.; Metin, D. Z.; Laufersky, G.; Gaston, N.; Halpert, J. E.; Hodgkiss, J. M., The Evolution of Quantum Confinement in Cspbbr3 Perovskite Nanocrystals. *Chemistry of Materials* **2017,** *29*, 3644-3652.

(21) Rossi, D.; Liu, X.; Lee, Y.; Khurana, M.; Puthenpurayil, J.; Kim, K.; Akimov, A. V.; Cheon, J.; Son, D. H., Intense Dark Exciton Emission from Strongly Quantum-Confined Cspbbr3 Nanocrystals. *Nano Letters* **2020**.

(22) Smock, S. R.; Williams, T. J.; Brutchey, R. L., Quantifying the Thermodynamics of Ligand Binding to $Cspbbr_3$ Quantum Dots. *Angewandte Chemie* **2018,** *130*, 11885-11889.

(23) Owen, J. S.; Park, J.; Trudeau, P.-E.; Alivisatos, A. P., Reaction Chemistry and Ligand Exchange at Cadmium−Selenide Nanocrystal Surfaces. *Journal of the American Chemical Society* **2008,** *130*, 12279-12281.

(24) Woo, J. Y.; Lee, S.; Lee, S.; Kim, W. D.; Lee, K.; Kim, K.; An, H. J.; Lee, D. C.; Jeong, S., Air-Stable Pbse Nanocrystals Passivated by Phosphonic Acids. *Journal of the American Chemical Society* **2016,** *138*, 876-883.

(25) Saran, R.; Heuer-Jungemann, A.; Kanaras, A. G.; Curry, R. J., Giant Bandgap Renormalization and Exciton–Phonon Scattering in Perovskite Nanocrystals. *Advanced Optical Materials* **2017,** *5*, 1700231.

(26) Shi, H.; Zhang, X.; Sun, X.; Chen, R.; Zhang, X., Direct and Indirect Recombination and Thermal Kinetics of Excitons in Colloidal All-Inorganic Lead Halide Perovskite Nanocrystals. *The Journal of Physical Chemistry C* **2019,** *123*, 19844-19850.

(27) Sebastian, M.; Peters, J. A.; Stoumpos, C. C.; Im, J.; Kostina, S. S.; Liu, Z.; Kanatzidis, M. G.; Freeman, A. J.; Wessels, B. W., Excitonic Emissions and above-Band-Gap Luminescence in the Single-Crystal Perovskite Semiconductors $Cspbbr_3$ and $Cspbcl_3$. *Physical Review B* **2015,** *92*, 235210.

(28) Cheng, O. H.-C.; Qiao, T.; Sheldon, M.; Son, D. H., Size- and Temperature-Dependent Photoluminescence Spectra of Strongly Confined $Cspbbr_3$ Quantum Dots. *Nanoscale* **2020,** *12*, 13113-13118.

(29) Ramade, J.; Andriambariarijaona, L. M.; Steinmetz, V.; Goubet, N.; Legrand, L.; Barisien, T.; Bernardot, F.; Testelin, C.; Lhuillier, E.; Bramati, A.; Chamarro, M., Exciton-Phonon Coupling in a $Cspbbr_3$ Single Nanocrystal. *Applied Physics Letters* **2018,** *112*, 072104.

(30) Lao, X.; Yang, Z.; Su, Z.; Wang, Z.; Ye, H.; Wang, M.; Yao, X.; Xu, S., Luminescence and Thermal Behaviors of Free and Trapped Excitons in Cesium Lead Halide Perovskite Nanosheets. *Nanoscale* **2018,** *10*, 9949-9956.

(31) Wu, W.; Liu, W.; Wang, Q.; Han, Q.; Yang, Q., Temperature-Dependent Photoluminescence of Pure and Mn-Doped Cspbcl3 Nanocrystals. *Journal of Alloys and Compounds* **2019,** *787*, 165-172.

(32) Becker, M. A.; Vaxenburg, R.; Nedelcu, G.; Sercel, P. C.; Shabaev, A.; Mehl, M. J.; Michopoulos, J. G.; Lambrakos, S. G.; Bernstein, N.; Lyons, J. L.; Stöferle, T.; Mahrt, R. F.; Kovalenko, M. V.; Norris, D. J.; Rainò, G.; Efros, A. L., Bright Triplet Excitons in Caesium Lead Halide Perovskites. *Nature* **2018,** *553*, 189-193.

4.3. The Reactivity of $CsPbBr_3$ Nanocrystals towards acid/base Ligands

ABSTRACT: Both alkyl phosphonate- and oleylphosphonate-capped $CsPbBr_3$ nanocrystal show near unity PLQY emission. Such excellent optical properties not only because of the excellent binding intensity of phosphonate group, but also due to the intrinsic defect-tolerance of lead halide materials. Here, we investigated the defect tolerance behavior quantitatively by striping the surface ligands partially. The stripping happen when adding neutral ligands toward quaternary amine (DDAB) caped $CsPbBr_3$ nanocrystals. Various exogenous acid/base ligands were tested in their neutral form by a combined computational and experimental approach. Our analysis indicates that DDABr-capped nanocrystals are inert towards most ligands, except for carboxylic, phosphonic and sulphonic acids. In agreement with the calculations, our experimental results indicate that the higher is the acidity of the ligands employed in the treatment, the more etching is observed. In details, dodecylbenzene sulfonic acid (pKa=-1.8) is found to etch the nanocrystals causing their complete degradation. On the other hand, oleic and oleylphosphonic acids (pKa 9.9 and 2, respectively) interact with surface bound DDA molecules, causing their displacement as DDABr in various amounts, which can be as high as 40% (achieved with oleylphosphonic acid). Despite the stripping of DDA ligands, the optical properties of the nanocrystals, as well as structure and morphology, remain substantially unaffected, empirically demonstrating the defect tolerance characterizing such materials. Our study provides not only a clear overview on the interaction between perovskite nanocrys-tals and neutral ligands, but also presents for the first time an effective ligand stripping strategy.

INTRODUCTION. Lead halide perovskite nanocrystals (NCs) with the general formula $APbX_3$ ($A=Cs^+$, $CH_3NH_3^+$, $CH(NH_2)_2^+$ and $X=Cl^-$, Br^-, I^-) is a family of band gap tunable semiconductors highly sought for optoelectronic and photonic applications.[1-12] Although this class of materials is often considered to be defect tolerant, a proper surface passivation remains the key to achieve highly efficient and stable emitters.[13-15] Therefore, understanding their surface chemistry, with a pivotal focus on the interplay between NC surface and the ligands shell, is fundamental for their implementation in technological applications.[15-18]

In the family of lead halide perovskites, $CsPbBr_3$ NCs can be prepared with desired size, shape and surface composition (for instance with either CsBr- or $PbBr_2$- terminated surfaces).[6, 19] Their colloidal synthesis typically relies on the use of primary amines and carboxylic acids (i.e. oleylamine and oleic acid) as surfactants, which bind to the surface of the NCs in the form of alkylammonium-Br and Cs-carboxylates, respectively.[20-22] Perovskite NCs bearing such surface passivation are characterized by a poor stability, since their purification, storage or exposure to air easily lead to protonation/deprotonation of carboxylate/alkylammonium species, with their consequent desorption from the surface.[23-24] With the aim of mitigating these problems, several post-synthetic ligand exchange strategies have been developed. These reactions usually consist in the replacement of Z-type ligands (alkylammonium-Br and Cs-carboxylates) with new Z-type ones, such as quaternary ammonium halides or inorganic salts containing pseudo halide anions (SCN^-, BF^{4-}).[25-27] These procedures can lead to a marked improvement of the NCs stability, but they can also trigger drastic structural and compositional transformation of the host NCs if the amount of added species is not well calibrated.[28-30]

While a substantial progress has been made in ligand exchange reactions employing Z-type ligands, a systematic study on the interactions between the surface of halide perovskite NCs and neutral ligands (L-type) is still lacking. For example, it is not known if Z-type ligands can be replaced by L-type ligands, as in the case of "classical" II-VI colloidal systems,[31-32] or if L-type ligands can bind to free sites (i.e. those not occupied by Z-type ligands) on the NCs surface to further enhance their stability, as also indicated in some recent works.[33-34] This is mainly due to the fact that such interactions have to be probed in completely aprotic conditions, which are not easily achieved. In fact, even when the working environment is air- and moisture-free and only aprotic solvents are employed, perovskite NCs are typically covered by ligands that can be involved in rapid proton exchange reactions with added neutral ligands. For example, a protonated (or deprotonated) native ligand such as RNH_3^+ (or $RCOO^-$) may donate (or accept) a proton to (from) a neutral free ligand, becoming itself a neutral species and be displaced from the surface of the NCs.[20, 22, 29]

To circumvent such problems, we have developed here an ad-hoc system to probe the interaction of $CsPbBr_3$ NCs with neutral ligands in a completely aprotic environment. In details, we employed $CsPbBr_3$ NCs coated by didodecyldimethylammonium bromide (DDABr) species only, that is, ligands which cannot lose or acquire protons.[23] Such NCs were then exposed to a series of organic ligands (listed in **Table 1**) with neutral head groups of varying acidity/basicity under strictly anhydrous conditions. We denote these ligands as *exogenous* to distinguish them from those already bound to the starting NCs. More specifically, based on a combination of density functional theory (DFT) calculations and experiments, we tested whether these exogenous ligands can interact with the NCs, promoting either a simple detachment of the native ligands, or more drastic effects such as etching, dissolution or phase transformations. With this combined approach, we demonstrate that, under aprotic conditions, most neutral species tested did not interact with the DDABr capped NCs even when employed in large excess, except for oleic acid (HOA), oleylphosphonic acid (OLPA) and dodecylbenzene sulfonic acid (DBSA). The etching degree of these molecules was found to follow their acidity, as also shown by calculations. Indeed, while DBSA, the strongest acid employed here, led to the complete etching of the NCs, HOA and OLPA were observed to interact as L-type ligands with a fraction of the bound DDA molecules, stripping them from the NCs surface (most likely in the form of DDABr). In particular, the treatment with OLPA was more effective than HOA (as the former is more acidic than the latter) in stripping ligands, leading to the removal of 40% of starting DDA ligands, while preserving the optical properties and colloidal stability of the NCs. To the best of our knowledge, this result not only represents the first empirical evidence of the defect tolerance of $CsPbBr_3$ NCs, but also the first documented case of a controlled ligand stripping approach to halide perovskite NCs. This outcome, in turn, opens new perspectives in the fabrication of devices based on colloidal perovskite NCs, where the amount of insulating ligand species must be minimized, while retaining the optical efficiency and colloidal stability to work with stable inks (especially if the devices are produced by ink jet technologies).

METHODS

Materials Deuterated dimethylsulfoxide (d-DMSO, 99.9 atom. % D), didodecyldimethylammonium bromide (DDABr, 98%), 1-octylamine (99%), dioctylamine (98%), trioctylamine (98%), 1-octanal (99%), dioctyl sulfide (96%), 1-octanoic acid (%), 10-undecenoic acid (98%), diisooctylphosphinic acid (90%), 1-octylphosphonic acid (99%), 1-octanol (99%), 1-octanethiol (98.5%) are purchased from Sigma. Didodecylamine (DDA, 97%), 9-heptadecanone (98%) are purchased from TCI chemicals. Trioctylphosphine (TOP, 97%), trioctylphosphine oxide (99 %, TOPO) are purchased from Strem Chemicals. All chemicals were used without further purification.

Stock solutions Cs-Pb- oleate solution: $Pb(CH_3COO)_2 .3H_20$ (760 mg), Cs_2CO_3 (160 mg) and OA (15.00 mL) are loaded into a 25 mL three-neck flask and degassed on a Schlenk line (90 °C, 3h) to form a solution containing Cs and Pb- oleates and to remove carbonic and acetic acids (by-products). DDABr solution: DDABr (4.43 g) is dissolved in toluene (10.00 mL). Benzoyl bromide solution: benzoyl bromide (1.00 mL) is dissolved in anhydrous toluene (10.00 mL). The Cs-Pb-oleate and the DDABr solutions are kept in air, while the benzoyl bromide is prepared and kept inside a nitrogen filled glovebox.

Synthesis of $CsPbBr_3$ nanocubes (NCs). The synthesis of $CsPbBr_3$ NCs and subsequent ligands exchange reactions are performed following our previously reported methods with some modification.[23, 35] Briefly, the synthesis of starting NCs is performed in air, in a vial (20mL) on a hot plate equipped with a thermocouple and a magnetic stirrer (1600rpm). The Cs-Pb-Oleate stock solution (1.50mL) is loaded into a vial along with the DDA stock solution (1.50mL) and 1-octadecene (9.00mL). The mixture is heated 70 °C at which point the benzoyl bromide stock solution (0.55mL) is injected. After 60 seconds, the reaction vial is cooled by plunging it into a water bath. The crude NC solution (3.00 mL) is then mixed with a toluene solution of DDAB (2 mL, 25 mM) and washed with ethyl acetate (20 mL). The NCs are separated by centrifugation at 6000 rpm, re-dispersed in a toluene solution of DDAB (1 mL, 2 mM), washed a second time with ethyl acetate (6 mL). The NCs are again separated by centrifugation at 6000 rpm, re-dispersed in a toluene solution of DDAB (1 mL, 2 mM), and washed a third time with ethyl acetate (6 mL). Finally, the NCs are once more separated by centrifugation and re-dispersed in neat toluene.

Reaction between organic ligands and DDA capped NCs. All organic ligands and solvent employed was anhydrous or degassed before using. Based on Method S3, the amount of exogenous ligands added was carefully calculated. The mixing process was operated in a glove box filled with N_2, and then the mixture was characterized by NMR without exposing the mixture to air/humidity. After the NMR characterization, the eventual NCs washing was performed by using EtAc to remove the excess of added ligands and the DDA ligands stripped out.

Inductively couple plasma – optical emission spectroscopy (ICP-OES). Same with Chapter 4.1.

Nuclear magnetic resonance. Same with Chapter 4.1.

To quantify the concentration of ligands, we evaporate the solvent from the NC dispersions under nitrogen flow and dissolve the solid residue in deuterated DMSO. We determine the concentration of ligands in the DMSO solution by comparing the integrated intensities of ligands' ^1H signals against that of a reference standard (maleic acid, 10 mM) measured independently following the PULCON (Pulse Length-based Concentration Determinatio) external standard procedure.[42]

Steady-state UV-Vis extinction spectroscopy, steady-state photoluminescence spectroscopy and photoluminescence quantum yields. Same with Chapter 4.1.

Transmission electron microscopy (TEM). Same with Chapter 4.1.

X-ray Photoelectron Spectroscopy (XPS). Same with Chapter 4.1.

Computational Methodology. The $CsPbBr_3$ nanocube models were encased by (100) facets, terminated by a $PbBr_2$ inner shell, which in turn is capped by a CsBr outer shell (**Figure 1a**).[43] This termination is consistent with the AX termination typically found in $CsPbX_3$ NCs and with those synthesized in this work that have A=DDA, Cs and X=Br. Although it is not realistic for the NCs to be completely deprived of organic ligands, for the sake of our computations, describing the outer shell in its fully inorganic form is the only way to promote computational consistency and avoid effects that are difficult to estimate in the calculations. Furthermore, we are considering both CsBr and $PbBr_2$ terminations in this study. The latter has been found in recent experimental works.[33, 44] In addition, in the case of CsBr terminated crystals, the $PbBr_2$ surface is accessible to exogenous ligands if CsBr surface vacancies are present.

Calculations are performed with the CP2K 6.1 package[45] at DFT/PBE level of theory[46] with a double-zeta type basis set (DZVP).[47] Scalar relativistic effects are included in the calculations by means of effective core potentials, while spin-orbit coupling is neglected since its impact on the relaxed structure is negligible and calculations would be prohibitively demanding. Binding free energies of ligands on the surface of nanocrystals are computed as:

$$\Delta G = G_{Complex} - (G_{Core} + G_{Ligand}) \qquad \text{(Eq. 1)}$$

where $G_{Complex}$ is the total free energy of the complex (so, the free energy of the NC functionalized with a single ligand) in its ground state. G_{Core} is the free energy of the core of the NC. G_{Ligand} is the free energy of the isolated ligand, individually optimized. The free energy can be decomposed in terms of enthalpic ΔH and entropic ΔS contributions:

$$\Delta G = \Delta H - T\Delta S \qquad \text{(Eq. 2)}$$

where T is the temperature, which we will always consider at 298.15K. For practical reasons, we can further decompose this expression as:

$$\Delta G_{Bond} = \Delta E_{ele} + \Delta E_{ZPE} - T(\Delta S_{vib} + \Delta S_{rot} + \Delta S_{tr}) \qquad \text{(Eq.3)}$$

where ΔE_{ele} is the electronic energy as obtained directly from the DFT calculations and ΔE_{ZPE} is the zero-point energy correction to the electronic energy. The expression of the entropy is based on the rigid-rotor harmonic oscillator approximation (RRHO)[48-50] that allows to decouple rotational, translational and vibrational contributions from each other. It must be noted that, due to the size of the NC model, no vibrational analysis is performed, so the definition of ground state, as referred to a global minimum of energy, must be more realistically considered as a local minimum of energy of the system. This is not expected to have a negative impact on the qualitative determination of the computed core-ligand bonding free energies, however this neglection entails that there is no change in the vibrational modes from the separated fragments to the super-molecular system. In other words, for all cases studied, the change in enthalpy is approximated as $\Delta H \sim \Delta E_{el}$, an approximation that is grounded also on the fact that ZPE correction is usually within a fraction of kcal/mol.[51] The change in entropy can be regarded as $\Delta S \sim (\Delta S_{\mathrm{rot}} + \Delta S_{\mathrm{tr}})$ and neglecting the vibrational term. This approximation of the entropy employed here is crude and is just meant to describe an upper bound correction to the free energy that tendentially favors separated fragments, if any. In the discussion in the main text, we provide a qualitative explanation of the role of entropy for each of the mechanisms studied. Details on the NC model, its size and stoichiometry, are provided in the main text. Implicit solvent effects are also neglected because the low dielectric constants of commonly employed solvents in the experiment affect very little the energetics of binding.

RESULT AND DISCUSSION

Preparation of the $CsPbBr_3$ model system. Colloidal $CsPbBr_3$ NCs capped with DDABr (**Figure 1a**) were prepared by following a recently published procedure by our group (see the Methods section for additional details).[23] Such NCs are prepared under inert atmosphere and without protic solvents to guarantee a completely proton-free system. These NCs will set the reference for all our surface treatments with neutral ligands. As shown in **Figure 1b**, the NCs have a cubic shape and are nearly monodisperse in size, with an average edge length of 5.9 ± 0.7 nm (**Figure S1** of the Supporting Information, SI). Their absorption and photo-luminescence (PL) spectra are reported in **Figure 1c** and their PL quantum yield (QY) is around 90±10%. As shown in **Figure 1d**, the ^1H nuclear magnetic resonance (NMR) spectrum of such NCs in toluene-d_8 features two broad signals in the 4.1-3.5 ppm range belonging to surface-bound DDA molecules.[35] The chemical shift of these two peaks, at lower fields compared to those of free DDABr molecules (characterized by two sharp peaks at 3.9 ppm and 3.7 ppm, see **Figure 1d**), indicates that the electron density of the bound species around the ^1H nuclei of DDA is lowered by the interaction with the surface of the NCs.[36] Signal broadening is due to ligands interacting with the NCs surface, which causes a slower mobility in solution i.e. with longest correlation times (τ_c), compared to correspondent free ligands.[36]

The composition of the inorganic core of the NCs was measured via energy dispersive X-ray spectroscopy (EDS) in the scanning electron microscope (SEM). On the other hand, the quantification of the bound ligand species was assessed by NMR analysis after dissolving the NCs in deuterated dimethyl sulfoxide (DMSO, see the experimental section for details).[37] The combination of these analyses indicated that the NCs are terminated by a $PbBr_2$ inner shell and are capped by a hybrid AX outer shell (A=DDA, Cs; X=Br, oleate), as depicted in **Figure 1a** (see the **Method S1** and **Table S1** for further details). Assuming that the core and inner shell regions are pristine, by following the [core](inner-shell){outer-shell} nomenclature proposed by Bodnarchuk *et al.*[24] the composition of the NCs can be conveniently written as:

$[CsPbBr_3](PbBr_2)\{Cs_{0.48}DDA_{0.42}Br_{0.87}Oleate_{0.03}(o)_{0.10}\}$

In the formula above, the AX outer layer is composed of two types of A cations (Cs^+ and DDA^+) and two types of X anions (Br^- and $Oleate^-$), with the addition of AX surface vacancies defined as (o). This overall composition corresponds to a surface (outer shell) coverage (occupation) of up to 90%, in line with the high photoluminescence quantum yield (PLQY) observed from these NCs (~100%). Although there is a residual fraction of oleate ligands bound to the surface of the NCs, this fraction is essentially negligible, and henceforth we will refer to these NCs as DDABr-capped NCs.

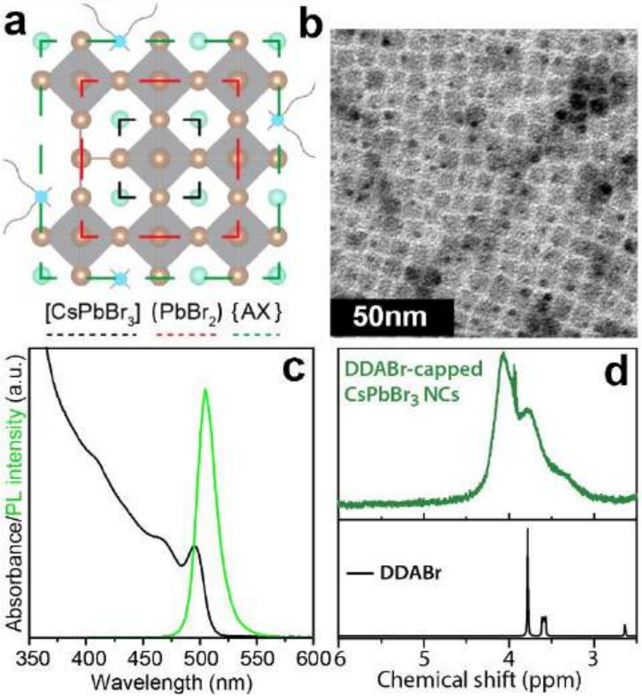

Figure 1. (a) Skeleton of a DDABr-capped $CsPbBr_3$ NC. (b) TEM images, (c) absorption and PL spectra, and (d) NMR spectrum of DDABr-capped $CsPbBr_3$ NCs in toluene-d_8.

Surface Reactivity of $CsPbBr_3$ nanocrystals from a computational perspective. Possible reactions between NCs and the exogenous organic ligands listed in **Table 1** include simple adsorption, as well as chemisorption and etching (that may lead to phase transformations). Here, by chemisorption we mean the process by which an initially neutral exogenous ligand becomes charged (through loss of one of its protons) and binds to the surface of the NCs as a charged species. For simplicity, in our calculations we consider all the A cations to be Cs only, unless otherwise stated. Although the complete absence of DDA ligands on the surface of NCs is not realistic, our computations describe the outer shell in its fully inorganic form as the only way to promote computational consistency and avoid effects, such ligand-ligand interactions, that are difficult to estimate in the calculations. Additionally, for simplicity, we have considered ligands with a short (octyl) ligand chain also for the description of oleic acid and oleylphosphonic acid, that is, octanoic acid (Oca) and octylphosphonic acid (OcPa).

All the considered surface reactions are schematically represented in **Figure 2**, whereas the correspondent chemical equilibria are described in more detail in the Supporting Information (**Method S2**). We note that favorable energetics for the removal of both ABr and $PbBr_2$ units may be indicative of NC dissolution, while the preferential removal of one unit in lieu of another could explain phase transformations, common in the Cs-Pb-Br system, and well-known in the field of halide perovskites.[38] The energetics of the surface reactions is computed for all ligands listed in **Table 1** using a 3 nm $CsPbBr_3$ NC and employing the equations defined in the methodology section. **Adsorption.** *Direct Ligand Absorption on {AX} and ($PbBr_2$) shells*. By adding exogenous neutral ligands to a colloidal suspension of NCs coated with native ligands, we can expect that their headgroups interact with the NC surface by attacking available surface binding sites, either on the available A^+ or Br^- ions on the outer shell, or on Pb^{2+} and Br^- on the inner shell (i.e. onto vacant sites). The binding of neutral protic ligands usually involves hydrogen bonding between the proton(s) located on the protic ligand's anchoring group and the Br anions, with the ligand's headgroup pointing towards the positive A or Pb sites of the outer and inner shells respectively. The binding of aprotic (basic) ligands occurs through the interaction of the ligand's headgroup directly on the A or Pb site. Calculated adsorption enthalpies are plotted in **Figure 3a**. Sketches of these binding features are displayed in **Figure 3b-e**. These results show that adsorption is exothermic for all ligands considered, and that adsorption onto the $PbBr_2$ surface (~10-35 kcal/mol) is generally more favorable than onto the CsBr surface (~2-15 kcal/mol). The binding energies of protic ligands roughly follows the same trend of their pKa, with more acidic ligands being more strongly bound to the surface. An except exception is octylamine (OcN) which, despite high pK_a values, interacts well with the CsBr surface due to two hydrogen bonds and with the N atom pointing favorably towards a Cs^+ ion at the surface (**Figure 3d**).

However, the adsorption energies computed above account only for binding enthalpies. The addition of an entropic contribution involves the loss of translational and rotational entropy. This in turn would entail, in principle, a significant energy penalty, only partly counterbalanced by an increase in the vibrational entropy (see for more details the computational methodology section). Ultimately, we estimate that the total energy penalty due to entropic contribution is in the interval 10-15 kcal/mol. Based on these qualitative observations and looking again at **Figure 3a**, we can expect that for ligands binding to the {AX} outer shell, the entropic penalty renders the free energies of adsorption slightly endergonic, whereas for the ($PbBr_2$) inner shell we can expect that some ligands could still bind to the NC surface. These observations are in line with a recent report showing that the addition of stoichiometric amounts of phosphonic acid (namely oleylphosphonic acid) to a dispersion of $CsPbBr_3$ NCs having PbX_2 terminated facets results in the surface binding of the acid in its neutral state.[33]

Table 1 – Neutral ligands considered and relative abbreviation of their names. Among parentheses approximate values for their pKa.

Protic ligands (pKa)	Abbreviation
HBr (-9)	HBr
Dodecylbenzenesulfonic acid (-1.8)	DBSa
Oleylphosphonic acid (2)	OLPA
Dioctylphosphinic acid (2)	DOPa
Oleic acid (9.9)	HOA
Octylthiol (10)	OcS
Octanol (16)	OcOH
Octylamine (40)	OcN
Dioctylamine (40)	DON

Aprotic ligands	Abbreviation
Dioctylsulfide	DOS
Trioctylamine	TON
Trioctylphosphine	TOP
Trioctylphosphine oxide	TOPO
Octanal	OcH
Dimethylsulphoxide	DMSO

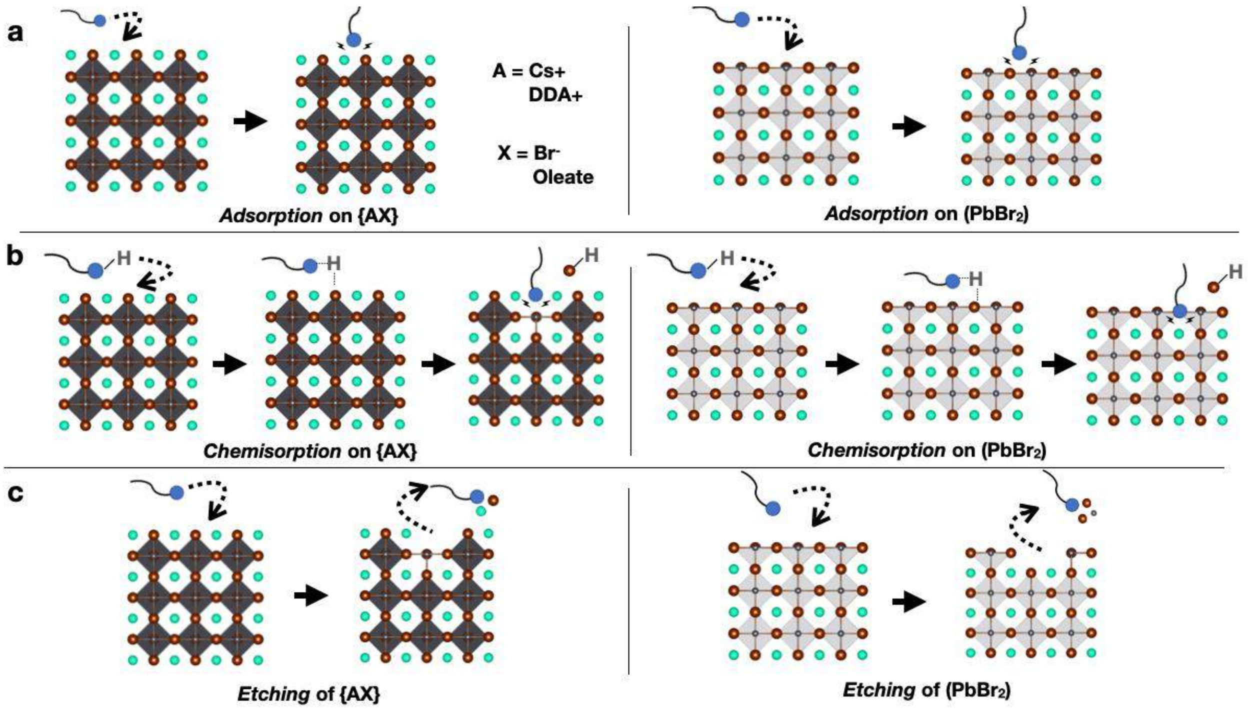

Figure 2. (a) Representation of direct adsorption of a neutral ligand on the outer {AX} or inner $PbBr_2$ shell. (b) Proton Induced Ligand Exchange. i..e. chemisorption, describes the event of protonation of the {AX} surface by a protic ligand: the incoming ligand passivates the {AX} surface and causes the removal of an anion that leaves the surface in its protonated form. On the right, same description for the ($PbBr_2$) shell. (c) The interaction of a neutral ligand with the outer or inner shell culminates with the etching of an ion pair or a Z-type ligand.

Chemisorption. *Proton Induced Ligand Exchange.* The second process we investigated is the proton induced ligand exchange. Since we have chosen the DDA^+ ligand to passivate cation sites, the only process eventually involving a proton transfer can occur when a ***protic*** ligand (HL) donates its proton to a surface anion (Br^-), promoting the desorption of HBr and the adsorption of L^- (equation 4). The computed enthalpies of chemisorption for protic ligands onto $CsPbBr_3$ NCs are shown in **Figure 4**. The trend follows roughly that of pKa, with stronger acids (lower pKa values) yielding lower enthalpy values. Anyways, positive enthalpy changes for all the organic ligands indicate their inability to displace Br- ions in the form of HBr, since the pKa of such ligands is higher than that of HBr. Our results also show that the enthalpic cost of chemisorption is generally slightly lower on $PbBr_2$ surfaces. Here we assume that the enthalpic contribution is dominant, with only a small contribution from the entropy, as the number of species is the same at both sides of the chemisorption reaction.

Although not strictly related to our reference NC model, we also considered the protonation process involving functionalized surfaces: e.g. protonation of the residual carboxylate moieties (e.g. oleate) bound to the surface of the NCs. This determines the release of the corresponding carboxylic acid, allowing for the insertion of the exogenous ligand, as anion, to the surface. In our calculations, octanoate (emulating the oleate), as the conjugated base of an acid with a pKa of ~5, can be displaced by acids stronger than the octanoic such as phosphonic, sulphonic and halic acids (see **Figure S2**). Very weak acids, such as amines, will not trigger any ligand exchange. It is remarkable that the trend for the ligand exchange follows closely the trend in pKa, although the medium in which these chemical processes is an organic solvent with a low dielectric constant. The key point is that, in an apolar solvent, the NC itself accepts protons and stabilizes the conjugated bases resulting from the dissociation of protic ligands, thus effectively mimicking the behavior of an amphoteric solvent.

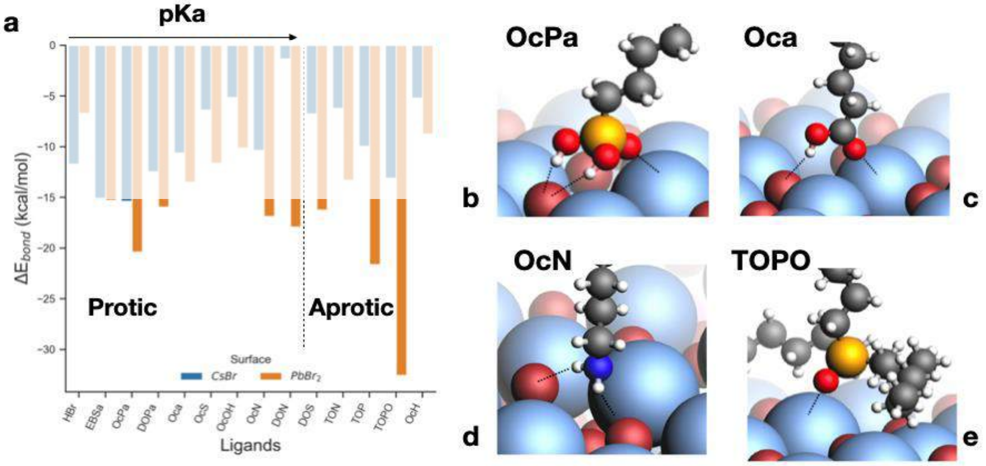

Figure 3. (a) Adsorption energy of neutral ligands on a bare CsBr (blue) or $PbBr_2$ (orange) NC surface. Values, expressed in kcal/mol, refer to the interaction of an isolated ligand on the outer or inner shell of the NC. Values outside the shaded regions indicate the possibility of overcoming the entropic energy penalty. This means that only ligands in the non-shaded area effectively bind to the surface. (b) Sketches of the binding features for octyl phosphonic acid (OcPa), octanoic acid (Oca), octylamine (OcN) and trioctylphophine oxide (TOPO). OcPa and Oca are representative of oleyl phosphonic acid (OLPA) and oleic acid (HOA).

Etching. *Ligand Induced Displacement of {ABr} and ($PbBr_2$) shells.* The last process we discuss is the ligand-induced displacement of ion-pairs from the NC surface: this resembles the Z-type ligand-induced displacement processes occurring in II-VI, III-V and IV-VI NCs.[31-32, 39] First, we note that the simple desorption, i.e. not assisted by ligands, of a CsBr ion pair from the NC surface is highly endothermic, requiring ca. 52 kcal/mol (blue bar in **Figure 5**) based on our calculations. In other words, a surface CsBr unit is strongly bound to the NC (even when considering 10-15 kcal/mol of entropic penalties that favors the displacement). Other AX ion pairs, representative of most used $CsPbBr_3$ passivating ligand pairs, such as DDABr, cesium octanoate, ammonium bromide, ammonium octanoate are also found to be strongly bound to the surface, although slightly less than CsBr, with energies of the same order of magnitude (> 44 kcal/mol, see **Figure S3**).

In the case of ligand induced displacement reactions (see **Method S2**), we expect entropic penalties to be small, and $\Delta G \sim \Delta H$. The enthalpies of these reactions are plotted in **Figure 5**. It is worth noting that the enthalpy of displacement decreases with increasing number of ligands per displaced moiety (CsBr or $PbBr_2$ units). In fact, at 1 ligand per displaced moiety the calculated enthalpy changes are endothermic for most ligands, but they become exothermic as the number of ligands is increased (up to 3 ligands per moiety). This effect is particularly strong for strong acids, with reductions of up to 30 kcal/mol being observed, while for basic ligands the reductions are in the 5-15 kcal/mol region. Furthermore, we observe that displacing a $PbBr_2$ unit is energetically more favorable than displacing a CsBr unit. The non-ligand-assisted displacement of a $PbBr_2$ unit costs ~28kcal/mol, which is about half of the energy required to remove CsBr (~52kcal/mol). Displacing a $PbBr_2$ unit with ligands is similarly more favorable. Among all ligands, phosphinic and phosphonic acids exhibit the most favorable energetics for displacing both $PbBr_2$ and CsBr units, suggesting that these ligands may undermine the integrity of the NCs. Basic ligands, on the other hand, appear unable to detach CsBr units, although some of them can extract $PbBr_2$ units (trioctylphosphine and trioctylphosphine oxide in particular). These findings apparently do not seem to be in line with the phase transformations observed in Cs-Pb-Br NC systems, namely the $CsPbBr_3 \rightarrow Cs_4PbBr_6$ transformation, which is triggered by treating the NC with primary amines.[30, 40] This process is instead induced by the protonation of the added primary amine operated by moisture/native ligands, as it will be discussed later in this work (see also **Figure S4**).

Finally, we also compared the ligand-induced displacement of other common {AX} pairs such as DDABr, DDA-Octanoate and Cs-octanoate (**Figure S3**). Also in this case, the energetics of displacement resembles the trends found in the CsBr case, further confirming that the enthalpies of etching are somehow independent on the native ligands capping the {AX} outer shell (i.e. independently of their inorganic or fully organic nature).

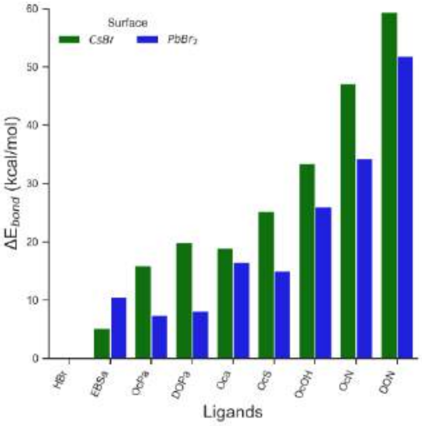

Figure 4. Energies related to events of proton-induced ligand exchange on both {AX} and ($PbBr_2$) surfaces. The graph shows how protic ligands are unable to displace bromide ions as HBr because this leaving group is the strongest acid of the series.

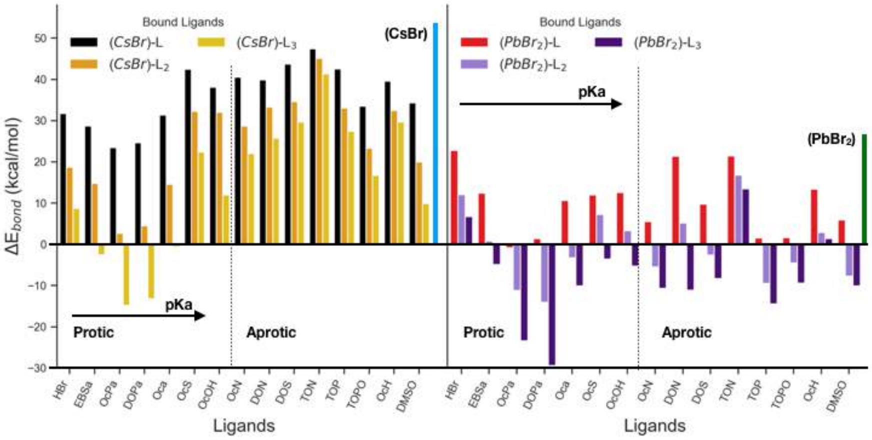

Figure 5. Ligand induced displacement of CsBr ion pairs and $PbBr_2$, after interaction of neutral ligands with bare surfaces. The presence of any of the investigated ligands lowers the energy required to displace CsBr and $PbBr_2$ shells. Excess ligand can further stabilize the leaving moieties: this is particularly relevant when excess ligand interacts with ($PbBr_2$) shells, where almost in all cases, theoretically, the presence of 3 ligands per $PbBr_2$ would strongly favor the displacement of the latter

Experimental Results

We tested the reactivity of DDABr capped NCs towards most of the neutral ligands listed in **Table 1** except for HBr, DMSO and octanol, as these are known to dissolve perovskite NCs. Moreover, we selected OLPA and HOA as representative of carboxylic and phosphonic acids as they are liquid and easier to handle with respect to octanoic acid and octylphosphonic acid (the latter is solid and poorly soluble in toluene). To do so, NC dispersions in toluene ([NCs] = ~16 µM) were treated with different amounts of exogenous ligands, ranging from 1 to 10 equivalents with respect to surface Br sites (considering 726 surface Br per NC, the concentration of surface sites in solution was calculated to be 7.8 mM, see Method S3 and Table S1). To avoid any moisture contamination, which could lead to deprotonation/protonation of the neutral ligands employed, all the operations were carried out in a N_2 filled glove box by using anhydrous solvents and ligands. The resulting products were thoroughly characterized optically, structurally, and chemically (see **Scheme 1** and the experimental section).

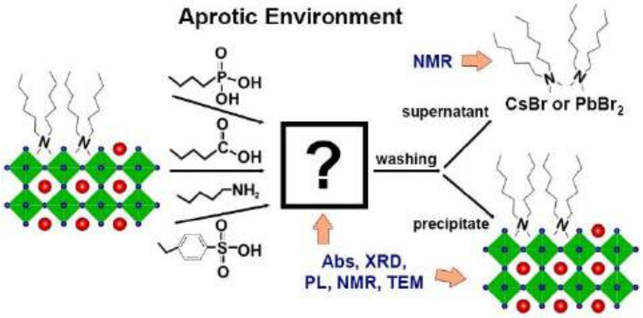

Scheme 1. Experimental procedure and characterization of the products

Our results show that DDABr-capped $CsPbBr_3$ NCs are inert towards most of ligands tested in this work, as shown in **Figures S5-6**. On the other hand, OLPA, HOA and DBSA were observed to interact with the NCs. The exposure of the NCs to various concentrations of OLPA (1, 3 or 10 equivalents) did not yield any significant difference in their optical properties (**Figure 6a**). Furthermore, XRD and TEM analyses of OLPA treated NCs show that their structural and morphological features remained preserved (**Figure 6b** and **S7**). To reveal if OLPA had any interaction with the surface of the NCs, we performed liquid state NMR analyses. The ^1H and Heteronuclear Single Quantum Coherence (HSQC) NMR spectra (for indirect ^{13}C detection) of the NCs exposed to OLPA revealed the emergence of two new distinct NMR peaks at 3.31 (with ^{13}C at 51.9) and 3.11 (with ^{13}C at 64.6) ppm (**Figure 6d-f, h-g**), whose intensity was observed to increase with the amount of OLPA added. The HSQC experiment, in the edited version, enabled to diphase the CH/CH_3 with respect to CH_2 and allowed to ascribe such new signals to CH_3 and CH_2 groups in α to nitrogen group of DDA, respectively (**Figure 6h**). Notably, such new NMR peaks are shielded (i.e. at lower ppm) compared to those of surface bound DDA and de-shielded (i.e. at higher ppm) with respect to those of free DDABr molecules (**Figure 6d-g**). Moreover, such new NMR peaks are broader (FWHM= 24 Hz for peak at 3.31 ppm; FWHM=32 Hz for peak at 3.11 ppm) with respect to those of free DDABr (FWHM = 6 Hz) and sharper compared to those of bound DDA (FWHM = 160 Hz). These results overall indicate that part of DDA molecules is interacting with both the NCs surface and with electron donating species. Such donating species are believed to be neutral OLPA only (acting as an L-type ligand), as also indicated by a control experiment in which the addition of OLPA to free DDABr molecules is observed to shift the diagnostic DDABr signals to lower ppm (**Figure 6g**).

To further elucidate the DDA-NCs surface interaction, we performed 2D Nuclear Overhauser Effect Spectroscopy (^1H–^1H NOESY) at 40°C[23] (see Figure 6i and S8). The NOESY evidences positive (blue) NOE cross peaks for OLPA signals (double bound region at 5.47 ppm) and negative (red) cross peaks for both the doublets of DDA (i.e. broad signals at 3.96 and 3.74 ppm and the new peaks at 3.31 end 3.11 ppm) (**Figure 6i**). These results indicate that OLPA molecules are free, while DDA species are in active dynamic binding with the surface of the NCs. Based on our NMR results, we conclude that OLPA molecules can interact with part of the DDA molecules present on the NCs surface. Following this assumption, the integration of the NMR peaks in the 4.1-3.2 ppm range indicates that 1/3 of DDA ligands interacts with OLPA when working with 3 or 10 eq of OLPA.

To better understand the effects of the OLPA-DDA interaction, we cleaned the 3eq OLPA-treated NCs via the addition of ethyl acetate followed by centrifugation, and we performed the NMR analysis of both the supernatant and the precipitate (i.e. washed NCs) re-dispersed in toluene-d_8 (**Scheme 1**). The NMR spectrum of the washed NCs indicated the absence of the peaks at 3.4 and 3.2 ppm in the washed NCs (Figure 6c), which were instead detected in the supernatant (Figure S9). The ^{31}P NMR analysis of the washed NCs also indicates the absence of surface bound OLPA molecules, in agreement with the NOESY results (**Figure S10 and 6i**). Eventually, quantitative NMR analysis, carried out on solutions obtained by dissolving the washed NCs in DMSO-d,[37] yielded a density of DDA ligands of 174 ligands/NC. Our NMR analysis, therefore, revealed that the treatment of DDABr capped NCs with OLPA (and subsequent washing) leads to the removal of ~40% of DDA surface ligands (the starting density was 291 ligands/NC), which corresponds to a reduction of DDA surface coverage from 42% to 25%. We would like to stress here that the density of DDA surface molecules cannot be reduced by simply further cleaning the starting DDABr capped NCs with ethyl acetate, therefore the stripping observed here is ascribed to the treatment with OLPA. Moreover, as shown in **Table S2**, the XPS analysis further supported that the treatment with OLPA did not lead to any etching of the core as the Cs/Pb/Br elemental ratio in the NCs remained unaltered. Notably, even after removing such a high fraction of DDA molecules, the optical properties of $CsPbBr_3$ NCs were not altered, experimentally proving the defect tolerance of such systems.

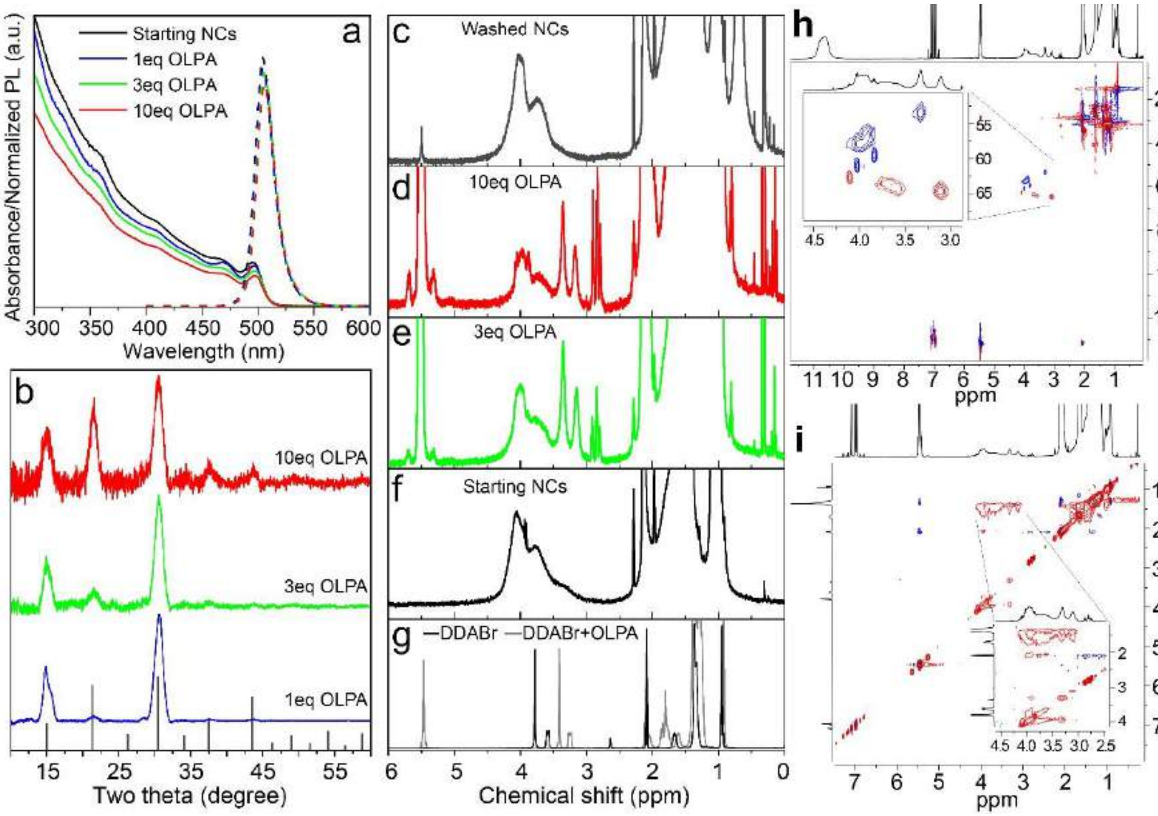

Figure 6. (a) Optical properties and (b) XRD patterns of DDABr-capped $CsPbBr_3$ NCs treated with 1, 3 or 10eq of OLPA. NMR spectra of (f) DDABr-capped $CsPbBr_3$, (d-e) OLPA treated and (c) washed (after the treatment with 3eq of OLPA) NCs. (g) NMR spectra of free DDABr molecules and DDABr with the addition of OLPA molecules. (h) Heteronuclear Single Quantum Coherence spectroscopy (HSQC) edited with the selection of CH_2 (red) and CH/CH_3 (blue) of DDABr-capped NCs treated with 3eq of OLPA in toluene-d_8. The extra peak at 3.31 ppm (with the ^{13}C at 53 ppm) was identified as CH_3 (blue) whereas the extra peak at 3.11 ppm (with the ^{13}C at 64.6 ppm) was associated to a CH_2 (red). The ^{13}C resonances are typical of CH_3 and CH_2 on nitrogen respectively. (i) 2D ^1H-^1H NOESY experiment performed at 40°C of DDABr-capped NCs treated with 3eq of OLPA in toluene-d_8. OLPA returns positive NOE (blue) cross peaks, characteristic of species with a short correlation times (τ_c), whereas DDABr broad signals at 3.96 and 3.74 ppm and the new extra peaks at 3.31 end 3.11 ppm exhibit negative (red) cross peaks, typical of species with long correlation times (τ_c), indicating that those species are dynamically interacting with the surface of the NCs.

The treatment of the NCs with HOA led to similar results: overall, the optical properties, structure and morphology of the final NCs were not affected by the addition of 1, 3 or even 10 eq of HOA (see **Figure 7a,b** and **Figure S11**). Also in this case, the ^{1}H NMR analysis indicated the emergence of a relatively broad NMR signal at ~3.4 ppm, whose intensity increased together with the amount of added HOA (**Figure 7c and S12**), and which disappeared upon washing the NCs with EtAc (**Figure 7c**). In analogy with the OLPA case, these results suggest that HOA can bind and strip a fraction of DDA molecules from the surface of the NCs. From a rough and qualitative analysis of the NMR spectra, it is possible to ascertain that the addition of 3eq of HOA leads to the stripping of only a minimal quantity (~2%) of surface DDA ligands (**Figure 7c**). On the other hand, DBSA was observed to interact with the NCs in a very different way. As shown in Figure S13, 1 eq of DBSA quenched the PL emission of the NCs and led to their precipitation. The XRD analysis evidences the absence of any Cs-Pb-Br phase, indicating the dissolution of the CsPbBr3 NCs (Figure S13)**.** Hence DBSA, even in low amounts, etches the NCs and cause its dissolution and precipitation.

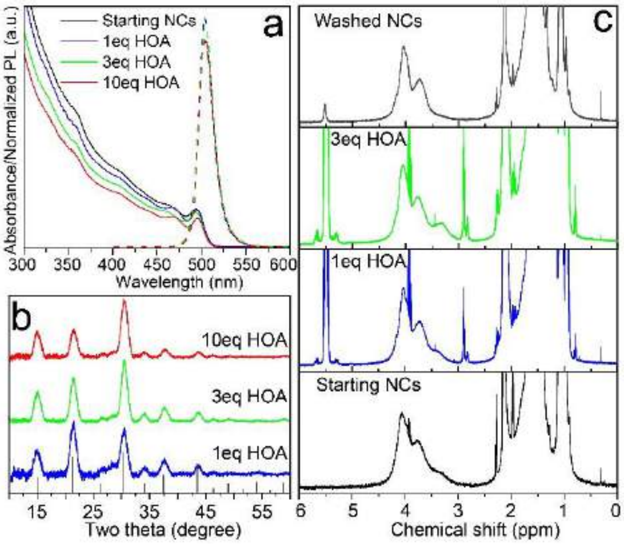

Figure 7. (a) Optical properties and (b) XRD patterns of DDABr capped CsPbBr$_3$ NCs treated with 1, 3 or 10eq of HOA. (c) NMR spectra of DDABr capped CsPbBr$_3$, HOA treated and washed (after the treatment with 3eq of HOA) NCs.

Overall, in agreement with the calculations, these results suggest that the higher is the acidity of the ligands employed in the treatment the higher is the etching degree: while HOA (pKa = 9.9) can strip a minor fraction of DDABr, OLPA (pKa = 2) is able to remove up to 40% of surface DDABr. The acidity of DBSA (pKa = -1.8), in turn, is possibly so high that leads to a severe etching of the NCs.

Conclusions

Based on the computational and experimental data of this work we can draw some conclusions on the reactivity of exogenous acid/base ligands towards CsPbBr$_3$ NCs:

i) The process of ligand adsorption, i.e. a ligand binding the NC surface, although enthalpically favored, has an important entropic penalty. From our calculations, adsorption of L-type ligands is mostly prevented on {ABr} surfaces, but could take place on (PbBr$_2$) ones, as also observed in recent experiments.[33]

ii) In the absence of native ligands that can accept protons, as in the case of DDABr-capped NCs, the chemisorption is highly unlikely as it is always energetically unfavorable to extract the conjugate base of a strong acid. In other words, organic acids are not able to bind {ABr} or (PbBr$_2$) surfaces via the displacement of Br$^-$ ions (in the form of HBr).

iii) The NC integrity can be undermined by etching which occurs through the displacement of ABr or PbBr$_2$ ion pairs operated by exogenous ligands. The etching process appears to be thermodynamically less costly for PbBr$_2$ rather than ABr surfaces. In either case, the stronger the acid the higher is the etching degree. Indeed, experimentally we observed that oleic acid (pKa = 9.9) can strip a minor fraction of DDABr, oleylphosphonic acid (pKa=2) can lead to the removal of up to 40% of DDA(Br), and dodecylbenzenesulfonic acid (pKa=-1.8) completely etches the NCs. Despite the loss of ligand coverage, the emission characteristics of the NC remain unaltered, demonstrating the high surface tolerance of these materials. This ligand stripping procedure also paves the way to control the surface ligand coverage of perovskite NCs, and, thus, to their use in optoelectronic devices, such as light emitting diodes (where electrical resistance of NCs film should be minimized via ligands removal, while retaining high PL emission).

iv) Basic ligands such as dioctylamine, trioctylphosphine and trioctylphosphine oxide, which were computationally expected to displace PbBr$_2$ units from the NCs, were experimentally observed to be inert even at high concentrations. In these cases, steric effects, not included in the calculations, are likely hindering any interaction between the ligands and the NCs. Of relevance is the case of octylamine which, analogous to primary alkyl amines, has been widely reported to drive CsPbBr$_3$→ Cs$_4$PbBr$_6$ (also called 3D→0D) NCs transformation. Our experimental data clearly show that neutral octylamine is not able to interact with the NCs when the system is completely aprotic (**Figure S14**). Interestingly, the same experiment if performed in a completely anydhrous conditions but employing a non-degassed octylamine led to the 3D→0D transformation (**Figure S4**). Our control experiments, thus, indicate that the presence of protons/moisture, profoundly influences the ligands-NCs interaction when dealing with halide perovskite NCs.

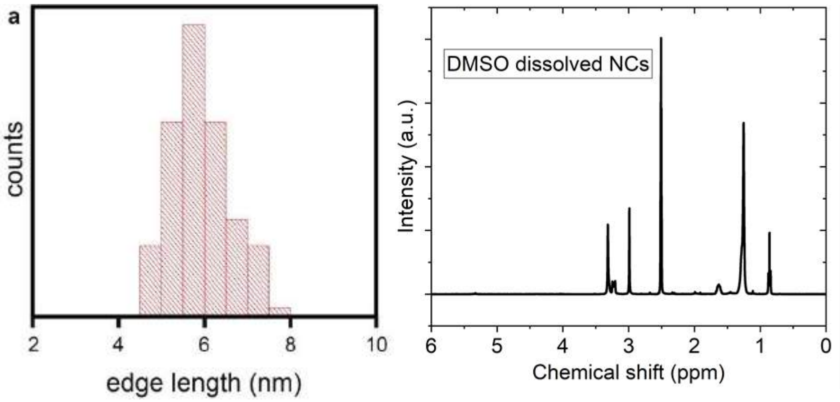

Figure S1. a) Size histogram of DDABr-capped nanocrystals obtained via analysis of TEM images; b) 1H-NMR of DMSO dissolved DDAB caped NCs.

Method S1. Determination of the NC stoichiometry, concentration and absorption coefficient

According to the composition obtained from EDS ($Cs_{1.0}Pb_{1.0}Br_{2.9}$), the DDA-capped $CsPbBr_3$ NCs appear to be terminated by a $PbBr_2$ inner shell and (partially) capped by a hybrid AX outer shell (A=Cs, DDA; X=Br, oleate). We assume that such nanocubes can be approximated to a charge balanced CsBr-capped $CsPbBr_3$ NC with an edge length of 6.4 nm containing 1694 Cs atoms, 1331 Pb atoms and 4356 Br atoms if fully capped (see Table S1).

Starting from this model, we determined the concentration of NCs in solution by measuring the concentration of Pb ions via inductively coupled plasma - optical emission spectrometry (ICP-OES), and dividing it for 1331 (Pb atoms per NC). Eventually, we measured the concentration of ligands (DDA, oleate) in the dispersions using quantitative NMR: we dissolved the NCs in DMSO and performed a quantitative NMR analysis, as shown in Figure S1b, which yielded a surface concentration of 291 DDA^+ molecules per NC (and 21 oleate species per NC).

These analyses allowed us to reveal the composition of DDABr-capped $CsPbBr_3$ NCs. Results are summarized in Table S1. Assuming that all ligands quantified by NMR are bound (indeed we did not find ^1H peaks ascribable to free OA or DDABr), the outer shell result to have a composition of $(Cs_{0.48}DDA_{0.42})(Br_{0.32}Oleate_{0.03})$. The evident Br-deficiency is most likely due to Br desorption under SEM-EDS analysis conditions. In order to maintain charge balance the actual Br content in the outer shell is expected to be around 87%. We therefore describe the NCs as:

$[CsPbBr_3](PbBr_2)\{(Cs_{0.48}DDA_{0.42})(Br_{0.87}Oleate_{0.03})(o)_{0.10}\}$

In the formula above, we define (o) as AX surface vacancies. This overall composition corresponds to a surface (outer shell) coverage (occupation) of 90%.

Table S1 – Composition of the DDA-capped $CsPbBr_3$ nanocrystals assuming that the total number of sites is that of a CsBr capped $CsPbBr_3$ NCs with an edge length of 6.4 nm

Site	Specie	Number of sites			
		Total	Core	Inner-shell	Outer shell
A	**total**	1694	1000	-	694
	Cs	1331	1000	-	331
	DDA	290	-	-	290
	Vac.	73	-	-	73
M	**total**	1331	729	602	-
	Pb	1331	729	602	-

X	**total**	4356	2430	1200	726
	Br	3860	2430	1200	230
	Oleate	20	-	-	20
	Vac.	476	-	-	476

Method S2. Surface Reactivity

Following the nomenclature introduced in the main text of the manuscript, the *adsorption* of a ligand L onto the ABr outer shell of the NCs (Figure 2a, left side) can be written as:

$[CsPbBr_3](PbBr_2)_k\{ABr\}_m + L \rightarrow [CsPbBr_3](PbBr_2)_k\{ABr\}_{m-1}\{ABr\text{-}L\}$ **(Eq. 1)**

where the added ligand will passivate a single {ABr} surface site. Accordingly, considering a fully de-capped outer-shell, the adsorption on the $PbBr_2$ shell can be written as (Figure 2a, right side):

$[CsPbBr_3](PbBr_2)_k + L \rightarrow [CsPbBr_3](PbBr_2)_{k-1}(PbBr_2\text{-}L)$ **(Eq.2)**

Protic ligands (HL) may also *chemisorb* onto the NCs' surface by donating their protons to surface anions (Figure 2b), and therefore chemisorption may lead only to the formation of HBr. If this process occurs on an ABr surface, it can be written as

$[CsPbBr_3](PbBr_2)_k\{ABr\}_m + HL \rightarrow [CsPbBr_3](PbBr_2)_k\{ABr\}_{m-1}\{ABr\text{-}HL\} \rightarrow [CsPbBr_3](PbBr_2)_k\{ABr\}_{m-1}\{AL\} + HBr$ **(Eq. 3)**

If instead it occurs on a $PbBr_2$ surface, it can be written as

$[CsPbBr_3](PbBr_2)_k + HL \rightarrow [CsPbBr_3](PbBr_{2k-1}(PbBr_2\text{-}HL) \rightarrow [CsPbBr_3](PbBr_2)_{k-1}(PbBr_2\text{-}L) + HBr$ **(Eq. 4)**

Finally, we also consider a more complex *etching* reaction in which the ligands remove portions of the original NCs. In particular we consider the removal of ABr or $PbBr_2$ units from the NCs (Figure 2c):[15]

$[CsPbBr_3](PbBr_2)_k\{ABr\}_m + nL \rightarrow [CsPbBr_3](PbBr_2)_k\{ABr\}_{m-1}\{o\} + AX\text{-}L_n$ **(Eq. 5)**

$[CsPbBr_3](PbBr_2)_k + nL \rightarrow [CsPbBr_3](PbBr_2)_{k-1}(o) + PbBr_2\text{-}L_n$ **(Eq. 6)**

where we introduced the notation {o} and (o) to indicate a surface vacancy at the outer and/or inner shells, respectively.

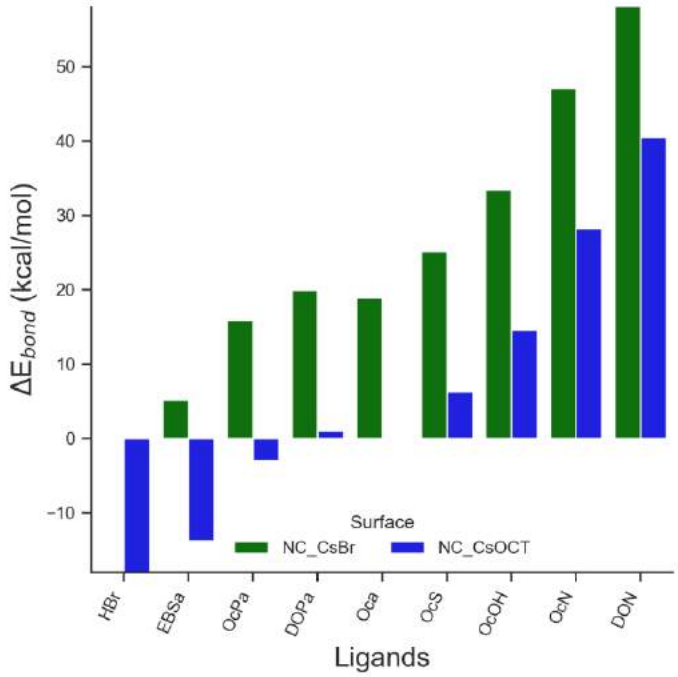

Figure S2. Energetics of proton-induced ligand exchange of bromide ions (green bars) and octanoate (blue bars) with a series of ligands of various acidity. Unlike bromide, octanoate can be displaced by acids stronger than the octanoic such as halic, sulphonic and phosphonic acids (negative values of blue bars).

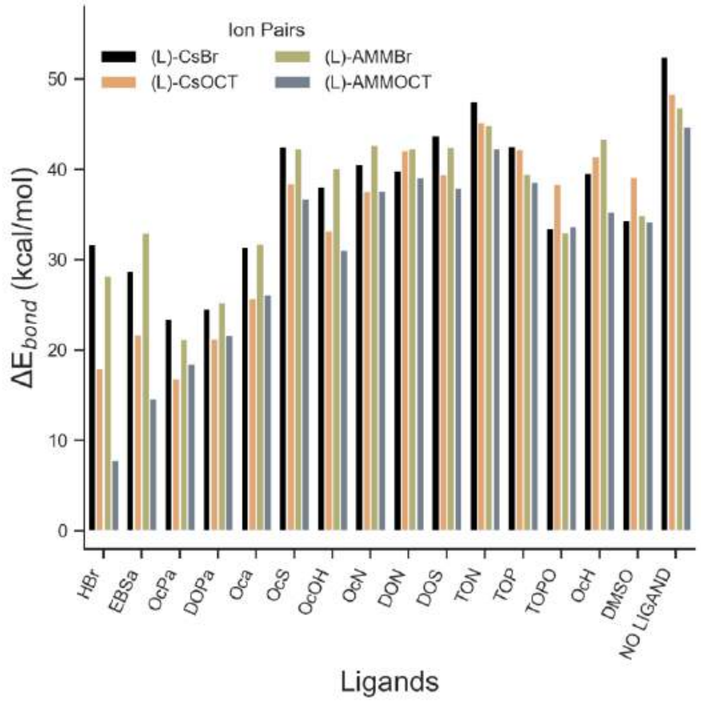

Figure S3. Ligand-induced displacement of the most commonly used passivating ligand pairs from the $CsPbBr_3$ NC surface. Caesium octanoate, ammonium bromide and ammonium octanoate are found to be bound to the surface with energies of the same order of magnitude of CsBr with only minor differences.

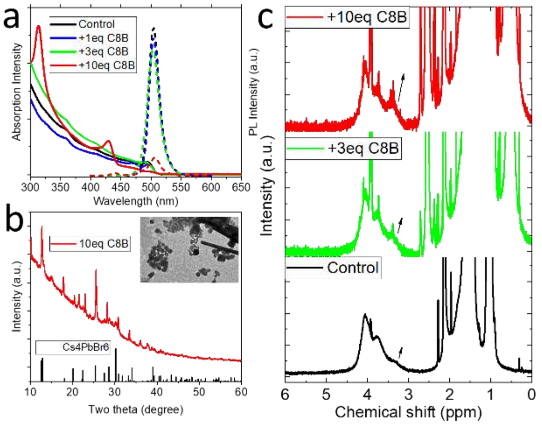

Figure S4. DDABr-capped $CsPbBr_3$ nanocrystals treated with 1-10 eq amount of non-degassed octylamine (C8B) and the corresponding (a) Absorption and PL intensity curves; (b) XRD pattern and (inset) TEM image; (c) ^1H NMR spectra. It is possible to notice here that non-degassed C8B is able to transform $CsPbBr_3$ NCs into Cs_4PbBr_6 (panel b), and to interact with the surface DDA molecules (panel c, black arrows).

Method S3. Addition of exogenous ligands.

The concentration of [NCs] in a given NC dispersion in toluene was determined by measuring the absorbance of the latter at λ = 400 nm and by employing the calibration curve reported by Jorick Maes *et al.* [J. Phys. Chem. Lett. 2018, 9, 3093−3097]. Typical [NCs] were in the 16-38 uM order.

Considering a concentration of 38 uM the equivalents of added exogenous ligands were calculated as follow:

$N_{\text{Surface site}} = 726$ per NCs; $N_A = 6.02*10^{23}$

1 eq ligands = $[NCs]\times N_A \times N_{\text{Surface site}} \times 1 = 5.7$ uM

3 eq ligands = $[NCs] \times N_A \times N_{\text{Surface site}} \times 3 = 17.1$ uM

10 eq ligands = [NCs] $\times N_A \times N_{\text{Surface site}} \times 10$= 57 uM

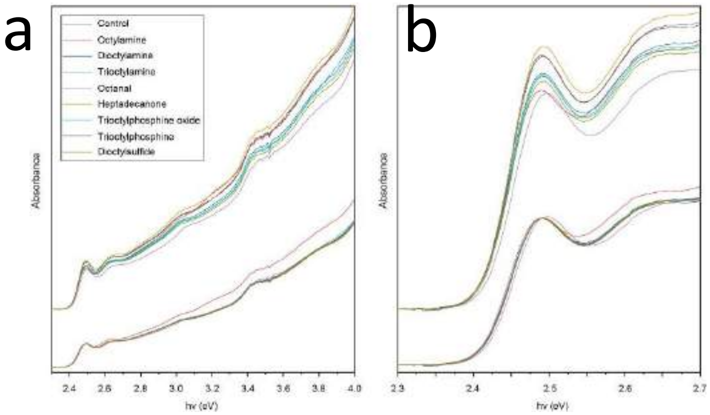

Figure S5. Photographs and (a-b) absorbance spectra of samples treated with basic ligands at a concentration of 10 ligands per surface site and diluted for analysis. Background (2.3 eV) subtracted spectra are shown on top, while spectra normalized at 2.489 eV are shown below.

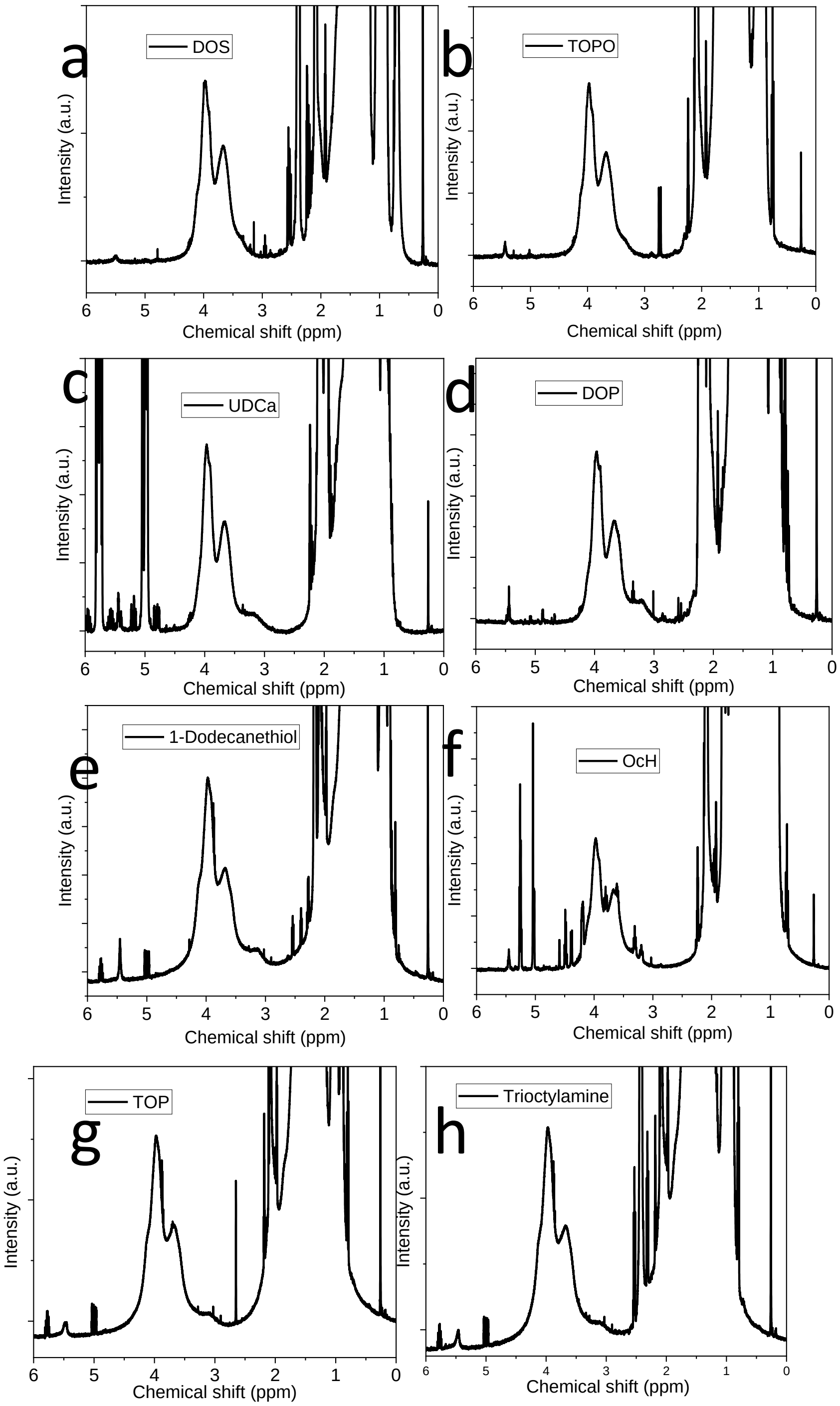

Figure S6. 1H-NMR spectra of DDAB NCs treated by various excess (10eq) neutral ligands: (a) Dioctylsulfide (Dos); (b) Trioctylphospine oxide (TOPO); (c) Undecanoic acid (UDCa); (d) Dioctylphosphinic acid (DOpa); (e) 1-Dodecanethiol (OcN); (f) Octanal (OcH); (g) trioctylphosphine (TOP); (h) Trioctylamine (TON).

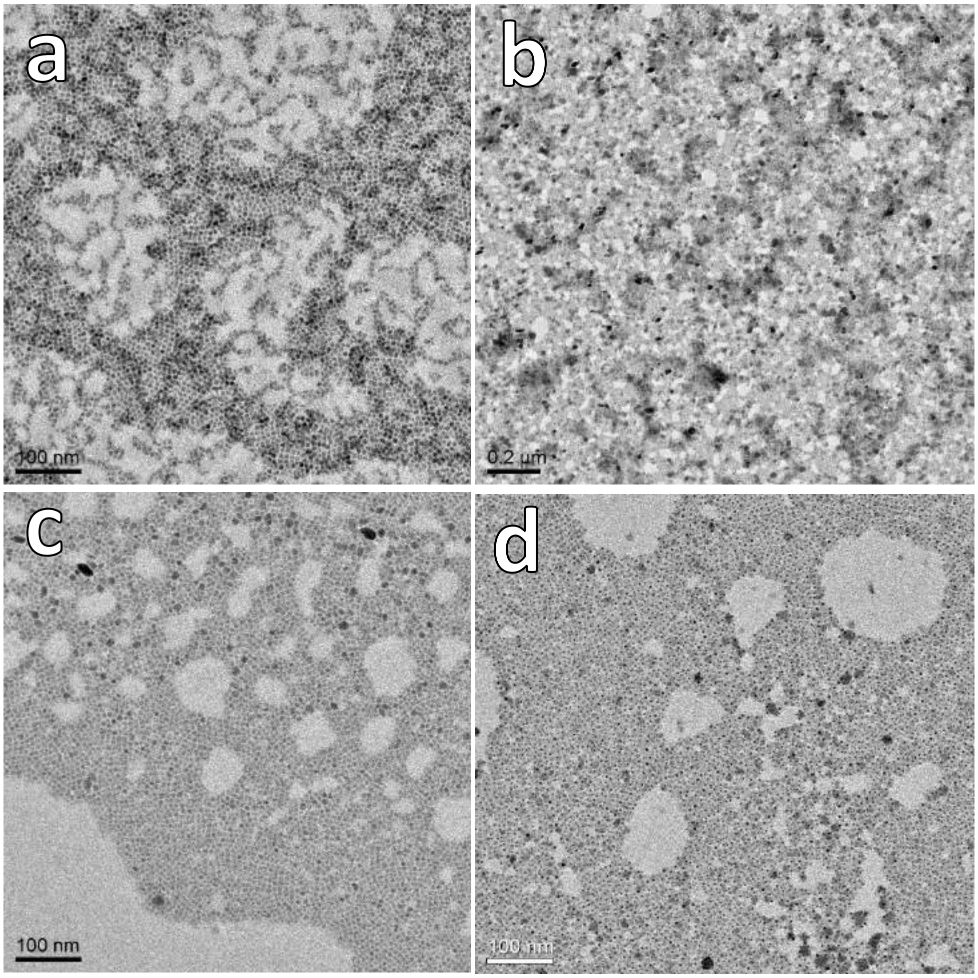

Figure S7. TEM images of (a) DDABr-capped starting NCs and (b) 1 eq, (c) 3eq, (d) 10eq OLPA treated NCs after washing.

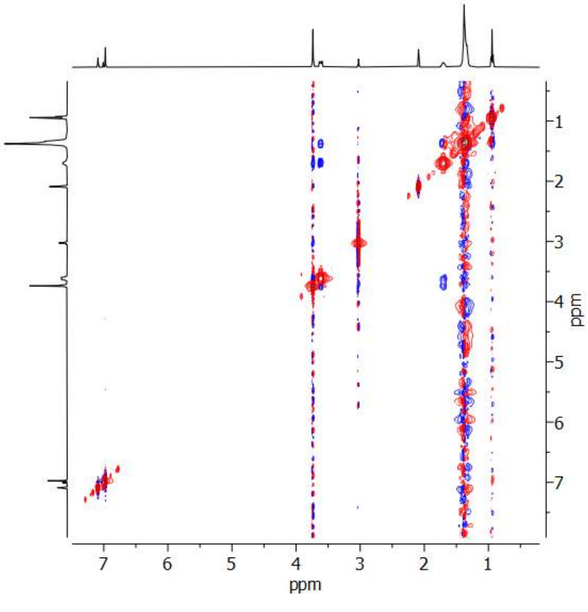

Figure S8. 2D ^{1}H-^{1}H NOESY experiment performed at 40°C of free DDABr molecules in toluene-d8. This temperature was employed in order to "break" the micelles that DDABr molecules form at room temperature (J. Phys. Chem. B 2004, 108, 1, 438–443). Such micelles, in fact, deliver red signals (specify), confusing the analyses. The free DDABr in returns positive NOE (blue) cross peaks, characteristic of species with a short correlation times (τ_c).

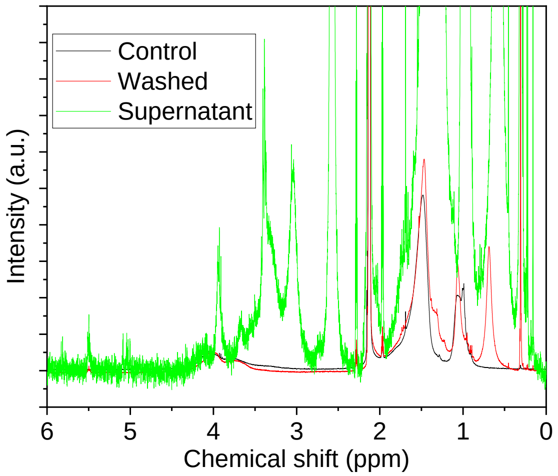

Figure S9. ^{1}H-NMR analysis of NC treated with 3eq of OLPA before (black curve) and after (red curve) a washing step with ethyl acetate (which consists in the addition of ethyl acetate, centrifugation and redispersion of the NCs in toluene-d8). The green curve is the ^{1}H-NMR analysis of the supernatant obtained in the washing step.

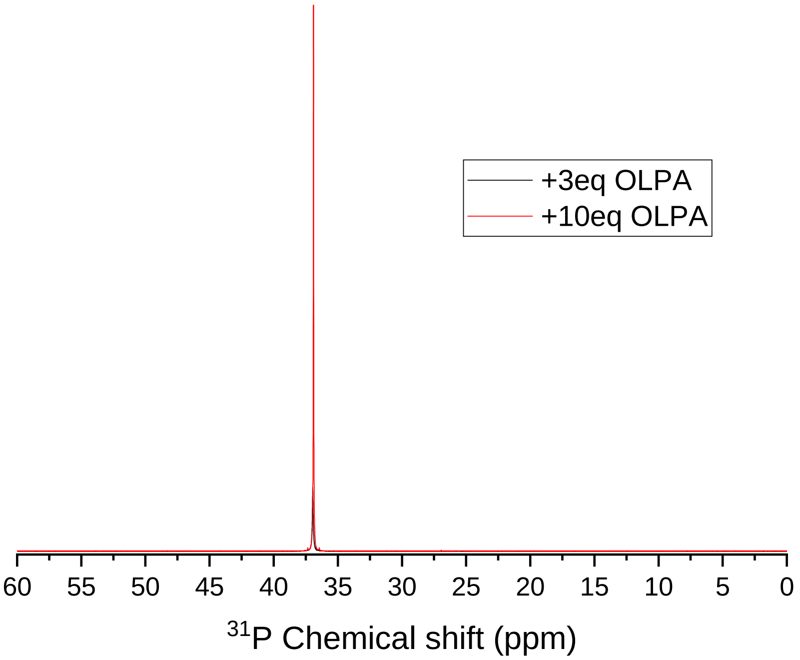

Figure S10. ^{31}P-NMR of 3eq OLPA (black line) and 10eq OLPA (red line) treated NCs after washing.

	Starting NCs	**NCs treated by 10eq OLPA**
Cs (at%)	20.2	21.0
Pb (at%)	19.4	19.8
Br (at%)	53.8	53.8
N (at%)	6.5	5.4

Table S2. XPS result of starting DDAB caped NCs and NCs after 10 eq OLPA treating.

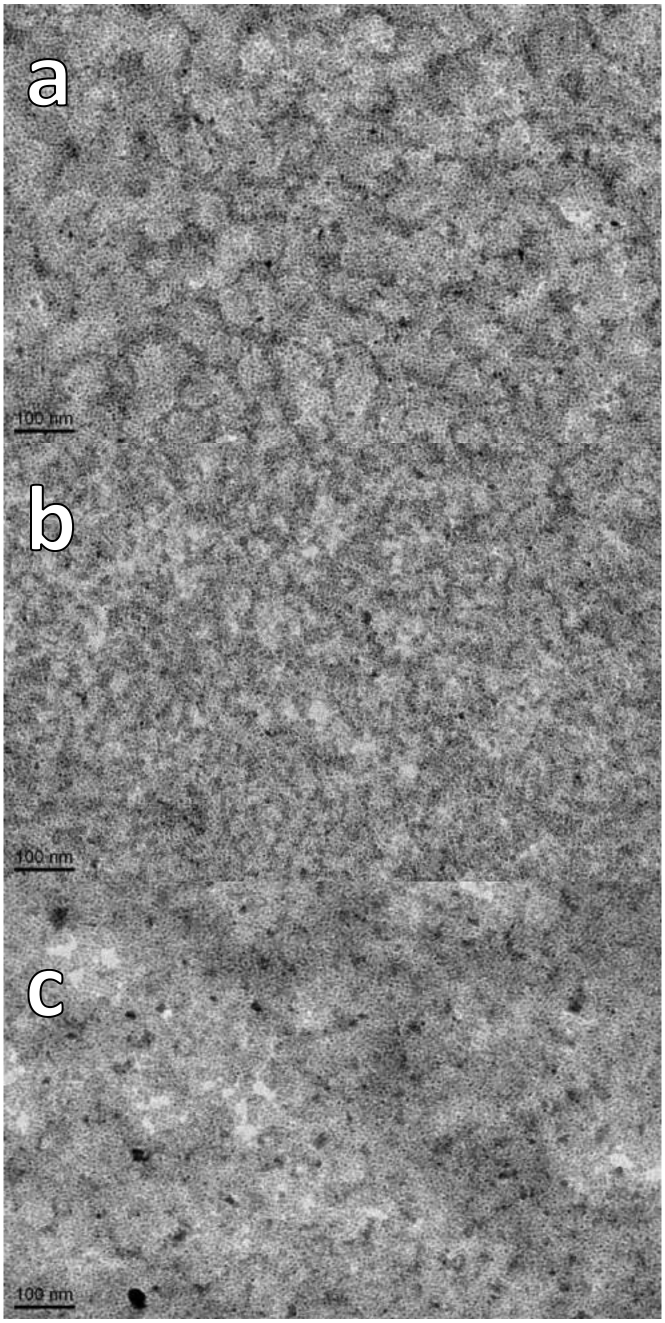

Figure S11. TEM images of (a) 1 eq HOA, (b) 3 eq HOA and (c) 10 eq HOA treated NCs after washing.

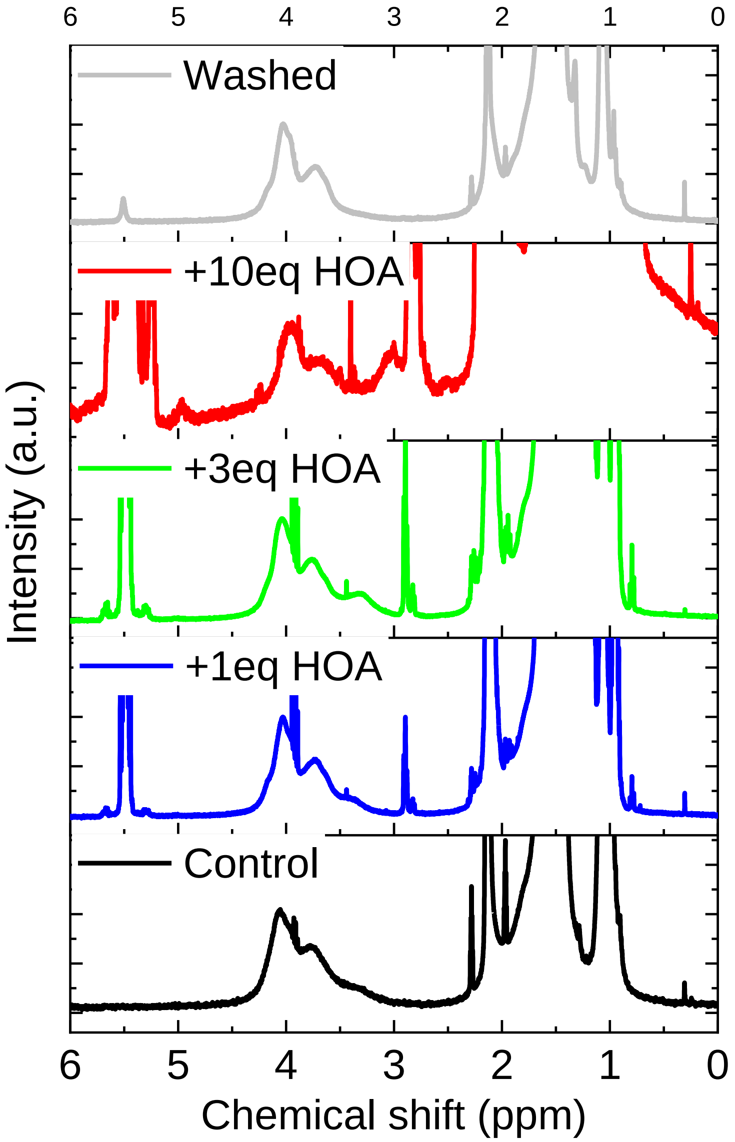

Figure S12. ^{1}H NMR analysis of DDABr-capped NCs, and 1 eq HOA, 3eq HOA, 10eq HOA treated NCs. The top panel shows the ^{1}H NMR analysis of NCs treated with 3eq of HOA and washed with ethylacetate.

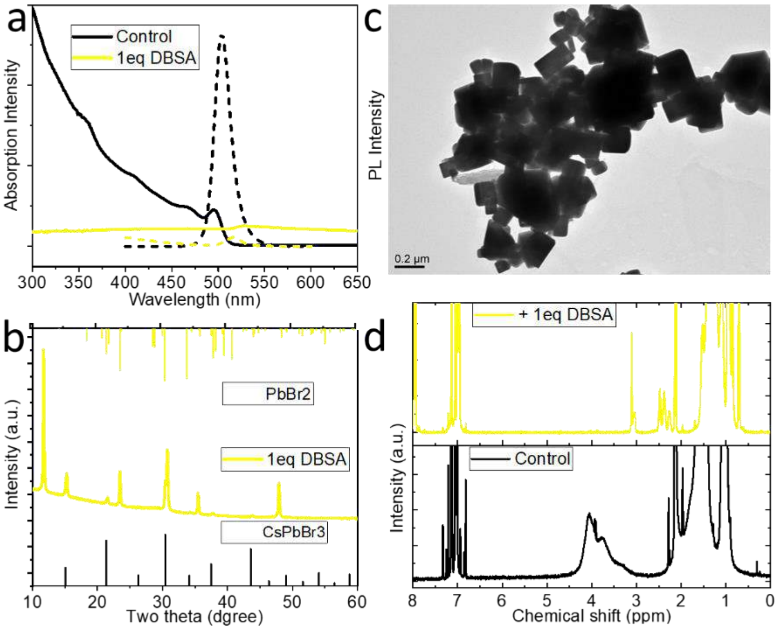

Figure S13. (a) Absorption and emission spectra, (b) XRD (c) TEM and (d) ^{1}H-NMR spectrum of DBSA treated NCs.

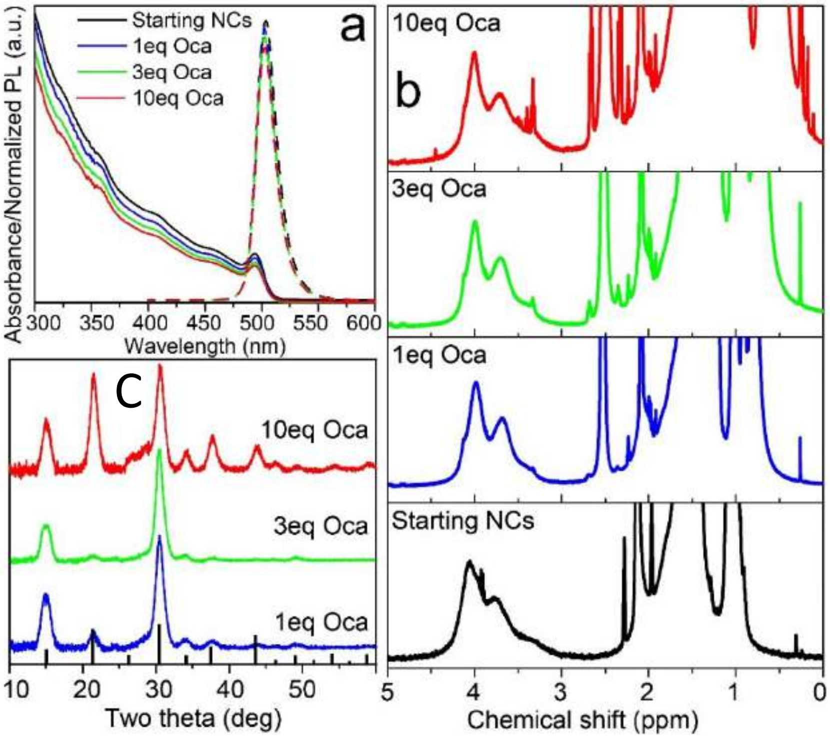

Figure S14. DDABr-capped CsPbBr$_3$ nanocrystals treated with 1-10 eq amount of degassed octylamine (C8B) and the corresponding (a) Absorption and PL intensity curves; (b) 1H-NMR; (c) XRD patterns.

REFERENCES:

(1) Jena, A. K.; Kulkarni, A.; Miyasaka, T., Halide Perovskite Photovoltaics: Background, Status, and Future Prospects. *Chemical Reviews* **2019,** *119*, 3036-3103.

(2) Sutherland, B. R.; Sargent, E. H., Perovskite Photonic Sources. *Nature Photonics* **2016,** *10*, 295.

(3) Kovalenko, M. V.; Protesescu, L.; Bodnarchuk, M. I., Properties and Potential Optoelectronic Applications of Lead Halide Perovskite Nanocrystals. *Science* **2017,** *358*, 745-750.

(4) Quan, L. N.; Rand, B. P.; Friend, R. H.; Mhaisalkar, S. G.; Lee, T.-W.; Sargent, E. H., Perovskites for Next-Generation Optical Sources. *Chem. Rev.* **2019,** *119*, 7444-7477.

(5) Yang, D.; Li, X.; Zeng, H., Surface Chemistry of All Inorganic Halide Perovskite Nanocrystals: Passivation Mechanism and Stability. *Adv. Mater. Interfaces* **2018,** *5*, 1701662.

(6) Shamsi, J.; Urban, A. S.; Imran, M.; De Trizio, L.; Manna, L., Metal Halide Perovskite Nanocrystals: Synthesis, Post-Synthesis Modifications, and Their Optical Properties. *Chem. Rev.* **2019,** *119*, 3296-3348.

(7) Akkerman, Q. A.; Rainò, G.; Kovalenko, M. V.; Manna, L., Genesis, Challenges and Opportunities for Colloidal Lead Halide Perovskite Nanocrystals. *Nat. Mater.* **2018,** *17*, 394-405.

(8) Protesescu, L.; Yakunin, S.; Bodnarchuk, M. I.; Krieg, F.; Caputo, R.; Hendon, C. H.; Yang, R. X.; Walsh, A.; Kovalenko, M. V., Nanocrystals of Cesium Lead Halide Perovskites (Cspbx3, X = Cl, Br, and I): Novel Optoelectronic Materials Showing Bright Emission with Wide Color Gamut. *Nano Lett.* **2015,** *15*, 3692-3696.

(9) Imran, M.; Caligiuri, V.; Wang, M.; Goldoni, L.; Prato, M.; Krahne, R.; De Trizio, L.; Manna, L., Benzoyl Halides as Alternative Precursors for the Colloidal Synthesis of Lead-Based Halide Perovskite Nanocrystals. *J. Am. Chem. Soc.* **2018,** *140*, 2656-2664.

(10) Liu, X.-K.; Xu, W.; Bai, S.; Jin, Y.; Wang, J.; Friend, R. H.; Gao, F., Metal Halide Perovskites for Light-Emitting Diodes. *Nat. Mater.* **2021,** *20*, 10-21.

(11) Gandini, M.; Villa, I.; Beretta, M.; Gotti, C.; Imran, M.; Carulli, F.; Fantuzzi, E.; Sassi, M.; Zaffalon, M.; Brofferio, C.; Manna, L.; Beverina, L.; Vedda, A.; Fasoli, M.; Gironi, L.; Brovelli, S., Efficient, Fast and Reabsorption-Free Perovskite Nanocrystal-Based Sensitized Plastic Scintillators. *Nat. Nanotechnol.* **2020,** *15*, 462-468.

(12) Fu, Y.; Zhu, H.; Chen, J.; Hautzinger, M. P.; Zhu, X. Y.; Jin, S., Metal Halide Perovskite Nanostructures for Optoelectronic Applications and the Study of Physical Properties. *Nat. Rev. Mater.* **2019,** *4*, 169-188.

(13) Zheng, X.; Hou, Y.; Sun, H.-T.; Mohammed, O. F.; Sargent, E. H.; Bakr, O. M., Reducing Defects in Halide Perovskite Nanocrystals for Light-Emitting Applications. *J. Phys. Chem. Lett.* **2019,** *10*, 2629-2640.

(14) ten Brinck, S.; Zaccaria, F.; Infante, I., Defects in Lead Halide Perovskite Nanocrystals: Analogies and (Many) Differences with the Bulk. *ACS Energy Lett.* **2019,** *4*, 2739-2747.

(15) Almeida, G.; Infante, I.; Manna, L., Resurfacing Halide Perovskite Nanocrystals. *Science* **2019,** *364*, 833-834.

(16) Zito, J.; Infante, I., The Future of Ligand Engineering in Colloidal Semiconductor Nanocrystals. *Accounts of Chemical Research* **2021,** *54*, 1555-1564.

(17) Smock, S. R.; Chen, Y.; Rossini, A. J.; Brutchey, R. L., The Surface Chemistry and Structure of Colloidal Lead Halide Perovskite Nanocrystals. *Accounts of Chemical Research* **2021,** *54*, 707-718.

(18) Xue, J.; Wang, R.; Yang, Y., The Surface of Halide Perovskites from Nano to Bulk. *Nat. Rev. Mater.* **2020,** *5*, 809-827.

(19) Qiao, T.; Son, D. H., Synthesis and Properties of Strongly Quantum-Confined Cesium Lead Halide Perovskite Nanocrystals. *Accounts of Chemical Research* **2021,** *54*, 1399-1408.

(20) De Roo, J.; Ibáñez, M.; Geiregat, P.; Nedelcu, G.; Walravens, W.; Maes, J.; Martins, J. C.; Van Driessche, I.; Kovalenko, M. V.; Hens, Z., Highly Dynamic Ligand Binding and Light Absorption Coefficient of Cesium Lead Bromide Perovskite Nanocrystals. *ACS Nano* **2016,** *10*, 2071-2081.

(21) Chen, Y.; Smock, S. R.; Flintgruber, A. H.; Perras, F. A.; Brutchey, R. L.; Rossini, A. J., Surface Termination of Cspbbr3 Perovskite Quantum Dots Determined by Solid-State Nmr Spectroscopy. *J. Am. Chem. Soc.* **2020,** *142*, 6117-6127.

(22) Smock, S. R.; Williams, T. J.; Brutchey, R. L., Quantifying the Thermodynamics of Ligand Binding to Cspbbr3 Quantum Dots. *Angew. Chem. Int. Ed. Engl.* **2018,** *57*, 11711-11715.

(23) Imran, M.; Ijaz, P.; Goldoni, L.; Maggioni, D.; Petralanda, U.; Prato, M.; Almeida, G.; Infante, I.; Manna, L., Simultaneous Cationic and Anionic Ligand Exchange for Colloidally Stable Cspbbr$_3$ Nanocrystals. *ACS Energy Lett.* **2019,** *4*, 819-824.

(24) Bodnarchuk, M. I.; Boehme, S. C.; ten Brinck, S.; Bernasconi, C.; Shynkarenko, Y.; Krieg, F.; Widmer, R.; Aeschlimann, B.; Günther, D.; Kovalenko, M. V.; Infante, I., Rationalizing and Controlling the Surface Structure and Electronic Passivation of Cesium Lead Halide Nanocrystals. *ACS Energy Lett.* **2019,** *4*, 63-74.

(25) Koscher, B. A.; Swabeck, J. K.; Bronstein, N. D.; Alivisatos, A. P., Essentially Trap-Free Cspbbr3 Colloidal Nanocrystals by Postsynthetic Thiocyanate Surface Treatment. *J. Am. Chem. Soc.* **2017,** *139*, 6566-6569.

(26) Ahmed, T.; Seth, S.; Samanta, A., Boosting the Photoluminescence of Cspbx3 (X = Cl, Br, I) Perovskite Nanocrystals Covering a Wide Wavelength Range by Postsynthetic Treatment with Tetrafluoroborate Salts. *Chem. Mater.* **2018,** *30*, 3633-3637.

(27) Wu, Y.; Wei, C.; Li, X.; Li, Y.; Qiu, S.; Shen, W.; Cai, B.; Sun, Z.; Yang, D.; Deng, Z.; Zeng, H., In Situ Passivation of Pbbr64– Octahedra toward Blue Luminescent Cspbbr3 Nanoplatelets with near 100% Absolute Quantum Yield. *ACS Energy Lett.* **2018,** *3*, 2030-2037.

(28) Liu, Z.; Bekenstein, Y.; Ye, X.; Nguyen, S. C.; Swabeck, J.; Zhang, D.; Lee, S.-T.; Yang, P.; Ma, W.; Alivisatos, A. P., Ligand Mediated Transformation of Cesium Lead Bromide Perovskite Nanocrystals to Lead Depleted Cs4pbbr6 Nanocrystals. *Journal of the American Chemical Society* **2017,** *139*, 5309-5312.

(29) Almeida, G.; Goldoni, L.; Akkerman, Q.; Dang, Z.; Khan, A. H.; Marras, S.; Moreels, I.; Manna, L., Role of Acid–Base Equilibria in the Size, Shape, and Phase Control of Cesium Lead Bromide Nanocrystals. *ACS Nano* **2018,** *12*, 1704-1711.

(30) Udayabhaskararao, T.; Houben, L.; Cohen, H.; Menahem, M.; Pinkas, I.; Avram, L.; Wolf, T.; Teitelboim, A.; Leskes, M.; Yaffe, O.; Oron, D.; Kazes, M., A Mechanistic Study of Phase Transformation in Perovskite Nanocrystals Driven by Ligand Passivation. *Chem. Mater.* **2018,** *30*, 84-93.

(31) De Roo, J.; De Keukeleere, K.; Hens, Z.; Van Driessche, I., From Ligands to Binding Motifs and Beyond; the Enhanced Versatility of Nanocrystal Surfaces. *Dalton Trans.* **2016,** *45*, 13277-13283.

(32) Zhou, Y.; Wang, F.; Buhro, W. E., Large Exciton Energy Shifts by Reversible Surface Exchange in 2d Ii–Vi Nanocrystals. *J. Am. Chem. Soc.* **2015,** *137*, 15198-15208.

(33) Zhang, B.; Goldoni, L.; Lambruschini, C.; Moni, L.; Imran, M.; Pianetti, A.; Pinchetti, V.; Brovelli, S.; De Trizio, L.; Manna, L., Stable and Size Tunable Cspbbr$_3$ Nanocrystals Synthesized with Oleylphosphonic Acid. *Nano Lett.* **2020,** *20*, 8847–8853.

(34) Quarta, D.; Imran, M.; Capodilupo, A.-L.; Petralanda, U.; van Beek, B.; De Angelis, F.; Manna, L.; Infante, I.; De Trizio, L.; Giansante, C., Stable Ligand Coordination at the Surface of Colloidal Cspbbr$_3$ Nanocrystals. *J. Phys. Chem. Lett.* **2019,** *10*, 3715-3726.

(35) Imran, M.; Ijaz, P.; Baranov, D.; Goldoni, L.; Petralanda, U.; Akkerman, Q.; Abdelhady, A. L.; Prato, M.; Bianchini, P.; Infante, I.; Manna, L., Shape-Pure, Nearly Monodispersed Cspbbr3 Nanocubes Prepared Using Secondary Aliphatic Amines. *Nano Lett.* **2018,** *18*, 7822-7831.

(36) Hens, Z.; Martins, J. C., A Solution Nmr Toolbox for Characterizing the Surface Chemistry of Colloidal Nanocrystals. *Chem. Mater.* **2013,** *25*, 1211-1221.

(37) Zhang, B.; Wang, M.; Ghini, M.; Melcherts, A. E. M.; Zito, J.; Goldoni, L.; Infante, I.; Guizzardi, M.; Scotognella, F.; Kriegel, I.; De Trizio, L.; Manna, L., Colloidal Bi-Doped Cs$_2$ag$_{1-X}$na$_x$incl$_6$ Nanocrystals: Undercoordinated Surface Cl Ions Limit Their Light Emission Efficiency. *ACS Mater. Lett.* **2020,** *2*, 1442-1449.

(38) Toso, S.; Baranov, D.; Manna, L., Hidden in Plain Sight: The Overlooked Influence of the Cs+ Substructure on Transformations in Cesium Lead Halide Nanocrystals. *ACS Energy Lett.* **2020,** *5*, 3409-3414.

(39) Leemans, J.; Dümbgen, K. C.; Minjauw, M. M.; Zhao, Q.; Vantomme, A.; Infante, I.; Detavernier, C.; Hens, Z., Acid–Base Mediated Ligand Exchange on near-Infrared Absorbing, Indium-Based Iii–V Colloidal Quantum Dots. *J. Am. Chem. Soc.* **2021,** *143*, 4290-4301.

(40) Palazon, F.; Almeida, G.; Akkerman, Q. A.; De Trizio, L.; Dang, Z.; Prato, M.; Manna, L., Changing the Dimensionality of Cesium Lead Bromide Nanocrystals by Reversible Postsynthesis Transformations with Amines. *Chem. Mater.* **2017,** *29*, 4167-4171.

(41) Wu, P. S. C.; Otting, G., Rapid Pulse Length Determination in High-Resolution Nmr. *Journal of Magnetic Resonance* **2005,** *176*, 115-119.

(42) Wider, G.; Dreier, L., Measuring Protein Concentrations by Nmr Spectroscopy. *J. Am. Chem. Soc.* **2006,** *128*, 2571-2576.

(43) ten Brinck, S.; Infante, I., Surface Termination, Morphology, and Bright Photoluminescence of Cesium Lead Halide Perovskite Nanocrystals. *ACS Energy Lett.* **2016,** *1*, 1266-1272.

(44) Zhang, B.; Goldoni, L.; Zito, J.; Dang, Z.; Almeida, G.; Zaccaria, F.; de Wit, J.; Infante, I.; De Trizio, L.; Manna, L., Alkyl Phosphonic Acids Deliver Cspbbr3 Nanocrystals with High Photoluminescence Quantum Yield and Truncated Octahedron Shape. *Chem. Mater.* **2019,** *31*, 9140-9147.

(45) Kühne, T. D.; Iannuzzi, M.; Ben, M. D.; Rybkin, V. V.; Seewald, P.; Stein, F.; Laino, T.; Khaliullin, R. Z.; Schütt, O.; Schiffmann, F.; Golze, D.; Wilhelm, J.; Chulkov, S.; Bani-Hashemian, M. H.; Weber, V.; Borštnik, U.; Taillefumier, M.; Jakobovits, A. S.; Lazzaro, A.; Pabst, H.; Müller, T.; Schade, R.; Guidon, M.; Andermatt, S.; Holmberg, N.; Schenter, G. K.; Hehn, A.; Bussy, A.; Belleflamme, F.; Tabacchi, G.; Glöß, A.; Lass, M.; Bethune, I.; Mundy, C. J.; Plessl, C.; Watkins, M.; VandeVondele, J.; Krack, M.; Hutter, J., Cp2k: An Electronic Structure and Molecular Dynamics Software Package - Quickstep: Efficient and Accurate Electronic Structure Calculations. *J. Chem. Phys.* **2020,** *152*, 194103.

(46) Perdew, J. P.; Burke, K.; Ernzerhof, M., Generalized Gradient Approximation Made Simple. *Phys. Rev. Lett.* **1996,** *77*, 3865-3868.

(47) VandeVondele, J.; Hutter, J., Gaussian Basis Sets for Accurate Calculations on Molecular Systems in Gas and Condensed Phases. *J. Chem. Phys.* **2007,** *127*, 114105.

(48) Pople, J. A.; Schlegel, H. B.; Krishnan, R.; Defrees, D. J.; Binkley, J. S.; Frisch, M. J.; Whiteside, R. A.; Hout, R. F.; Hehre, W. J., Molecular Orbital Studies of Vibrational Frequencies. *International Journal of Quantum Chemistry* **1981,** *20*, 269-278.

(49) Stratmann, R. E.; Burant, J. C.; Scuseria, G. E.; Frisch, M. J., Improving Harmonic Vibrational Frequencies Calculations in Density Functional Theory. *J. Chem. Phys.* **1997,** *106*, 10175-10183.

(50) G Fogarasi, a.; Pulay, P., Ab Initio Vibrational Force Fields. *Annual Rev. Phys. Chem.* **1984,** *35*, 191-213.

(51) Procacci, P., Reformulating the Entropic Contribution in Molecular Docking Scoring Functions. *J. Comput. Chem.* **2016,** *37*, 1819-1827.

Chapter 5: Surface Chemistry of Lead Free Metal Halide Nanocrystals.

ABSTRACT: Comparing with lead halide materials, the investigation on the surface chemistry of lead free metal halide materials is much limited. Here, the two types of the most important lead free metal halide materials (double perovskite and Sb based metal halide NCs) were used as study sample. Their surface chemistry was discussed in detail and its optical-physical process. For lead-free metal halide materials, they are not defect-tolerance anymore and thus its NCs form usually has a low PLQY due to surface traps. Considering the low efficiency of lead free metal halide NCs, the possible effort on colloidal metal halide nanocrystals should extend to quantum confinement related properties (e.g. size dependent lifetime-temperature relation).

5.1 Surface Chemistry of Colloidal Bi-doped $Cs_2Ag_{1-x}Na_xInCl_6$ Nanocrystals

ABSTRACT: The $Cs_2AgInCl_6$ double perovskite is one of the most important lead-free metal halide materials. Upon doping with Bi^{3+} and Na^+ cations, $Cs_2Ag_{0.6}Na_{0.4}InCl_6$ bulk crystals were observed to have a bright broadband emission with an 86% PLQY. However, the colloidal Bi^{3+} doped $Cs_2Ag_{0.6}Na_{0.4}InCl_6$ NCs was only reported with a PLQY of ~20%. Such difference in the PLQY between bulk and nano crystals could attribute to the surface vacancies of NCs. It motivated us to explore the surface chemistry of colloidal NCs of double perovskite. Here, we investigated the ligand shell of Bi-doped $Cs_2Ag_{0.6}Na_{0.4}InCl_6$ NCs via NMR analysis. that the NMR analysis revealed that both amines and carboxylic acids were bound and homogeneously distributed on the surface of the NCs. However, even when optimizing the ligand shell (employing a combination of dodecanoic acid and decylamine), the maximum PLQY measured for these NCs was only 37%. No further improvements were observed when exploiting post-synthesis ligand exchange procedures (involving Cs-oleate, different ammonium halides, thiocyanates and sulfonic acids). DFT calculations indicate that a small fraction of unpassivated surface sitesis sufficient to create deep trap states, opposite to the case of LHP NCs which exhibit much higher defect tolerance. The further transient absorption measurements (TA) also evidenced that an ultrafast trapping of holes (most likely mediated by surface Cl-trap states) competes with their localization at the $AgCl_6$ octahedra, from where, instead, they can undergo an optically active recombination yielding the observed PL emission. Our results highlight that such double perovskite is not defect-tolerant and alternative passivation strategies would be required in order to boost its PL emission.

INTRODUCTION. Lead halide perovskite nanocrystals (NCs) are one of the most promising luminescent nanomaterials due to its potential applications in optoelectronic devices.[1-4] However, the intrinsic toxicity of Pb can limit their applications.[5] Therefore, current efforts are aiming at developing non-toxic metal halide materials featuring a bright luminescence and, if possible, high stability.[6] In this regard, the so-called double perovskite (DP) NCs, with a chemical formula $A_2B^+B^{3+}X_6$, have been developed as alternative materials. DP still has a 3D perovskite skeleton but two $[Pb^{2+}X_6]$ were replaced by the corner-sharing $[B^+X_6]$ and $[B^{3+}X_6]$ octahedra.[7] Among the members of this large family of materials, some of them including Cs_2AgBiX_6 (X=Cl, Br, I), $Cs_2AgInCl_6$, $Cs_2NaInCl_6$, $Cs_2NaBiCl_6$ and Cs_2AgSbX_6 (X=Cl, Br) NCs are emissive.[8-15] In particular, $Cs_2AgInCl_6$ has a direct bandgap and thus became most promising DP material. However, the PL emission from this material is weak, due to the parity forbidden nature of the band-edge transition.[16-17] Recently, doping and alloying strategies have been employed to improve the optical properties of $Cs_2AgInCl_6$ NCs.[13, 18-21] For instance, doping with either Mn^{2+} or Bi^{3+} ions improved the PLQY of NCs to 16% or 11%, respectively,[22-23] while doping $Cs_2AgInCl_6$ NCs with rare earth ions accelerated the NIR emitting (at ~1000nm with Yb^{3+} and at ~1537 nm with Er^{3+}).[24-26] On the other hand, alloyed $Cs_2AgIn_xBi_{1-x}Cl_6$ or $Cs_2Ag_{1-x}Na_xInCl_6$ NCs display enhanced PL emission with yellow or white color.[4, 27-31] For example, Yang *et al.* demonstrated that the by Bi^{3+} doping, the $Cs_2AgIn_{0.9}Bi_{0.1}Cl_6$ NCs has a PLQY as high as 36%.[31] In another work, Luo *et al.* obtained 1% Bi^{3+} doped $Cs_2Ag_{0.6}Na_{0.4}InCl_6$ bulk powders exhibiting a bright white emission with a PLQY of ~86% which is currently a record value for DPs. [4] To extending such doping strategy to the nanoscale, the 1% Bi-doped $Cs_2Ag_{1-x}Na_xInCl_6$ NCs also be prepared, but only with PLQY values of ~22%.[32] The notable difference in PLQY between bulk powders and colloidal NCs of such DP material can be induced by the abundant surface defects of NCs, which are known to strongly affect the optical properties of both traditional semiconductor and Pb-based perovskite NCs.[33-36] While our knowledge on the surface passivation of Pb-based perovskite NCs is reaching maturity, much less is known on the ligand shell of double perovskite NCs.[14, 37-41]

To shed light on the surface shell of DP NCs, in the present work we modified the colloidal synthesis of Bi-doped $Cs_2Ag_{1-x}Na_xInCl_6$ NCs with special ligands combination in order to detect, *via* NMR spectroscopy. Our ^1H NMR analysis and nuclear Overhauser effect spectroscopy (NOESY), proved that both carboxylate and alkylammonium species were bound and homogeneously intermixed on the surface of the NCs. Alsowe also systematically investigated how the size, morphology and optical properties of Bi-doped $Cs_2Ag_{1-x}Na_xInCl_6$ NCs was influenced by the chain lengths of alkylamines and carboxylic acids (Scheme 1). Two findings emerged from our study: first, both ligands are essential for the formation of the NCs; second, a variation in the ligands' chain length had a minor effect on the size, shape of the NCsand PLQY, with the highest value (37%) obtained by using a combination of dodecanoic acid (C12A) and decylamine (C10B) (Scheme 1). Our DFT calculations indicate that the limited PLQY of this DP NC system can be attributed to undercoordinated Cl ions. The unpassivated surface site, even in small amounts still result in the formation of deep trap states and suppress the radiative process. The combined experimental and theoretical study indicate tha DPs materials are much less surface tolerant than the LHP materials. Especially in NCs form with a large surface/volume ratio, a complete passivation of surface trap states should be achieved to approach ideal PLQY.

EXPERIMENTAL SECTION

Chemicals. Bismuth(III) acetate [Bi(ac)$_3$, 99.99%], cesium carbonate (Cs_2CO_3, 99%), silver acetate [Ag(ac), 99.99%], sodium acetate [Na(ac), 99%], indium(III) acetate [In(ac)$_3$, 99.99%], benzoyl chloride (99%), oleylamine (C18B, 70%), oleic acid (C18A, 90%), hexane (anhydrous, 95%), ethyl acetate (EtAc, 99.9%), dioctyl ether (DOE, 99%), octanoic acid (C8A, ≥99%), decanoic acid

(C10A, 98%), dodecanoic acid (C12A, 98%), myristic acid (C14A, 99%), palmitic acid (C16A, 99%), phenylacetic acid (PhAc, 99%), octylamine (C8B, 99%), decylamine (C10B, 99%), dodecylamine (C12B, 98%), tetradecylamine (C14B, 95%), hexadecylamine (C16B, 98%), dimethyl sulfoxide-d (DMSO-d6, 99.9%) and chloroform-d ($CDCl_3$, 99.8%) were purchased from Sigma-Aldrich.

Synthesis of Bi-doped $Cs_2Ag_{1-x}Na_xInCl_6$ NCs. Bi-doped $Cs_2Ag_{1-x}Na_xInCl_6$ NCs were prepared following an approach developed by our group with minor changes.[31] In a typical synthesis, 0.25 mmol of Cs_2CO_3, 0.15 mmol of Ag(ac), 0.1 mmol of Na(ac), 0.25 mmol of $In(ac)_3$, 2.5 μmol of $Bi(ac)_3$ and 3.77 mmol of the desired carboxylic acid were mixed with 4 mL of DOE into a 20 mL glass vial under air (Scheme 1). The mixture was heated up to 90 °C under vigorous stirring for 15 min to dissolve the metal cation precursors. Then, 1.25 mmol of the desired alkylamine was added into the flask and the temperature was increased up to 120 °C. At this point, a solution of 1.72 mmol of benzoyl chloride in 600 μL of DOE was swiftly injected to trigger the reaction, which was immediately quenched by immersing the flask in an ice-water bath. The product was centrifuged at 4500 rpm for 5 min and the precipitate was dispersed in 3 mL of hexane for further characterizations.

Transmission Electron microscopy (TEM). Same with Chapter 4.1.

X-ray diffraction (XRD). Same with Chapter 4.1.

Elemental analysis. The elemental analysis was performed via energy dispersive X-ray spectroscopy (EDS) on a JEOL JSM-7500FA SEM-Analytical field-emission scanning electron microscopy (SEM) with an Oxford X-Max 80 system equipped with an 80 mm^2 silicon drift detector (SDD). To detect the small concentration of Bi inside the Bi-doped $Cs_2Ag_{1-x}Na_xInCl_6$ NCs, inductively coupled plasma mass spectrometry (ICP-MS) was preferred. This was carried out using an iCAP-TQ triple quadrupole spectrometer (ThermoFisher Scientific). The instrument was set with the following parameters to analyze the samples: plasma power 1550 W; spray chamber temperature 2.7°C; cool flow 14 l/min; aux flow 0.8l/min. To prepare the sample for the analysis, 2 μL of the as-synthesized samples were diluted in 2 mL of hexane, then 10 μL of these diluted samples were dissolved in 100 μL of nitric acid (HNO_3 60% v/v). The solution was further diluted by 10 mL of Milli-Q water and analyzed.

UV−vis Absorption, PL and PLQY Measurements. Similar with Chapter 4.1.

NMR measurements. For these analyses, the samples of PhAc-C18B require a different washing step: (1) the crude solution (5 ml) was centrifuged at 6000 rpm for 5 min. (2) The precipitate was redispersed with 1 ml of anhydrous $CHCl_3$ shaking vigorous to get a turbid brown solution; (3) The turbid solution was left to sediment for 2 hours and the transparent supernatant was collected; (4) EtAc (1 times in volume) was added to supernatant resulting in a turbid dispersion that was centrifuged at 4500 rpm for 5 min; (5) the precipitate was redispersed in $CHCl_3$ (1ml) and reprecipitated with the addition of EtAc (1 times in volume) and centrifugation at 4500 rpm for 5 min; (6) the precipitate was collected and redispersed in 0.6 ml of $CDCl_3$. All NMR spectra were acquired at 300 K on a Bruker Advance III 400 MHz spectrometer, equipped with a Broad Band Inverse probe (BBI). *^1H NMR spectra* were accumulated after an automatic 90° optimization on each sample tube, with 120 transients, 65526 digit points, no steady scans, at a fixed receiver gain (1 or 64 according to sample concentration), over a spectral width of 20.55 ppm (offset at 6.18ppm). An apodization function equivalent to 0.3 Hz was applied to the FIDs before Fourier transform. All spectra were referred to the residual non-deuterated solvent signal, at 7.26 ppm or at 2.50 ppm, for $CDCl_3$ and DMSO-d6 respectively. *2D Nuclear Overhauser effect spectroscopy (^1H-^1H NOESY):* the experiment (noesygpph, Bruker library)[48] was acquired in $CDCl_3$ with 64 scans, a relaxation delay of 2s, a mixing time of 350 ms, by using 2048 data points in the direct dimension and 256 increments.

Computational Methodology. For the classical molecular dynamics (MD) simulations the interactions between atoms/ions were modelled by a CHARMM force field. In particular, the interactions between the inorganic core ions Cs, Ag, In, Cl and carboxylate/ammonium headgroup atoms were modeled by only non-bonded interactions, the Lennard-Jones and the Coulomb potentials. The corresponding parameters were fitted using an adaptive rate Monte Carlo optimization algorithm as described in the literature and implemented in our own developed auto-FOX code[1]. Here, radial distribution functions (rdf) between pairs of atoms are initially computed at a higher level of theory, by performing ab-initio DFT molecular dynamics for 10 ps. Then, these rdfs are fitted at the lower level methodology, in our case a classical force-field, using the rate adaptive algorithm. This approach has been successful to obtain parameters for CdSe nanocrystals capped with oleate ligands[2] and more recently also for perovskite nanocrystals (publications to be released soon). The forcefield parameters describing the oleylammonium and phenyacetate ligands were taken using the MATCH algorithm[3], which obtains the parameters by comparison of chemical fragments as present in the literature. Finally, a starting nanocrystal of 6nm was prepared by randomly displacing 80% of surface Cl by Phenylacetate and 50% of Cs ions by oleylammonium. This was done using the nano-CAT set of tools developed by us[4].

The classical MD simulations on our nanocrystal model consisted of three successive steps. (1) an initial structure relaxation by a steepest-descent minimization. (2) a 1.5 ns equilibration run in vacuum at constant volume and temperature (300K) allowing the ligands to diffuse on the NC surface. In both stages, the position of the inorganic core atoms, i.e. Cs, Ag, In and Cl, were restrained to a fixed position using a very stiff harmonic potentia to maintain the NC integrity. (3) Finally, a production run of 10 ns at 300K , still in vacuum, where also the inorganic core were allowed to relax. All simulations were performed using GROMACS[5].

For the electronic structure calculations, we have carried out atomistic simulations at the density functional theory level using the PBE exchange− correlation functional and a double-ζ basis set plus polarization functions on all atoms as implemented in the CP2K 6.1. All structures have been optimized in vacuum. Scalar relativistic effects were incorporated as effective core potential functions in the basis set. Spin−orbit coupling effects were not included, but their impact on the relaxed structural properties was demonstrated to be negligible for similar systems. More details on how the models were built is found in the main text.

[1] van Beek, B. Automated Forcfield Optimization Extension 0.7.4, https://github.com/nlesc-nano/auto-FOX

[2] Cosseddu, S.; Infante, I. Force Field Parametrization of Colloidal CdSe Nanocrystals Using an Adaptive Rate Monte Carlo Optimization Algorithm. *J. Chem. Theory Comput.* **2017**, *13*, 297–308.

[3] Yesselman, J.D.; Price, D.J.; Knight, J.L.; Brooks III, C.L. MATCH: An atom-typing toolset for molecular mechanics force fields, *J. Comput. Chem.*, **2012,** *33*, 189-202.

[4] van Beek, B. Nano-CAT 0.6.1, https://github.com/nlesc-nano/nano-CAT

[5] Berendsen, H. J. C.; van der Spoel, D.; van Drunen, R. GROMACS: a message-passing parallel molecular dynamics implementation. *Comp. Phys. Commun.*, **1995**, *91*, 43–56.

RESULT AND DISCUSSION

i) Characterization of Bi-doped $Cs_2Ag_{1-x}Na_xInCl_6$ NCs' ligand shell. The standard synthesis of metal halide NCs relies on a combination of oleylamine (C18B) and oleic acid (C18A) as surfactants,[12, 29, 37, 43-47] whose alkyl and alkene protons are characterized by almost overlapping ^{1}H NMR, and thus make the NMR analysis complicated.[14, 44, 48-50] The free protons of COOH and NH_2 groups could return sufficiently separated signals in NMR spectra. Unfortunately, the chemical shift of these free protons is highly dependent on the concentration and PH, making their identification not trivial by ^{1}H NMR.[51-52] Thus, here, to avoid above disadvantage of standard ligands, we employed C18B and PhAc in their synthesis. These molecules can be easily distinguished *via* ^{1}H NMR, as the C18B is characterized by alkenyl protons while the PhAc by aromatic ones. This combination of ligands yields homogeneous cubic NCs with a mean size of 24.4 nm and can be cleaned well by polar solvent0 (Figure 1a). Based on our XRD analysis, the crystal structure of the NCs is pure and matches with the DP $Cs_2AgInCl_6$ structure (ICSD number 244519). The NCs feature an absorption peak at 3.7 eV and a PL emission at 2 eV (Figure S1) with a PLQY of 20% (Figure 2b and Table S2), same with previous report.[32]

These NCs with high concentration were dispersed in $CDCl_3$ and analyzed by ^{1}H NMR. Both C18B and PhAc signals are broadened and shifted with respect to those of free ligands (Figure 1c and Figure S2) indicating both C18B and PhAc are bound to the NCs' surface. Particularly, the α-H (**2**) of C18B has a signal at 2.6 ppm and the alkenyl protons (**10,11**) of C18B has a signal at 5.3 ppm. The α-H proton (**23**) closest to the carboxyl group of PhAc is at 3.6 ppm and the aromatic protons (**25-29**) of PhAc is at 7.1 ppm to 7.4 ppm. In ^{1}H-^{1}H NOESY characterization both PhAc and C18B molecules have longer correlation times (τ_c) and show negative sign (red) with respect to those of the corresponding free ligands which show blue positive signal (Figure 1d and S3-5).[53] PhAc and C18B show not only intra ligand NOE cross peak interactions, but also inter ligand NOE cross peak interactions (Figure 1d). These results indicate that alkylammonium and carboxylate species are space proximal to each other, therefore suggesting that they are homogeneously intermixed on the surface of double perovskite NCs (see Figure 1e, upper sketch). In order to obtain information on the ligand density of our DP NCs, we dissolved the NCs in dimethyl sulfoxide-d6 solvent and, subsequently acquired a quantitative ^{1}H NMR spectrum (Figure S6).[54] The result indicated that the surface density of DP NCs is 4.9 ligands/nm^2, with PhAc:C18B ratio of bound species of 1.52:1. These numbers indicate that ~52% of Cs surface sites are occupied by oleylammonium cations, and ~80% of Cl surface sites are occupied by phenyl acetate anions (see SI for details).

To support the NMR analysis, we carried out MD simulations on a $Cs_2AgInCl_6$ NC model capped by C18B and PhAc ligands (see SI for further info on the force-field employed and the simulations details). The simulation result match well with NOESY evidence (Figure S7), which also show both PhAc and C18B ligands are bound and homogenously intermixing on the surface. The time-average distance between the PhAc aromatic rings and segments of the C18B alkyl chains was also calculated (Figure 1f). The aromatic rings peak of PhAc is closer (0.54 nm) to the initial aliphatic chains segments of the C18B.

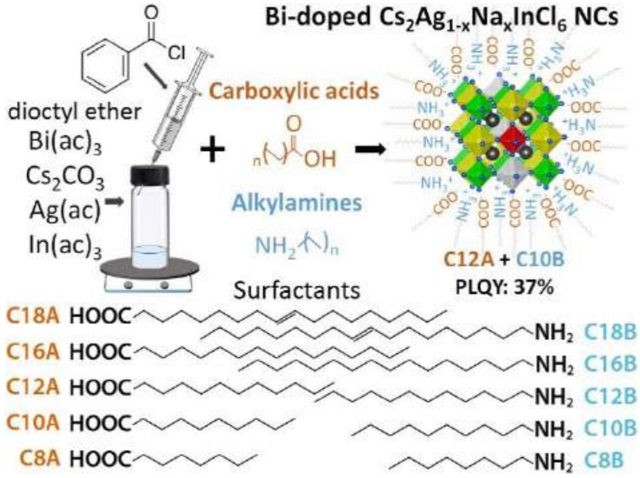

Scheme 1. Colloidal approach to obtain Bi-doped $Cs_2Ag_{1-x}Na_xInCl_6$ NCs with different ligand combinations.

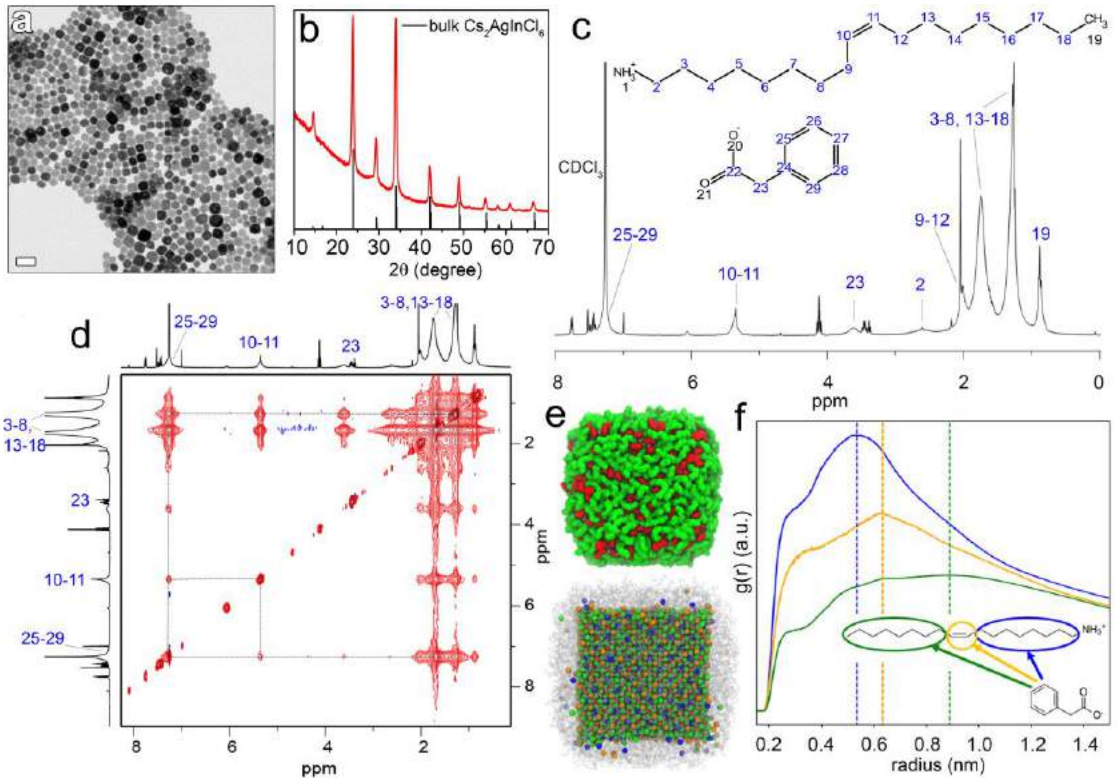

Figure 1. (a) TEM image, the scale bar is 50 nm and (b) XRD pattern of PhAc-C18B NCs. (c) ^{1}H NMR spectra and the (d) corresponding ^{1}H-^{1}H NOESY NMR spectra of PhAc+C18B NCs NCs in CDCl$_3$. (e, top panel) Screenshort from an MD simulation of a $Cs_2AgInCl_6$ NC capped by PhAc (red molecules, occupying 82% of surface Cl sites) and C18B (green molecules, occupying 54% of surface Cs sites) at room temperature. (e, bottom panel) Similar screenshot represented by stick and ball (Cs: orange, Ag: blue, In: red, Cl: green) and surface ligands by grey lines. (f) Average radial distribution function (RDF) between aromatic group pf PhAc and different segments of the C18B.

ii) Ligand Effect on Size, Morphology and Optical Properties. Our surface characterization indicated that both alkylamines and carboxylic acids was necessary to construct the ligands shell of our DP NCs.

To elucidate the role of both alkylamines and carboxylic acids in the synthesis of Bi-doped $Cs_2Ag_{1-x}Na_xInCl_6$ NCs, in analogy to what we have done for LHP NCs,[49] we ran a series of experiments by varying the hydrocarbon chain length of these surfactants (see also Scheme 1) and characterized the corresponding NC products. In most of the cases, colloidal NC with sizes ranging from 8.9 to 23.2 nm were obtained (Figure S8 and Table S2), except for the C8A, C16A. No clear relation between the size of the NCs and chosen ligands was found by TEM analysis (Figure S8). The XRD patterns of all the samples have a pure phase of $Cs_2AgInCl_6$ crystal structure (ICSD number 244519) (Figure S9).

The absorption and PL emission curves of all samples are similar with a peak at ~3.5 eV and ~2.05 eV, respectively (Figure 2a and Figure S10). The excitonic feature observed experimentally in the absorption spectra at ~3.5 eV stems from optically active states within the CB well above the band edge (Figure 3c). Instead, the broad PL band originates from the recombination of electrons and holes localized at the band edges on $BiCl_6$ and $AgCl_6$ octahedra, respectively (Figure 3c).[4, 32] These materials feature an optically inactive region close to the lowest edge-to-edge transition with negligible oscillator strength (Figure 3c) resulting in a large Stokes shift (1.5 eV).[32]

In our work, the optical properties observed are almost identical on the different chain length of carboxylic acids and alkyl amines combination (Figure 2a and Figure S10). The noticeable difference in optical properties is observed for their PLQY, which varies from 0% to 37%. The highest value was achieved by employing C12A+C10B ligands.

To further increase its PLQY, the optimal batchsynthesized with C12A+C10B (Figure 2a), were also subjected to ligand exchange. In detail, the NCs were treated by various exogenous ligands including Cs-oleate, decyl- and docecylammonium chloride and bromide, didodecylammonium bromide, didecyldimethylammonium chloride, sodium thiocynate and dodecylbenzenesulfonic acid (Figure S11). However, No increase of the PLQY was observed for the optimal batch of DP NCs. It suggest the ligand pairs that are commonly employed with LHP NCs, don’t work effectively on DPs materials.[37, 53]

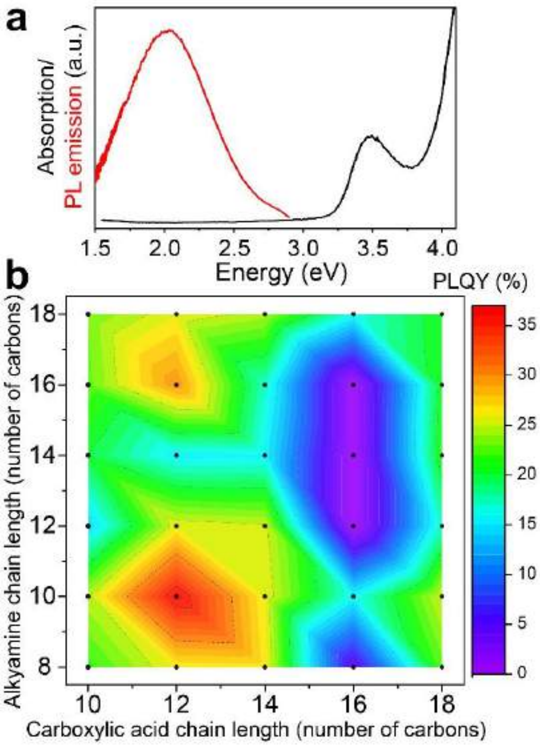

Figure 2. a) Absorption and PL emission curves of the optimal NC batch with C12A+C10B. b) 2D plot of PLQY as a function of the chain length of amines and carboxylic acids.

To understand the reason behind the limited PLQY of our DP NCs, even when passivated with a high density if surface ligands(as detected by NMR analysis), we performed DFT calculations taking as a model system a cubic NC featuring a $Cs_{324}Ag_{65}Na_{43}In_{108}Cl_{756}$ stoichiometry. This corresponds to a diameter of about 3.0 nm DP NCs. The Bi^{3+} dopant was ingnored in the model since it is not expected to influence the surface properties of the NCs. Unlike standard $CsPbBr_3$ NCs, we note that even the fully passivated DPs NC presents strongly localized states at the valence band maximum (VB, Figure 3a). As illustrated in the orbital density plot, these states, although being "shallow", are primarily composed of 3p atomic orbitals of Cl ions at the NC surface (Figure 3a). We then proceeded by a step-by-step displacement of CsCl ion pairs surrounding a reference Cl, which simulate a gradual decapping of the initial perfectly passivated NC surface terminated by CsCl ions. The gradual decapping is shown in the top of Figure 3b, and was performed by keeping the reference Cl ion either above a Na^+ or a Ag^+ cation. As shown in the left panel ofFigure 3b, the displacement of two CsCl pairs above a Na ion leads to the formation of traps above the VB. The trap states is more evident following with the displacement of a third CsCl couple (Figure 3b, middle panel). This effect is less pronounced when the displacement occurs above an Ag ion, because the d orbitals of Ag allow the molecular orbitals near the CB edge to be more delocalized throughout the NC (Figure 3b, right panel). As contrast, the same CsCl displacement in the corresponding LHP NCs ($Cs_{324}Pb_{216}Cl_{756}$ NC model) is much more tolerant to the emergence of mid-gap states (Figure S12). Overall, our calculation evidence that deep states inside the band gap of DP NCs are much easier formed in this material system by unpassivated surface sites comparing with the LHP materials. To further support our calculation, we performed TA spectroscopy experiments on two representative samples: one has a highest (~37%, made with C12A+C10B) PLQY and another one has a lower (~15%, made with C10A+C12B) PLQY, respectively (Figure 3d-f). We excited the systems with light pulses with a temporal resolution close to 20 fs in a region well above the bandgap (*i.e.*, 285 nm, 4.35 eV) and probed in a range around 1.90 - 3.64 eV (340-650 nm), which cover the most specific spectral signatures of the NCs. In this way we were able to detect the carrier recombination after the photoexcitation on relevant timescales. In the TA spectra of the high PLQY sample (Figure 3d), three main signatures was identified assigning to bleach signals which are due to the ultrafast filling of states after the photoexcitation that overlap with a broad photoinduced absorption (PIA) signal (see SI for more information): i) a feature at around 3.46 eV (358 nm) is assigned to the main transition involving the deep electronic states in the CB of the DP NCs, corresponding to the ground state absorption (Figure 2a and 3c), ii) two bands located at around 2.61 eV (475 nm) and 1.95 eV (635 nm), assigned to localized states within the bandgap, the latter ascribable to the $BiCl_6 \rightarrow AgCl_6$ transition which is responsible for the observed PL emission of our NCs.[32] The similar rise time (~0.5ps) of all these bleach signatures indicates that they share a common state. When comparing the energy level scheme as depicted in Figure 3c, the common state could be connected to the VB states, i.e. the holes. As contrast, in the low PLQY sample (Figure 3e) such features are either entirely absent or very weak. Instead, a new and extremely short living feature is observed at ~3.1 eV which ascribed to the presence of surface trap-related transitions with a fast decay (Figure S13). The main difference between the two samples analyzed is that the features assigned to the excitonic and Bi-Ag transitions are nearly absent in the low PLQY sample. This can be tentatively explained by that the photo-excited holes are immediately trapped by the uncoordinated Cl states above Ag and Na ions. Thus, the main optically active recombination channels are suppressed, leading to an overall decrease of the overall PL efficiency. Moreover, if focusing our attention on the decay dynamics of the feature at ~1.95 eV assigned to the Bi-Ag transition, we can observe a much faster recombination rate in the low PLQY sample (Figure 3f). Taken together, our TA results indicate that surface hole trapping should play a major role in lowering the PLQY of our NCs by suppressing the efficient localization of holes at the $AgCl_6$ octahedra and therefore suppress the radiative recombination.

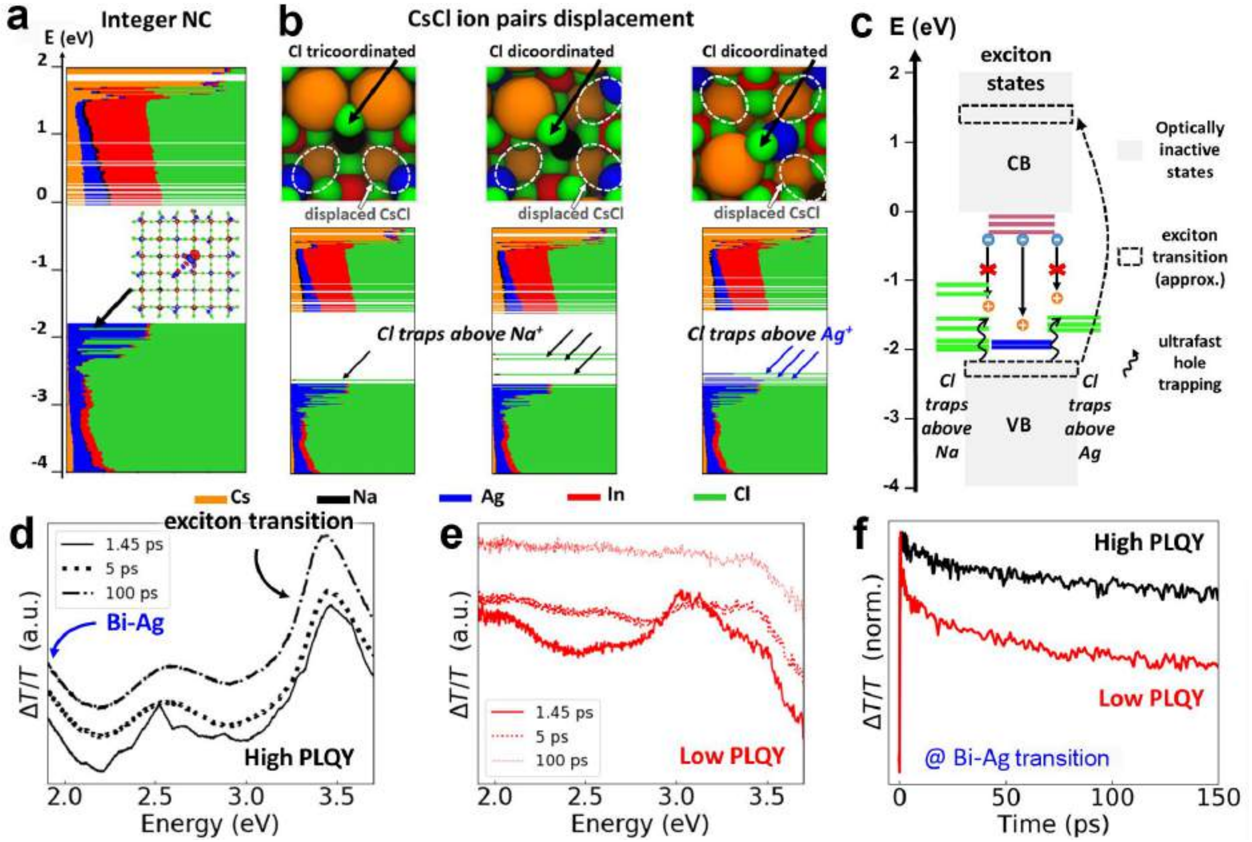

Figure 3. (a) Electronic structure of a ~3.0 nm $Cs_2Ag_{0.60}Na_{0.40}InCl_6$ NC model by DFT/PBE method. (b) Top: Stick and ball view of CsCl displacements. Bottom: emergence of mid-gap states by reducing the coordination number of a surface Cl which lies either above a Na ion (left and middle panels) or above an Ag ion (right panel). (c) Electronic structure describing the ultrafast hole trapping mechanism. Transient absorption spectra for representative high PLQY sample (d) and low PLQY sample (e). (f) Pump-probe dynamics of the two samples at 1.95 eV (the Bi-Ag transition).

CONCLUSION. In summary, our work has shed light on the surface ligand shell of DPs NCs, using Bi-doped $Cs_2Ag_{1-x}Na_xInCl_6$ NCs as representative case. The combination of various experimental analyses, , modeling and electronic structure analysis led us to conclude that this material is much less surface tolerant than the corresponding LHP materials. Therefore, alternative surface passivation strategies for colloidal DP NCs, for example the core-shell structure or more efficient ligands passivation is required for the optimization of its optical properties.

Table S1. SEM-EDS and ICP elemental analyses of Bi-doped $Cs_2Ag_{1-x}Na_xInCl_6$ NCs synthesized using different carboxylic acid-alkylamine combinations.

Sample	**Bi/In**	**Cs/In**	**Ag/In**	**Na/In**	**Cl/In**
C10A+C8B	1.07%	2.2	0.71	0.5	6.11
C10A+C10B	1.08%	2.16	0.67	0.46	5.55
C10A+C12B	0.35%	2.24	0.67	0.44	6.17
C10A+C14B	1.58%	2.07	0.7	0.5	6.01
C10A+C16B	1.78%	2.02	0.62	0.5	6.3
C10A+C18B	1.65%	2.1	0.72	0.54	6.1
C12A+C8B	0.87%	2.3	0.6	0.66	6.1
C12A+C10B	1.03%	2	0.52	0.35	5.3
C12A+C12B	0.91%	2.2	0.7	0.51	6
C12A+C14B	1.01%	1.85	0.62	0.54	5.17
C12A+C16B	0.80%	2	0.58	0.45	5.3
C12A+C18B	1.42%	2.2	0.62	0.55	6.1
C14A+C8B	0.67%	2.14	0.39	0.34	6.01
C14A+C10B	0.84%	2.1	0.46	0.4	5.87
C14A+C12B	0.92%	2.66	0.57	0.51	6.72
C14A+C14B	1.50%	2.07	0.69	0.46	5.6
C14A+C16B	0.80%	2.06	0.6	0.41	5.5
C14A+C18B	1.60%	1.99	0.58	0.53	4.91
C16A+C8B	1.40%	2.03	0.67	0.41	5.7
C16A+C10B	1.20%	2.24	0.62	0.47	5.96
C16A+C12B	1.20%	1.86	0.46	0.52	4.6
C16A+C14B	1.05%	1.93	0.67	0.46	5.34
C16A+C16B	1.30%	2.12	0.7	0.5	6.02
C16A+C18B	1.70%	2.1	0.7	0.5	6.3
C18A+C8B	1.10%	1.9	0.7	0.21	5.2
C18A+C10B	0.86%	2	0.55	0.4	5.76
C18A+C12B	0.97%	2.12	0.52	0.53	6.09
C18A+C14B	1.05%	2.07	0.72	0.46	5.55
C18A+C16B	1.30%	2.02	0.67	0.37	5.4
C18A+C18B	1%	2.2	0.7	0.51	6.2
PhAc+C18B	1.30%	2.3	0.65	0.62	6.0

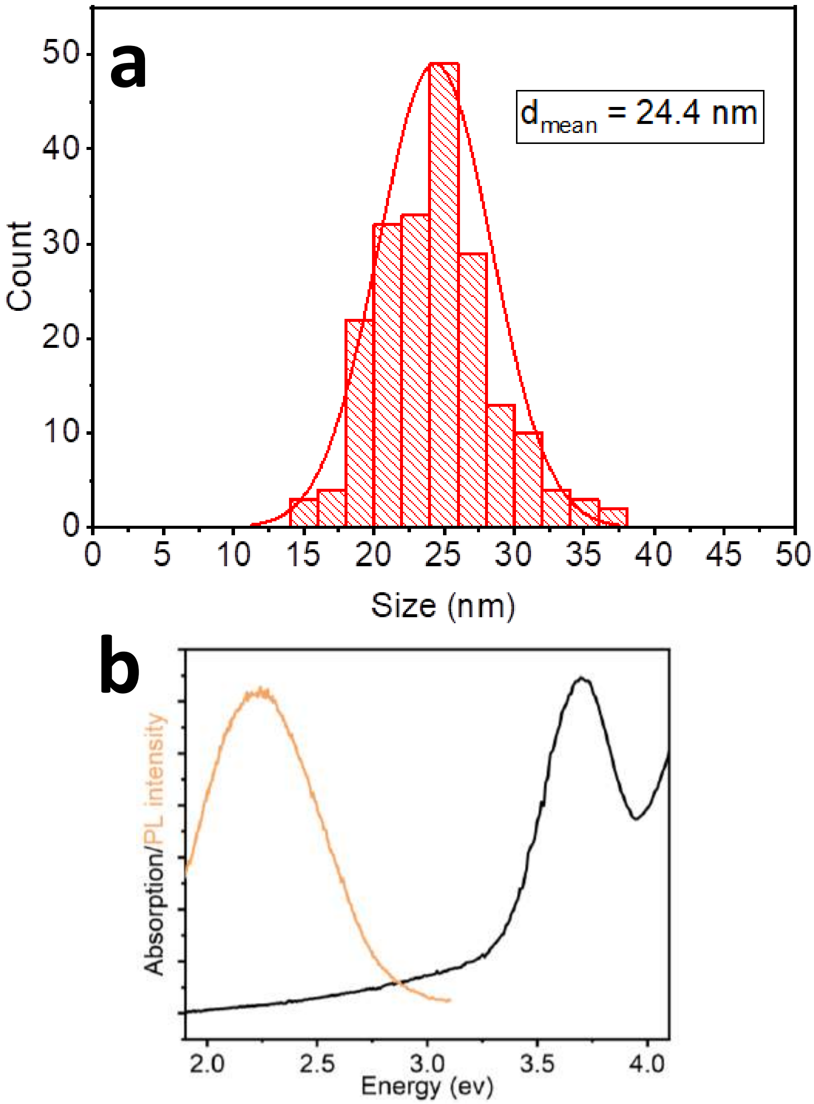

Figure S1. a) Size distribution histogram and b) absorption and PL spectra of Bi-doped $Cs_2Ag_{1-x}Na_xInCl_6$ NCs synthesized by employing PhAc and oleylamine (C18B).

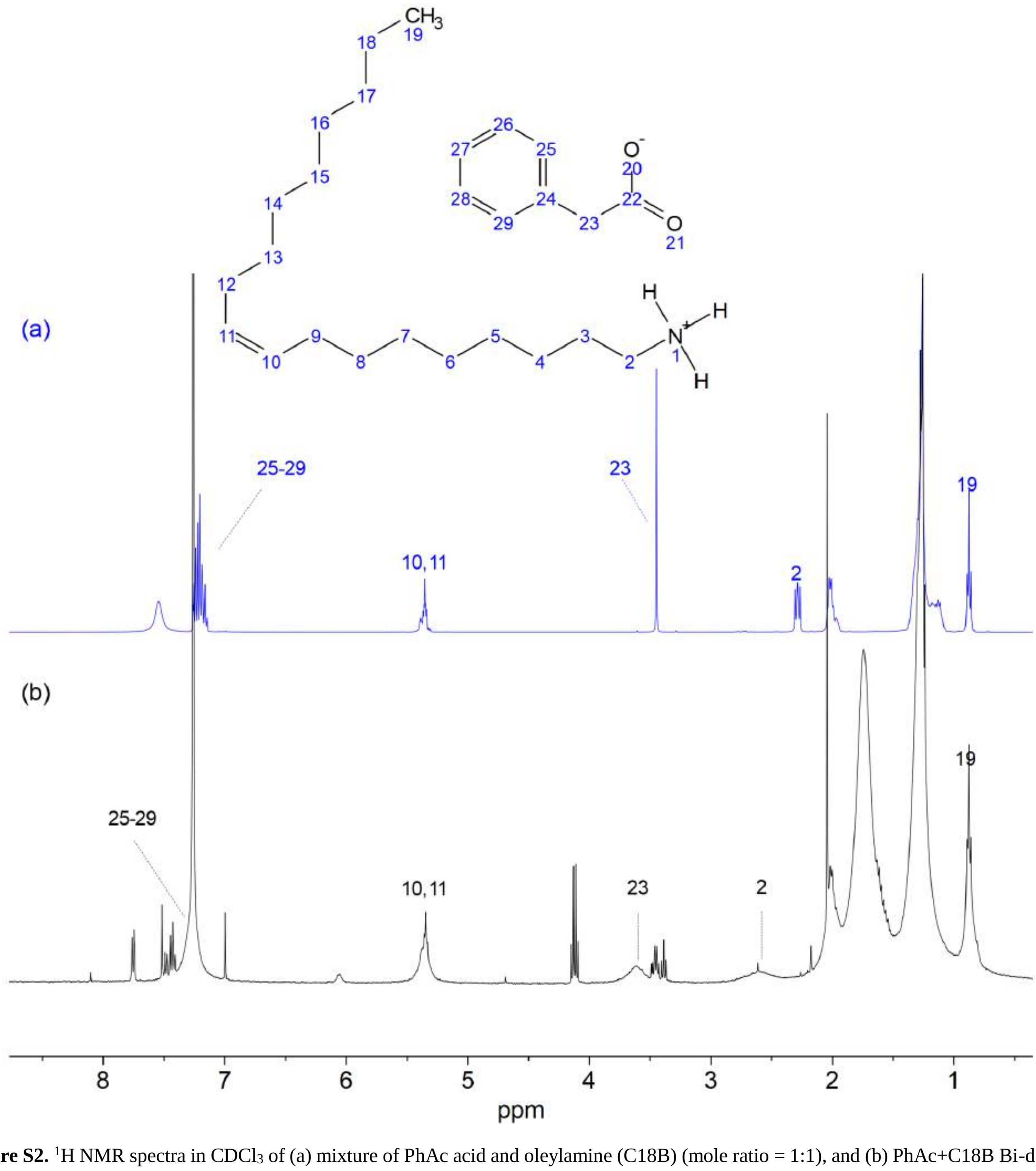

Figure S2. ^{1}H NMR spectra in $CDCl_3$ of (a) mixture of PhAc acid and oleylamine (C18B) (mole ratio = 1:1), and (b) PhAc+C18B Bi-doped $Cs_2Ag_{1-x}Na_xInCl_6$ NCs (the same spectrum reported in Figure 1c); diagnostic peaks are assigned.

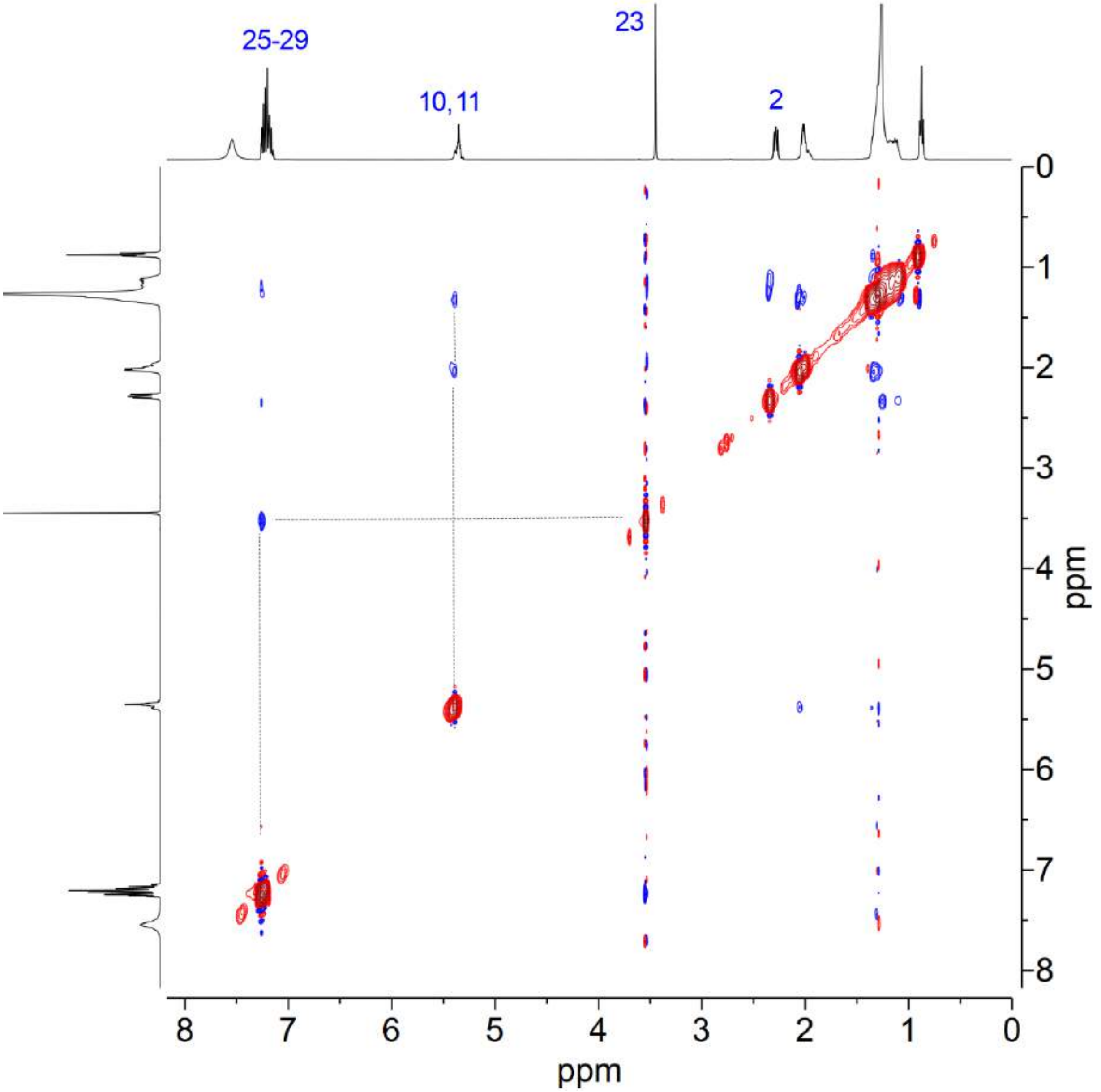

Figure S3. ^{1}H-^{1}H 2D NOESY spectrum in $CDCl_3$ of mixture of PhAc and oleylamine (C18B) (mole ratio = 1:1), as free ligands, all the cross peaks show positive (blue) sign, indicating a fast correlation time (τ_c) for both species in solution.

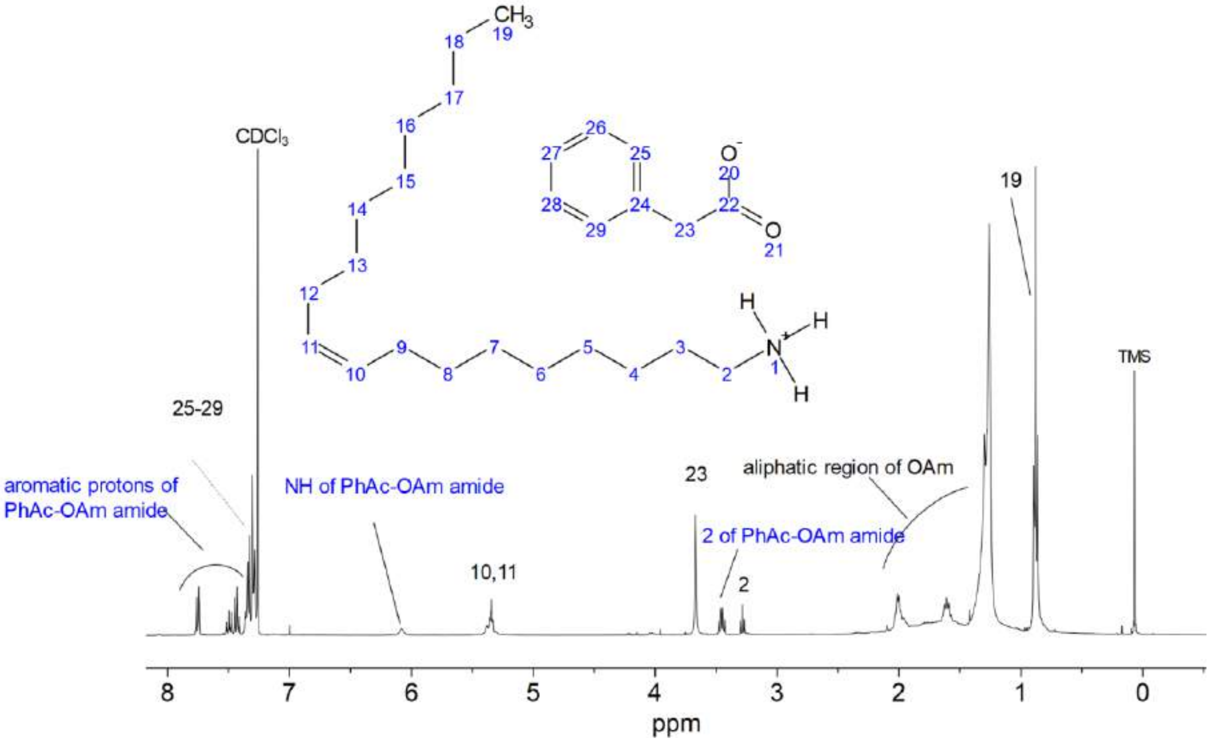

Figure S4. ^{1}H NMR spectrum in $CDCl_3$ of Bi-doped $Cs_2Ag_{1-x}Na_xInCl_6$ NCs made with PhAc and oleylamine (OAm in this figure) and not subjected to the cleaning step with EtAc. It is possible to detect here the presence of free ligands and of the amide formed by the condensation of PhAc and OAm (PhAc-OAm amide), diagnostic peaks are assigned. The corresponding NOESY spectrum was shown in Figure S5.

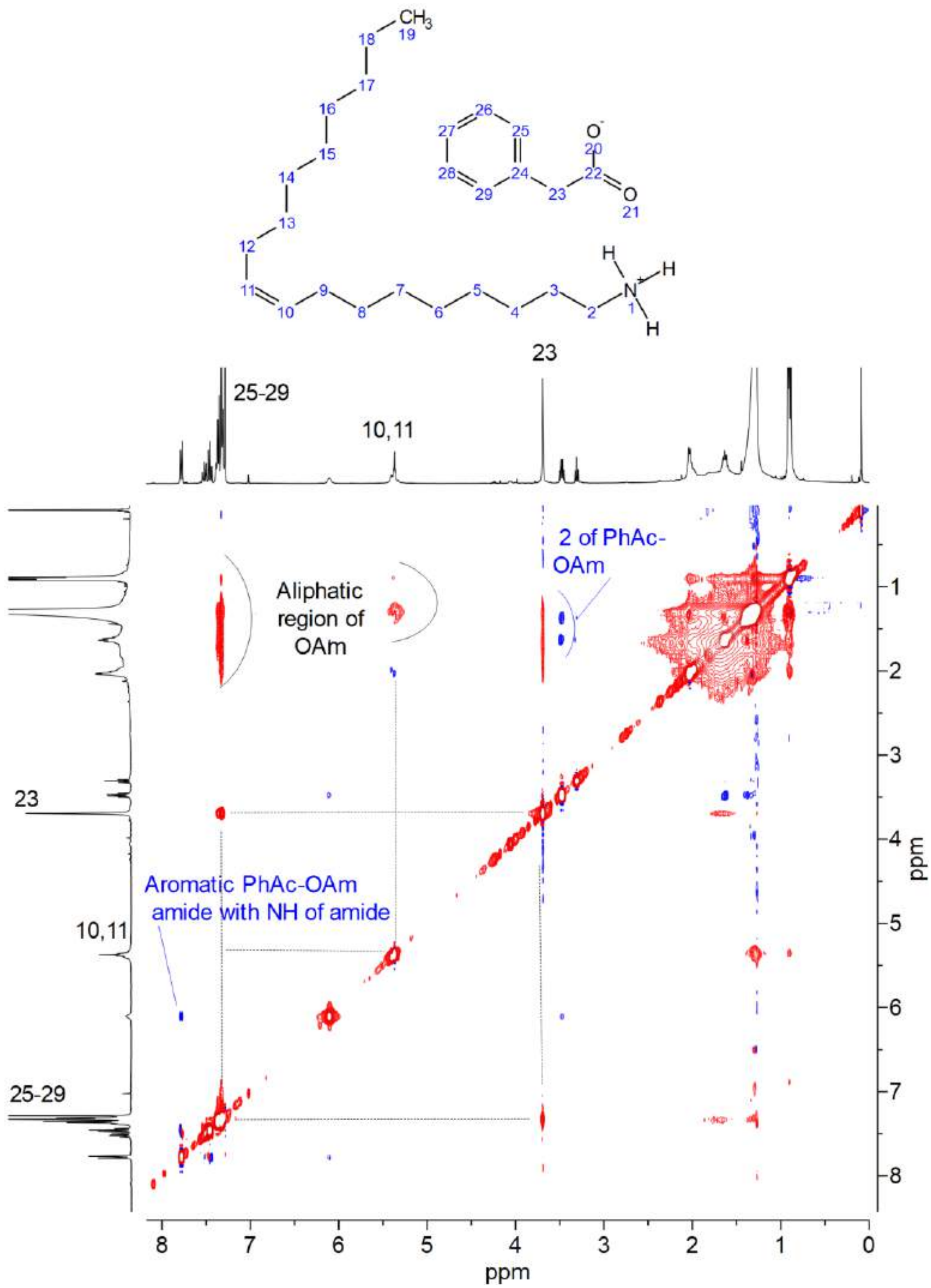

Figure S5. ^{1}H-^{1}H 2D NOESY spectrum in CDCl$_3$ of Bi-doped Cs$_2$Ag$_{1-x}$Na$_x$InCl$_6$ NCs made with PhAc and oleylmaine (OAm in this figure) and not subjected to the cleaning step with EtAc. Ligands dynamically interacting with the NCs' surface return negative sign (red) cross peaks due to a long correlation time (τ_c), whereas impurity such as PhAc-OAm amide returns positive sign (blue) cross peak, indicating a fast correlation time(τ_c), similar to that of free molecules in solution. PhAc-OAm amide, therefore, is not bound to the NC surface.

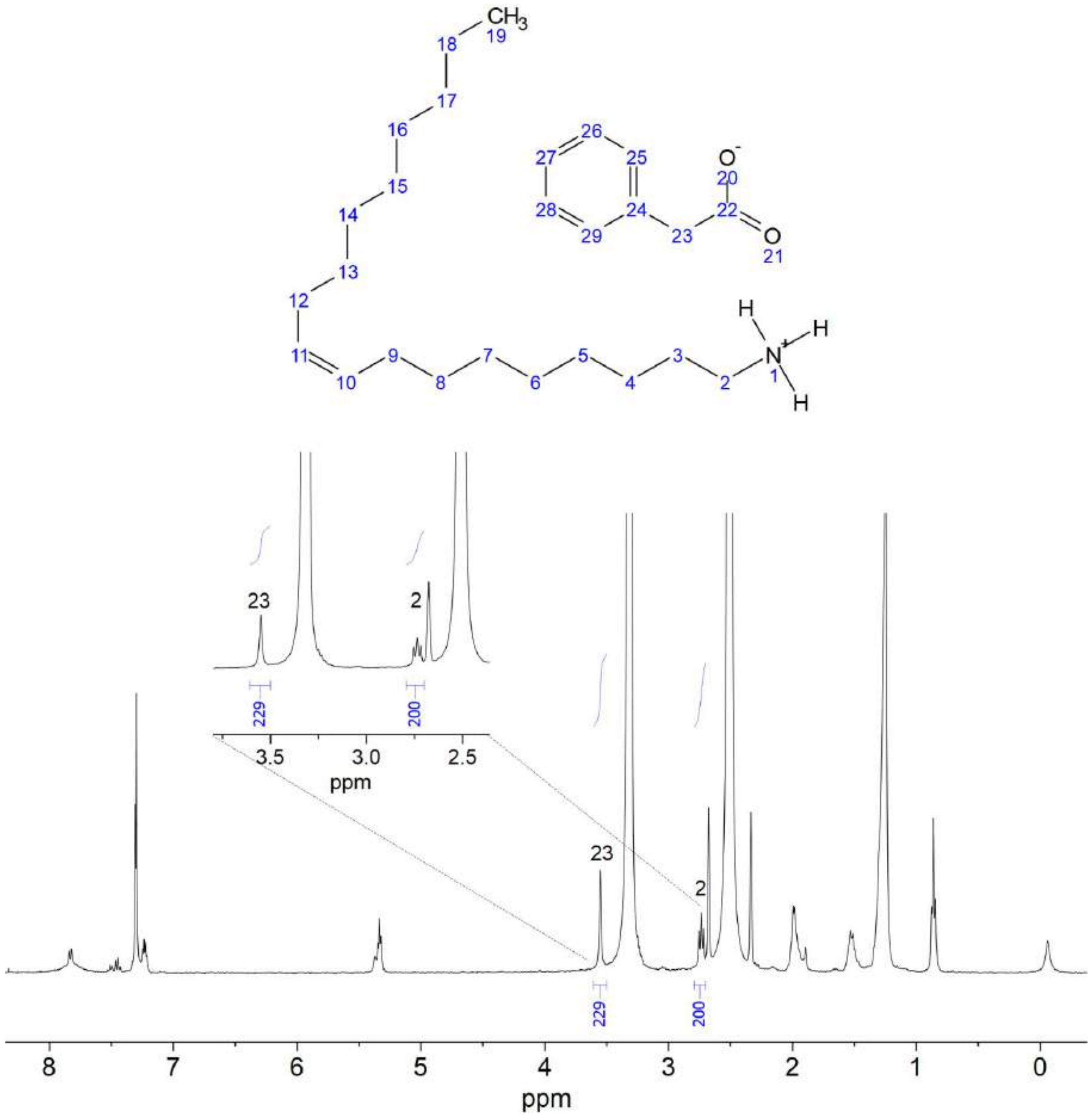

Figure S6. ^{1}H NMR spectrum of Bi-doped $Cs_2Ag_{1-x}Na_xInCl_6$ NCs after their dissolution in DMSO-d6. The ratio between the integrated areas of the peaks at 3.3 ppm (**23**, representative of the PhAc) and at 2.5 ppm (**2,** representative of the oleylamine) is 1.15:1.

Estimate of the number of surface sites passivated by PhAc and C18B

A cubic NC having a side of 24.4 nm (and surface terminated by CsCl) the surface area is 3572.16nm^2 and it is characterized by 13256 Cl and 13254 Cs surface sites.

The NMR analysis yielded a number of PhAc species per NC of 10575 and a number of C18B species per NC of 6932. The resulting surface coverage is 4.92 ligands/nm^2 with 80% of Cl surface sites are occupied by PhAc and 52% of Cs surface sites occupied by C18B.

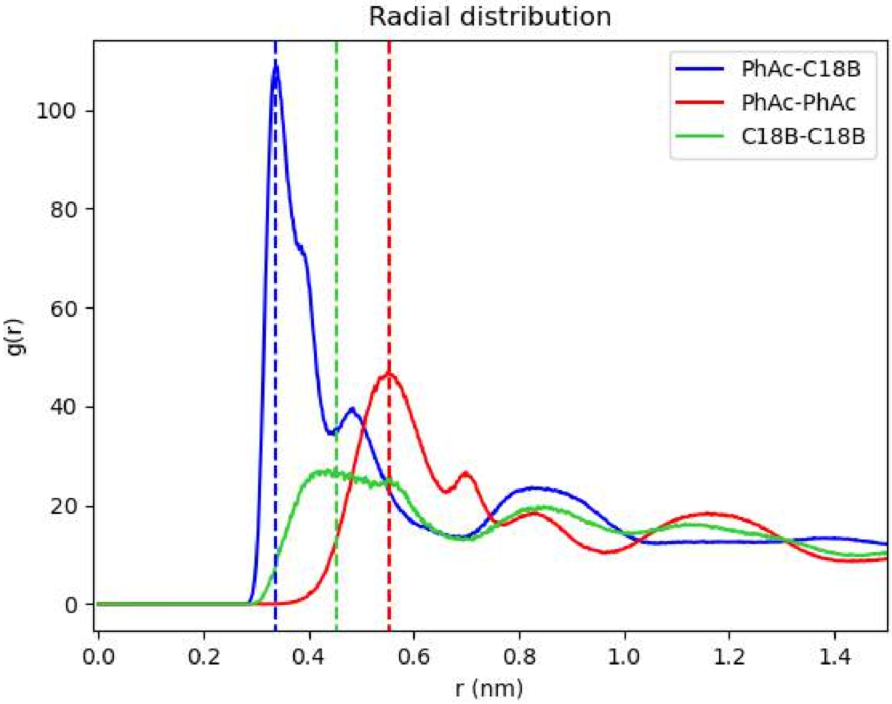

Figure S7. Time-average radial distribution functions obtained from the MD simulations at room temperature of a ~6.0 nm $Cs_2AgInCl_6$ NC capped with 82% PhAc / 54% C18B, corresponding to the probability of finding: (red) PhAcs ligands around a given PhAc ligand; (green) C18B ligands around a given C18B ligand; (blue) PhAcs ligands around a given C18B ligand or viceversa. For each curve, the dashed line indicates the radial distance at the initial maximum which characterizes the average distance between nearest-neighbor ligands. The distances between ligands are calculated using the positions of their head groups (carbon atoms of the anchoring carboxylate groups and nitrogen atoms of the anchoring ammonium groups for PhAc and C18B, respectively). The figure shows that the relative distance between PhAc and OLAM is shorter than pairs of PhAc and OLAM combinations indicating that the two types of ligands are intermixed.

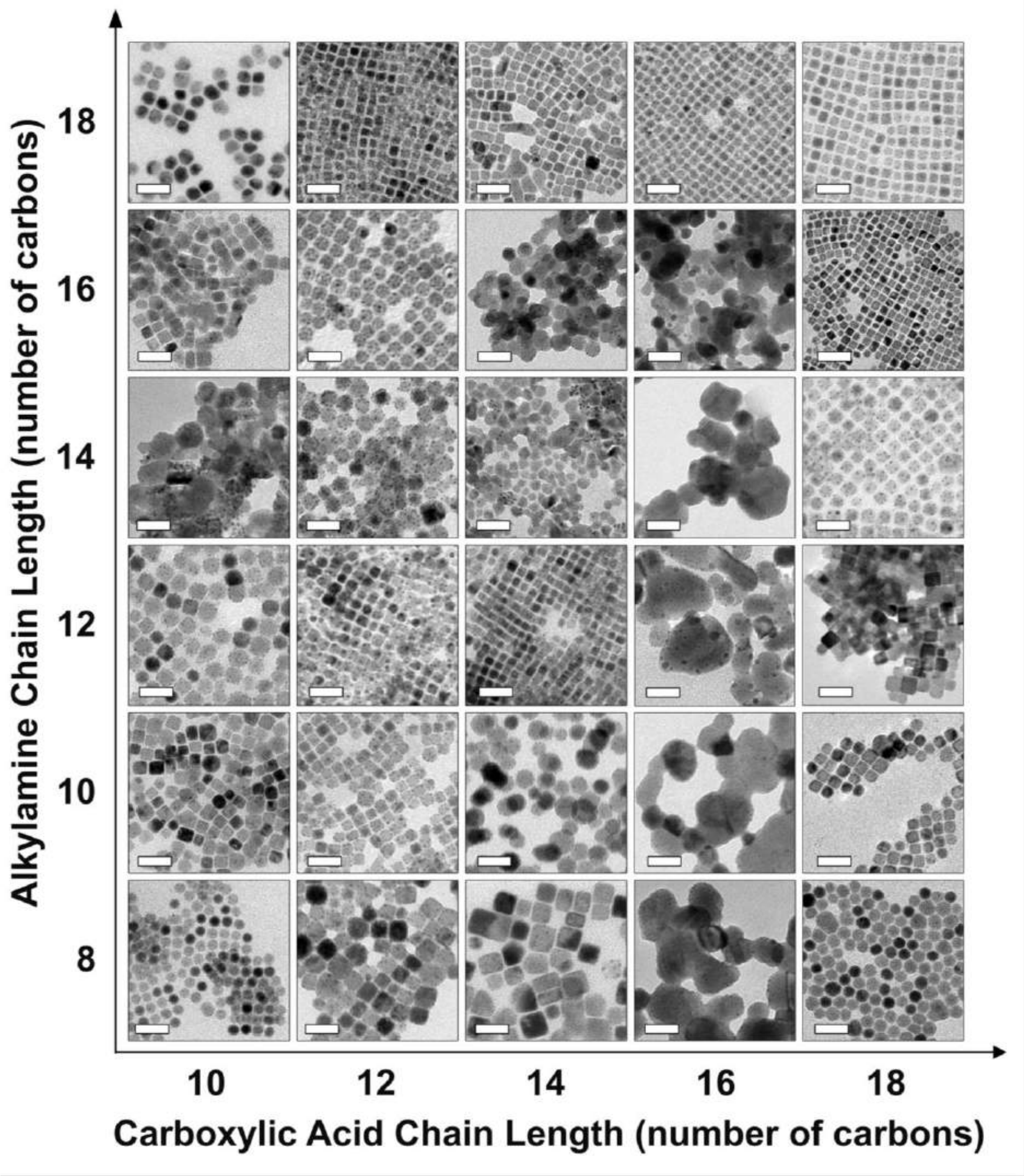

Figure S8. TEM images of Bi-doped $Cs_2Ag_{1-x}Na_xInCl_6$ NCs synthesized with different combinations of alkylamines and carboxylic acids. Scalebars are 50nm.

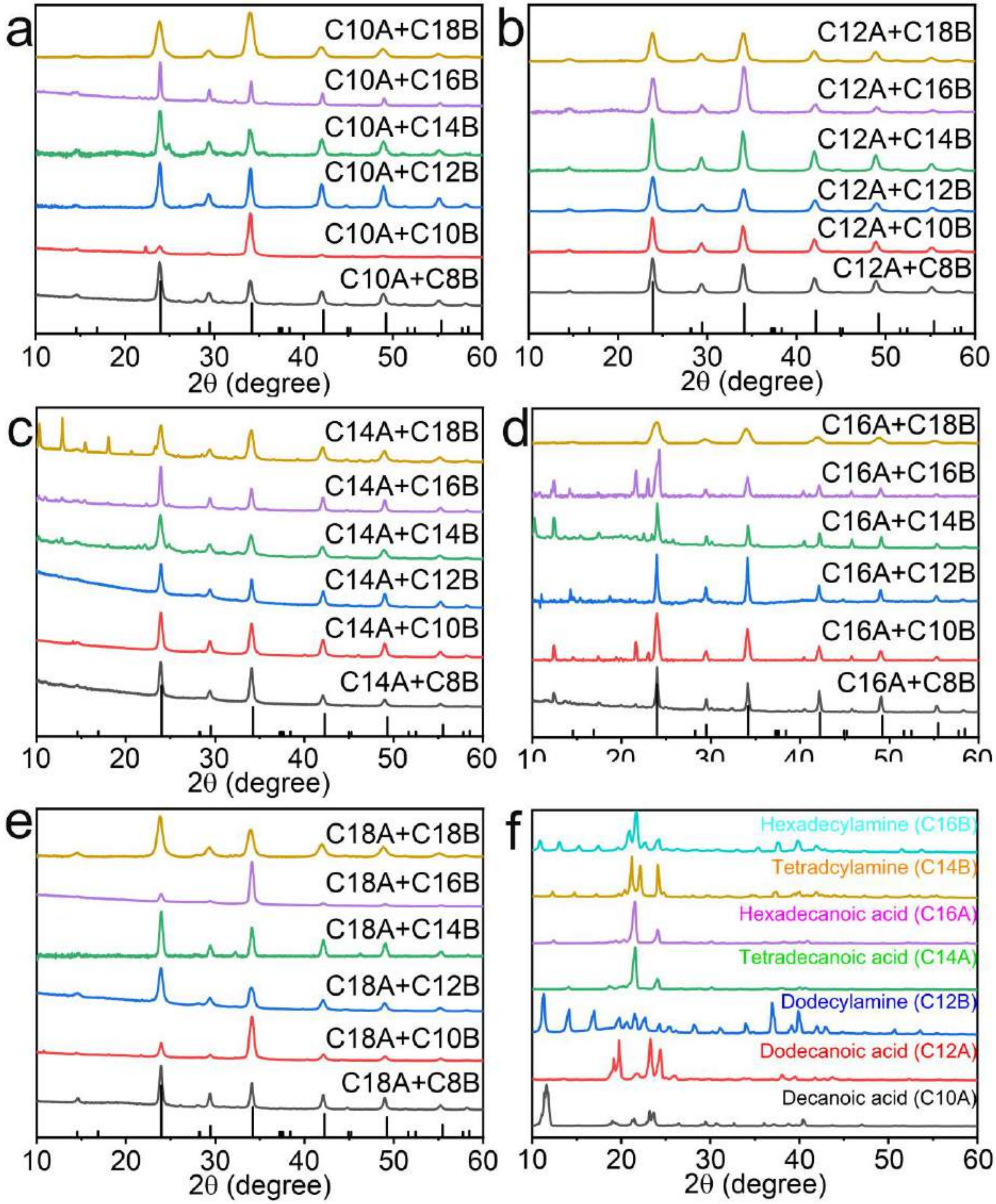

Figure S9. (a-e) XRD patterns of samples obtained with different combinations of alkylamines and carboxylic acids. (f) XRD patterns of hexadecilamine (C16B), tetradecylamine (C14B), hexadecanoic acid (C16A) and tetradecanoic acid (C14A). The impurity peaks present in some of the products in (a-e) can be attributed to the presence of either alkylamines and/or carboxylic acids shown in (f) which could not be washed away from the nanocrystals.

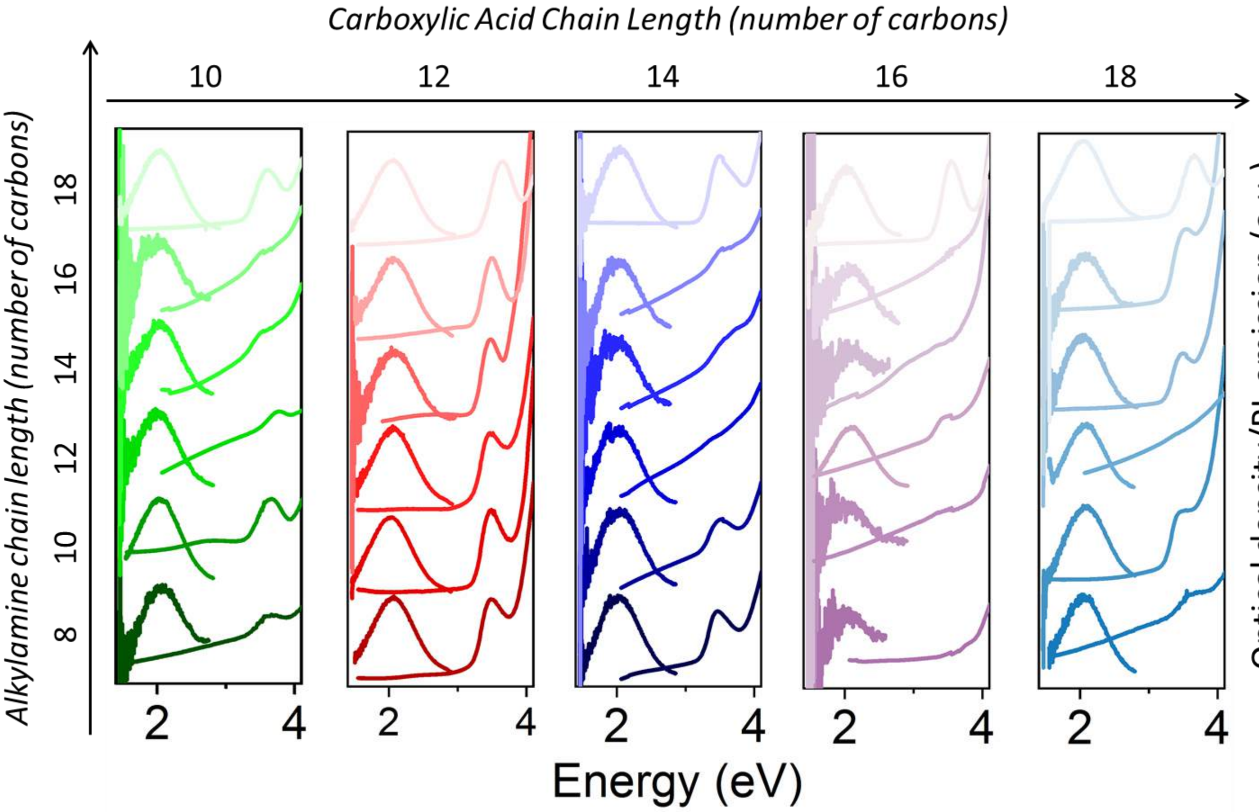

Figure S10. Absorption spectra and PL emission curves of Bi-doped $Cs_2Ag_{1-x}Na_xInCl_6$ NCs obtained with different combinations of alkylamines and carboxylic acids.

Table S2. PLQY values and mean NC size measured for Bi-doped $Cs_2Ag_{1-x}Na_xInCl_6$ NCs synthesized using different carboxylic acid-alkylamine combinations.

Sample	**PLQY (%)**	**Mean Size (nm)**
C10A-C8B	22	16.1 ± 1.7
C10A-C10B	25	14.4 ± 3.1
C10A-C12B	14	17.4 ± 2.9
C10A-C14B	20	21.1 ± 4.5
C10A-C16B	23	50.2 ± 14.5
C10A-C18B	23	14.3 ± 1.7
C12A-C8B	26	20.5 ± 2.1
C12A-C10B	37	12.5 ± 1.2
C12A-C12B	26	13.1 ± 1.9
C12A-C14B	15	17.2 ± 2.9
C12A-C16B	30	14.1 ± 2.9
C12A-C18B	26	9.9 ± 1.1
C14A-C8B	27	23.2 ± 5.3
C14A-C10B	26	19.3 ± 3.4
C14A-C12B	25	10.5 ± 1.2
C14A-C14B	16	13.7 ± 2.6
C14A-C16B	17	19.2 ± 2.9
C14A-C18B	24	14.2 ± 1.5
C16A-C8B	4	Heavily aggregated
C16A-C10B	16	Heavily aggregated
C16A-C12B	0	Heavily aggregated
C16A-C14B	0	Heavily aggregated
C16A-C16B	0	Heavily aggregated
C16A-C18B	16	8.9 ± 1.1
C18A-C8B	23	17.8 ± 2.5
C18A-C10B	25	18.0 ± 2.3
C18A-C12B	17	16.5 ± 3.8
C18A-C14B	21	14.5 ± 1.5
C18A-C16B	21	13.0 ± 1.5
C18A-C18B	21	12.0 ± 0.9

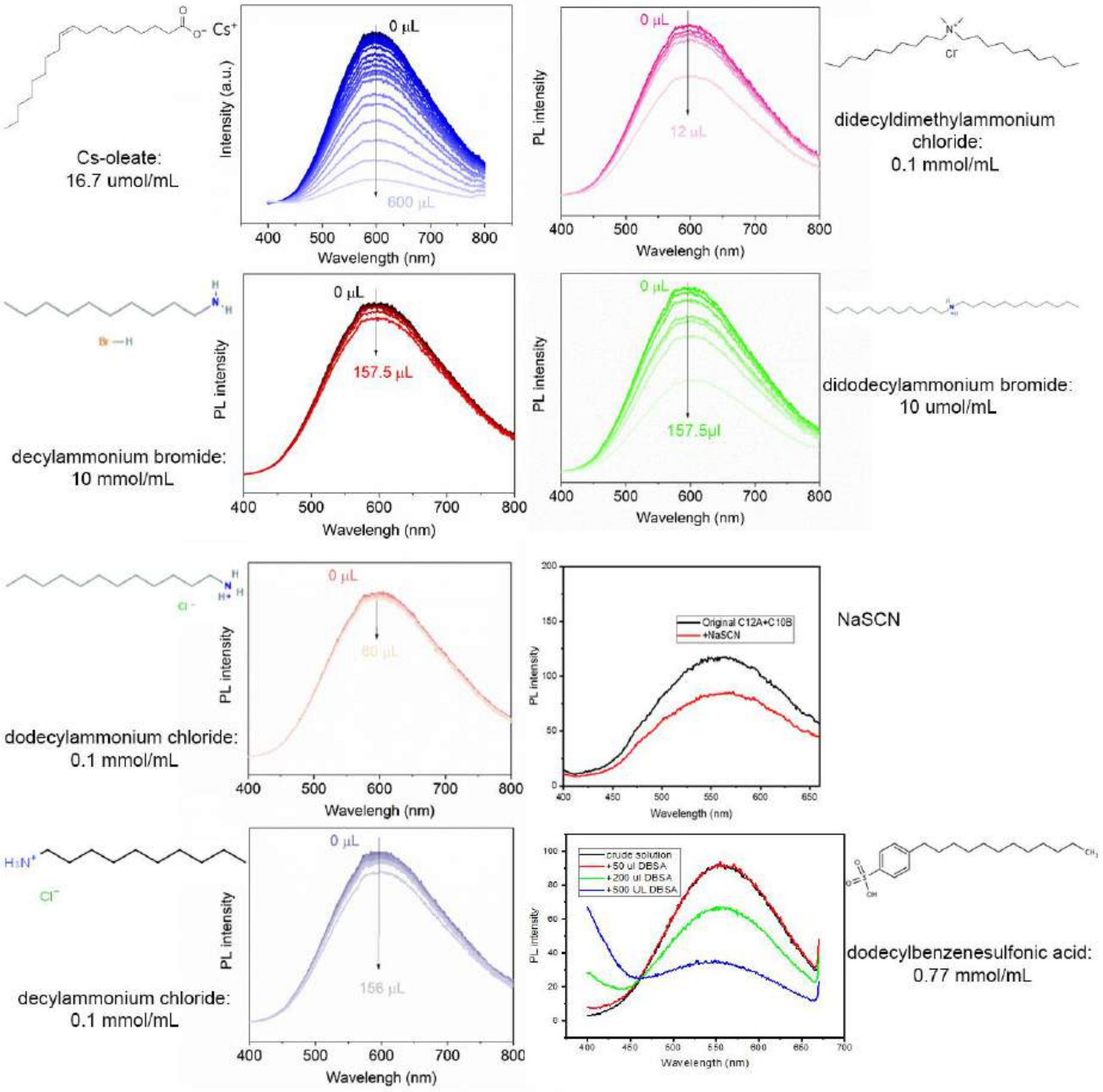

Figure S11. Variation of the PL emission of DP NCs obtained with C12A-C10B and exposed to different ligand pairs.

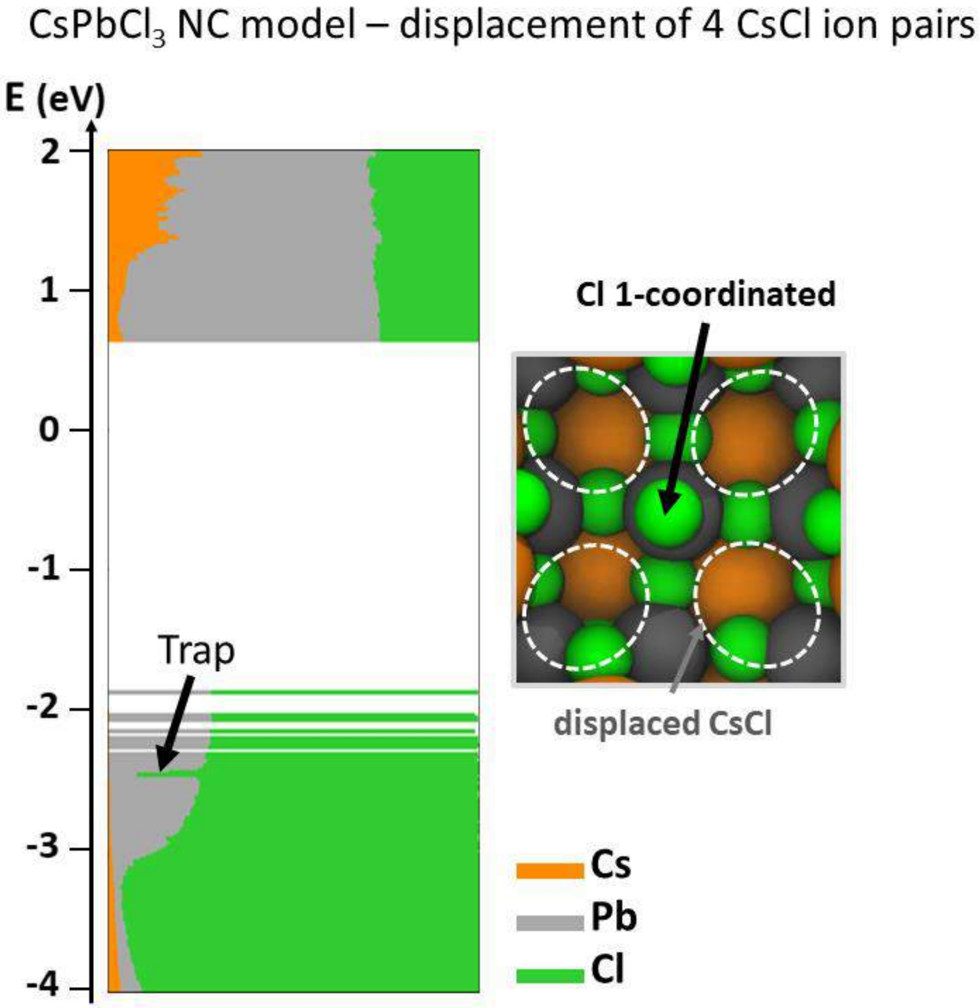

Figure S12. (left) Electronic structure of a ~3.0 nm $Cs_{324}Pb_{216}Cl_{756}$ NC model optimized at the DFT/PBE level of theory after the removal of four CsCl ion pairs around a Cl ion. This Cl ion although coordinated by only one nearby ion (the Pb below it), contributes to the formation of "shallow" trap states, well within the valence band. This is in strike contrast with the double perovskite nanocrystal presented in the main text. (right) Relaxed structure of the NC model illustrating the one-coordinated Cl surrounding.

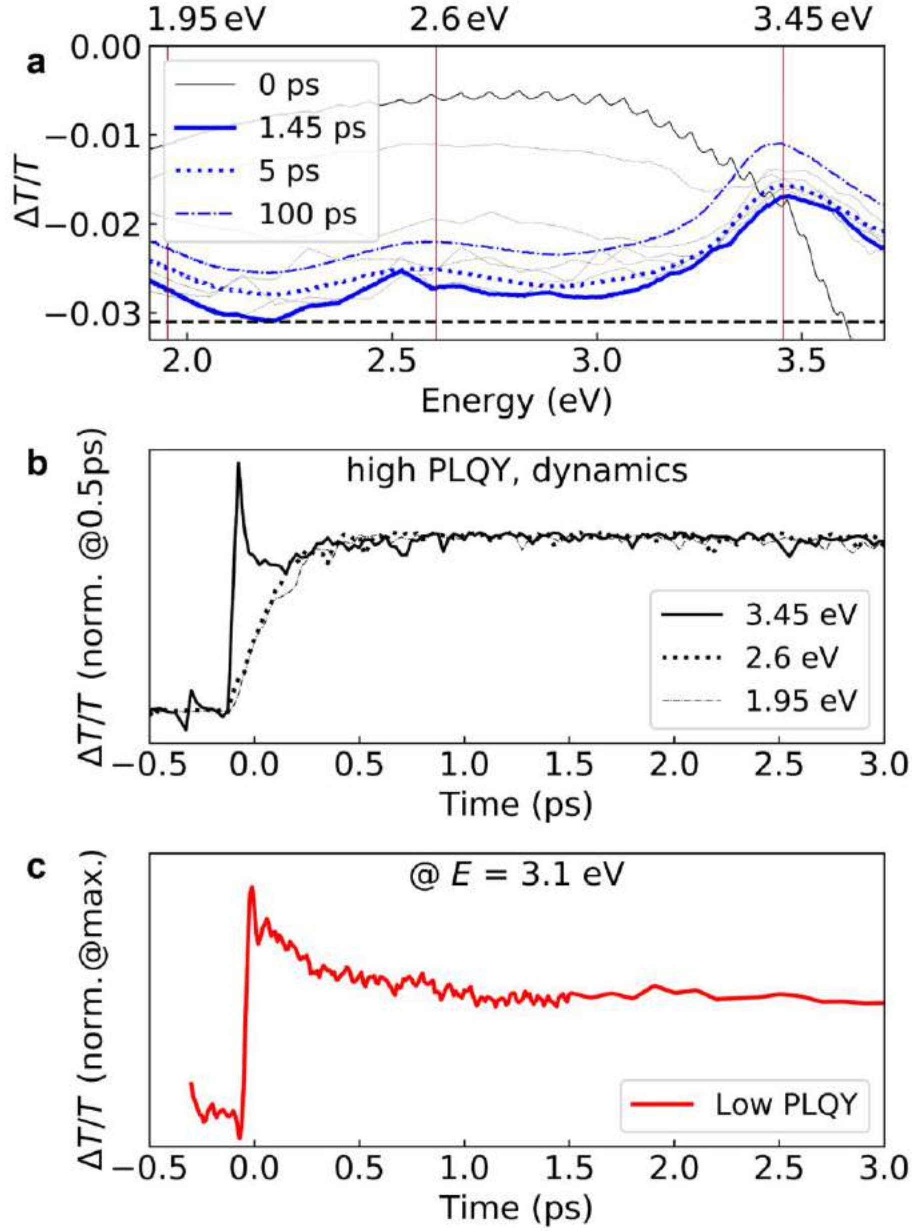

Figure S13. a) Transient absorption spectra for the representative high PLQY sample. The three major bleach features, corresponding to the transition involving electronic states deep in the conduction band and the localized exciton, are clearly visible. A broad photoinduced absorption (PIA) covers the entire spectral region, superimposing a strong negative background. Overlapped to this negative PIA signal, which arises immediately after photoexcitation (0 ps) and has fully evolved within approximately 1.45 ps (grey thin lines), there is the simultaneous rise of the bleach features mentioned above. The PIA signal might be due to the presence of very dense optically inactive states within the valence band (VB) and conduction band (CB) that become accessible after photoexcitation only. b) Pump-probe dynamics in the first few picoseconds at the three main feature (E = 1.95 eV, 2.6V and 3.45 eV, as highlighted in the first panel). The similar rise time of approximately 0.5 ps of these transitions indicates that they share a common state which, in our case, it is most probably connected to the hole since the dynamics in the CB does not contribute significantly to the signal. c) Pump-probe dynamics of representative low PLQY sample~~s~~ (15%) at E = 3.1eV. This novel transition is most probably related to transitions involving surface trap states. The immediate signal rise time indicates that an ultrafast hole trapping takes place followed by a recovery of the signal, and thus a depletion of this state, within a few picoseconds only.

REFERENCES:

(1) Yuan, M.; Quan, L. N.; Comin, R.; Walters, G.; Sabatini, R.; Voznyy, O.; Hoogland, S.; Zhao, Y.; Beauregard, E. M.; Kanjanaboos, P.; Lu, Z.; Kim, D. H.; Sargent, E. H., Perovskite Energy Funnels for Efficient Light-Emitting Diodes. *Nat. Nanotechnol.* **2016,** *11*, 872-877.

(2) Angewandte Chemie International EditionAkkerman, Q. A.; Rainò, G.; Kovalenko, M. V.; Manna, L., Genesis, Challenges and Opportunities for Colloidal Lead Halide Perovskite Nanocrystals. *Nat. Mater.* **2018,** *17*, 394-405.

(3) He, X.; Qiu, Y.; Yang, S., Fully-Inorganic Trihalide Perovskite Nanocrystals: A New Research Frontier of Optoelectronic Materials. *Adv. Mater.* **2017,** *29*.

(4) Luo, J.; Wang, X.; Li, S.; Liu, J.; Guo, Y.; Niu, G.; Yao, L.; Fu, Y.; Gao, L.; Dong, Q.; Zhao, C.; Leng, M.; Ma, F.; Liang, W.; Wang, L.; Jin, S.; Han, J.; Zhang, L.; Etheridge, J.; Wang, J.; Yan, Y.; Sargent, E. H.; Tang, J., Efficient and Stable Emission of Warm-White Light from Lead-Free Halide Double Perovskites. *Nature* **2018,** *563*, 541-545.

(5) Song, Z.; Shrestha, N.; Watthage, S. C.; Liyanage, G. K.; Almutawah, Z. S.; Ahangharnejhad, R. H.; Phillips, A. B.; Ellingson, R. J.; Heben, M. J., Impact of Moisture on Photoexcited Charge Carrier Dynamics in Methylammonium Lead Halide Perovskites. *J. Phys. Chem. Lett.* **2018,** *9*, 6312-6320.

(6) Leng, M.; Chen, Z.; Yang, Y.; Li, Z.; Zeng, K.; Li, K.; Niu, G.; He, Y.; Zhou, Q.; Tang, J., Lead-Free, Blue Emitting Bismuth Halide Perovskite Quantum Dots. *Angew. Chem., Int. Ed. Engl.* **2016,** *55*, 15012-15016.

(7) Filip, M. R.; Hillman, S.; Haghighirad, A. A.; Snaith, H. J.; Giustino, F., Band Gaps of the Lead-Free Halide Double Perovskites $Cs_2BiAgCl_6$ and $Cs_2BiAgBr_6$ from Theory and Experiment. *J. Phys. Chem. Lett.* **2016,** *7*, 2579-2585.

(8) Vasala, S.; Karppinen, M., $A_2B'B''O_6$ Perovskites: A Review. *Prog. Solid State Chem.* **2015,** *43*, 1-36.

(9) Xuan, T.; Xie, R.-J., Recent Processes on Light-Emitting Lead-Free Metal Halide Perovskites. *Chem. Eng. J.* **2020,** *393*, 124757.

(10) Pham, H. Q.; Holmes, R. J.; Aydil, E. S.; Gagliardi, L., Lead-Free Double Perovskites $Cs_2InCuCl_6$ and $(CH_3NH_3)_2InCuCl_6$: Electronic, Optical, and Electrical Properties. *Nanoscale* **2019,** *11*, 11173-11182.

(11) Lv, K.; Qi, S.; Liu, G.; Lou, Y.; Chen, J.; Zhao, Y., Lead-Free Silver-Antimony Halide Double Perovskite Quantum Dots with Superior Blue Photoluminescence. *Chem. Commun. (Cambridge, U. K.)* **2019,** *55*, 14741-14744.

(12) Dahl, J. C.; Osowiecki, W. T.; Cai, Y.; Swabeck, J. K.; Bekenstein, Y.; Asta, M.; Chan, E. M.; Alivisatos, A. P., Probing the Stability and Band Gaps of $Cs_2AgInCl_6$ and $Cs_2AgSbCl_6$ Lead-Free Double Perovskite Nanocrystals. *Chem. Mater.* **2019,** *31*, 3134-3143.

(13) Zhou, J.; Rong, X.; Zhang, P.; Molokeev, M. S.; Wei, P.; Liu, Q.; Zhang, X.; Xia, Z., Manipulation of Bi^{3+}/In^{3+} Transmutation and Mn^{2+}-Doping Effect on the Structure and Optical Properties of Double Perovskite $Cs_2NaBi_{1-x}In_xCl_6$. *Adv. Opt. Mater.* **2019,** *7*, 1801435.

(14) Zhang, Y.; Shah, T.; Deepak, F. L.; Korgel, B. A., Surface Science and Colloidal Stability of Double-Perovskite $Cs_2AgBiBr_6$ Nanocrystals and Their Superlattices. *Chem. Mater.* **2019,** *31*, 7962-7969.

(15) Yang, D.; Li, X.; Zhou, W.; Zhang, S.; Meng, C.; Wu, Y.; Wang, Y.; Zeng, H., $CsPbBr_3$ Quantum Dots 2.0: Benzenesulfonic Acid Equivalent Ligand Awakens Complete Purification. *Adv. Mater.* **2019,** *0*, 1900767.

(16) Luo, J.; Li, S.; Wu, H.; Zhou, Y.; Li, Y.; Liu, J.; Li, J.; Li, K.; Yi, F.; Niu, G.; Tang, J., $Cs_2AgInCl_6$ Double Perovskite Single Crystals: Parity Forbidden Transitions and Their Application for Sensitive and Fast Uv Photodetectors. *ACS Photonics* **2017,** *5*, 398-405.

(17) Meng, W.; Wang, X.; Xiao, Z.; Wang, J.; Mitzi, D. B.; Yan, Y., Parity-Forbidden Transitions and Their Impact on the Optical Absorption Properties of Lead-Free Metal Halide Perovskites and Double Perovskites. *J. Phys. Chem. Lett.* **2017,** *8*, 2999-3007.

(18) Zhao, F.; Song, Z.; Zhao, J.; Liu, Q., Double Perovskite $Cs_2AgInCl_6$:Cr^{3+}: Broadband and near-Infrared Luminescent Materials. *Inorg. Chem. Front.* **2019,** *6*, 3621-3628.

(19) Dave, K.; Fang, M. H.; Bao, Z.; Fu, H. T.; Liu, R. S., Recent Developments in Lead-Free Double Perovskites: Structure, Doping, and Applications. *Chem. - Asian J.* **2020,** *15*, 242-252.

(20) Zhao, X.-G.; Yang, D.; Ren, J.-C.; Sun, Y.; Xiao, Z.; Zhang, L., Rational Design of Halide Double Perovskites for Optoelectronic Applications. *Joule* **2018,** *2*, 1662-1673.

(21) Chen, N.; Cai, T.; Li, W.; Hills-Kimball, K.; Yang, H.; Que, M.; Nagaoka, Y.; Liu, Z.; Yang, D.; Dong, A.; Xu, C. Y.; Zia, R.; Chen, O., Yb- and Mn-Doped Lead-Free Double Perovskite Cs_2AgBiX_6 ($X = Cl^-$, Br^-) Nanocrystals. *ACS Appl. Mater. Interfaces* **2019,** *11*, 16855-16863.

(22) Locardi, F.; Cirignano, M.; Baranov, D.; Dang, Z.; Prato, M.; Drago, F.; Ferretti, M.; Pinchetti, V.; Fanciulli, M.; Brovelli, S.; De Trizio, L.; Manna, L., Colloidal Synthesis of Double Perovskite $Cs_2AgInCl_6$ and Mn-Doped $Cs_2AgInCl_6$ Nanocrystals. *J. Am. Chem. Soc.* **2018,** *140*, 12989-12995.

(23) Liu, Y.; Jing, Y.; Zhao, J.; Liu, Q.; Xia, Z., Design Optimization of Lead-Free Perovskite $Cs_2AgInCl_6$:Bi Nanocrystals with 11.4% Photoluminescence Quantum Yield. *Chem. Mater.* **2019,** *31*, 3333-3339.

(24) Lee, W.; Hong, S.; Kim, S., Colloidal Synthesis of Lead-Free Silver–Indium Double-Perovskite $Cs_2AgInCl_6$ Nanocrystals and Their Doping with Lanthanide Ions. *J. Phys. Chem. C* **2019,** *123*, 2665-2672.

(25) Mahor, Y.; Mir, W. J.; Nag, A., Synthesis and Near-Infrared Emission of Yb-Doped $Cs_2AgInCl_6$ Double Perovskite Microcrystals and Nanocrystals. *J. Phys. Chem. C* **2019,** *123*, 15787-15793.

(26) Arfin, H.; Kaur, J.; Sheikh, T.; Chakraborty, S.; Nag, A., Bi^{3+}-Er^{3+} and Bi^{3+}-Yb^{3+} Codoped $Cs_2AgInCl_6$ Double Perovskite near-Infrared Emitters. *Angew. Chem., Int. Ed.* **2020,** *59*, 11307-11311.

(27) Du, K. Z.; Meng, W.; Wang, X.; Yan, Y.; Mitzi, D. B., Bandgap Engineering of Lead-Free Double Perovskite $Cs_2AgBiBr_6$ through Trivalent Metal Alloying. *Angew. Chem., Int. Ed.* **2017,** *56*, 8158-8162.

(28) Tran, T. T.; Panella, J. R.; Chamorro, J. R.; Morey, J. R.; McQueen, T. M., Designing Indirect–Direct Bandgap Transitions in Double Perovskites. *Mater. Horiz.* **2017,** *4*, 688-693.

(29) Manna, D.; Das, T. K.; Yella, A., Tunable and Stable White Light Emission in Bi^{3+}-Alloyed $Cs_2AgInCl_6$ Double Perovskite Nanocrystals. *Chem. Mater.* **2019,** *31*, 10063-10070.

(30) Gray, M. B.; Majher, J. D.; Strom, T. A.; Woodward, P. M., Broadband White Emission in $Cs_2AgIn_{1-x}Bi_xCl_6$ Phosphors. *Inorg. Chem.* **2019,** *58*, 13403-13410.

(31) Yang, B.; Mao, X.; Hong, F.; Meng, W.; Tang, Y.; Xia, X.; Yang, S.; Deng, W.; Han, K., Lead-Free Direct Band Gap Double-Perovskite Nanocrystals with Bright Dual-Color Emission. *J. Am. Chem. Soc.* **2018,** *140*, 17001-17006.

(32) Locardi, F.; Sartori, E.; Buha, J.; Zito, J.; Prato, M.; Pinchetti, V.; Zaffalon, M. L.; Ferretti, M.; Brovelli, S.; Infante, I.; De Trizio, L.; Manna, L., Emissive Bi-Doped Double Perovskite $Cs_2Ag_{1-x}Na_xInCl_6$ Nanocrystals. *ACS Energy Lett.* **2019,** *4*, 1976-1982.

(33) Peng, W.; Anand, B.; Liu, L.; Sampat, S.; Bearden, B. E.; Malko, A. V.; Chabal, Y. J., Influence of Growth Temperature on Bulk and Surface Defects in Hybrid Lead Halide Perovskite Films. *Nanoscale* **2016,** *8*, 1627-34.

(34) Zheng, X.; Chen, B.; Dai, J.; Fang, Y.; Bai, Y.; Lin, Y.; Wei, H.; Zeng, Xiao C.; Huang, J., Defect Passivation in Hybrid Perovskite Solar Cells Using Quaternary Ammonium Halide Anions And cations. *Nat. Energy* **2017,** *2*, 17102.

(35) Bohn, B. J.; Tong, Y.; Gramlich, M.; Lai, M. L.; Doblinger, M.; Wang, K.; Hoye, R. L. Z.; Muller-Buschbaum, P.; Stranks, S. D.; Urban, A. S.; Polavarapu, L.; Feldmann, J., Boosting Tunable Blue Luminescence of Halide Perovskite Nanoplatelets through Postsynthetic Surface Trap Repair. *Nano Lett.* **2018,** *18*, 5231-5238.

(36) Barker, A. J.; Sadhanala, A.; Deschler, F.; Gandini, M.; Senanayak, S. P.; Pearce, P. M.; Mosconi, E.; Pearson, A. J.; Wu, Y.; Srimath Kandada, A. R.; Leijtens, T.; De Angelis, F.; Dutton, S. E.; Petrozza, A.; Friend, R. H., Defect-Assisted Photoinduced Halide Segregation in Mixed-Halide Perovskite Thin Films. *ACS Energy Lett.* **2017,** *2*, 1416-1424.

(37) Shamsi, J.; Urban, A. S.; Imran, M.; De Trizio, L.; Manna, L., Metal Halide Perovskite Nanocrystals: Synthesis, Post-Synthesis Modifications, and Their Optical Properties. *Chem. Rev.* **2019,** *119*, 3296-3348.

(38) ten Brinck, S.; Zaccaria, F.; Infante, I., Defects in Lead Halide Perovskite Nanocrystals: Analogies and (Many) Differences with the Bulk. *ACS Energy Lett.* **2019,** *4*, 2739-2747.

(39) Yang, D.; Li, X.; Zeng, H., Surface Chemistry of All Inorganic Halide Perovskite Nanocrystals: Passivation Mechanism and Stability. *Adv. Mater. Interfaces* **2018,** *5*, 1701662.

(40) Yang, D.; Cao, M.; Zhong, Q.; Li, P.; Zhang, X.; Zhang, Q., All-Inorganic Cesium Lead Halide Perovskite Nanocrystals: Synthesis, Surface Engineering and Applications. *J. Mater. Chem. C* **2019,** *7*, 757-789.

(41) Zhang, Y.; Siegler, T. D.; Thomas, C. J.; Abney, M. K.; Shah, T.; De Gorostiza, A.; Greene, R. M.; Korgel, B. A., A "Tips and Tricks" Practical Guide to the Synthesis of Metal Halide Perovskite Nanocrystals. *Chem. Mater.* **2020,** *32*, 5410-5423.

(42) Patai, S., *The Chemistry of Acyl Halides*. John Wiley & Sons Ltd: UK, 1972.

(43) Imran, M.; Caligiuri, V.; Wang, M.; Goldoni, L.; Prato, M.; Krahne, R.; De Trizio, L.; Manna, L., Benzoyl Halides as Alternative Precursors for the Colloidal Synthesis of Lead-Based Halide Perovskite Nanocrystals. *J. Am. Chem. Soc.* **2018,** *140*, 2656-2664.

(44) De Roo, J.; Ibáñez, M.; Geiregat, P.; Nedelcu, G.; Walravens, W.; Maes, J.; Martins, J. C.; Van Driessche, I.; Kovalenko, M. V.; Hens, Z., Highly Dynamic Ligand Binding and Light Absorption Coefficient of Cesium Lead Bromide Perovskite Nanocrystals. *ACS Nano* **2016,** *10*, 2071-2081.

(45) Han, P.; Zhang, X.; Mao, X.; Yang, B.; Yang, S.; Feng, Z.; Wei, D.; Deng, W.; Pullerits, T.; Han, K., Size Effect of Lead-Free Halide Double Perovskite on Luminescence Property. *Sci. China: Chem.* **2019,** *62*, 1405-1413.

(46) Lamba, R. S.; Basera, P.; Bhattacharya, S.; Sapra, S., Band Gap Engineering in $Cs_2(Na_xAg_{1-x})BiCl_6$ Double Perovskite Nanocrystals. *J. Phys. Chem. Lett.* **2019,** *10*, 5173-5181.

(47) Yao, M. M.; Wang, L.; Yao, J. S.; Wang, K. H.; Chen, C.; Zhu, B. S.; Yang, J. N.; Wang, J. J.; Xu, W. P.; Zhang, Q.; Yao, H. B., Improving Lead-Free Double Perovskite $Cs_2NaBiCl_6$ Nanocrystal Optical Properties Via Ion Doping. *Adv. Opt. Mater.* **2020**, 1901919.

(48) Yoo, D.; Woo, J. Y.; Kim, Y.; Kim, S. W.; Wei, S. H.; Jeong, S.; Kim, Y. H., Origin of the Stability and Transition from Anionic to Cationic Surface Ligand Passivation of All-Inorganic Cesium Lead Halide Perovskite Nanocrystals. *J. Phys. Chem. Lett.* **2020,** *11*, 652-658.

(49) Pan, A.; He, B.; Fan, X.; Liu, Z.; Urban, J. J.; Alivisatos, A. P.; He, L.; Liu, Y., Insight into the Ligand-Mediated Synthesis of Colloidal $CsPbBr_3$ Perovskite Nanocrystals: The Role of Organic Acid, Base, and Cesium Precursors. *ACS Nano* **2016,** *10*, 7943-7954.

(50) Smock, S. R.; Williams, T. J.; Brutchey, R. L., Quantifying the Thermodynamics of Ligand Binding to $CsPbBr_3$ Quantum Dots. *Angew. Chem., Int. Ed.* **2018,** *57*, 11711-11715.

(51) Almeida, G.; Goldoni, L.; Akkerman, Q.; Dang, Z.; Khan, A. H.; Marras, S.; Moreels, I.; Manna, L., Role of Acid–Base Equilibria in the Size, Shape, and Phase Control of Cesium Lead Bromide Nanocrystals. *ACS Nano* **2018,** *12*, 1704-1711.

(52) Almeida, G.; Goldoni, L.; Akkerman, Q.; Dang, Z.; Khan, A. H.; Marras, S.; Moreels, I.; Manna, L., Role of Acid-Base Equilibria in the Size, Shape, and Phase Control of Cesium Lead Bromide Nanocrystals. *ACS Nano* **2018,** *12*, 1704-1711.

(53) Nenon, D. P.; Pressler, K.; Kang, J.; Koscher, B. A.; Olshansky, J. H.; Osowiecki, W. T.; Koc, M. A.; Wang, L.-W.; Alivisatos, A. P., Design Principles for Trap-Free $CsPbX_3$ Nanocrystals: Enumerating and Eliminating Surface Halide Vacancies with Softer Lewis Bases. *J. Am. Chem. Soc.* **2018,** *140*, 17760-17772.

(54) Almeida, G.; Ashton, O. J.; Goldoni, L.; Maggioni, D.; Petralanda, U.; Mishra, N.; Akkerman, Q. A.; Infante, I.; Snaith, H. J.; Manna, L., The Phosphine Oxide Route toward Lead Halide Perovskite Nanocrystals. *J. Am. Chem. Soc.* **2018,** *140*, 14878-14886.

5.2 Optical center analysis of $Rb_7Sb_3Cl_{16}$ Nanocrystals

ABSTRACT: The Sb^{3+} based metal halide is another important metal halide material. The emission color of Sb^{3+} could be adjust from blue to red by changing its surrounding environment. In some reports, the PLQY of Sb^{3+} doped materials could reach over 90% PLQY. In present study, the colloidal $Rb_7Sb_3Cl_{16}$ NCs which comprised by both isolated $[SbCl_6]^{3-}$ octahedra and isolated $[Sb_2Cl_{10}]^{4-}$ dimers of octahedra were obtained. To clarify which is the excitation center (the single octahedral, the dimers or both) in such comprised structure, we compared the $Rb_7Sb_3Cl_{16}$ NCs with Sb-doped Rb_3InCl_6 NCs together. The latter containing only isolated $[SbCl_6]^{3-}$ octahedra. The two system were traced to have remarkably similar behaviors of optical emission. It indicated the $[SbCl_6]^{3-}$ octahedra is the only emissive center, and the dimer is non-emissive. Density functional theory calculations suggest that the $[SbCl_6]^{3-}$ octahedra are optically active in emission because the local arrangement of the Rb^+ ions around the octahedra limits the elongation of the Sb-Cl bonds upon excitation and, thus, helps to confine the self-trapped exciton in them. Conversely, in the $[Sb_2Cl_{10}]^{4-}$ dimers, the constraining effect of the surrounding Rb^+ ions is less marked, so that the Sb-Cl bonds fully break upon photoexcitation, opening up an efficient non-radiative channel for the self-trapped excitons.

INTRODUCTION

LHP NCs have been intensively studied due to its excellent optical properties.[1-7] However the intrinsic toxicity of Pb^{2+} limit their commercial application.[8-9] For these reasons, extensive efforts are being devoted to seek for alternative non-toxic metal halide NC systems with compatible optical properties of LHP NCs.[10-19] Beside the above mentioned DPs, Sb related metal halides are particularly another promising materials, as some of them have been reported to show bright emission in both the bulk and nanoscale.[19-31] For example, Sb-doped $Cs_2NaInCl_6$ and Cs_2KInCl_6 DPs bulk exhibit a blue-green emission with PLQY values of ~80% and 90%, respectively.[20, 22-23, 25] Similarly, Sb-doped bulk Rb_3InCl_6 and Cs_3InCl_6 and their hydrated counterparts feature a bright green or yellow PL emission with PLQY of 95%.[19, 26-29] In addition, Sb^{3+} doped Cs_2SnCl_6 powders exhibit a broadband orange-red emission with a PLQY of 37%,[7]and the Sb^{3+} doped Cs_2ZnCl_4 crystals show a near infrared (NIR) emission with a 70% PLQY.[31] Similar to the DPs case, the Sb-doped NC counterparts, in turn, have been reported to have lower PLQY values (~20% in the case of $Cs_2NaInCl_6$ and Cs_2KInCl_6, ~40% for Rb_3InCl_6 and 8% for Cs_2SnCl_6). It could be caused by the undercoordinated surface Cl^- ions generating non-radiative defect states, as discussed in Chapter 5.1.[30, 32] Such Sb-doped systems are characterized by the presence of $[SbCl_6]^{3-}$ octahedra as emitter centers. More specifically, Sb-doped metal halides reported so far are characterized by: i) analogous near-UV absorption features originating from $^1S_0 \rightarrow {}^3P_0$ and $^1S_0 \rightarrow {}^3P_1$ transitions of $[SbCl_6]^{3-}$ octahedral, such transition is parity allowed but with spin forbidden; ii) PL emission stemming from self-trapped excitons (STE) recombining in the Sb centers, usually with large Stokes shifts and long emission lifetimes (microsecond timescale).[19-24, 26-28, 33]

While the Sb-doped systems have been synthesized and carefully studied, not much is known about pure antimony chloride materials (with a high concentration of Sb).[14-16, 34-37] In this regard, two compounds have been reported so far, namely $Cs_3Sb_2Cl_9$ (reported at the 80s andnon-emissive at RT)[16, 38-40] and $Rb_7Sb_3Cl_{16}$ (recently reported in the form of single crystals).[14] The latter is characterized by a unique 0D crystal structure comprising isolated $[SbCl_6]^{3-}$ octahedra and $[Sb_2Cl_{10}]^{4-}$ dimers (Scheme 1, left panel), respectively. The dimers was comprised by two corner sharing $[SbCl_6]^{3-}$ octahedral. $Rb_7Sb_3Cl_{16}$ crystals exhibit a broad green PL emission (560 nm) with low PLQY (~3.8%) at room temperature.[14] Interestingly, at low temperatures (e.g. 7K) the PLQY of these crystals increases to near unity. With the aim to better elucidate the optical features of $[SbCl_6]^{3-}$ octahedra and $[Sb_2Cl_{10}]^{4-}$ dimers, we synthesized $Rb_7Sb_3Cl_{16}$ NCs and using the Sb-doped Rb_3InCl_6 NCs as control sample which only has isolated $[SbCl_6]^{3-}$ octahedra as emitter center (Scheme 1, right panel).[30] The result of our spectroscopic investigation combined with DFT calculations indicated:

i) In $Rb_7Sb_3Cl_{16}$ NCs, the $[Sb_2Cl_{10}]^{4-}$ dimers are inactive in PL. Only isolated $[SbCl_6]^{3-}$ octahedra are responsible for the broad green emission. Existence of inactive part explains the low PLQY of such NCs (≤1%) compared to that of Sb-doped Rb_3InCl_6 NCs with a PLQY of 40%.[30]

ii) Sb-doped Rb_3InCl_6 NCs and $Rb_7Sb_3Cl_{16}$ NCs share very similar emission peaks that emerge when exciting at different energies (namely 3.5 eV and 4.66 eV) at different temperatures. Hence, both materials are characterized by the same emissive center, the isolated $[SbCl_6]^{3-}$ octahedra. Furthermore, the double emission should stem from two non-degenerate states of the $[SbCl_6]^{3-}$ octahedra but not from two different emissive centers.

iii) At ~100K, the PLQY of both systems is saturated, with a long PL lifetimes in the order of microseconds. When further lowering the temperature down to 5K, the PL lifetimes increase up to milliseconds with no further improvement of PLQY. The milliseconds lifetime generate from the strong triplet character, spin-forbidden of ($^3P_0$) of $[SbCl_6]^{3-}$ octahedra.

The optical behavior of $[SbCl_6]^{3-}$ octahedra and $[Sb_2Cl_{10}]^{4-}$ dimers is clearly described in this work. Such Sb based NCs could has a potential on some applications such as solid-state lighting,[41-42] X-ray scintillation,[43-44] and thermometry.[5, 24]

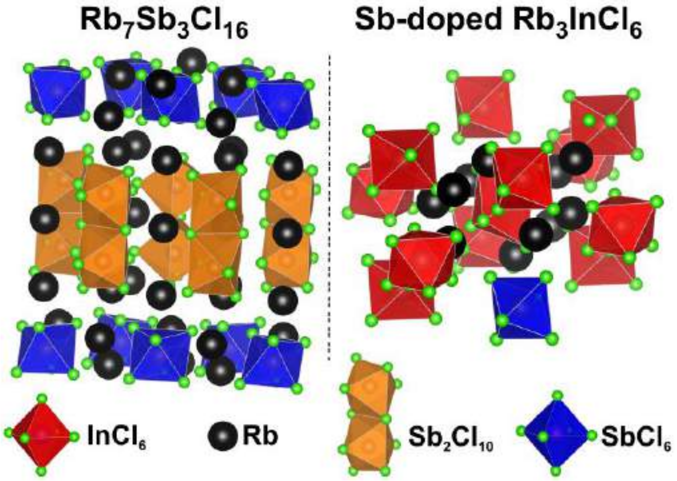

Scheme 1. Structures skeleton of $Rb_7Sb_3Cl_{16}$ and Sb-doped Rb_3InCl_6 nanocrystals.

EXPERIMENTAL SECTION

Chemicals. Rubidium carbonate (Rb_2CO_3, 99%), antimony acetate [Sb(ac)$_3$, 99.99%], Indium acetate [In(ac)$_3$, 99.99%], benzoyl chloride (99%), oleylamine (90%), oleic acid (90%), phenylacetic acid (PhAc, 99%), hexane (anhydrous, 95%), ethyl acetate (EtAc, 99.9%), dioctyl ether (DOE, 99%), dimethyl sulfoxide-d (DMSO-d, 99.9%) and chloroform-d ($CDCl_3$, 99.8%) were purchased from Sigma-Aldrich. All the solvent were anhydrous or degassed before using.

Synthesis of $Rb_7Sb_3Cl_{16}$ NCs. In a typical synthesis, 0.25 mmol of Rb_2CO_3, 0.21 mmol of Sb(ac)$_3$, 3.77 mmol of oleic acid and 1.25 mmol oleylamine were mixed with 4 mL of DOE into a 20 mL glass vial under N_2 protection. The mixture was vigorous heated up to 150 °C under stirring for 5 min to dissolve the metal cation precursors. Subsequently, the temperature was cooled down to 140 °C. At this point, 220 ul (1.72 mmol) of benzoyl chloride in 500 µL of DOE was swiftly injected into the solution to trigger the reaction, which was immediately quenched by immersing the flask in an ice-water bath. The crude solution was added by 10 ml EtAc and then was centrifuged at 4500 rpm for 5 min. The precipitate was dispersed in 3 mL of hexane or chloroform for further characterizations.

Synthesis of Sb-doped Rb_3InCl_6 NCs. Rb_2CO_3 (0.375 mmol), In(ac)$_3$(0.225 mmol), Sb(ac)$_3$(0.025 mmol), 4 ml DOE, 1.2 ml oleic acid, 0.6 ml oleylamine were mixed in a in a 20 ml glass vial under N_2. The mixture was heated on a hotplate up to 140 °C and a solution of 220 µl benzoyl chloride in 0.5 ml of degassed DOE was swiftly injected into the vial. Immediately after the injection, the reaction was quenched by immersion in an ice-water bath. 3 ml of hexane were added to the solution, which was then centrifuged at 4000 rpm for 5 min, and the supernatant was discarded. The precipitated NCs were redispersed in 6 mL of hexane, and centrifuged at 5500 rpm for 5 min. The precipitated NCs were discarded and the supernatant was precipitated by adding 3 ml ethyl acetate and centrifuged at 4000 rpm for 5 min. The precipitated NCs were dispersed in 1.5 ml of hexane and centrifuged at 5500 rpm for 5 min. The supernatant was stored in a vial inside a N_2 filled glovebox for further characterizations.

Transmission Electron microscopy (TEM). Similar with Chapter 4.1.

Powder X-ray diffraction (PXRD). Similar with Chapter 4.1.

Scanning electron microscopy (SEM) energy dispersive X-ray spectroscopy (EDS) and inductively coupled plasma optical spectrometry (ICP-OES). The elemental analysis was performed via energy dispersive X-ray spectroscopy (EDS) on a JEOL JSM-7500FA SEM-Analytical field-emission scanning electron microscopy (SEM) with an Oxford X-Max 80 system equipped with an 80 mm^2 silicon drift detector (SDD). Regarding the small ratio of Mn inside the doped NCs, inductively coupled plasma optical spectrometry (ICP-OES) was carried with an iCAP 6000 spectrometer (Thermo Scientific). The NCs was digested by aqua regia and further diluted by 10 mL of Milli-Q water.

UV−vis Absorption, Photoluminescence (PL) and PL Quantum Yield (QY) Measurements. The UV−visible absorption spectra were recorded using a Varian Cary 300 UV−vis absorption spectrophotometer. Photoluminescence (PL) spectra were acquired using either a 3.5 eV or a 4.66 eV Minilite Continuum Laser as excitation sources with a pulse frequency of 15 Hz and collected with a TM-C10083CA Hamamatsu Spectrometer. Time-resolved PL decays were acquired using the same excitation sources whereas the emitted light was detected by a Hamamatsu R943-02 time-correlated single-photon counting unit coupled to an Oriel Instruments Cornerstone 260 monochromator. PL excitation spectra were acquired us-ing a Varian Cary Eclipse. Temperature-dependent experiments were conducted placing a film of NCs drop-casted onto a glass substrate into a closed circle He cryostat with direct optical access. PL quantum yield was measured using 2,5-Diphenyloxazole as a standard.

Computational Methodology.

Sb-doped Rb_3InCl_6. We have performed atomistic simulations at the Γ point of a Rb_3InCl_6 2x2x2 supercell doped with one Sb^{3+} ion (replacing one In^{3+} ion). The structural relaxation of such supercell was carried out at the density functional theory (DFT) level using the PBE exchange–correlation functional[1] and a double-ζ basis set plus polarization functions on all atoms[2] as implemented in the CP2K 6.1 code[3]. Scalar relativistic effects have been included as effective core potentials. To achieve the occupation of the Sb(5p)-Cl(3p) MOs, thus probing the lowest excited states at the $[SbCl_6]^{3-}$ center, the Sb-Cl bonds were elongated manually by 0.6 Å along the three octahedral axes (one at a time) and the three resulting supercells were relaxed in the triplet state at the same level of theory. The electronic structure of the singlet ground state was then computed on the equilibrium geometry of each of these excited states.

$Rb_7Sb_3Cl_{16}$. We have also performed atomistic simulations at the Γ point of a hexagonal $Rb_7Sb_3Cl_{16}$ cell model, prepared by replacing the disordered layer of $[Sb_2Cl_{10}]^{4-}$ dimers by a partially ordered one, consistently with the work of Benin at al.[4] The structural relaxation of the cell was carried out at the level of theory reported for the Sb-doped Rb_3InCl_6 supercell using the CP2K 6.1 package. The lowest excited states involving hexacoordinated Sb^{3+} ions were probed with the same strategy described above for the Sb-doped Rb_3InCl_6 system. Here, the manual elongation of Sb-Cl bonds was operated along the three octahedral axes of a $[SbCl_6]^{3-}$ center, and along three non-equivalent axes of a $[Sb_2Cl_{10}]^{4-}$centre (the other three being equivalent by symmetry).

RESULT AND DISCUSSION

Structural and optical characterization. The $Rb_7Sb_3Cl_{16}$ NCs were prepared by modifying the standard hot injection method reported by our group.[45] In details, metal precursors were mixed with oleic acid and oleylamine in dioctyl ether under inert atmosphere (N_2). The mixture was heated up to 150 °C to obtain transparent solution and set back to 140 °C after dissolution. Finally, benzoyl chloride was swiftly injected to trigger the NCs formation and the reaction was subsequently quenched by ice-bath. It is important to highlight that is the dissolution should be performed above 150 °C. At lower dissolution temperatures (i.e. 140°C), RbCl NCs would dominate the final product (see Figure S1). The dissolution temperature might influence the reactivity of Sb-ligands complex and play a role on the final product (RbCl or $Rb_7Sb_3Cl_{16}$). The $Rb_7Sb_3Cl_{16}$ NCs have a disk-like shape with a diameter of ~50 nm (Figure 1a). The XRD pattern of NCs match well with the recently reported hexagonal $Rb_7Sb_3Cl_{16}$ crystal structure (Figure 1b).[14] The SEM-EDS indicated that the NCs have a $Rb_{6.9}Sb_3Cl_{17.4}$ composition (Figure S2), in agreement with XRD result. Such crystal structure is composed of isolated $[SbCl_6]^{3-}$ octahedra and isolated $[Sb_2Cl_{10}]^{4-}$ dimers (Scheme 1, left panel). The enhanced XRD peaks (e.g. 23.6°) was attributed to the anisotropy of our NCs which has a disk like shape (see Figure S1a of the SI).

Sb-doped Rb_3InCl_6 NCs were well characterized by Zhu et al.[30] The NCs had a mean size of 14 nm, a monoclinic crystal structure (P121/c1 space group) and the doping concentration of Sb^{3+} is 0.1%.(Figure 1e-f). In such NCs, isolated $[SbCl_6]^{3-}$ is the only emitter center which surrounded by $[InCl_6]^{3-}$ octahedra. (Scheme 1, right panel).

The $Rb_7Sb_3Cl_{16}$ NCs had absorption peak centered at 3.85 eV (~325 nm) while its the PL peak centered at 2.2 eV (~556 nm) (Figure 1c). The PL excitation (PLE) spectrum measured at the maximum PL peak (~556 nm) had three distinguished excitation peaks at 3.5, 3.8 and 4.4 eV, in agreement with the fine structure of the energy level of hexa-coordinated Sb^{3+} ions.[30] In PLE spectra, these peaks was clearly broadened than the isolated $[SbCl_6]^{3-}$ octahedral. It properly indicate that both isolated $[SbCl_6]^{3-}$ octahedra and $[Sb_2Cl_{10}]^{4-}$ dimers are absorbing light. The Sb-doped Rb_3InCl_6 NCs has similar PL spectra,[30] and showed analogous, but sharper PLE peaks related to optical transitions of the isolated $[SbCl_6]^{3-}$ (Figure 1g).

Notably, the PL profile of both systems at RT, was essentially unchanged upon varying the excitation energy from from 3.5 to 4.66 eV (red and blue curves in Figure 1c and 1g, respectively, and Figure S3). This indicates that the radiative recombination in both systems occurs either from the same excited state or from degenerate excited states. The respective PL decay profiles recorded under both excitation energies, revealing almost identical traces (Figure 1d, h), which further support both system has the same excited state or from degenerate excited states. The discrepancy between the lifetime of both system (ns level for $Rb_7Sb_3Cl_{16}$ NCs and the μs level for Sb-doped Rb_3InCl_6 NCs) can be ascribed to the presence of non-radiative recombination pathways. Finally, in both system, the PL intensity show linear relation with the excitation intensity (10^{-3} to 10^1 mW) and decay trace is independent on the excitation intensity (Figure S4). It confirm that the emission stems from self-trapped excitons (STEs) for both systems.

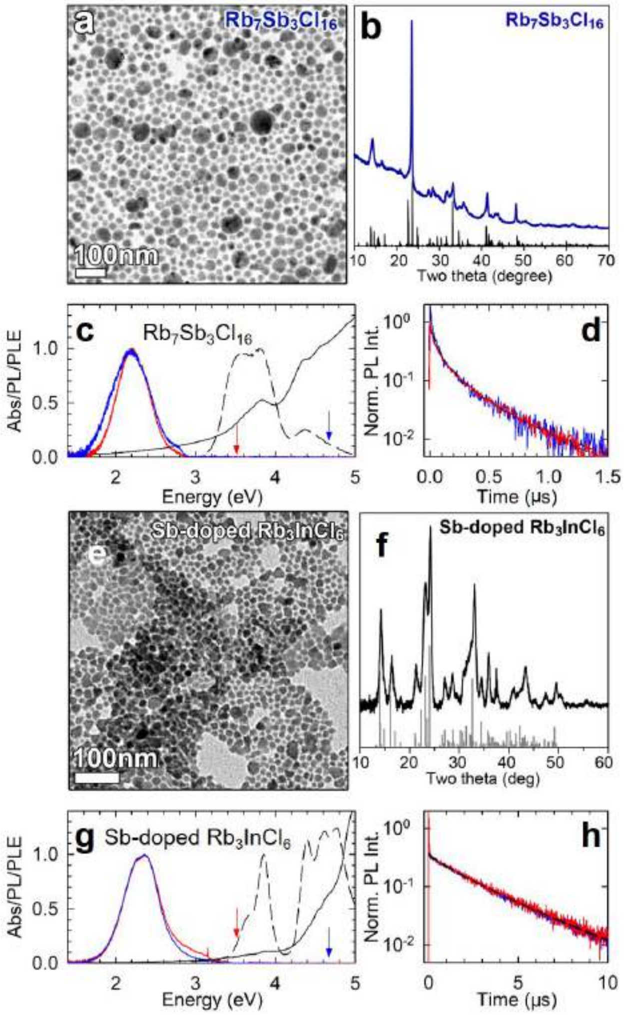

Figure 1. (a) TEM image and (b) XRD pattern of $Rb_7Sb_3Cl_{16}$ NCs and the pattern of hexagonal $Rb_7Sb_3Cl_{16}$ single crystal. (c) Absorption, PL and PL excitation spectra of $Rb_7Sb_3Cl_{16}$ NCs. The PL profiles were obtained by exciting at 3.5 eV (red curve) and 4.66 eV –(blue curve), respectively. (d) PL decay of $Rb_7Sb_3Cl_{16}$ NCs under 3.5 eV and 4.66 eV excitation energies. (e) TEM image and (f) XRD pattern of Sb-doped Rb_3InCl_6 NCs and pattern of bulk Rb_3TlCl_6 (ICSD number 300228). (g) Absorption, PL and PL excitation spectra and (h) PL decay of Sb-doped Rb_3InCl_6 NCs.

Temperature dependent optical properties. The optical properties of both system at different temperature (300 K to 5 K) were collected to better elucidate the photophysics. The $Rb_7Sb_3Cl_{16}$ NCs show an increasingly stronger dependence of the PL profile on the excitation energy (E_{exc}) with decreasing temperature, similar with what reported on corresponding bulk materials.[14] Specifically, the PL peak undergoes a red shift under 3.5 eV excitation (Figure 2a, red curves, hereafter dubbed as peak **A**) supposedly associated with the expansion of the lattice at low temperatures. Differently, under 4.66 eV excitation, an additional high energy PL component progressively emerges (peak **B**), eventually becoming dominant for T<100 K (Figure 2a, blue curves and S5). In the Recently reported bulk materials, Benin *et al.* tentatively ascribed the dual emission to the radiative recombination of STEs located in isolated octahedral and dimers, respectively, but their exact origin is still not known.[14] To well explain the origin of dual emission, we also investigated the PL T-dependence of Sb-doped Rb_3InCl_6 NCs which has only isolated $[SbCl_6]^{3-}$ octahedra as emission center. Surprisingly, the Sb-doped Rb_3InCl_6 NCs feature both peaks **A** and **B** at cryogenic temperatures with E_{exc}=3.5 eV and 4.66 eV, respectively (Figure 2b).It strongly suggest that the observed behavior is an intrinsic property of the $[SbCl_6]^{3+}$ octahedra alone. Upon lowering the temperature from 300 K down to 100 K, the PL intensity of both samples grows rapidly and its peaks shape narrows (Figure 2c-d). The FWHM of both samples under 3.5 eV excitation follows a nearly identical trend with temperature (Figure S6) that is well reproduced by the expression typically used to described the phonon-related homogeneous broadening of the PL peak

$$FWHM(T) = 2.36\sqrt{S}E_{ph}\sqrt{\coth(E_{ph}/k_BT)} \quad (1)$$

For both samples, S, the Huang-Rhys factor, and E_{ph}, the phonon energy, are respectively found to be ~60 and ~18 meV (~145 cm^{-1}), which is fully consistent with the internal vibrational mode of $[SbCl_6]^{3-}$ octahedra. The above result prove that the emissive center in the two material systems is the same.[46]

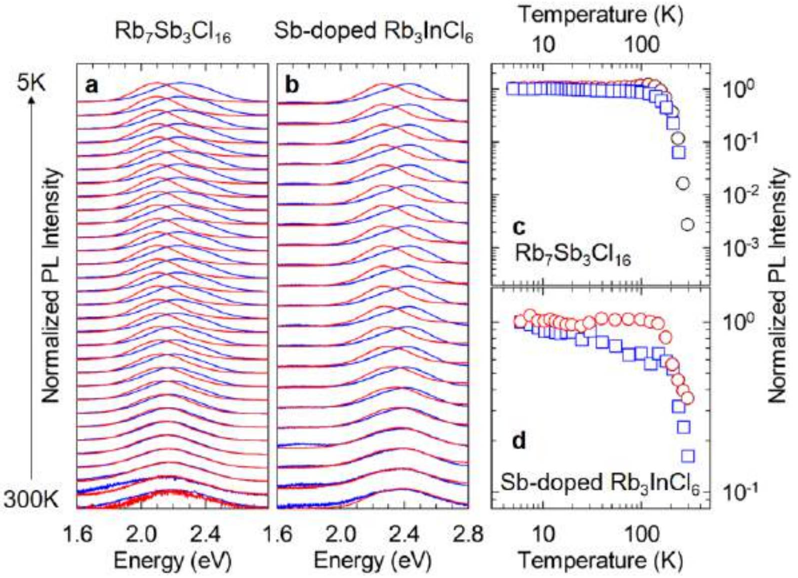

Figure 2. Normalized PL spectra of (a) $Rb_7Sb_3Cl_{16}$ NCs and (b) Sb-doped Rb_3InCl_6 NCs by cooling down the temperature from 300 K to 5K excited at 3.5 eV (red curve) and 4.66 eV (blue curve) respectively. The integrated PL intensities of (c) $Rb_7Sb_3Cl_{16}$ NCs and (d) Sb-doped Rb_3InCl_6 NCs under 3.5 eV and 4.66 eV excitation as a function of temperature (red circles and blue squares, respectively).

To further investigate the photophysical mechanisms supporting the observed T-dependence of the PL, the time-resolved PL as a function of T was measured at E_{exc}=3.5 eV and 4.66 eV, respectively (Figure 3). $Rb_7Sb_3Cl_{16}$ NCs show a drastic lengthening of the PL decay time, independent on the value of excitation energy, spanning almost 6 orders of magnitude (Figures 3a-d and S7). Interestingly, the τ vs. T trend can be fitted by double-S-shape suggesting two distinct temperature-dependent regimes. Specifically, for Range I (100 K $\leqslant$ T $\leqslant$ 300 K), the 100-fold lengthening of the PL lifetime correspond well to the significant PL intensity growth reported in Figure 2c, thus indicating that in Range I the progressive suppression of thermally assisted nonradiative recombination channels is the dominant process determining the optical behavior. In Range II (100 k to 5K), , the PL lifetimes undergo an additional lengthening of 3 orders of magnitude, with almost constant PL intensity (Figure 2c). It indicate that the effect is fully radiative and most likely arises from the thermal equilibrium between two different emissive. Consistently, the experimental data in Range II match well by the equation expression:

$$\tau(T) = \frac{1+\exp(-\Delta E_{1-2}/k_B T)}{\tau_1^{-1}+\tau_2^{-1}\exp(-\Delta E_{1-2}/k_B T)} \qquad (2)$$

where ΔE_{1-2} is the energy difference between a two different emissive state (labelled as **1** and **2**) respectively featuring PL radiative lifetimes τ_1 and τ_2. The value ΔE_{1-2} is fitted as ~6-7 meV independent of the excitation conditions. This result indicates that state **1** is associated with the $^3P_0 \rightarrow {}^1S_0$ transition, which has negligible oscillator strength, whereas state **2** is ascribed to the $^3P_1 \rightarrow {}^1S_0$ transition and featuring a finite oscillator strength, in agreement with our below calculations on the electronic structure of $[SbCl_6]^{3-}$ isolated octahedral and previous report. [30]

The time-dependent PL profiles of Sb-doped Rb_3InCl_6 NCs show different behavior to the $Rb_7Sb_3Cl_{16}$ NCs. In Range I, no considerable variation of the PL decay is observed, in agreement with its high PLQY at RT. However, in Range II, the τ vs. T trend is analogous to the $Rb_7Sb_3Cl_{16}$ NCs both qualitatively and quantitatively(Figure 3d), with ΔE_{1-2} values of 7 meV, also in agreement with results on Sb-doped bulk materials.[47] These results further corroborate the picture that the emissive centers are isolated $[SbCl_6]^{3-}$ octahedra in both systems.

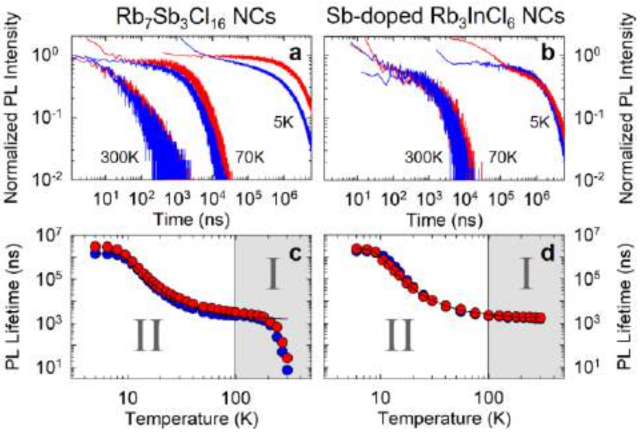

Figure 3. Normalized PL decay spectra of (a) $Rb_7Sb_3Cl_{16}$ NCs and (b) Sb-doped Rb_3InCl_6 NCs collected at different temperature under E_{exc}=3.5 and 4.66 eV (red and blue curves. respectively). PL lifetimes, τ, of (c) $Rb_7Sb_3Cl_{16}$ and (d) Sb-doped Rb_3InCl_6 NCs under 3.5 and 4.66 eV excitation (red and blue circles, respectively), extracted by the fitting value of (a) and (b). The temperature was divided into ranges I and II.

Computational analysis. The DFT calculation was performed to further support the observed optical properties in the previous section and to deduce the role of both isolated $[SbCl_6]^{3-}$ octahedra and $[Sb_2Cl_{10}]^{4-}$ dimers in the dual emission.

Sb-doped Rb$_3$InCl$_6$. The density of states (DOS) of the ground state (GS) Sb-doped Rb_3InCl_6 2x2x2 supercell was calculated(see details in the computational section in the SI),[30] as illustrated in Figure 4a. Here, four states arise after Sb^{3+} doping: one Sb(5s)-Cl(3p) antibonding molecular orbital (MO) at the top of valence band (VB) and three Sb(5p)-Cl(3p) antibonding MO inside the conduction band (CB) (Figure 4b). The HOMO-LUMO gap in the $[SbCl_6]^{3-}$ octahedron is computed at 3.63 eV in agreement with the experiment result (~3.5 eV). The lowest triplet states was computed to investigate the possible radiative recombination pathway, because these are the first optically active transitions from the GS occurring in hexacoordinated Sb^{3+} ions.[30] As reported in Figure 4c, after the structural relaxation, all three triplet states comprise by elongated Sb-Cl bonds. Interestingly, the presence of such non-equivalent elongations is influenced by the position of six Rb^+ ions, which were viewed as the second coordination shell of a $[SbCl_6]^{3-}$ octahedron and (Figure 4a). Indeed, these Rb^+ shell have a fundamental role in preventing a full bond rupture during the elongation of Sb-Cl elongation and in providing two LUMO→HOMO (emission) energy channels,. These two channels with ~1.2 eV Stokes shift likely correspond to the two emissive states presented in Figure 2.

Rb$_7$Sb$_3$Cl$_{16}$. The DOS of the ground-state of the $Rb_7Sb_3Cl_{16}$ system at the Γ point, was illustrated in Figure 5a-c. As pointed out by Benin at al.,[14] the topmost VB edge states are mainly contributed by the isolated octahedra, represented in blue in Figure 5c. The isolated octahedra show similar behaviour with the $[SbCl_6]^{3-}$ in Sb-doped Rb_3InCl_6.

Similarly, The excited states of the $[Sb_2Cl_{10}]^{4-}$ dimers was investigated by probing the three non-equivalent Cl-Sb-Cl elongations, here again associated to the presence of zero, one or two Rb^+ ions (Figure 5b) from the second coordination shell. In the simulation, the absence of Rb either along one or two elongation directions cause the collapse of the associated antibonding MO inside the VB, and form non-radiative channels.

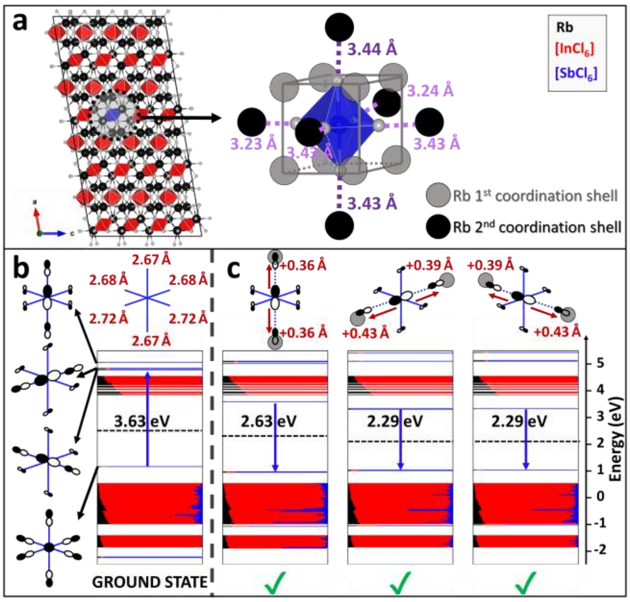

Figure 4. (a) Scheme of the Rb_3InCl_6 2x2x2 supercell doped with 1 Sb^{3+} ion, composed of Rb^+ ions (black), $[InCl_6]^{3-}$ octahedra (red, with grey Cl^-) and 1 $[SbCl_6]^{3-}$ octahedron (blue, with grey Cl^-) along the *b*-axis. First and second coordination shell of Rb^+ ions around $[SbCl_6]^{3-}$ was labeled as light grey and black, respectively. (b) Ground state electronic (GSE) structure of the supercell computed by the DFT/PBE theory at the Γ point. (c) Three lowest triplet states same as (b) but after structural relaxation.

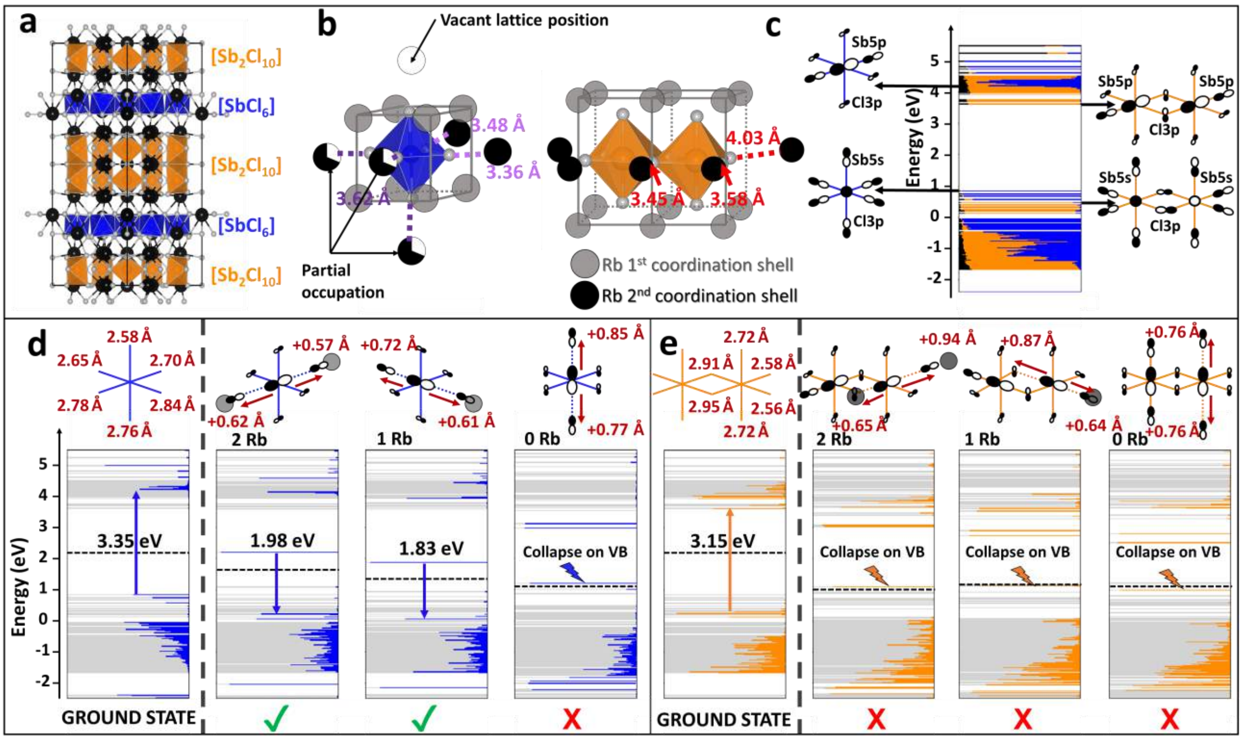

Figure 5. (a) View along the (110)-axis of the $Rb_7Sb_3Cl_{16}$ cell model, composed of isolated $[SbCl_6]^{3-}$ octahedra (blue) and $[Sb_2Cl_{10}]^{4-}$ dimers (orange) and Rb^+ ions (black). (b) First (light grey) and second (black) coordination shell of Rb^+ ions around $[SbCl_6]^{3-}$ octahedron and $[Sb_2Cl_{10}]^{4-}$ dimer. (c) Ground state electronic (GSE) structure of the $[SbCl_6]^{3-}$ centers and $[Sb_2Cl_{10}]^{4-}$ centers computed by the DFT/PBE theory at the Γ point. (d) Similar with Figure 4b for the electronic band of isolated $[SbCl_6]^{3-}$ unit. (e) Similar with Figure 4b for the electronic structure of dimeric $[Sb_2Cl_{10}]^{4-}$ unit.

CONCLUSION. By integrating the above computational data with the spectroscopic measurements, several conclusion were presented below:

I) In the $Rb_7Sb_3Cl_{16}$ system, 1/3 of the Sb cations are distributed in isolated octahedra, which we can assume to have a 2/3 probability of recombining radiatively.The remaining 2/3 of Sb cations are distributed in the dimers, which only don't have radiative channels. As a result, only 1/5 of the Sb centers can potentially emit in $Rb_7Sb_3Cl_{16}$ NCs. Conversely, all the Sb center are likely radiative due to the presence of a complete Rb coordination shell in Sb-doped Rb_3InCl_6 NCs. These simulation could explain why $Rb_7Sb_3Cl_{16}$ NCs have a much lower PLQY than the Sb-doped Rb_3InCl_6 NCs.

II) Our DFT calculations indicate that in $Rb_7Sb_3Cl_{16}$ NCs only the isolated octahedra can emit and the dimers do not emit even at cryogenic temperatures. This is in agreement with that the Sb-doped Rb_3InCl_6 and $Rb_7Sb_3Cl_{16}$ NC samples exhibit almost identical temperature dependent spectroscopic characteristics..

III) The double emission of both $Rb_7Sb_3Cl_{16}$ and Sb-doped Rb_3InCl_6 NCs stems from two non-degenerate states of the isolated $[SbCl_6]^{3-}$ octahedron, at cryogenic temperature.

IV) The lifetime extending below 100 K can be well explained by the two excited state ($^3P_0$ and $^3P_1$). The lowest excited state ($^3P_0$) has a strong triplet character and thus substantially spin-forbidden, while the next slightlt higher energy state is the $^3P_1$ with a weak transition dipole moment. At room temperature, the $^3P_0$ and $^3P_1$ can exchange their population, with the faster $^3P_1$ more likely to emit (microsecond timescale). However, at cryogenic temperature, the $^3P_0$ is the only state that becomes populated and cannot transfer back population to the higher energy $^3P_1$ state. In this case, the emission lifetime becomes much longer in the millisecond timescale.

Overall, in this work we demonstrate that in $Rb_7Sb_3Cl_{16}$ nanocrystals, the isolated $[SbCl_6]^{3-}$ octahedra are the only active emitters and $[Sb_2Cl_{10}]^{4-}$ is not emissive. The results of our study provide a guideline for developing brightly emitting metal halide systems based on Sb^{3+} ions. The rich optical behavior of the Sb-based metal halides, as evidenced in this work, can be exploited in various applications (such as optical sensing, thermometry, etc.)

Supporting Figure

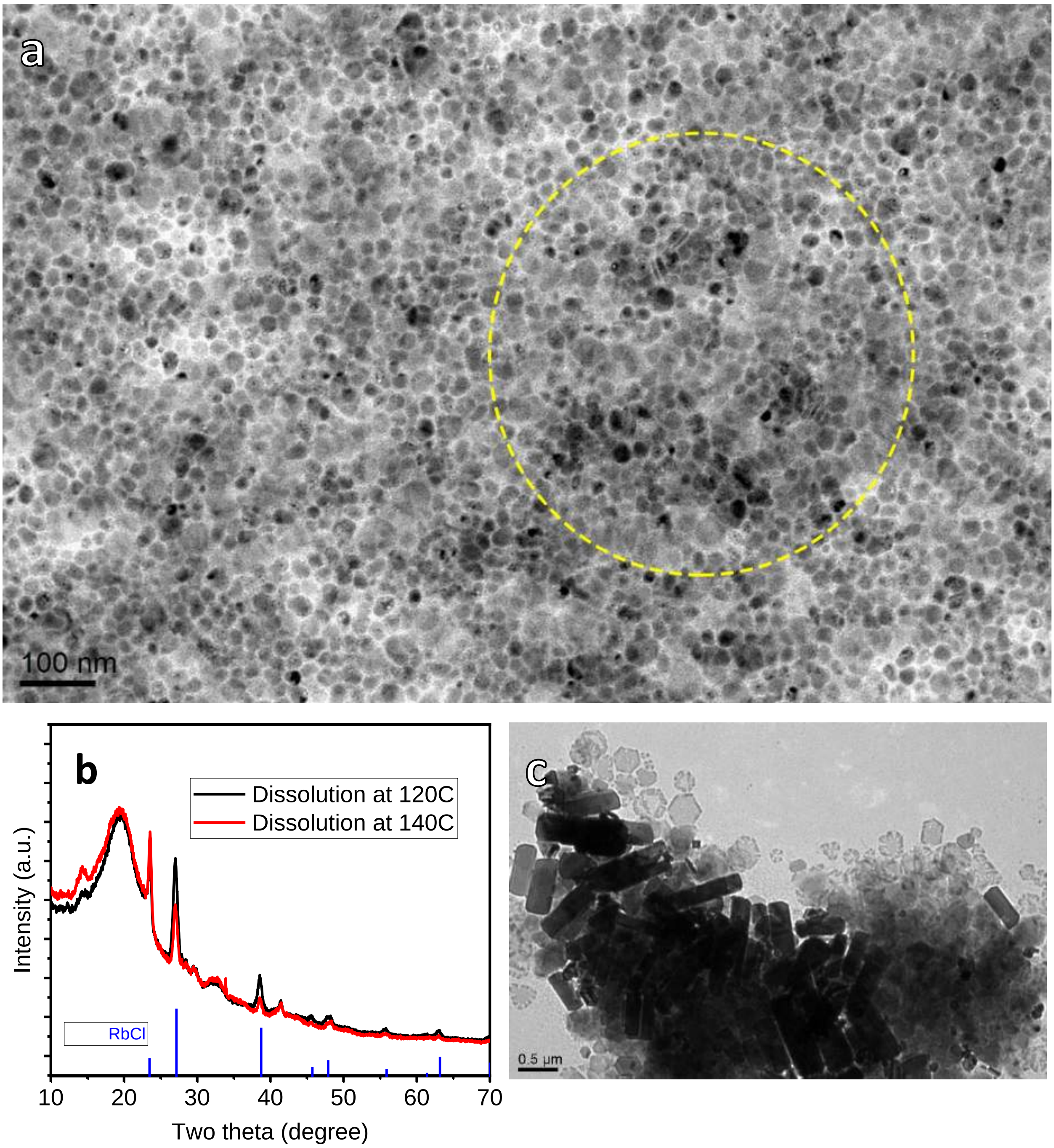

Figure S1. (a) TEM picture of $Rb_7Sb_3Cl_{16}$ NCs in which it is possible to spot some NCs perpendicularly aligned to the TEM grid (present in the area selected with a dotted yellow line). (b) XRD pattern of the products of the synthesis obtained when dissolving the precursors at either 120°C or 140°C. (c) and (b) TEM image of the product of the synthesis obtained when dissolving the precursors at 140°C.

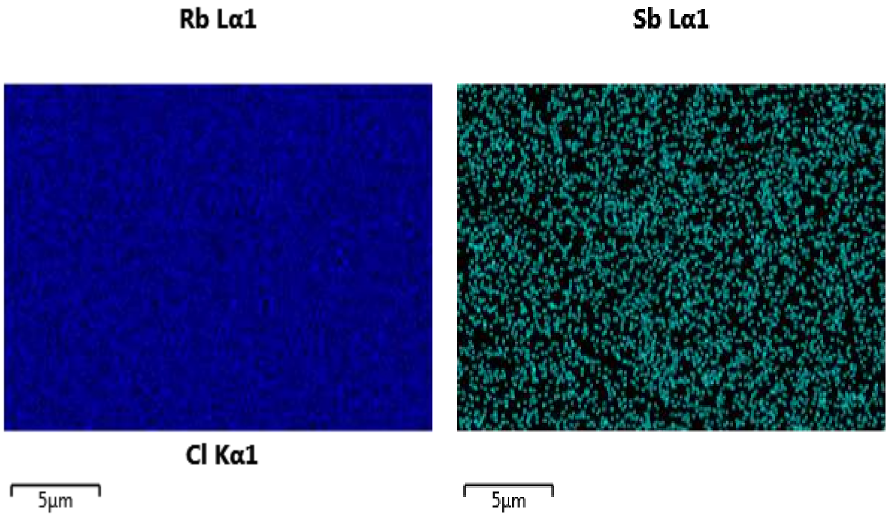

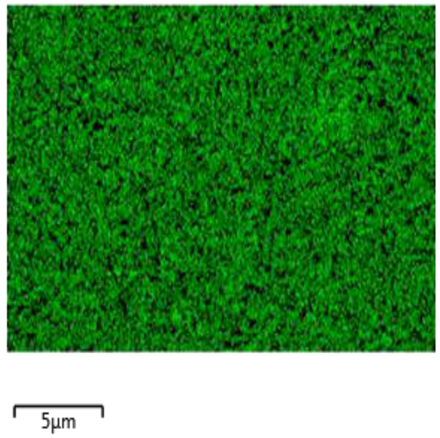

Map Sum Spectrum	Line Type	Wt %	Wt % Sigma	Atomic %
Cl	K series	39.11	0.79	63.60
Rb	K series	37.69	1.16	25.42
Sb	L series	23.20	0.64	10.99
Total		100.00		100.00

Figure S2 - The measured Rb:Sb:Cl molar ratio is 2.31:1:5.79 that can be normalized as 7: 3: 17.

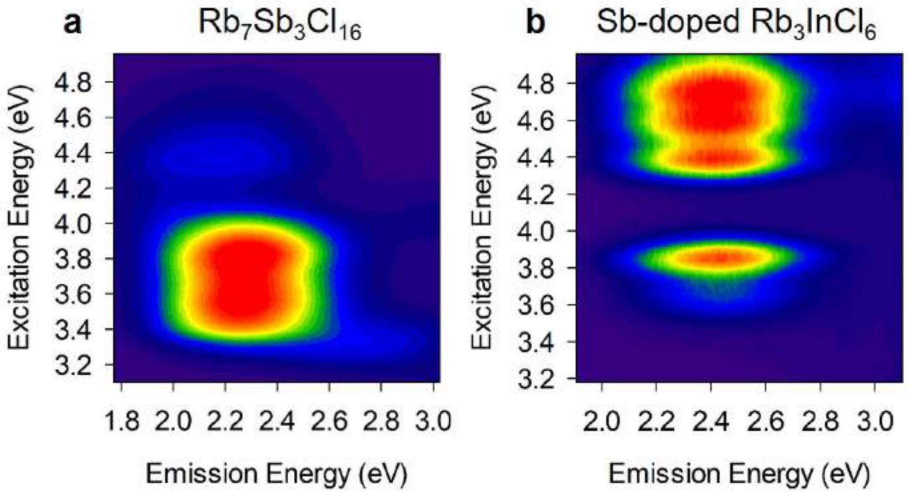

Figure S3 – PL/PL excitation contour plots of (a) $Rb_7Sb_3Cl_{16}$ and (b) Sb-doped Rb_3InCl_{16} NCs.

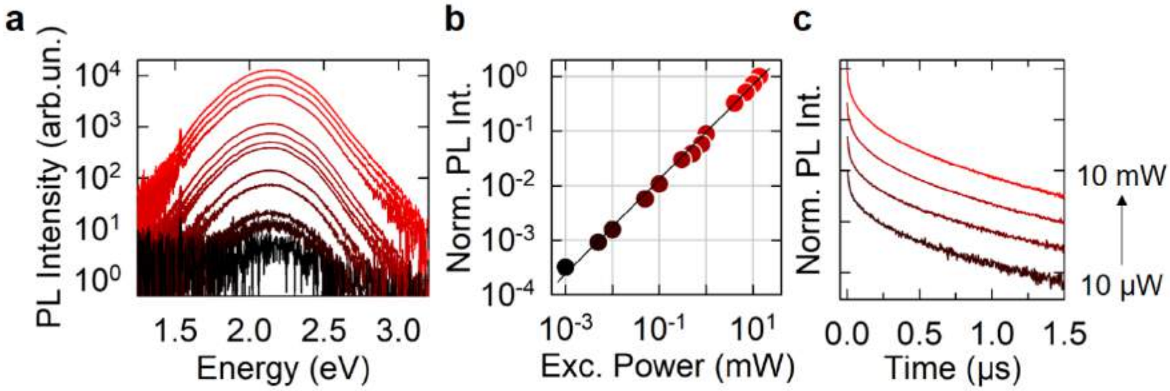

Figure S4 – (a) $Rb_7Sb_3Cl_{16}$ NCs PL spectra and (b) integrated PL intensity at increasing 3.5 eV excitation power from 1 μW (black) to 10 mW (red). The black line in 'b' is the result of the linear fitting yielding a slope of 0.98. (c) Normalized time-resolved PL traces at increasing 3.5 eV excitation power from 10 μW to 10 mW with 1 order of magnitude step each. The curves have been offset for clarity.

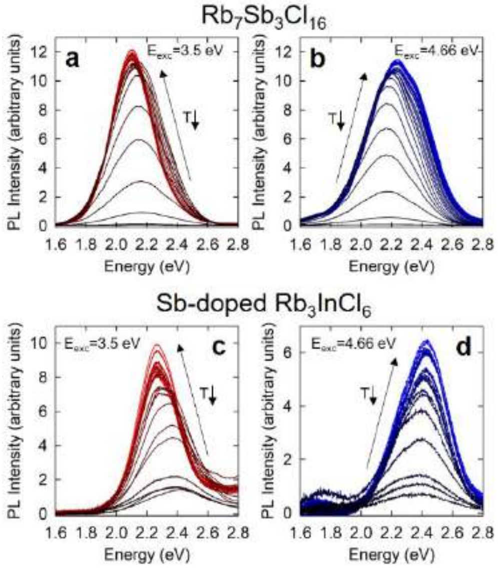

Figure S5 – $Rb_7Sb_3Cl_{16}$ NCs PL spectra under (a) 3.5 eV and (b) 4.66 eV excitation energies upon lowering the temperature from T=300K (black curves) down to 5K (red and blue curves, respectively). Sb-doped Rb_3InCl_{16} NCs PL spectra under (c) 3.5 eV and (d) 4.66 eV excitation energies upon lowering the temperature from T=300K (black curves) down to 5K (red and blue curves, respectively).

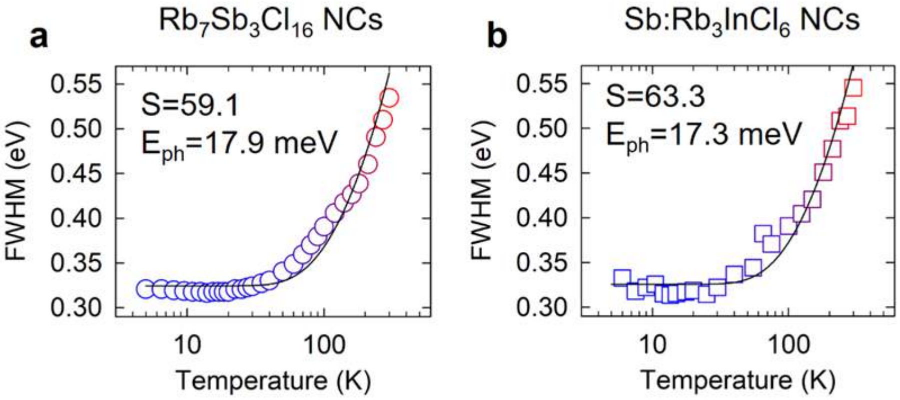

Figure S6 – Temperature dependence of the full width at half maximum (FWHM) of the (a) $Rb_7Sb_3Cl_{16}$ and (b) Sb-doped Rb_3InCl_6 NCs PL spectra under 3.5 eV excitation. The black lines are the results of the fitting procedures with Eq.(3). The results of the fitting procedures are reported in the respective panels.

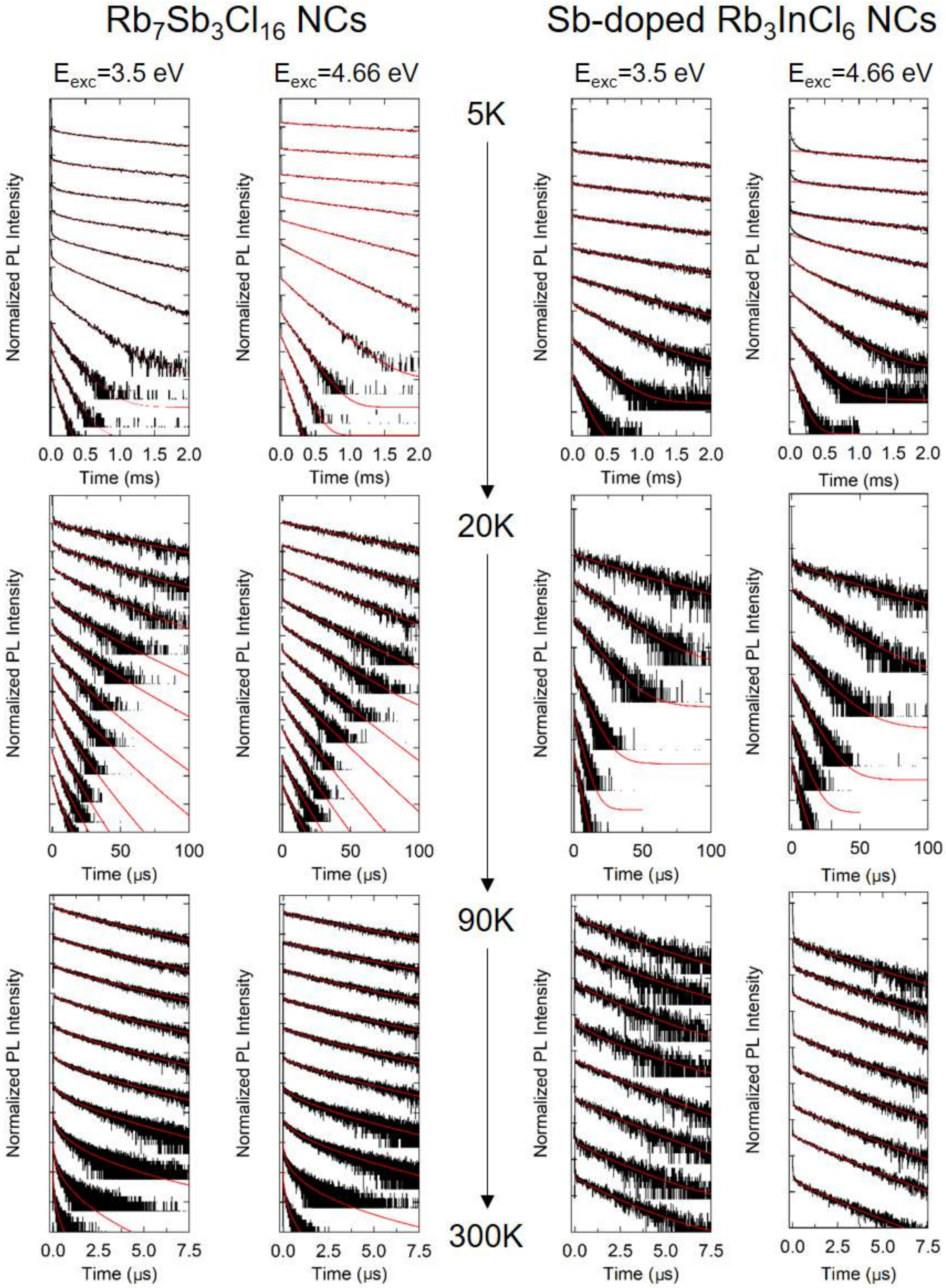

Figure S7 – PL decay traces of (left column) $Rb_7Sb_3Cl_{16}$ NCs and (right column) Sb-doped Rb_3InCl_6 NCs as a function of temperature, divided in three sets: set I (5K<T<20K, from top to bottom curves), set II (20K<T<90K, from top to bottom curves) and set III (90K<T<300K, from top to bottom curves). The excitation energy is indicated on the top of the respective column. Black lines are experimental data, the fitting curves to a stretched single exponential function are in red.

REFERENCES:

1. Gandini, M.; Villa, I.; Beretta, M.; Gotti, C.; Imran, M.; Carulli, F.; Fantuzzi, E.; Sassi, M.; Zaffalon, M.; Brofferio, C.; Manna, L.; Beverina, L.; Vedda, A.; Fasoli, M.; Gironi, L.; Brovelli, S., Efficient, fast and reabsorption-free perovskite nanocrystal-based sensitized plastic scintillators. *Nat. Nanotechnol.* **2020,** *15* (6), 462-468.
2. Jeong, M.; Choi, I. W.; Go, E. M.; Cho, Y.; Kim, M.; Lee, B.; Jeong, S.; Jo, Y.; Choi, H. W.; Lee, J.; Bae, J.-H.; Kwak, S. K.; Kim, D. S.; Yang, C., Stable perovskite solar cells with efficiency exceeding 24.8% and 0.3-V voltage loss. *Science* **2020,** *369* (6511), 1615.
3. Lin, K.; Xing, J.; Quan, L. N.; de Arquer, F. P. G.; Gong, X.; Lu, J.; Xie, L.; Zhao, W.; Zhang, D.; Yan, C.; Li, W.; Liu, X.; Lu, Y.; Kirman, J.; Sargent, E. H.; Xiong, Q.; Wei, Z., Perovskite light-emitting diodes with external quantum efficiency exceeding 20 per cent. *Nature* **2018,** *562* (7726), 245-248.
4. Wang, Z.; Lin, Q.; Wenger, B.; Christoforo, M. G.; Lin, Y.-H.; Klug, M. T.; Johnston, M. B.; Herz, L. M.; Snaith, H. J., High irradiance performance of metal halide perovskites for concentrator photovoltaics. *Nat. Energy* **2018,** *3* (10), 855-861.
5. Yakunin, S.; Benin, B. M.; Shynkarenko, Y.; Nazarenko, O.; Bodnarchuk, M. I.; Dirin, D. N.; Hofer, C.; Cattaneo, S.; Kovalenko, M. V., High-resolution remote thermometry and thermography using luminescent low-dimensional tin-halide perovskites. *Nat. Mater.* **2019,** *18* (8), 846-852.
6. Protesescu, L.; Yakunin, S.; Bodnarchuk, M. I.; Krieg, F.; Caputo, R.; Hendon, C. H.; Yang, R. X.; Walsh, A.; Kovalenko, M. V., Nanocrystals of Cesium Lead Halide Perovskites ($CsPbX_3$, X = Cl, Br, and I): Novel Optoelectronic Materials Showing Bright Emission with Wide Color Gamut. *Nano Lett.* **2015,** *15* (6), 3692-3696.
7. Shamsi, J.; Urban, A. S.; Imran, M.; De Trizio, L.; Manna, L., Metal Halide Perovskite Nanocrystals: Synthesis, Post-Synthesis Modifications, and Their Optical Properties. *Chem. Rev.* **2019,** *119* (5), 3296-3348.
8. Babayigit, A.; Ethirajan, A.; Muller, M.; Conings, B., Toxicity of organometal halide perovskite solar cells. *Nat. Mater.* **2016,** *15* (3), 247-251.
9. Li, X.; Zhang, F.; He, H.; Berry, J. J.; Zhu, K.; Xu, T., On-device lead sequestration for perovskite solar cells. *Nature* **2020,** *578* (7796), 555-558.
10. Li, Y.; Yang, T.; Xu, Z.; Liu, X.; Huang, X.; Han, S.; Liu, Y.; Li, M.; Luo, J.; Sun, Z., Dimensional Reduction of Cs2AgBiBr6: A 2D Hybrid Double Perovskite with Strong Polarization Sensitivity. *Angew. Chem. Int. Ed. Engl.* **2020,** *59* (9), 3429-3433.
11. Locardi, F.; Cirignano, M.; Baranov, D.; Dang, Z.; Prato, M.; Drago, F.; Ferretti, M.; Pinchetti, V.; Fanciulli, M.; Brovelli, S.; De Trizio, L.; Manna, L., Colloidal Synthesis of Double Perovskite $Cs_2AgInCl_6$ and Mn-Doped $Cs_2AgInCl_6$ Nanocrystals. *J. Am. Chem. Soc.* **2018,** *140* (40), 12989-12995.
12. Luo, J.; Wang, X.; Li, S.; Liu, J.; Guo, Y.; Niu, G.; Yao, L.; Fu, Y.; Gao, L.; Dong, Q.; Zhao, C.; Leng, M.; Ma, F.; Liang, W.; Wang, L.; Jin, S.; Han, J.; Zhang, L.; Etheridge, J.; Wang, J.; Yan, Y.; Sargent, E. H.; Tang, J., Efficient and stable emission of warm-white light from lead-free halide double perovskites. *Nature* **2018,** *563* (7732), 541-545.
13. Jellicoe, T. C.; Richter, J. M.; Glass, H. F. J.; Tabachnyk, M.; Brady, R.; Dutton, S. E.; Rao, A.; Friend, R. H.; Credgington, D.; Greenham, N. C.; Böhm, M. L., Synthesis and Optical Properties of Lead-Free Cesium Tin Halide Perovskite Nanocrystals. *J. Am. Chem. Soc.* **2016,** *138* (9), 2941-2944.
14. Benin, B. M.; McCall, K. M.; Wörle, M.; Morad, V.; Aebli, M.; Yakunin, S.; Shynkarenko, Y.; Kovalenko, M. V., The Rb7Bi3−3xSb3xCl16 Family: A Fully Inorganic Solid Solution with Room-Temperature Luminescent Members. *Angew. Chem. Int. Ed. Engl.* **2020,** *59* (34), 14490-14497.
15. Cai, T.; Shi, W.; Hwang, S.; Kobbekaduwa, K.; Nagaoka, Y.; Yang, H.; Hills-Kimball, K.; Zhu, H.; Wang, J.; Wang, Z.; Liu, Y.; Su, D.; Gao, J.; Chen, O., Lead-Free $Cs_4CuSb_2Cl_{12}$ Layered Double Perovskite Nanocrystals. *J. Am. Chem. Soc.* **2020,** *142* (27), 11927-11936.
16. Wang, X.; Ali, N.; Bi, G.; Wang, Y.; Shen, Q.; Rahimi-Iman, A.; Wu, H., Lead-Free Antimony Halide Perovskite with Heterovalent Mn2+ Doping. *Inorg. Chem.* **2020,** *59* (20), 15289-15294.
17. Benin, B. M.; Dirin, D. N.; Morad, V.; Wörle, M.; Yakunin, S.; Rainò, G.; Nazarenko, O.; Fischer, M.; Infante, I.; Kovalenko, M. V., Highly Emissive Self-Trapped Excitons in Fully Inorganic Zero-Dimensional Tin Halides. *Angew. Chem. Int. Ed. Engl.* **2018,** *57* (35), 11329-11333.
18. Lee, B.; Stoumpos, C. C.; Zhou, N.; Hao, F.; Malliakas, C.; Yeh, C.-Y.; Marks, T. J.; Kanatzidis, M. G.; Chang, R. P. H., Air-Stable Molecular Semiconducting Iodosalts for Solar Cell Applications: Cs2SnI6 as a Hole Conductor. *J. Am. Chem. Soc.* **2014,** *136* (43), 15379-15385.
19. Majher, J. D.; Gray, M. B.; Liu, T.; Holzapfel, N. P.; Woodward, P. M., Rb3InCl6: A Monoclinic Double Perovskite Derivative with Bright Sb3+-Activated Photoluminescence. *Inorg. Chem.* **2020,** *59* (19), 14478-14485.
20. Zeng, R.; Zhang, L.; Xue, Y.; Ke, B.; Zhao, Z.; Huang, D.; Wei, Q.; Zhou, W.; Zou, B., Highly Efficient Blue Emission from Self-Trapped Excitons in Stable Sb3+-Doped Cs2NaInCl6 Double Perovskites. *J. Phys. Chem. Lett.* **2020,** *11* (6), 2053-2061.
21. Wu, S.; Li, W.; Hu, J.; Gao, P., Antimony doped lead-free double perovskites (Cs2NaBi1−xSbxCl6) with enhanced light absorption and tunable emission. *J. Mater. Chem. C* **2020,** *8* (39), 13603-13611.
22. Gray, M. B.; Hariyani, S.; Strom, T. A.; Majher, J. D.; Brgoch, J.; Woodward, P. M., High-efficiency blue photoluminescence in the Cs2NaInCl6:Sb3+ double perovskite phosphor. *J. Mater. Chem. C* **2020,** *8* (20), 6797-6803.

23. Noculak, A.; Morad, V.; McCall, K. M.; Yakunin, S.; Shynkarenko, Y.; Wörle, M.; Kovalenko, M. V., Bright Blue and Green Luminescence of Sb(III) in Double Perovskite Cs2MInCl6 (M = Na, K) Matrices. *Chem. Mater.* **2020,** *32* (12), 5118-5124.

24. McCall, K. M.; Morad, V.; Benin, B. M.; Kovalenko, M. V., Efficient Lone-Pair-Driven Luminescence: Structure–Property Relationships in Emissive 5s2 Metal Halides. *ACS Mater. Lett.* **2020,** *2* (9), 1218-1232.

25. Liu, X.; Xu, X.; Li, B.; Yang, L.; Li, Q.; Jiang, H.; Xu, D., Tunable Dual-Emission in Monodispersed Sb3+/Mn2+ Codoped Cs2NaInCl6 Perovskite Nanocrystals through an Energy Transfer Process. *Small* **2020,** *16* (31), 2002547.

26. Li, J.; Tan, Z.; Hu, M.; Chen, C.; Luo, J.; Li, S.; Gao, L.; Xiao, Z.; Niu, G.; Tang, J., Antimony doped Cs2SnCl6 with bright and stable emission. *Front. Optoelectron.* **2019,** *12* (4), 352-364.

27. Han, P.; Luo, C.; Yang, S.; Yang, Y.; Deng, W.; Han, K., All-Inorganic Lead-Free 0D Perovskites by a Doping Strategy to Achieve a PLQY Boost from <2 % to 90 %. *Angew. Chem. Int. Ed. Engl.* **2020,** *59* (31), 12709-12713.

28. Jing, Y.; Liu, Y.; Jiang, X.; Molokeev, M. S.; Lin, Z.; Xia, Z., Sb3+ Dopant and Halogen Substitution Triggered Highly Efficient and Tunable Emission in Lead-Free Metal Halide Single Crystals. *Chem. Mater.* **2020,** *32* (12), 5327-5334.

29. Liu, X.; Xu, X.; Li, B.; Liang, Y.; Li, Q.; Jiang, H.; Xu, D., Antimony-Doping Induced Highly Efficient Warm-White Emission in Indium-Based Zero-Dimensional Perovskites. *CCS Chem.* **2020,** *2* (2), 216-224.

30. Zhu, D.; Zaffalon, M. L.; Zito, J.; Cova, F.; Meinardi, F.; De Trizio, L.; Infante, I.; Brovelli, S.; Manna, L., Sb-Doped Metal Halide Nanocrystals: A 0D versus 3D Comparison. *ACS Energy Lett.* **2021,** *6* (6), 2283-2292.

31. Su, B.; Li, M.; Song, E.; Xia, Z., Sb3+-Doping in Cesium Zinc Halides Single Crystals Enabling High-Efficiency Near-Infrared Emission. *Adv. Funct. Mater.* **2021,** *n/a* (n/a), 2105316.

32. Jing, Y.; Liu, Y.; Zhao, J.; Xia, Z., Sb3+ Doping-Induced Triplet Self-Trapped Excitons Emission in Lead-Free Cs2SnCl6 Nanocrystals. *The Journal of Physical Chemistry Letters* **2019,** *10* (23), 7439-7444.

33. Arfin, H.; Kshirsagar, A. S.; Kaur, J.; Mondal, B.; Xia, Z.; Chakraborty, S.; Nag, A., ns2 Electron (Bi3+ and Sb3+) Doping in Lead-Free Metal Halide Perovskite Derivatives. *Chem. Mater.* **2020,** *32* (24), 10255-10267.

34. Tan, Z.; Hu, M.; Niu, G.; Hu, Q.; Li, J.; Leng, M.; Gao, L.; Tang, J., Inorganic antimony halide hybrids with broad yellow emissions. *Sci. Bull.* **2019,** *64* (13), 904-909.

35. Yang, B.; Hong, F.; Chen, J.; Tang, Y.; Yang, L.; Sang, Y.; Xia, X.; Guo, J.; He, H.; Yang, S.; Deng, W.; Han, K., Colloidal Synthesis and Charge-Carrier Dynamics of $Cs_2AgSb_{1-y}Bi_yX_6$ (X: Br, Cl; $0 \leq y \leq 1$) Double Perovskite Nanocrystals. *Angew. Chem. Int. Ed. Engl.* **2019,** *58* (8), 2278-2283.

36. Morad, V.; Yakunin, S.; Kovalenko, M. V., Supramolecular Approach for Fine-Tuning of the Bright Luminescence from Zero-Dimensional Antimony(III) Halides. *ACS Mater. Lett.* **2020,** *2* (7), 845-852.

37. Liu, F.; Zhang, T.; Mondal, D.; Teng, S.; Zhang, Y.; Huang, K.; Wang, D.; Yang, W.; Mahadevan, P.; Zhao, Y. S.; Xie, R.; Pradhan, N., Light-Emitting Metal–Organic Halide 1D and 2D Structures: Near-Unity Quantum Efficiency, Low-Loss Optical Waveguide and Highly Polarized Emission. *Angew. Chem. Int. Ed. Engl.* **2021,** *60* (24), 13548-13553.

38. Timmermans, C. W. M.; Cholakh, S. O.; Blasse, G., The luminescence of Cs3Bi2Cl9 and Cs3Sb2Cl9. *J. Solid State Chem.* **1983,** *46* (2), 222-233.

39. Liu, Y.-L.; Yang, C.-L.; Wang, M.-S.; Ma, X.-G.; Yi, Y.-G., Theoretical insight into the optoelectronic properties of lead-free perovskite derivatives of Cs3Sb2X9 (X = Cl, Br, I). *J. Mater. Sci.* **2019,** *54* (6), 4732-4741.

40. Pradhan, A.; Sahoo, S. C.; Sahu, A. K.; Samal, S. L., Effect of Bi Substitution on Cs3Sb2Cl9: Structural Phase Transition and Band Gap Engineering. *Cryst. Growth Des.* **2020,** *20* (5), 3386-3395.

41. Wang, Z.-P.; Wang, J.-Y.; Li, J.-R.; Feng, M.-L.; Zou, G.-D.; Huang, X.-Y., [Bmim]2SbCl5: a main group metal-containing ionic liquid exhibiting tunable photoluminescence and white-light emission. *Chem. Commun.* **2015,** *51* (15), 3094-3097.

42. Li, D.; Wu, W.; Wang, S.; Zhang, X.; Li, L.; Yao, Y.; Peng, Y.; Luo, J., A one-dimensional dual emissive hybrid perovskite with flexibly tunable white-light emission. *J. Mater. Chem. C* **2020,** *8* (20), 6710-6714.

43. Morad, V.; Shynkarenko, Y.; Yakunin, S.; Brumberg, A.; Schaller, R. D.; Kovalenko, M. V., Disphenoidal Zero-Dimensional Lead, Tin, and Germanium Halides: Highly Emissive Singlet and Triplet Self-Trapped Excitons and X-ray Scintillation. *J. Am. Chem. Soc.* **2019,** *141* (25), 9764-9768.

44. Yu, D.; Wang, P.; Cao, F.; Gu, Y.; Liu, J.; Han, Z.; Huang, B.; Zou, Y.; Xu, X.; Zeng, H., Two-dimensional halide perovskite as β-ray scintillator for nuclear radiation monitoring. *Nat. Commun.* **2020,** *11* (1), 3395.

45. Imran, M.; Caligiuri, V.; Wang, M.; Goldoni, L.; Prato, M.; Krahne, R.; De Trizio, L.; Manna, L., Benzoyl Halides as Alternative Precursors for the Colloidal Synthesis of Lead-Based Halide Perovskite Nanocrystals. *J. Am. Chem. Soc.* **2018,** *140* (7), 2656-2664.

46. Rodrigues, J. E. F. S.; Escanhoela, C. A.; Fragoso, B.; Sombrio, G.; Ferrer, M. M.; Álvarez-Galván, C.; Fernández-Díaz, M. T.; Souza, J. A.; Ferreira, F. F.; Pecharromán, C.; Alonso, J. A., Experimental and Theoretical Investigations on the Structural, Electronic, and Vibrational Properties of Cs2AgSbCl6 Double Perovskite. *Industrial Engin. Chem. Res.* **2021**.

47. Oomen, E. W. J. L.; Smit, W. M. A.; Blasse, G., On the luminescence of Sb3+in Cs2NaMCl6(with M=Sc,Y,La): a model system for the study of trivalent s2ions. *J. Phys. C: Solid State Phys.* **1986,** *19* (17), 3263-3272.

Chapter 6: Structural insight into stabilized $CsPbBr_3$ Nanoclusters

ABSTRACT

$CsPbBr_3$ nanoclusters have been synthesized by several groups and mostly employed as single source precursors for the synthesis of anisotropic perovskite nanostructures or perovskite-based heterostructures. Yet, a detailed characterization of such clusters is still lacking due to their high instability. In this work, we were able to stabilize $CsPbBr_3$ nanoclusters by carefully selecting ad-hoc ligands (benzoic acid together with oleylamine) to passivate their surface. The clusters have a narrow absorption peak at 400 nm, a band edge emission peaked at 410 nm at room temperature, and their composition is identified as $CsPbBr_{2.3}$. Synchrotron X-ray pair distribution function measurements indicate that the clusters exhibit a disk-like shape, with a thickness smaller than 2 nm and a diameter of 13 nm, and their crystal structure is a highly distorted orthorhombic $CsPbBr_3$. Based on small and wide angle X-ray scattering analyses, the clusters tend to form a 2D hexagonal packing with short range order and a lamellar packing with long range order.

INTRODUCTION

Nanoclusters (NCLs) are a class of well-defined species that are intermediate in size between molecules and nanocrystals (NCs).[1-7] They are characterized by an inorganic core, composed of a well-defined number of atoms, passivated by an organic shell made of a stoichiometric amount of surfactants. Having discrete sizes, NCLs can be generally considered as perfectly monodisperse NCs and, indeed, they exhibit narrow optical absorption peaks, in the order of homogeneously broadened lines.[8] In turn, given their small size, they have large surface-to-volume ratios, and their photoluminescence has a low yield and is often dominated by broad trap emission.[6, 9-13] NCLs have been found to form at the early stages of several colloidal syntheses of NCs. Their isolation and characterization has been often aimed at gaining a better understanding of the nucleation and growth of NCs beyond classical nucleation theory and, consequently at achieving a higher control over NCs' syntheisis.[2-3, 6, 8, 14] In this regard, studies on NCLs have revealed that their oriented attachment, continuous growth or dissolution over time (with the consequent supply of monomers) are key processes involved in the nucleation and growth of NCs. [8, 10, 15-18]

In addition to their relevance *per se*, NCLs are currently of great interest as they can be used as single-source reagents.[2, 6, 10, 16, 19-23] They represent, in this context, an opportunity to develop new synthetic routes to various types of nanomaterials. The use of NCLs as a single-source precursor can avoid the poorly controllable pyrolytic step in which precursors are converted into monomers (typically occurring at high temperatures), thus enabling greater synthetic control.[19] This is particularly relevant in the synthesis of nano-heterostructures (or in general in seeded growth approaches) and of those NC systems in which the reactivity of the available precursors cannot be finely tuned, as in the case of III-V semiconductors (e.g. InP and InAs).[15, 24] The interest in such compounds has led, in the last decades, to the isolation and characterization of several NCLs of II-VI and III-V semiconductor materials,[16] namely CdS,[3, 20, 25-26] CdSe,[17, 26-27] CdTe,[20, 26] ZnS,[20, 26] ZnSe,[20, 26] ZnTe,[18, 20] PbSe[28], InP,[2, 15, 21] and InAs.[24, 29-30] Only recently, with the emergence of lead halide perovskites, NCLs of $APbBr_3$ (A=methyalmmonium or Cs) materials were discovered.[6, 10, 13, 22, 31-32] $CsPbBr_3$ NCLs have been found to form at room temperature in the presence of a high concentration of oleylamine and oleic acid, with usually high Pb to Cs feed ratios (ranging from 2.5:1 to 6:1).[22, 31-32] $CsPbBr_3$ NCLs have been employed as single source precursors for the synthesis of quantum confined nanostructures (nanowires, nanoplatelets),[6] NCs with complex geometries (i.e. $CsPbBr_3$ hexapods)[22] and heterostructures (i.e. $CsPbBr_3-Pb_4S_3Br_2$).[23] Instead, conventional metal halide precursors (e.g. Cs-oleate and $PbBr_2$ or Cs-carbonate, Pb-acetate and benzoyl bromide)[33-34] lead to a fast nucleation and growth of $CsPbBr_3$ NCs, making it extremely difficult to perform any seeded growth approach or to synthesize heterostructures.[35]

Despite their importance in the synthesis of perovskite based nanostructures, stable $CsPbBr_3$ NCLs have never been successfully prepared and, consequently, characterized in depth.[32] In fact, the $CsPbBr_3$ NCLs reported so far typically grow larger already at room temperature over a timespan of a few minutes and they cannot be purified with the use of polar solvents.[6, 13, 31] With the aim of increasing the stability of such materials, different strategies have been pursued: Ke *et al.* used either aluminum nitrate nonahydrate as a coordination complex together with oleylamine and oleic acid,[32] or a combination of benzoic acid and benzylamine.[36] In both cases, no stable and/or pure $CsPbBr_3$ NCLs could be isolated. To circumvent such issues, we have developed here a new strategy based on oleylamine and benzoic acid ligands (which have been successfully employed to prepare the more conventional CdSe, CdS and InP semiconductor NCLs[4, 11, 37-38]) to synthesize stable $CsPbBr_3$ NCLs (Scheme 1). These nanostructures are characterized by a sharp excitonic absorption peak at 399 nm and a room temperature photoluminescence (PL) emission featuring a sharp peak at 410 nm and a long tail extending up to 600 nm. While the peak at 410 nm can be ascribed to band-edge emission, the broad tail is attributed to surface trap states, similar to what has been observed in NCLs of II-VI or III-V compounds.[12, 39] Our clusters can be washed with polar solvents, and they are found to be stable over 1 week at room temperature both in concentrated hexane solutions (> 50 mg/ml) and in solid form (under N_2). Such stability allowed us to perform a detailed chemical and structural analysis by combining different techniques, comprising, *inter alia*, pair distribution function (PDF) as well as small and wide-angle X-ray scattering (SAXS, WAXS). The composition of the NCLs was estimated to be $CsPbBr_{2.3}$, and their crystal structure was identified by PDF data as orthorhombic $CsPbBr_3$, although highly distorted. Convergent evidence from PDF, SAXS and WAXS analyses on solid samples indicated that the clusters have an anisotropic, disk-like shape, with a 1.6±0.4 nm thickness and 13±2 nm diameter (Scheme 1). Based on SAXS, the clusters assemble in solid samples with 4.4 nm and 2.5 nm periodicities, indicating a hexagonal short range order and a lamellar long range order. We hypothesize that such mesophase could be the reason for our NCLs' enhanced stability, similar to what reported for CdS NCLs.[4, 40]

Our work not only provides a way to produce stable NCLs to be employed on demand as single source precursors for the synthesis of perovskite based complex structures, but also sheds light onto perovskite NCLs by revealing that they are not similar to classical

NCLs, which have more isotropic shapes and sizes in the order of 1-3 nm. Instead, the present NCLs are confined platelets with larger lateral dimensionality.

EXPERIMENTAL SECTION

Chemicals. 1-Octadecene (ODE, tech, 90%), oleic acid (OA, tech, 90%), benzoic acid (BA, 99%), oleylamine (OLA, tech, 70%), lead (II) bromide ($PbBr_2$, 98%), cesium carbonate (Cs_2CO_3, 99%), were purchased from Sigma-Aldrich. All reagents were used as received without any further experimental purification.

Synthesis of Cesium oleate precursors. In a typical synthesis, Cs_2CO_3 (0.652 g, 2 mmol), OA (2.5 mL, 7.5 mmol) were loaded into a 50 mL three-neck flask, degassed for 2 h at 100 °C, until the solution turned clear.

Synthesis of $CsPbBr_3$ NCLs. 71 mg $PbBr_2$ was mixed with 100 mg benzoic acid, 0.5 ml oleylamine and 4.5 ml ODE in N_2 filled 20 ml glass vails. The mixture was heated at 150 °C for 5 min in order to obtain a clear solution. After cooling back to room temperature, 150 µl of Cs-oleate stock solution was injected into the clear solution, and the resulting mixture was kept under stirring at room temperature (25 °C). After about 3 hours, 20 ml ethyl acetate were added and the resulting mixture was centrifuged at 6000 rpm for 10 min, the supernatant was discarded and the precipitate was redispersed in 1 mL of anhydrous hexane for storage.

Elemental analysis. The elemental analysis was performed via energy dispersive X-ray spectroscopy (EDS) on a JEOL JSM-7500FA SEM-Analytical field-emission scanning electron microscopy (SEM) with an Oxford X-Max 80 system equipped with an 80 mm^2 silicon drift detector (SDD). X-ray Photoelectron Spectroscopy (XPS) was performed on a Kratos Axis UltraDLD spectrometer, equipped with a monochromatic Al Kα source, which was operated at 20 mA and 15 kV. Spectra were charge corrected to the main line of the carbon 1s spectrum (adventitious carbon) set to 284.8 eV. Spectra were analyzed using CasaXPS software (version 2.3.24).

UV−vis Absorption, Photoluminescence (PL) The UV−visible absorption spectra were recorded using a Varian Cary 300 UV−vis absorption spectrophotometer. The PL spectra were collected by a Varian Cary Eclipse fluorescence spectrophotometer.

Pair distribution function (PDF). PDF measurements were performed at the National Synchrotron Light Source (NSLS-II) of the Brookhaven National Laboratory. The 28ID-2 beamline was used, with a primary X-ray beam of 67.17 keV (0.1846 Å) energy and 0.5 mm x 0.5 mm spot size. A Perkin Elmer XRD 1621 digital imaging detector (2048 x 2048 pixels of 200 x 200 µm size) orthogonal to the beam was put 242 mm downstream the sample to optimize PDF measurements. Nickel was measured as a standard reference material to calibrate the wavelength and the detector position/orientation. Fresh samples were enclosed into small bags of ultralene (Figure S1) and sealed, to preserve cluster properties prior and during X-ray measurements. An empty bag was measured for background estimation. X-ray measurements were performed at 270 K, with no filters and without spinning the sample. Diffraction images were azimuthally integrated and converted into intensity profiles versus 2ϑ and versus momentum transfer (Q) by using the FIT2D program.[37] PDF profiles were calculated up to interatomic distances r of 40 Å from Q profiles by the program PDFGetX3.[38] The parameters for PDF calculation (background subtraction scale factor, minimum and maximum values of Q, degree of data-correction polynomial) were optimized to reduce termination effects and to enhance the signal to noise ratio. The Q_{max} parameter was set to 21.2 $Å^{-1}$.

The PDF profile was refined by using a python script based on the DiffPy-CMI library.[39] The fits were executed for interatomic distances above 2.0 Å, to avoid finite-size artifacts in the low r range, and with a step of 0.05 Å. The fitting model was defined as the convolution of the PDF contribution due to a bulk crystal structure and that due to the nanocrystal shape. The model parameters were refined separately, i.e. by keeping constant all the others, with the following order: scale factor, nanocrystal shape parameters: radius in the case of spherical shape or polar/equatorial radii in the case of spheroidal shape, peak shape parameters: Q_{broad}, (peak broadening from increased intensity noise at high Q) and delta1 (coefficient for 1/r contribution to the peak sharpening), atomic displacement parameters lattice parameters, atomic position parameters and crystallographic occupancy. The crystal symmetry has been applied to constrain lattice and atomic parameters.

In a first stage, a simplified fit procedure restricted to r<13 Å was used to screen the 22 CsPbBr crystal structures present in ICSD. 10 refinement cycles were performed, by using a spherical nanocrystal shape and isotropic displacement factors. The atomic positions and crystallographic occupancies were kept fixed. In a second stage the full PDF range was exploited to carry out a more elaborate refinement of the selected crystal phase. 50 refinement cycles were performed, where the atomic displacement parameters were kept isotropic in the first 25 cycles, then set to anisotropic in the last 25 cycles. A spheroidal NC shape was used, and the displacement parameters of each element and the atomic parameters of each atom were refined separately.

Small and Wide-angle X-ray scattering (SAXS, WAXS) analyses. SAXS and WAXS data were collected at the XMI-Lab[40] by using a Fr-E+ superbright microsource (CuKα) coupled to a SMAX3000 camera (Rigaku). SAXS data were collected by a multiwire Triton detector, at about 1.140 m sample-to-detector distance (SDD); Kapton windows were inserted upstream and downstream the sample to keep it at atmospheric pressure (flight tube at about 10^{-1} mbar vacuum pressure). SAXS data from solutions were obtained by filling a glass capillary with 50 mg/ml solution of clusters in hexane, and a capillary with the only hexane as a buffer, for solvent scattering subtraction. 1D-folded SAXS profiles were fitted by using the ATSAS suite.[41] SAXS microscopies were collected in scanning mode on solid samples, inserted in ultralene bags, with 0.2 mm step size, and were processed by the in-house developed SUNBIM package,[42] exploiting the multimodal imaging approach.[43] WAXS data were collected at selected positions on the sample (simultaneously to SAXS data acquisition), by inserting an Image Plate (IP) detector at a 28 mm SDD downstream the sample, and using a RAXIA scanner for off-line readout.

Dynamic Light Scattering (DLS). The Malvern Zetasizer (Nano Series, Nano ZS) instrument was used to determine the hydro-diameter of the NCs. Three measurements with 10-20 acquisitions were taken for each sample.

High-Angle Annular Dark-Field Scanning Transmission Electron Microscopy (HAADF-STEM). HAADF-STEM images were acquired using an image-Cs-corrected JEM-2200FS microscope, operated at 200 kV. The specimen was prepared by drop casting the sample suspended in octane onto an ultrathin carbon/holey carbon/Cu grid.

Scheme 1. Synthesis, shape and structure of $CsPbBr_3$ NCLs.

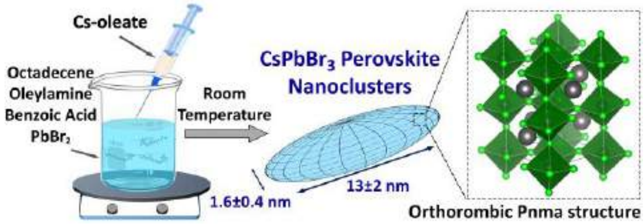

RESULTS AND DISCUSSION

Synthesis of $CsPbBr_3$ NCLs. The $CsPbBr_3$ NCLs reported in this work were synthesized following the procedure reported by Peng *et al.*[6] and by substituting oleic acid with benzoic acid. The obtained crude solution was optically transparent and colorless, and the product could be precipitated as a white solid by the addition of ethyl acetate (i.e. antisolvent) followed by centrifugation after 2-3 minutes. In order to define the elemental composition of the NCLs we performed XPS and SEM-EDS analyses (Figure S2, S3 and Table S2, S3). Both analyses indicated that the NCLs have a $CsPbBr_{2.3}$ composition with oleylammonium and carboxylate ions (the latter identified via XPS analysis, see Table S3) ensuring charge balance. Unfortunately, a precise quantification of the two surfactants could not be achieved as the clusters degraded if subjected to multiple washing steps (required to get rid of excess unbound ligands). The $CsPbBr_3$ NCLs were characterized by a sharp excitonic absorption peak at ~399 nm, along with two additional absorption peaks at higher energies (353 and 318 nm), the same as the reported NCLs by Peng *et al.* and by other groups,[6, 22-23, 31] and representing the fine exciton structure (Figure 1a). The PL emission of the NCLs was composed of a relatively narrow peak at 410 nm and a broad tail extending up to 600 nm, which have been tentatively ascribed to band gap and surface trap emission, respectively. Such optical features indicate that our NCLs are in the strong confinement regime, since their absorption peak falls: i) at higher energies with respect to that of bulk $CsPbBr_3$ and of 2 monolayer (ML) thick $CsPbBr_3$ nanoplatelets (~100nm diameter);[48] ii) at lower energies with respect to that of Cs_4PbBr_6 structures, in which all the $PbBr_6$ octahedra are disconnected from each other.[49] Indeed, our NCLs featured optical properties that are analogous to those of 1ML micron-sized nanosheets with formula $(oleylammonium)_2PbBr_4$.[50-52] Those nanosheets do not contain Cs^+ cations, hence the $[PbBr_6]^{4-}$ octahedra form a 2D network limited to 1ML and are stabilized by oleylammonium ions. Such nanosheets are characterized by an excitonic absorption peak located at ~398 nm, similar to the present work, but they lack a fine excitonic structure (i.e. they do not feature an absorption peak at 350 nm),[50-52] as instead is seen in our samples. The PL emission of such nanosheets is also similar to that of our NCLs, which have a PL peak located at ~403 nm and a long tail toward lower energies.[51-52] Overall these considerations indicate that the confinement in our NCLs is similar to that of 1ML organic-inorganic lead bromide nanosheets.

HAADF-STEM analysis was performed in order to reveal the morphology of the NCLs, which appeared as thin (~2nm) elongated nanostructures (Figure 1a). According to DLS measurements, the clusters dispersions in hexane were composed of objects having large hydrodynamic diameters (in the range of 500 nm and 50 nm), indicating that the NCLs formed large assemblies (Figure 1c). Upon dilution, such assemblies gradually disappeared, and, below the concentration of 0.5 mg/ml, the NCLs solution became light green in color, with absorption at 420nm, indicating the formation of $CsPbBr_3$ NCs, as shown in Figure S4. Overall, these findings suggest that the concentration of the NCLs in solution influences their aggregation, which in turn plays a key role in their stabilization.

The cluster samples were found to be stable up to two weeks when stored as concentrated dispersions in hexane (50 mg/ml) at room temperature, after which an absorption peak at 420 nm was observed, signifying again the formation of 3D perovskite nanostructures (Figure S5). The validated stability of the NCLs allowed us to perform powder XRD (XPD) measurements and synchrotron experiments, which were optimized to carry out PDF, the latter particularly suited to investigate the local structure of nanomaterials (Figure 1d).[54] It can be noted that a portion of the XRD reflections of the NCLs matched with those of the orthorhombic $CsPbBr_3$ phase (Figure 1d) apart from the peaks at $2\theta < 10°$ that could not be indexed with any known Cs-Pb-Br crystal phase, thus being tentatively ascribed to a supramolecular arrangement of the NCLs.

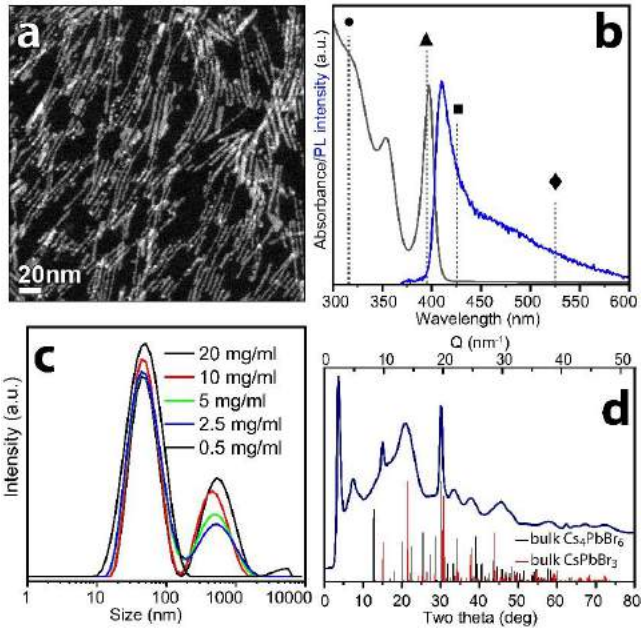

Figure 1. (a) HAADF-STEM image and (b) absorption and photoluminescence spectra of purified $CsPbBr_3$ NCLs. The vertical dashed lines represent the spectral positions of the absorption peaks related to the following species, if they were present in the sample: 0D Cs_4PbBr_6 (●),[53] 1 monolayer (oleylammonium)$_2PbBr_4$ nanosheets (▲),[50-52] $CsPbBr_3$ nanoplateletes with 2 monolayers (■)[48] and bulk $CsPbBr_3$ (♦). (c) DLS analysis of $CsPbBr_3$ NCLs dispersions in hexane at different concentrations. (d) XPD pattern of $CsPbBr_3$ NCLs measured at the NSLS-II synchrotron source. 2θ values are those for CuKα radiation for the sake of comparison. The bulk reflections of orthorhombic $CsPbBr_3$ (ICSD 98751) and Cs_4PbBr_6 (ICSD 162158) structures are reported as red and black bars, respectively.

The local structure of the NCLs was investigated by calculating the PDF profile from the measured XPD pattern shown in Figure 1d. To this aim, all existing crystal phases in the ISCD database were screened against PDF data by using a fitting procedure that was restricted to interatomic distances < 13 Å, both to avoid interference with the supramolecular arrangement and to increase the sensitivity of the identification. The results indicate that the best match with the PDF profile could be achieved with the orthorhombic Pnma crystal structure (Figure S6).[55-56] A more elaborate refinement procedure was then carried out on the selected orthorhombic crystal phase to retrieve information about the anisotropic atomic motion and NCLs shape. The best fit, reported in Figure 2a, was achieved when setting the shape of the NCLs as an oblate spheroid having equatorial and polar diameters of 13±2 nm and 1.6±0.4 nm, respectively, (Figure 2a and Table S1). In such a model, Cs^+ cations are characterized by an anisotropic motion along the [101] and [-101] directions (Figure 2b-d, pink spheroids), while the Br^- anions in general positions fluctuate along the [001] direction (Figure 2b-d, longer red disks).

To further confirm these results, we also performed a micro-structural analysis by whole profile fitting (WPF) of the synchrotron XPD profile (see Figure S7, S8), which returned an estimate of the average size for crystallite domains of 10.7 nm, from the (020) reflection and 2.3 nm, from the (101) reflection. Such dimensions agree with the PDF shape determination if the polar axis of the spheroid is directed along the [101] direction (n.b. the size values returned by the WPF should not be considered strictly quantitative: the low goodness of the fit indicates the low efficiency of this approach, likely due to the high preferred orientation and anisotropy of the NCLs). An additional confirmation of the shape anisotropy of the clusters was obtained by SAXS measurements of 50 mg/ml solutions of NCLs in hexane (such measurement is not sensitive to the atomic structure of the clusters, but only to their nanoscale morphology). The SAXS fitting indicated an asymmetric pair distribution function [p(r)], peaked at about 2.5 nm, featuring a maximum inter-atomic distance (i.e. cluster long axis) of about 13 nm and a radius of gyration of 4 nm, which is consistent with an object having a disk-like shape and dimensions as those estimated by PDF (see also Figure S9 and discussion therein).

In order to further investigate the NCLs packing, we performed combined SAXS and WAXS measurements in the solid state. The SAXS signal (Figure 2e,g) explains the XRD peaks at small angles in terms of ordered stacking of the NCLs in a superstructure, while the WAXS signal (Figure 2 f, h) is consistent with XPD measurements and reveals an elongation direction of the NCLs orthogonal to the stacking direction (compare Figures 2e, 2f, and Scheme 2). Indeed, based on the whole profile fit in Figure S7, the most intense partial diffraction rings appearing in Figure 2f could be clearly identified as the (101)/(020) and (202)/(040) reflections relative to the orthorhombic $CsPbBr_3$ crystal phase. Moreover, the simultaneous collection of SAXS and WAXS patterns at the same sample position allowed to reveal the coherent orientation of the NCLs in the assembly: i) the stacking direction can be extracted by the partial rings of the SAXS pattern (Figure 2e); ii) the NCLs orientation is defined by the main WAXS partial rings (Figure 2f) perpendicular to the stacking direction. It is worth to note that the partial rings in the SAXS pattern (Figure 2e) fulfill the Q-positions (Figure 2g) expected for a hexagonal packing: Q, $Q\sqrt{3}$, 2Q (i.e. (100), (110), (200) reflections, respectively).[40] However the further peak expected at $Q\sqrt{7}$ is missing, and it is apparently replaced by a broad peak appearing around 5.2 nm^{-1} (2θ=7.4°) in the WAXS pattern (Figures 2h). At the same time, no peaks are detected around 0.6 nm^{-1} (which would be expected in the case of a periodic arrangement along the equatorial plane of ∼10nm clusters). Such results have been confirmed at any sample position by collecting scanning SAXS microscopies (Figure S10). As a consequence, a 2D hexagonal symmetry can be expected with a short range order, with unit cell parameter a=4.4/cos30°= 5.1 nm, while a lamellar stacking is observed on a larger length scale, with periodicities of 4.4 and 2.5 nm (Scheme 2). Such two periodicities could refer to vertically aligned or shifted (close-packed) clusters. The lack of long range order in three dimensions can be likely ascribed to the hindrance in the equatorial plane of the clusters (Figure 2a and Figure S8), preventing them from getting close enough to form a regular 3D assembly.

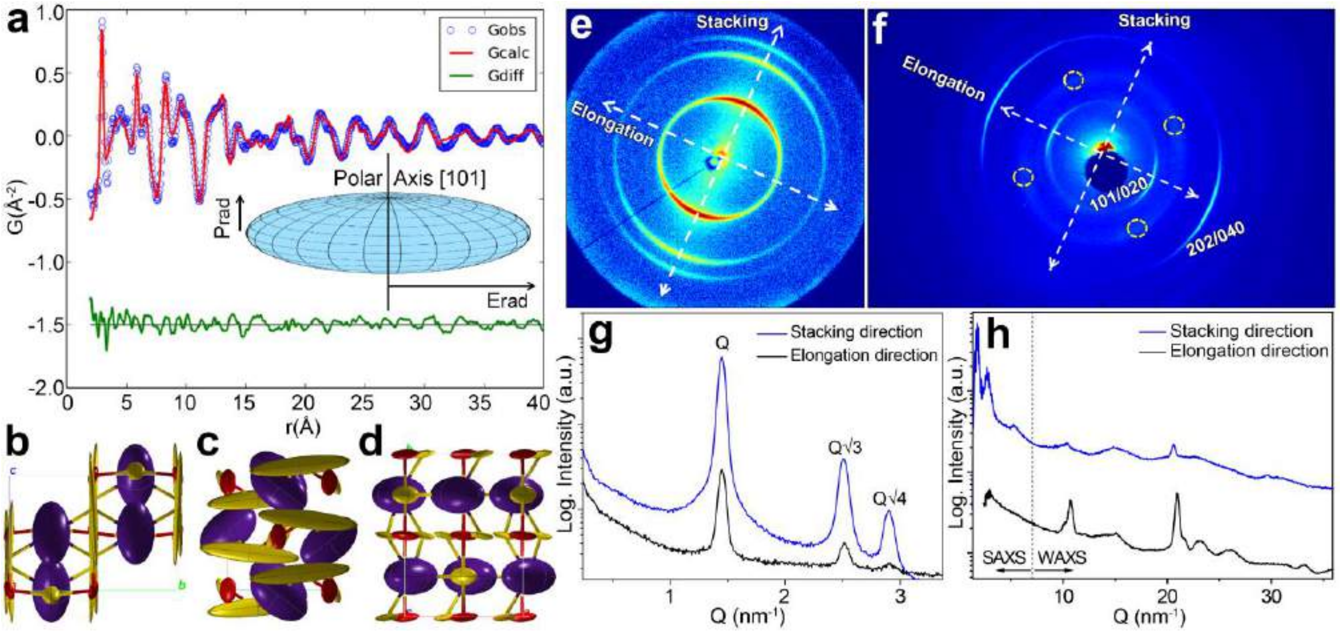

Figure 2. PDF fit (a) and refined crystal structure viewed normal to a, b, c axes (b, c, d panels, respectively) of the orthorhombic $CsPbBr_3$ phase. Pb, Cs and Br ions are shown in red, pink and yellow, respectively. Thermal ellipsoids at 50% probability level represent their atomic anisotropic displacement factors. Inner picture of (a): schematic view of the NCL shape, based on PDF refinement and micro-structural analysis of the XPD profile. Erad and Prad are respectively the equatorial and polar radii parameters (Table S1). SAXS (e) and WAXS (f) 2D patterns simultaneously collected at the XMI-Lab, at a selected sample position; (g) 1D folded SAXS pattern from the line cuts indicated by the white arrows in (e); (h) 1D folded WAXS patterns from the line cuts indicated by the white arrows in (f).

Scheme 2. NCLs arrangement according to SAXS and WAXS patterns.

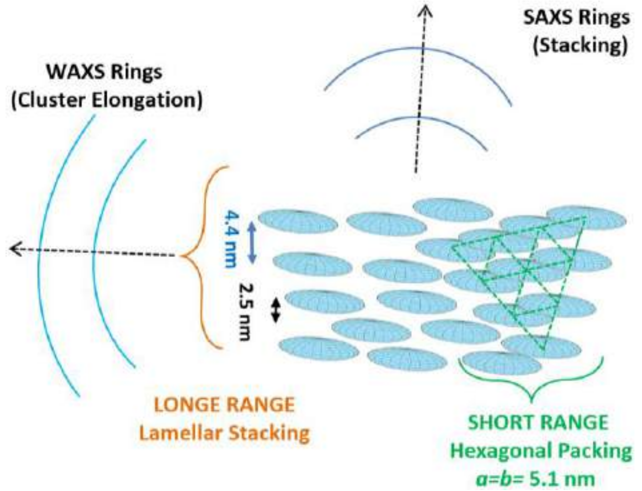

Trap Emission at Low Temperature. After revealing the structure and the superstructures of CsPbBr3 NCLs, their optical properties at cryogenic temperature were studied in details. As shown in Figure 1b, the NCLs in hexane solution has a trap emission range from 450nm to 600 nm at RT. By PLE spectra, such broad trap emission was ascribed to the 400 nm absorption, corresponding to the band absorption of NCLs, as shown in Figure S10. At low temperatures, the broad emission became much brighter, as shown in Figure 6a and Figure S11. By cooling down the sample from RT to 77 K (boiling point of liquid N_2), the broadband yellow-white emission gradually dominated, as shown in Figure S10. By subsequent cooling the sample to 7K, another broad blue-green emission peak gradually appear and finally dominated. The PLE spectra in Figure 6b indicate that the two broadband emission still come from the bandgap absorption of NPLs. As shown in Figure S12 and S13, the broadband emission is independent on the NCL's concentration and ligands type. We thus exclude the possibility that the broad emission come from the cluste-cluster interaction or from ligands. We tentatively ascribe the broad emission to the surface trap or the self-trapped exciton (STE) in the NPLs lattice.

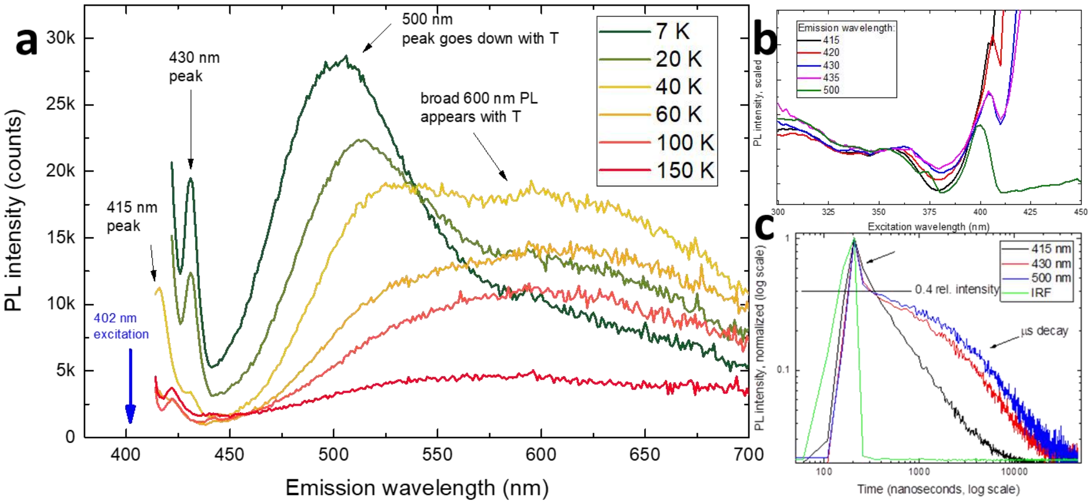

Figure 3. (a) PL spectra of NPLs at different temperature; (b) PLE spectra of each emission peak at 7K; (c) PL lifetime decay curve for different emission peaks at 7K.

Overall, we can state that, on average, the NCLs could be described as 1 monolayer-thick platelets. Yet, their peculiar morphology, crystal structure and surface chemistry make them behave differently from previously reported perovskite nanoplatelets. For example, both ultrathin organic-inorganic (oleylammonium)$_2$PbBr$_4$ nanosheets (1 monolayer thick)[50-52] and few monolayers thick CsPbBr$_3$ platelets[57] have been shown in previous works to assemble in layered structures with high preferred orientation. Such orientation was evident from the XRD patterns, which featured several equally spaced peaks in the small angle range and also intense peaks in the wide angle range that were related to the in-plane crystalline order. Also, the previously reported nanoplatelets featured a cubic CsPbBr$_3$ structure.[51, 57] Conversely, the NCLs in the present work exhibit a distorted orthorhombic CsPbBr$_3$ phase and they are not able to form layered structures with long range order. Instead, they assemble based on their particular shape and size, as discussed in this work. For these reasons, the NCLs presented here are considered different from "simple nanoplatelets".

Table S1. Refinement parameters derived from the PDF fit of the orthorhombic CsPbBr$_3$.crystal phase. R$_w$ is the weighted agreement factor between observed and calculated PDF; Delta1 is the coefficient for 1/*r* contribution to the peak sharpening*;* Erad and Prad are the equatorial and polar radii of the spheroidal shape (Fig. 2a in the main text) assumed for the nanocluster; *a*,*b*,*c* are the length of the unit cell axes.

Rw	0.257
Delta1	2.5±0.5
Erad (Å)	64±9
Prad (Å)	8±2
a,b,c (Å)	8.5±0.2, 11.8±0.1, 8.0±0.2

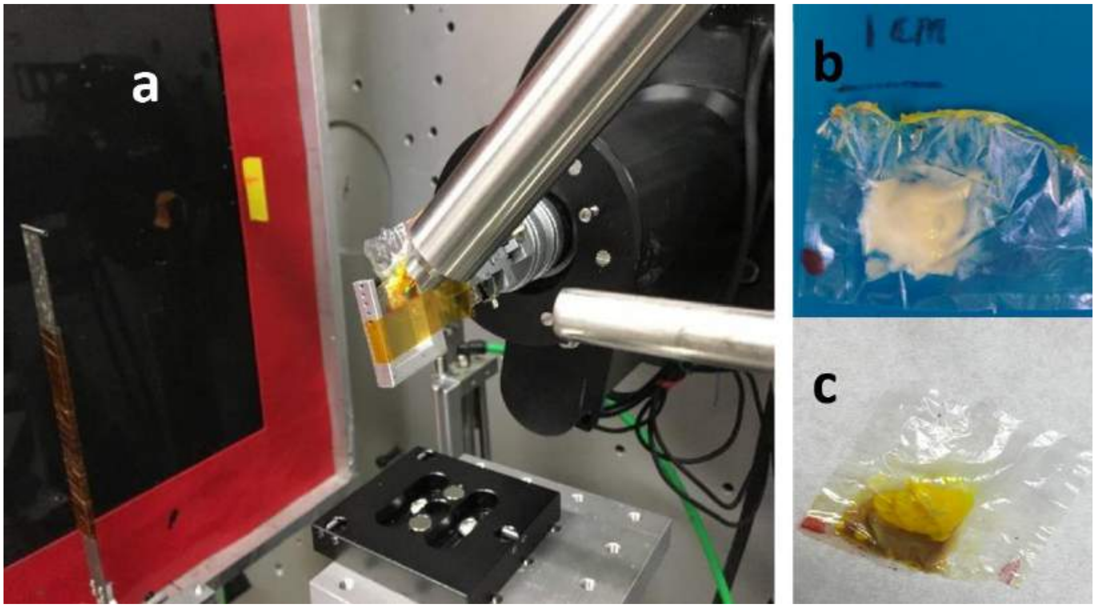

Figure S1. Experimental setup for PDF measurements, with the nanocluster sample put in an ultralene bag (a) and (b) fresh NCLs sample for test; (c) NCLs sample after heating.

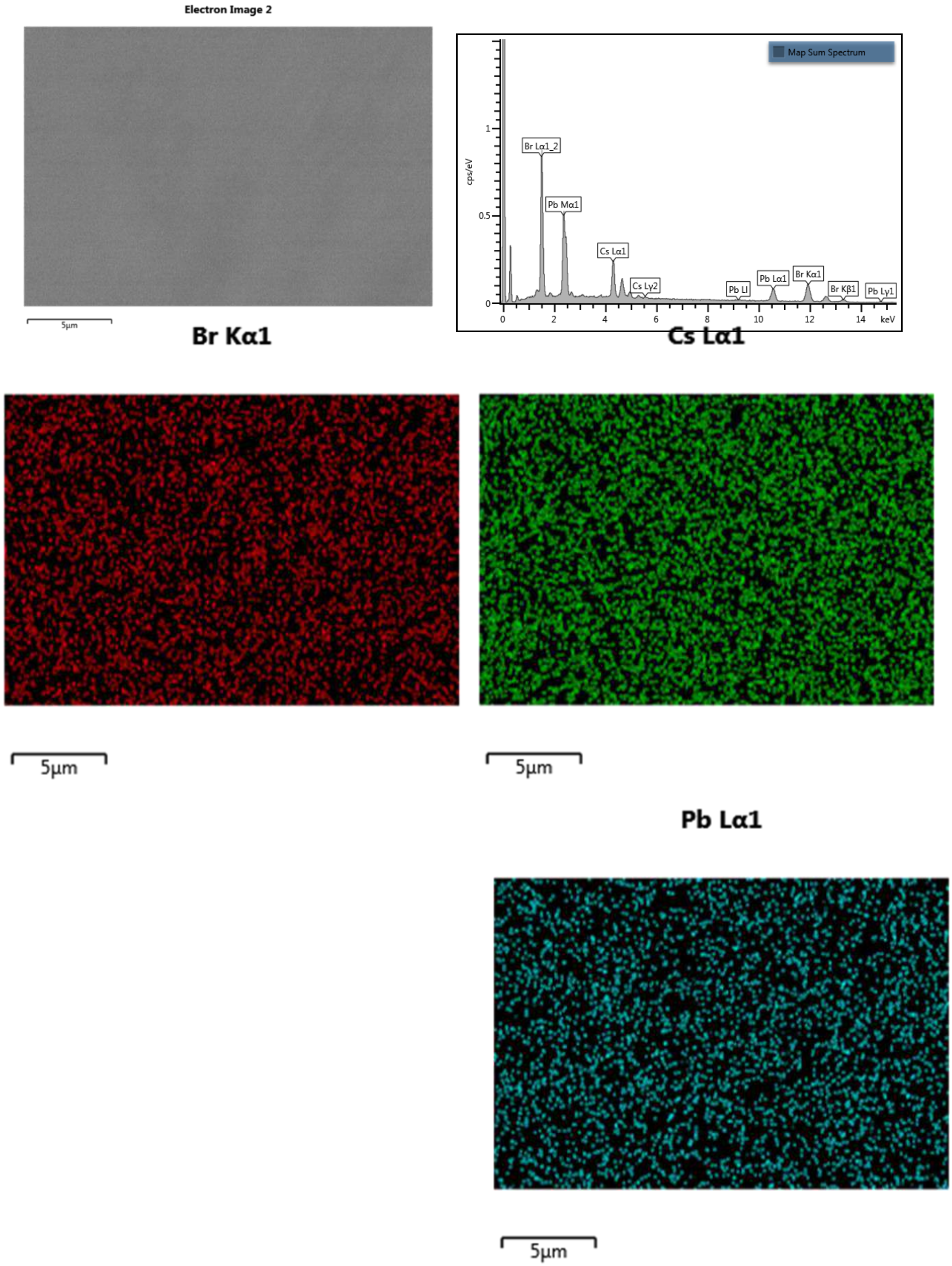

Figure S2. SEM-EDS mapping of the purified $CsPbBr_3$ nanoclusters sample.

Table S2. SEM-EDS analysis of the purified $CsPbBr_3$ nanoclusters sample.

Map Sum Spectrum	Line Type	Wt%	Wt% Sigma	Atomic %
Br	K series	35.10	0.75	53.56
Cs	L series	25.09	0.53	23.02
Pb	L series	39.80	0.84	23.42
Total		100.00		100.00

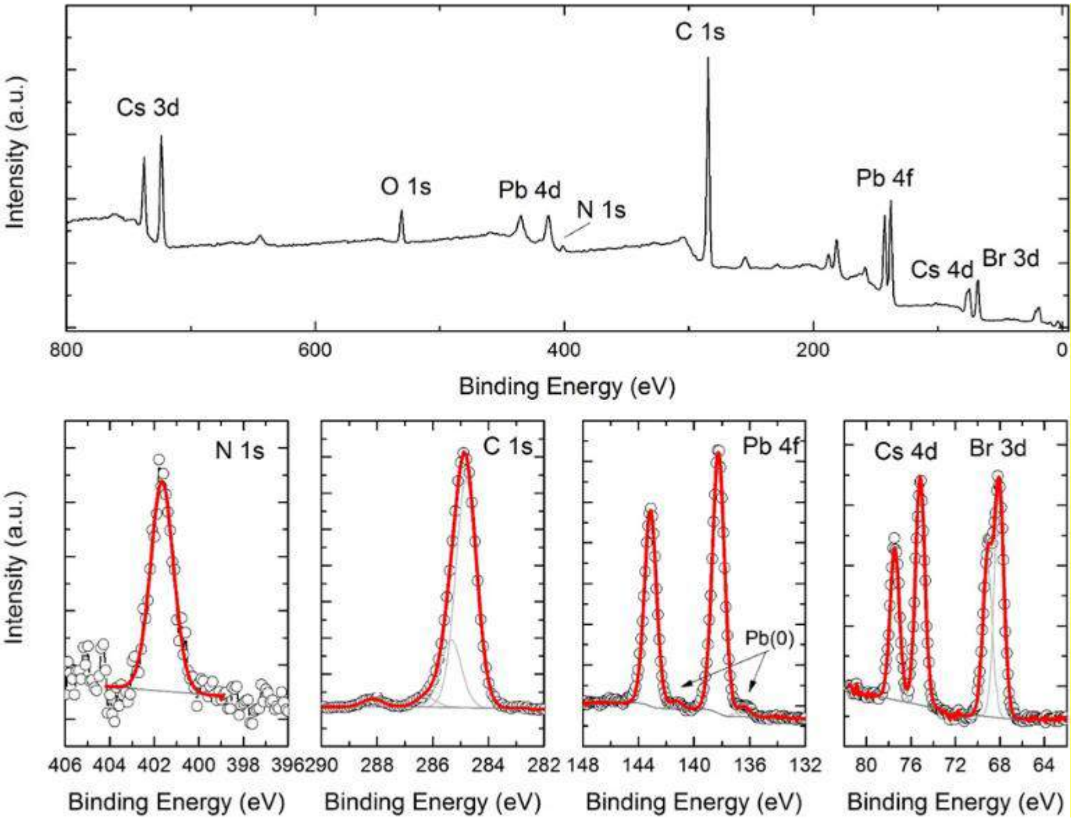

Figure S3. XPS spectra of the purified $CsPbBr_3$ nanoclusters sample.

Table S3. XPS result of the purified $CsPbBr_3$ nanoclusters sample. The COO^- content was estimated from the area of the C 1s component centered at 288.1±0.2 eV, while that of NH_3^+ from the N 1s peak at 401.6 eV, in agreement with what reported by Gonella et al., *J. Phys. Chem.* B 2005, 109, 38, 18003–18009.

Element	Mol ratio (%)
Cs	16.3
Pb	17.1
Br	39.9
COO^-	16.0
NH_3^+	10.7

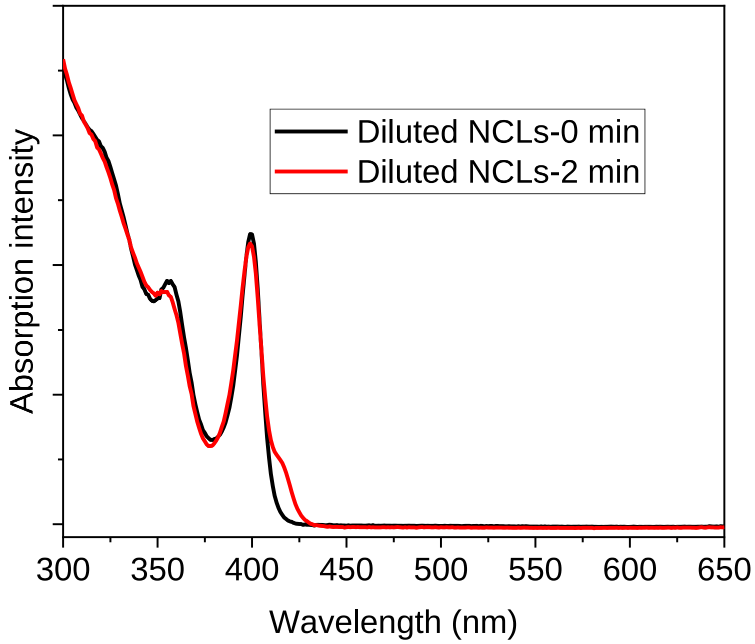

Figure S4. Optical absorption spectra of a diluted dispersion of NCLs in hexane (0 min) and their transformation into $CsPbBr_3$ after 2 min of ageing in atmosphere.

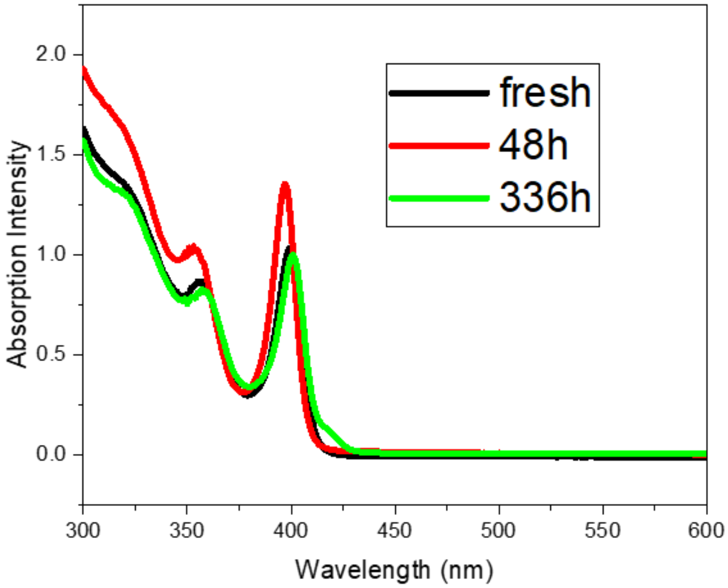

Figure S5. Time evolution of the optical absorption spectrum of concentrated (50 mg/ml) $CsPbBr_3$ nanoclusters dispersed in hexane.

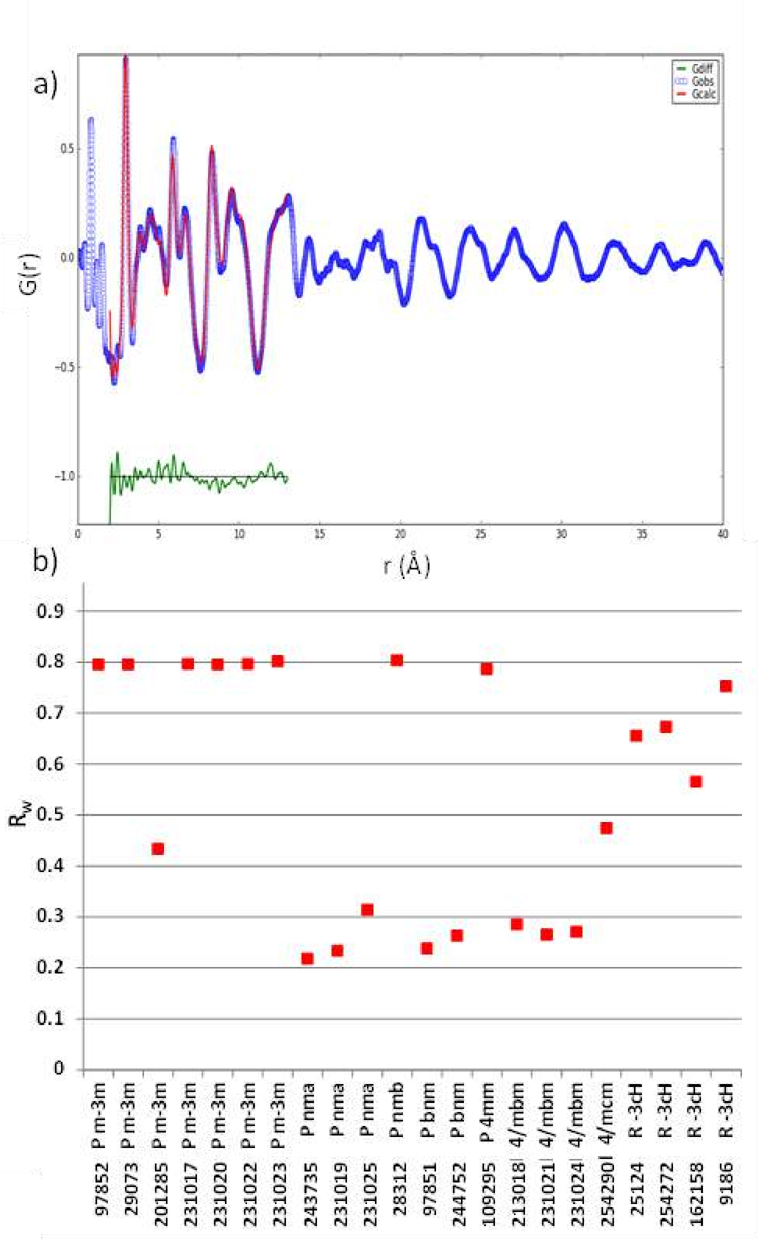

Figure S6. (a) PDF profile of the $CsPbBr_3$ NCLs fitted in a restricted range by the crystal phase Pnma. Experimental (blue dots), calculated (red line) and difference (green line) PDF values are shown. (b) Results of the crystal phase identification procedure. Weighted agreement factor (R_w) between observed and calculated PDF, obtained by refining 22 Cs-Pb-Br crystal phases present inthe ISCD, identified by their space group and entry code. The Pnma crystal structures n.231019[1] and 243735[2], which minimize R_w and are in fact very similar, best fit the PDF profile.

---

[1] Patrick Cottingham and Richard L. Brutchey : Chem. Mater. 2018, 30, 6711−6716.

[2] Matthew R. Linaburg, Eric T. McClure, Jackson D. Majher, and Patrick M. Woodward Chem. Mater. 2017, 29, 8, 3507–3514.

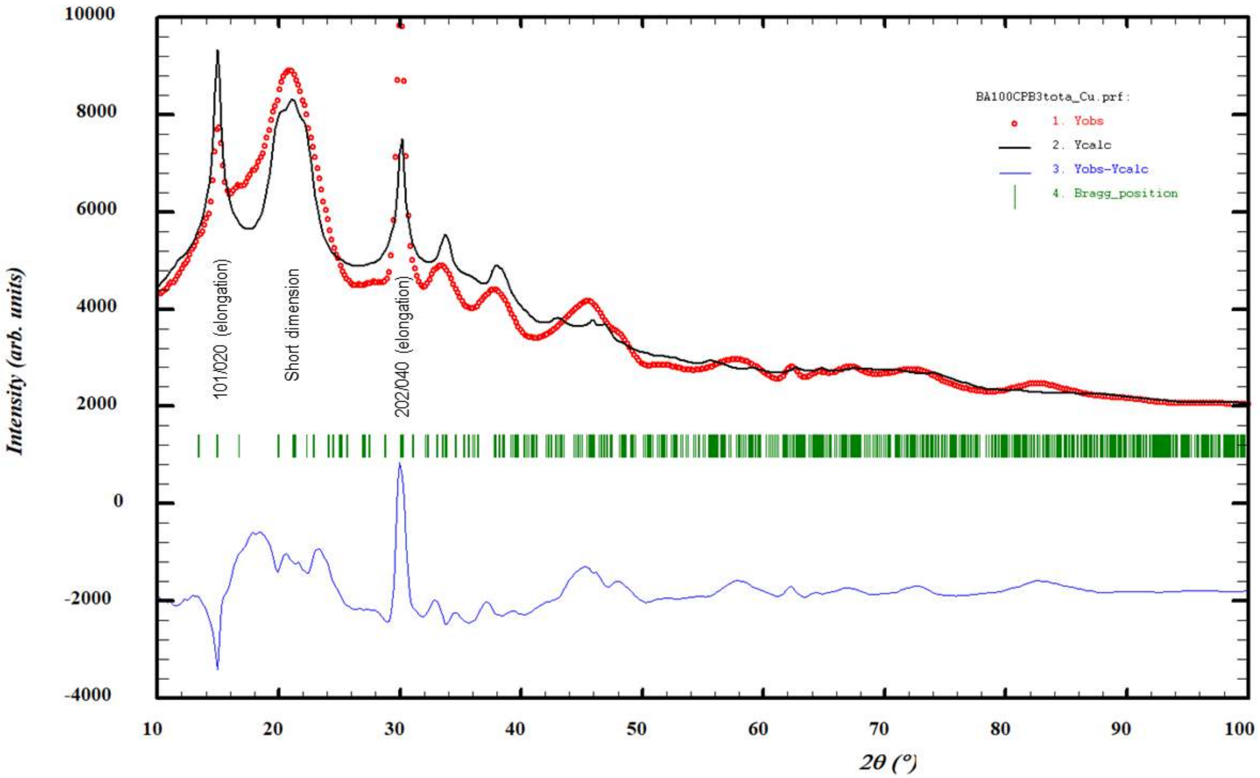

Figure S7. Whole profile fitting of the synchrotron XRD pattern (reported in Figure 1d of the main text), showing the anisotropic shape of clusters, based on the significantly different FWHM of the diffraction peaks.

Whole profile fitting in Figure S5 was performed by using the program FullProf[3]. Although a perfect fit could not be achieved, probably due to high preferred orientation and anisotropy of the nanoclusters, a size difference of at least a factor 4 was found along the two main perpendicular directions (i.e. 2.3 and 10.7 nm for the 101 and 020 reflections, respectively). Based on the FWHM of all peaks in the calculated profile, the program returned an overall disk-like shape of the single cluster, as reported in Figure S6.

---

[3] Juan Rodríguez-Carvajal Recent advances in magnetic structure determination by neutron powder diffraction Physica B: Condensed Matter 192, 1993, 55-69.

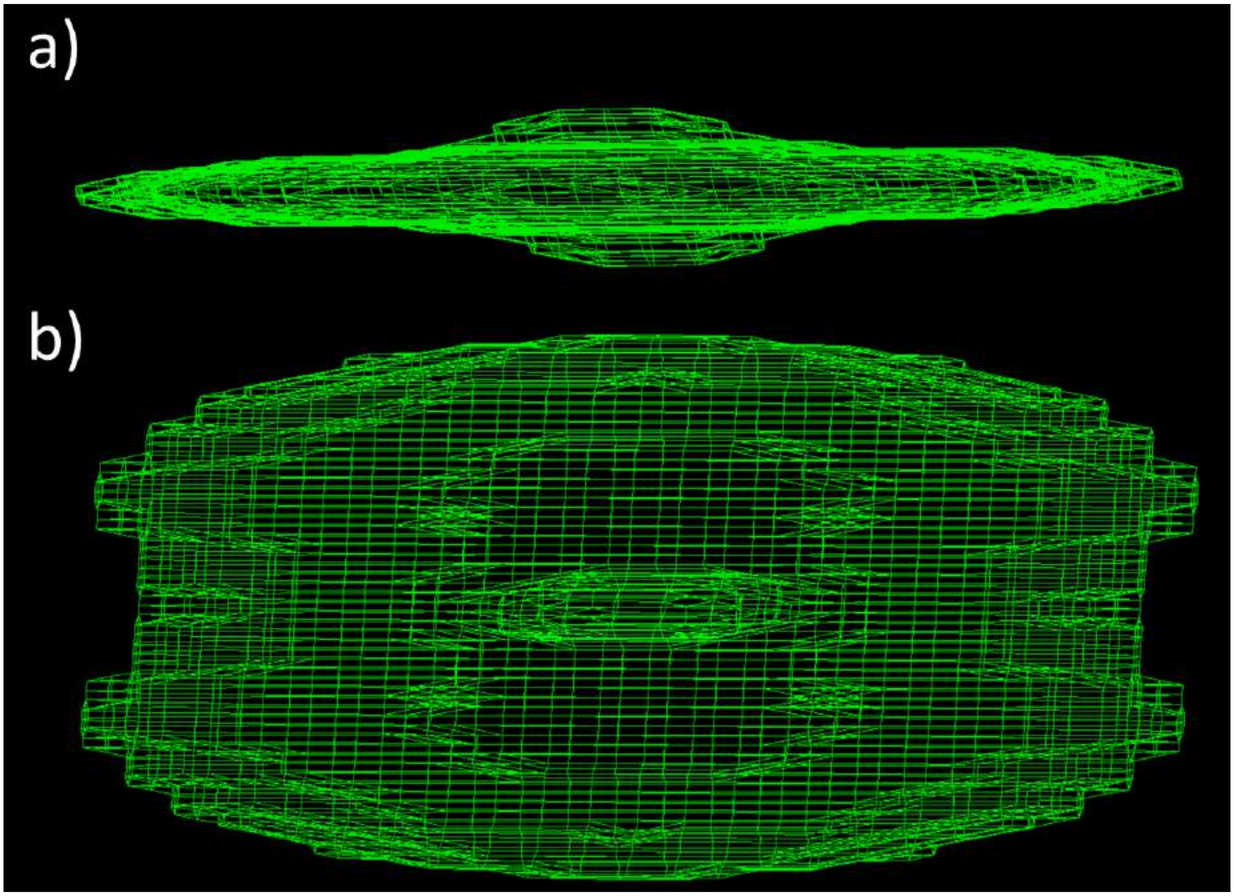

Figure S8. Overall the clusters shape resulting from the whole profile fit. View parallel (a) and perpendicular (b) to the equatorial plane.

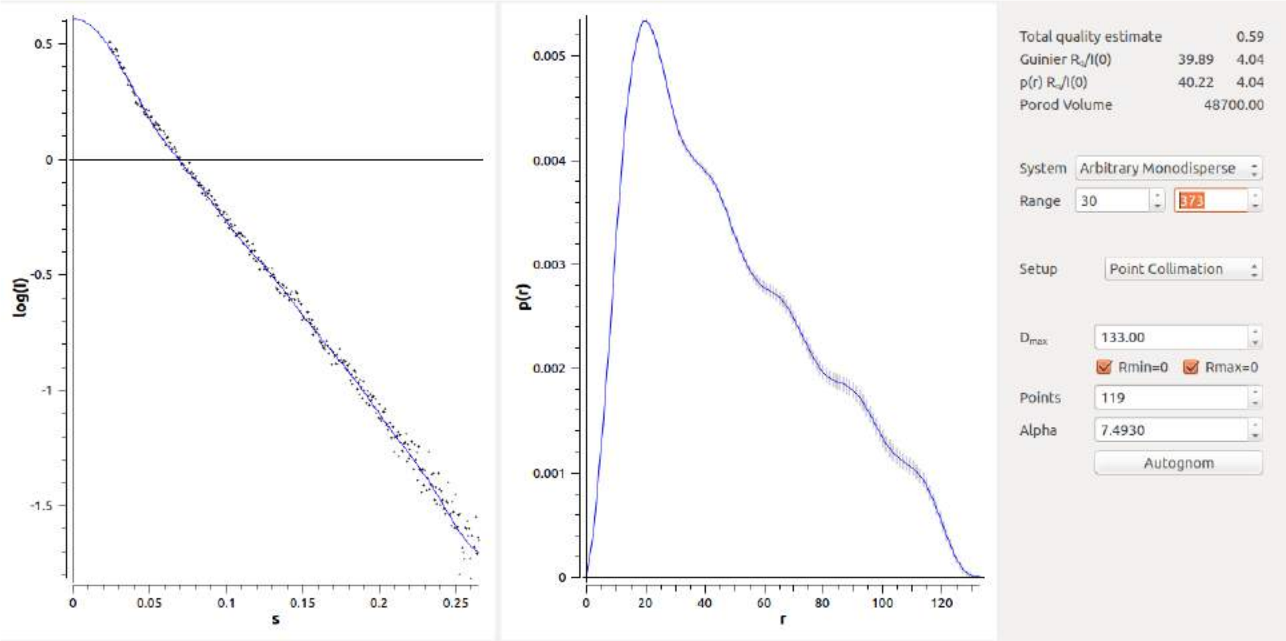

Total quality estimate 0.59
Guinier R_g/I(0) 39.89 4.04
p(r) R_g/I(0) 40.22 4.04
Porod Volume 48700.00

System Arbitrary Monodisperse
Range 30 373

Setup Point Collimation

D_{max} 133.00
☑ Rmin=0 ☑ Rmax=0
Points 119
Alpha 7.4930

Figure S9. Fit of the 1D-folded SAXS pattern from 50 mg/ml solutions of clusters in hexane, returning a 4.0±0.4 nm gyration radius for the cluster, and clearly showing an asymmetric pair distribution function p(r) peaked at about 2.5 nm and featuring a maximum inter-atomic distance (i.e. cluster long axis) of about 13.3 nm (reported numbers for the scattering vector (s) and the direct space vector ® are in Å^{-1} and Å units, respectively).

The NCL geometrical parameters determined by SAXS measurements are compatible with those determined by PDF. The maximum interatomic distance D_{max} resulting from SAXS measurements is compatible with the NCL equatorial length of 13 nm estimated by PDF. In addition, the SAXS determination of the radius of gyration (4.0±0.4 nm) is in agreement with PDF determinations of the NCL shape. In fact, the radius of gyration for an oblate ellipsoid having equatorial and polar radii respectively Erad and Prad is given by[4]:

$$R_g = \frac{8}{5} E_{rad}{}^2 + \frac{E_{rad}+4P_{rad}}{E_{rad}+2P_{rad}}.$$

Thus, if we consider the experimental values determined by PDF: Erad=6 nm and Prad=0.8 nm we expect Rg=3.9 nm.

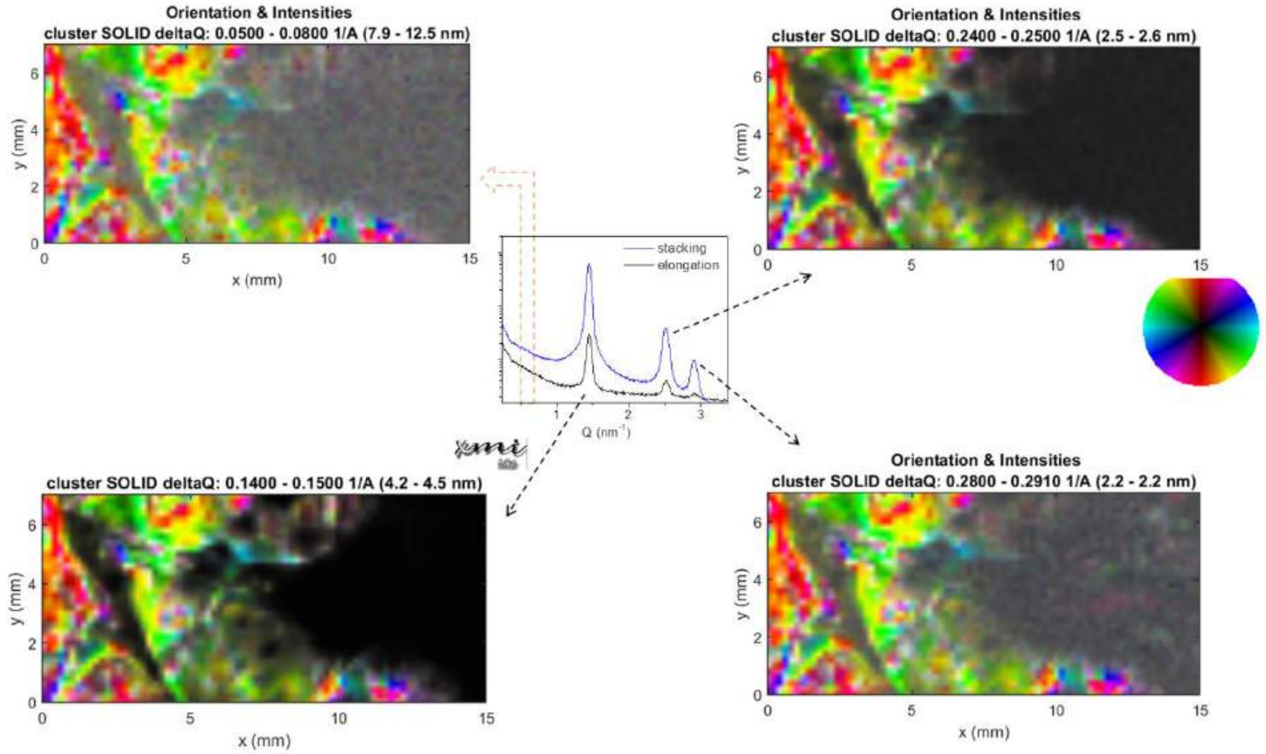

Figure S10. Orientation/Intensity SAXS microscopies for each of the three peaks detected in the SAXS pattern, and for the low-Q range diffuse scattering related to the particle form factor. The preferred azimuthal orientation of the scattering and the relevant direction is described by the local colour, based on the colour wheel on the right side of the figure. Colour brightness is proportional to the scattering intensity.

The orientation of the nanoscale ordered domains at any sample position is indicated in Fig. S8 by a well-defined color, according to the color wheel on the right side of the Figure. SAXS microscopies show that all partial rings in the SAXS pattern are always mutually aligned, although their overall orientation can change across the investigated sample area. The orientation distribution of the diffuse scattering appearing at small Q-values is also plotted in the top left corner of Fig. S8, and shows to be coherent (similar distribution of colors) with the orientation distribution obtained for the three diffraction peaks. Since diffuse scattering can be

---

[4] John Satterly, Formulae for Volumes, Surface Areas and Radii of Gyration of Spheres, Ellipsoids and Spheroids

The Mathematical Gazette 44, 347 (1960), 15-19.

ascribed to the form factor of the NCLs, this indicates that the spheroids are oriented with their short and long axes respectively parallel and perpendicular to the stacking direction.

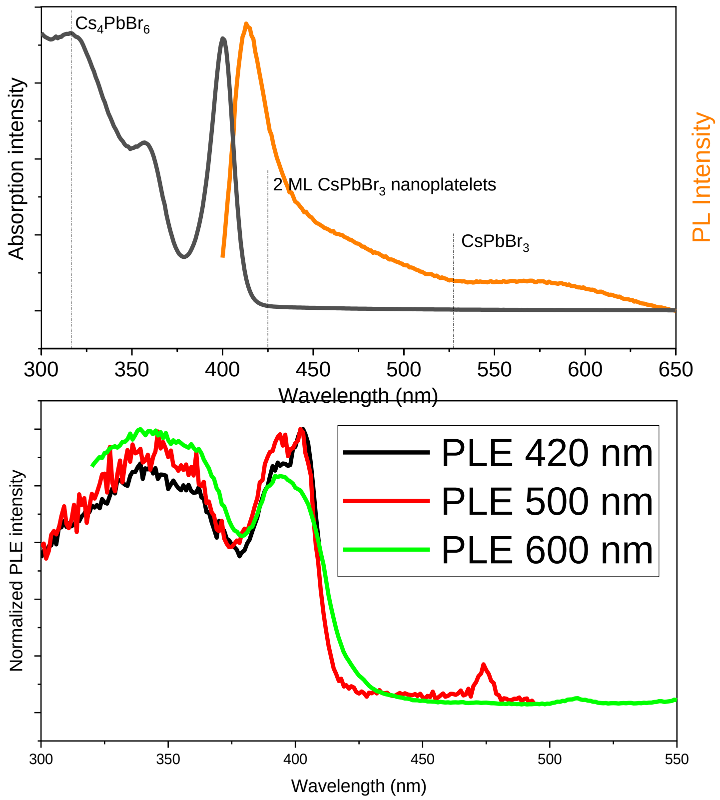

Fig. S10. (Top) Absorption and PL spectra of concentrated NPLs hexane solution; (Bottom) PLE spectra of the emission peak at 420 nm, 500 nm and 600 nm.

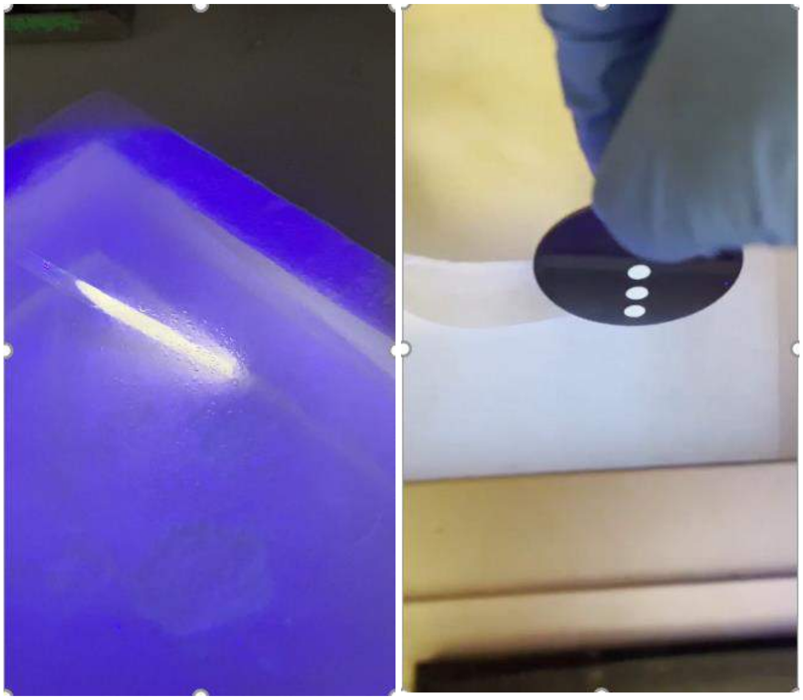

Fig. S11. (Left) Image of NPLs hexane solution after immerging into liquid N2 under UV light; (Right) Image of NPLs solid deposits after immerging into liquid N2 under UV light.

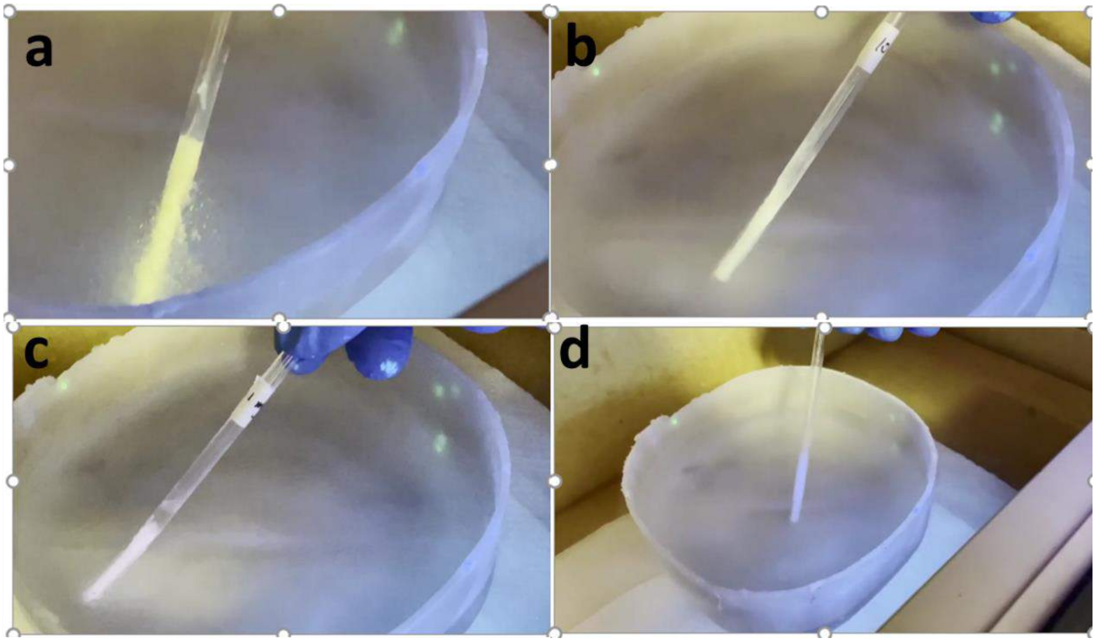

Fig. S12. (a) Image of NPLs hexane (100 mg/ml) solution after immerging into liquid N2 under UV light; (b) Image of NPLs hexane (10 mg/ml) solution after immerging into liquid N2 under UV light; (c) Image of NPLs hexane (1 mg/ml) solution after immerging into liquid N2 under UV light; (d) Image of control sample-hexane (0 mg/ml) solution after immerging into liquid N2 under UV light. The control sample was obtained by the same procedures with NPLs but without Cs-oleate injection.

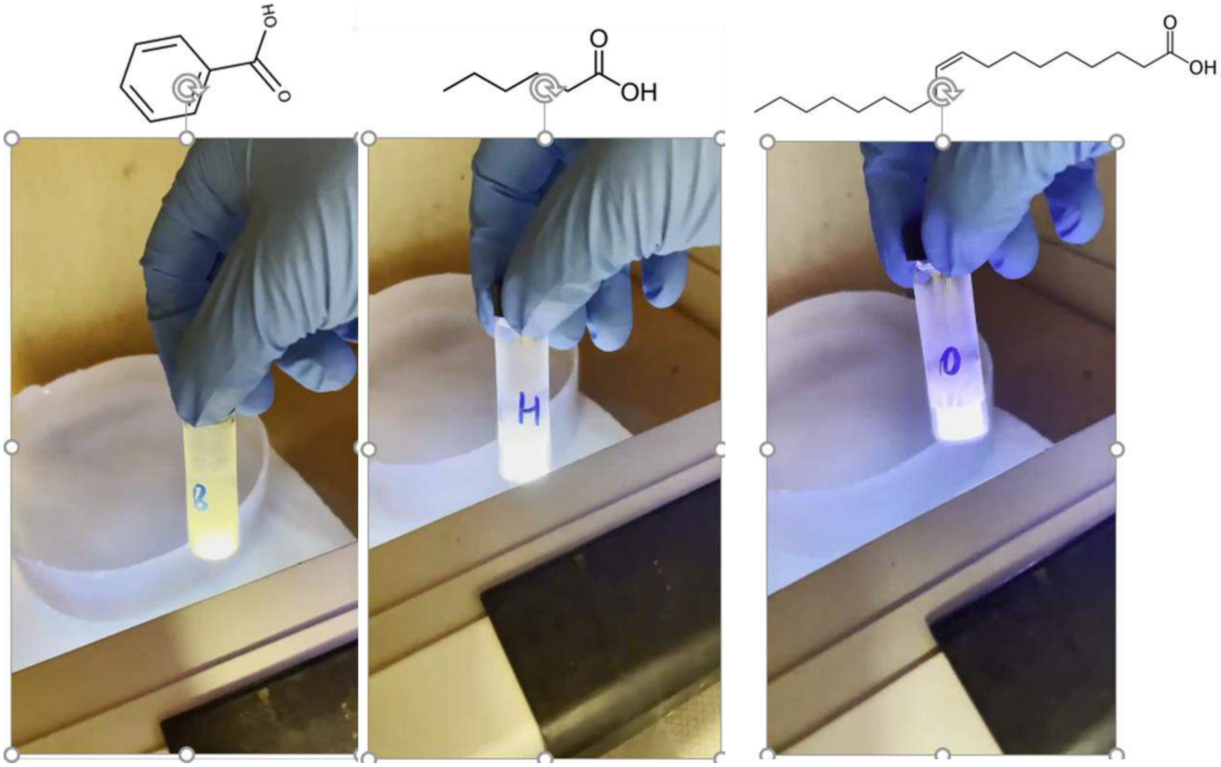

Fig. S13. (left) Image of NPLs hexane (caped by benzoic acid) solution after immerging into liquid N2 under UV light; (middle) Image of NPLs hexane (caped by hexanoic acid) solution after immerging into liquid N2 under UV light; (right) Image of NPLs hexane (caped by oleic acid) solution after immerging into liquid N2 under UV light.

REFERENCES:

1. Xie, R.; Li, Z.; Peng, X., Nucleation kinetics vs chemical kinetics in the initial formation of semiconductor nanocrystals. *J. Am. Chem. Soc.* **2009,** *131* (42), 15457-15466.
2. Gary, D. C.; Terban, M. W.; Billinge, S. J. L.; Cossairt, B. M., Two-Step Nucleation and Growth of InP Quantum Dots via Magic-Sized Cluster Intermediates. *Chem. Mater.* **2015,** *27* (4), 1432-1441.
3. Zhu, T.; Zhang, B.; Zhang, J.; Lu, J.; Fan, H.; Rowell, N.; Ripmeester, J. A.; Han, S.; Yu, K., Two-Step Nucleation of CdS Magic-Size Nanocluster MSC–311. *Chem. Mater.* **2017,** *29* (13), 5727-5735.
4. Zhang, B.; Zhu, T.; Ou, M.; Rowell, N.; Fan, H.; Han, J.; Tan, L.; Dove, M. T.; Ren, Y.; Zuo, X.; Han, S.; Zeng, J.; Yu, K., Thermally-induced reversible structural isomerization in colloidal semiconductor CdS magic-size clusters. *Nat. Commun.* **2018,** *9* (1), 2499.
5. Williamson, C. B.; Nevers, D. R.; Nelson, A.; Hadar, I.; Banin, U.; Hanrath, T.; Robinson, R. D., Chemically reversible isomerization of inorganic clusters. *Science* **2019,** *363* (6428), 731.
6. Peng, L.; Dutta, A.; Xie, R.; Yang, W.; Pradhan, N., Dot–Wire–Platelet–Cube: Step Growth and Structural Transformations in CsPbBr3 Perovskite Nanocrystals. *ACS Energy Lett.* **2018,** *3* (8), 2014-2020.
7. Mule, A. S.; Mazzotti, S.; Rossinelli, A. A.; Aellen, M.; Prins, P. T.; van der Bok, J. C.; Solari, S. F.; Glauser, Y. M.; Kumar, P. V.; Riedinger, A.; Norris, D. J., Unraveling the Growth Mechanism of Magic-Sized Semiconductor Nanocrystals. *J. Am. Chem. Soc.* **2021,** *143* (4), 2037-2048.

8. Ouyang, J.; Zaman, M. B.; Yan, F. J.; Johnston, D.; Li, G.; Wu, X.; Leek, D.; Ratcliffe, C. I.; Ripmeester, J. A.; Yu, K., Multiple Families of Magic-Sized CdSe Nanocrystals with Strong Bandgap Photoluminescence via Noninjection One-Pot Syntheses. *J. Phys. Chem. C* **2008,** *112* (36), 13805-13811.
9. Palencia, C.; Yu, K.; Boldt, K., The Future of Colloidal Semiconductor Magic-Size Clusters. *ACS Nano* **2020,** *14* (2), 1227-1235.
10. Beecher, A. N.; Yang, X.; Palmer, J. H.; LaGrassa, A. L.; Juhas, P.; Billinge, S. J. L.; Owen, J. S., Atomic Structures and Gram Scale Synthesis of Three Tetrahedral Quantum Dots. *J. Am. Chem. Soc.* **2014,** *136* (30), 10645-10653.
11. Cossairt, B. M.; Owen, J. S., CdSe Clusters: At the Interface of Small Molecules and Quantum Dots. *Chem. Mater.* **2011,** *23* (12), 3114-3119.
12. Vickers, E. T.; Xu, K.; Dreskin, B. W.; Graham, T. A.; Li, X.; Zhang, J. Z., Ligand Dependent Growth and Optical Properties of Hybrid Organo-metal Halide Perovskite Magic Sized Clusters. *J. Phys. Chem. C* **2019,** *123* (30), 18746-18752.
13. Gebauer, D.; Völkel, A.; Cölfen, H., Stable Prenucleation Calcium Carbonate Clusters. *Science* **2008,** *322* (5909), 1819.
14. Xie, L.; Shen, Y.; Franke, D.; Sebastián, V.; Bawendi, M. G.; Jensen, K. F., Characterization of Indium Phosphide Quantum Dot Growth Intermediates Using MALDI-TOF Mass Spectrometry. *J. Am. Chem. Soc.* **2016,** *138* (41), 13469-13472.
15. Friedfeld, M. R.; Stein, J. L.; Cossairt, B. M., Main-Group-Semiconductor Cluster Molecules as Synthetic Intermediates to Nanostructures. *Inorg. Chem.* **2017,** *56* (15), 8689-8697.
16. Jiang, Z.-J.; Kelley, D. F., Role of Magic-Sized Clusters in the Synthesis of CdSe Nanorods. *ACS Nano* **2010,** *4* (3), 1561-1572.
17. Zhang, J.; Rowland, C.; Liu, Y.; Xiong, H.; Kwon, S.; Shevchenko, E.; Schaller, R. D.; Prakapenka, V. B.; Tkachev, S.; Rajh, T., Evolution of Self-Assembled ZnTe Magic-Sized Nanoclusters. *J. Am. Chem. Soc.* **2015,** *137* (2), 742-749.
18. Cumberland, S. L.; Hanif, K. M.; Javier, A.; Khitrov, G. A.; Strouse, G. F.; Woessner, S. M.; Yun, C. S., Inorganic Clusters as Single-Source Precursors for Preparation of CdSe, ZnSe, and CdSe/ZnS Nanomaterials. *Chem. Mater.* **2002,** *14* (4), 1576-1584.
19. Wang, Y.; Zhou, Y.; Zhang, Y.; Buhro, W. E., Magic-Size II–VI Nanoclusters as Synthons for Flat Colloidal Nanocrystals. *Inorg. Chem.* **2015,** *54* (3), 1165-1177.
20. Friedfeld, M. R.; Johnson, D. A.; Cossairt, B. M., Conversion of InP Clusters to Quantum Dots. *Inorg. Chem.* **2019,** *58* (1), 803-810.
21. Peng, L.; Dutta, S. K.; Mondal, D.; Hudait, B.; Shyamal, S.; Xie, R.; Mahadevan, P.; Pradhan, N., Arm Growth and Facet Modulation in Perovskite Nanocrystals. *J. Am. Chem. Soc.* **2019,** *141* (40), 16160-16168.
22. Imran, M.; Peng, L.; Pianetti, A.; Pinchetti, V.; Ramade, J.; Zito, J.; Di Stasio, F.; Buha, J.; Toso, S.; Song, J.; Infante, I.; Bals, S.; Brovelli, S.; Manna, L., Halide Perovskite–Lead Chalcohalide Nanocrystal Heterostructures. *Journal of the American Chemical Society* **2021,** *143* (3), 1435-1446.
23. Tamang, S.; Lee, S.; Choi, H.; Jeong, S., Tuning Size and Size Distribution of Colloidal InAs Nanocrystals via Continuous Supply of Prenucleation Clusters on Nanocrystal Seeds. *Chem. Mater.* **2016,** *28* (22), 8119-8122.
24. Li, L.; Zhang, J.; Zhang, M.; Rowell, N.; Zhang, C.; Wang, S.; Lu, J.; Fan, H.; Huang, W.; Chen, X.; Yu, K., Fragmentation of Magic-Size Cluster Precursor Compounds into Ultrasmall CdS Quantum Dots with Enhanced Particle Yield at Low Temperatures. *Angew. Chem. Int. Ed. Engl.* **2020,** *59* (29), 12013-12021.
25. Zhou, Y.; Jiang, R.; Wang, Y.; Rohrs, H. W.; Rath, N. P.; Buhro, W. E., Isolation of Amine Derivatives of (ZnSe)34 and (CdTe)34. Spectroscopic Comparisons of the (II–VI)13 and (II–VI)34 Magic-Size Nanoclusters. *Inorg. Chem.* **2019,** *58* (3), 1815-1825.
26. Wang, Y.; Zhang, Y.; Wang, F.; Giblin, D. E.; Hoy, J.; Rohrs, H. W.; Loomis, R. A.; Buhro, W. E., The Magic-Size Nanocluster (CdSe)34 as a Low-Temperature Nucleant for Cadmium Selenide Nanocrystals; Room-Temperature Growth of Crystalline Quantum Platelets. *Chem. Mater.* **2014,** *26* (7), 2233-2243.
27. Evans, C. M.; Guo, L.; Peterson, J. J.; Maccagnano-Zacher, S.; Krauss, T. D., Ultrabright PbSe Magic-sized Clusters. *Nano Lett.* **2008,** *8* (9), 2896-2899.
28. Kim, T.; Park, S.; Jeong, S., Diffusion dynamics controlled colloidal synthesis of highly monodisperse InAs nanocrystals. *Nat. Commun.* **2021,** *12* (1), 3013.
29. Srivastava, V.; Dunietz, E.; Kamysbayev, V.; Anderson, J. S.; Talapin, D. V., Monodisperse InAs Quantum Dots from Aminoarsine Precursors: Understanding the Role of Reducing Agent. *Chem. Mater.* **2018,** *30* (11), 3623-3627.
30. Xu, Y.; Zhang, Q.; Lv, L.; Han, W.; Wu, G.; Yang, D.; Dong, A., Synthesis of ultrasmall CsPbBr3 nanoclusters and their transformation to highly deep-blue-emitting nanoribbons at room temperature. *Nanoscale* **2017,** *9* (44), 17248-17253.
31. Xu, K.; Allen, A. L. C.; Luo, B.; Vickers, E. T.; Wang, Q.; Hollingsworth, W. R.; Ayzner, A. L.; Li, X.; Zhang, J. Z., Tuning from Quantum Dots to Magic Sized Clusters of CsPbBr3 Using Novel Planar Ligands Based on the Trivalent Nitrate Coordination Complex. *J. Phys. Chem. Lett.* **2019,** *10* (15), 4409-4416.

32. Shamsi, J.; Urban, A. S.; Imran, M.; De Trizio, L.; Manna, L., Metal Halide Perovskite Nanocrystals: Synthesis, Post-Synthesis Modifications, and Their Optical Properties. *Chem. Rev.* **2019,** *119* (5), 3296-3348.
33. Xu, K.; Vickers, E. T.; Luo, B.; Allen, A. L. C.; Chen, E.; Roseman, G.; Wang, Q.; Kliger, D. S.; Millhauser, G. L.; Yang, W.; Li, X.; Zhang, J. Z., First Synthesis of Mn-Doped Cesium Lead Bromide Perovskite Magic Sized Clusters at Room Temperature. *J. Phys. Chem. Lett.* **2020,** *11* (3), 1162-1169.
34. Liu, B.; Xu, G. Q.; Gan, L. M.; Chew, C. H.; Li, W. S.; Shen, Z. X., Photoluminescence and structural characteristics of CdS nanoclusters synthesized by hydrothermal microemulsion. *Journal of Applied Physics* **2000,** *89* (2), 1059-1063.
35. Nevers, D. R.; Williamson, C. B.; Savitzky, B. H.; Hadar, I.; Banin, U.; Kourkoutis, L. F.; Hanrath, T.; Robinson, R. D., Mesophase Formation Stabilizes High-Purity Magic-Sized Clusters. *J. Am. Chem. Soc.* **2018,** *140* (10), 3652-3662.
36. Altamura, D.; Lassandro, R.; Vittoria, F. A.; De Caro, L.; Siliqi, D.; Ladisa, M.; Giannini, C., X-ray microimaging laboratory (XMI-LAB). *J. Appl. Crystallogr.* **2012,** *45* (4), 869-873.
37. Manalastas-Cantos, K.; Konarev, P. V.; Hajizadeh, N. R.; Kikhney, A. G.; Petoukhov, M. V.; Molodenskiy, D. S.; Panjkovich, A.; Mertens, H. D. T.; Gruzinov, A.; Borges, C.; Jeffries, C. M.; Svergun, D. I.; Franke, D., ATSAS 3.0: expanded functionality and new tools for small-angle scattering data analysis. *J. Appl. Crystallogr.* **2021,** *54* (1), 343-355.
38. Siliqi, D.; De Caro, L.; Ladisa, M.; Scattarella, F.; Mazzone, A.; Altamura, D.; Sibillano, T.; Giannini, C., SUNBIM: a package for X-ray imaging of nano- and biomaterials using SAXS, WAXS, GISAXS and GIWAXS techniques. *J. Appl. Crystallogr.* **2016,** *49* (3), 1107-1114.
39. Bunk, O.; Bech, M.; Jensen, T. H.; Feidenhans'l, R.; Binderup, T.; Menzel, A.; Pfeiffer, F., Multimodal x-ray scatter imaging. *New Journal of Physics* **2009,** *11* (12), 123016.

Chapter 7: Summary and Outlook

Summary: In this thesis, the surface chemistry of different metal halide NCs was investigated.

Two new synthesis approaches to produce LHP NCs were developed by employing phosphonic acids (PAs) as the sole surfactants. In details, I used either alkyl or oleyl PAs and analyzed the corresponding products. The NMR analysis of these samples indicated that the NCs are passivated by (SPECIFY). In general, PA-capped NCs show near unity PLQY with uncommon truncated shape, and high stability against dilution.

In yet another study, we investigated the interaction between neutral ligands and LHP NCs, namely DDABr-capped $CsPbBr_3$ NCs. Among various neutral ligands tested, it was found out that OLPA molecules are able to strip a large fraction of DDA surface species. Specifically, the addition of 3 equivalents (with respect to Br surface sites) of OLPA molecules results in 40% of DDA stripping out from NC's surface. Surprisingly, after such loss of ligands the PLQY, morphology and phase of $CsPbBr_3$ NCs remain unaltered, empirically confirming the defect tolerance of LHP NCs.

We also studied the surface chemistry of Pb-free double perovskite NCs. We optimized the optical properties of Bi-doped Cs2(Na,Ag)InCl6 NCs by systematically varying the ligands combination (amine+carboxylic acid). We found out that both ligands are anchored to the surface of the NCs and the ligands density is 4.9 ligands/nm^2. Moreover, we observed that even with the best ligands combination the PLQY of the NCs was still low (37%) indicating that even a "good" surface passivation is not enough to efficiently passivate these NCs. These results combined with our DFT calculations suggest that such DP NCs are characterized by a high density of non-radiative surface traps, most likely due to Cl vacancies.

We also investigated the optical physical behavior of Sb^{3+} centers in different coordination environment. The $Rb_7Sb_3Cl_{16}$ NCs were composed by isolated $[SbCl_6]^{3-}$ octahedra and $[Sb_2Cl_{10}]^{4-}$ dimer. The isolated $[SbCl_6]^{3-}$ octahedra show dual emission under different excitation, whereas the $[Sb_2Cl_{10}]^{4-}$ dimer is non-emissive even in cryogenic temperature. The rich optical behavior of the Sb-based metal halides was evidenced in this work and it provide a guideline for developing brightly emitting metal halide systems based on Sb^{3+} ions.

In the final part, we have investigated a special LHP species, so called NCLs, which was regard as intermediate between molecular precursors and solid LHP NCs. We here firstly revealed their shape and structure by SXAX, WAXS and PDF analysis. The NCLs has an orthorhombic $CsPbBr_3$ phase and an oblate spheroid shape having equatorial length of 13±2 nm and polar diameters of 1.6±0.4 nm. The investigation on the structure of $CsPbBr_3$ NCs show some light on the pre-nucleation stage of LHP NCs.

Outlook:

Lead halide perovskite nanocrystals

LHP NCs are still the most promising candidates for LED, PV applications, due to their excellent optical properties. However, their instability limits their commercial application. A solution to improve their stability would be their encapsulation inside robust inorganic shell materials (eg. CdS, ZnS, $NaYF_4$). The growth of such inorganic shells requires a long reaction time and high temperatures (> 200 °C). At those temperatures LHP NCs are not stable and tend to dissolve or being etched. In this regard, our new developed PA synthesis method has a high boiling point and avoid the use of amine. The PA assisted synthesis method could be helpful on the shell growth of LHP NCs.

The ligand stripping procedure, developed here, could be exploited to produce LHP NC films with improved electric conductivity, due to the minimal content of insulating ligands. Such NC films could be then tested/employed in LED devices.

Lead free metal halide nanocrystals

Lead free metal halide NCs are defect sensitive and thus its optical properties is not comparable to its bulk counterpart and LHP NCs. New passivation strategy targeting on lead free metal halide NCs should be developed. Specially, the $Rb_7Sb_3Cl_{16}$ NCs could be suitable for thermometry application which don't rely on high PLQY but on the sensitive lifetime-temperature relation.

Perovskite nanoclusters

Perovskite NCLs are a very new species and their structure was just revealed by our work. Due to the uniform size and shape of NCLs, they have a strong tendency to form large superstructure. In such structures, the non-radiative channel of single NCL might be suppressed by NCL-NCL interaction in the superstructure. Therefore, we expect that the NCLs will show an aggregation dependent emission behavior. In details, we expect that the NCL superstructures will have a brighter PLQY (than that of isolated NCLs) and different superstructure will have different optical behavior, although they share the same repeating units.

Acknowledgments

When I received the PHD offer, three years ago, I had no confidence to complete the PHD period aboard. In that time, I told myself if I could complete the 12 km running, then you must can complete the PHD running also. I indeed completed 12 km running in that time, and indeed completed my PHD period now. Here I would like to thanks the following people. Thank to them who support me in the past three years.

I would like to thank Liberato Manna and Luca de Trizio firstly. Liberato always have passion on academic discussion and have infinite patience for me. Liberato also often give some guideline for my research work. Some of them is in my heart like ‘before starting a project, evaluating if it would be interesting for your science community’ and ‘always write a simple story and focus one or two point of it’. I would also like to thank him for giving me the chance to complete an important review paper in the last stage and I think it is the best ending gift for me. A lot thanks to Luca de Trizio, who is my super supervisor and super friend at the same time. Luca give me the most idea and discussion on my PHD period. He is always high efficient and positive. Also, Luca pay most effort on correcting my ‘magic English’ in my manuscript and thesis writing. Moreover, Luca is also the supervisor for the ‘PHD degree’ of climbing major. I really enjoy this sport!

Here also a special thanks to Kui Yu, which is the supervisor in my bachelor and master period. She recommended me to Liberato and give me a lot encourage in the aboard PHD life. Thanks a lot!

I also thanks to Ivan Infante, Luca Goldoni, Juliette Zito, Zhiya Dang, Dmitry Baranov, Sergio Brovelli, Valerio Pinchetti, Simone Lauciello, Guilherme Almeida, Ahmed L Abdelhady, Mengjiao Wang, Fang Chen, Muhammad Imran, Sungwook Park, Mai Ngoc An, Stefano Toso, Ying Liu, Dongxu Zhu, Zheming Liu, Zhaohui Shen, Aniruddha Ray, Michele Ghini. For all discussion and help from them in lab and office.

I also thanks to the excellent technicians, including Simone Nitti, Gabriele La Rosa, Giammarino Pugliese, Filippo Drago and Francesco De Donato. They always provide necessary help on purchasing, shipping, test and technique support. A lot thanks to Iulia Manolache Orlatan who help me in course and enrollment.

I feel also happy to supervise the Angela E. M. Melcherts, who is very smart and positive student. It’s very nice to work with you on research and we also have very nice discussion on economy and politics, although in very different views.

In the last, give the most many thanks to my family, my parents and my young brother. Thanks to your support. I miss you all so much!

Thanks to all the mentioned people. Genova is not a joke! Great Genova!

About the Author

Name: 张保卫/Baowei Zhang
Birth Date: 1992-08-27
Email: baowei.zhang@iit.it;
1971197959@qq.com

Education

PHD: 2018-2022

Italian Institute of Technology-*Genova University*
https://en.wikipedia.org/wiki/Istituto_Italiano_di_Tecnologia;

PHD major: Nanochemistry
Synthesis of lead and lead-free metal halide materials (perovskite) and its surface chemistry and optical-physical process in strong quantum confined region;

PHD supervisor: Liberato Manna,
Ranked #24 among the top 100 Chemists of the 2000-2010 decade by Thomson Reuters; citation: 49956
information link: https://www.iit.it/it/people-details/-/people/liberato-manna;
https://scholar.google.it/citations?user=hWWqp5MAAAAJ&hl=en&oi=ao.

Master: 2015-2018

Sichuan University, Physics College;

Master major: Physical chemistry
Nucleation and phase transformation of colloidal semiconductor quantum dots;

Master supervisor: 余睽/Kui Yu,
Changjiang Distinguished Professorship，
Associate Editors of ACS Applied Material & interface;
information link: http://iamp.scu.edu.cn/en/s-faculty/201806/142.html

Bachelor: 2011-2015

Sichuan University, Chemistry College;

Bachelor major: Physical chemistry
Nucleation and growth of colloidal semiconductor quantum dots;

Bachelor supervisor: 余睽/Kui Yu,

Publication list:

Google scholar link: https://scholar.google.it/citations?user=9ojO9mkAAAAJ&hl=en

9. **Zhang, B.**; et al Anisotropic perovskite nanocrystals. *Chemical Review*. **2022.** (**invited article, *In preparation.)***

8. **Zhang, B.;** Altamura, D.; Caliandro, R.; Giannini, C.; Peng, L.; De Trizio, L.; Manna; L. Stable CsPbBr3 Nanoclusters feature a Disk-like Shape and a Distorted Orthorhombic Structure. *J. Am. Chem. Soc.* **2022. Accepted.**

7. Zaccaria, F.; **Zhang, B.;** Goldoni, L.; Imran, M.; Zito, J.; van Beek, B.; Lauciello, S.; De Trizio, L.; Manna, L.; Infante, I. The Reactivity of $CsPbBr_3$ Nanocrystals towards acid/base Ligands; *ACS Nano* **2022,** *16*, 1, 1444–1455.

6. **Zhang, B.**; Pinchettic, V.; Zito, J.; Ray, A.; Melcherts, A. E. M.; Ghini, m.; Pianetti, A.; Infante, I.; Brovellic, S.; De Trizio, L.; Manna, L. Isolated $[SbCl_6]_3$- Octahedra are the Only Active Emitters in $Rb_7Sb_3Cl_{16}$ Nanocrystals. *ACS Energy Lett.* **2021,** *6*, 3952−3959.

5. **Zhang, B**.; Goldoni, L.; Lambruschini, C.; Moni, L.; Imran, M.; Pianetti, A.; Pinchetti, V.; Brovelli, S.; De Trizio, L.; Manna, L., Stable and Size Tunable $CsPbBr_3$ Nanocrystals Synthesized with Oleylphosphonic Acid. *Nano Lett.* **2020,** *20* (12), 8847-8853.

4. **Zhang, B**.; Wang, M.; Ghini, M.; Melcherts, A. E. M.; Zito, J.; Goldoni, L.; Infante, I.; Guizzardi, M.; Scotognella, F.; Kriegel, I.; De Trizio, L.; Manna, L., Colloidal Bi-Doped $Cs_2Ag_{1-x}Na_xInCl_6$ Nanocrystals: Undercoordinated Surface Cl Ions Limit their Light Emission Efficiency. *ACS Mater. Lett.* **2020,** *2* (11), 1442-1449.

3. **Zhang, B.**; Goldoni, L.; Zito, J.; Dang, Z.; Almeida, G.; Zaccaria, F.; de Wit, J.; Infante, I.; De Trizio, L.; Manna, L., Alkyl Phosphonic Acids Deliver $CsPbBr_3$ Nanocrystals with High Photoluminescence Quantum Yield and Truncated Octahedron Shape. *Chem. Mater.* **2019,** *31* (21), 9140-9147.

2. **Zhang, B.**; Zhu, T.; Ou, M.; Rowell, N.; Fan, H.; Han, J.; Tan, L.; Dove, M. T.; Ren, Y.; Zuo, X.; Han, S.; Zeng, J.; Yu, K., Thermally-induced reversible structural isomerization in colloidal semiconductor CdS magic-size clusters. *Nat. Commun.* **2018,** *9* (1), 2499.1-1.

1. Zhu, T.; **Zhang, B.**; Zhang, J.; Lu, J.; Fan, H.; Rowell, N.; Ripmeester, J. A.; Han, S.; Yu, K., Two-Step Nucleation of CdS Magic-Size Nanocluster MSC–311. *Chem. Mater*. **2017,** *29* (13), 5727-5735.